RHEOLOGY, STRUCTURE, AND STABILITY OF CARBON NANOTUBE –

UNSATURATED POLYESTER RESIN DISPERSIONS

Except where reference is made to the work of others, the work described in this thesis is my own or was done in collaboration with my advisory committee. This thesis does not include proprietary or classified information.

_____

Matthew Jay Kayatin

Certificate of Approval:

_____	_____
Steve R. Duke Associate Professor Chemical Engineering	Virginia A. Davis, Chair Assistant Professor Chemical Engineering
_____	_____
W. Robert Ashurst Assistant Professor Chemical Engineering	George T. Flowers Dean Graduate School

RHEOLOGY, STRUCTURE, AND STABILITY OF CARBON NANOTUBE – UNSATURATED POLYESTER RESIN DISPERSIONS

Matthew Jay Kayatin

A Thesis

Submitted to

the Graduate Faculty of

Auburn University

in Partial Fulfillment of the

Requirements for the

Degree of

Master of Science

Auburn, Alabama
December 19, 2008

RHEOLOGY, STRUCTURE, AND STABILITY OF CARBON NANOTUBE –

UNSATURATED POLYESTER RESIN DISPERSIONS

Matthew Jay Kayatin

_____
Signature of Author

_____
Date of Graduation

THESIS ABSTRACT

RHEOLOGY, STRUCTURE, AND STABILITY OF CARBON NANOTUBE – UNSATURATED POLYESTER RESIN DISPERSIONS

Matthew Jay Kayatin

Master of Science, December 19, 2008
(B.S., West Virginia University, 2005)

279 Typed Pages

Directed by Virginia A. Davis

In this research, the first detailed study characterizing the dispersion of carbon nanotubes into an isophthalic unsaturated polyester resin was performed. To eludicate the potential for mechanical property enhancement, dispersions of various carbon nanotubes were studied prior to cure by means of bulk rheological behavior. The greatest enhancement in viscoelastic response was found upon the incorporation of single-walled carbon nanotubes over both acid oxidized single-walled carbon nanotubes and vapor grown carbon fibers. The application of high shear mixing was found to be effective in reducing initial nanotube aggregate size, but unable to exfoliate individual single-walled carbon nanotubes alone.

For single-walled carbon nanotube dispersions, an intriguing concentration dependant linear viscoelastic response was observed; this resulted from elastic nanotube

network formation, through the percolation threshold. Between nanotube loadings of 0.025% vol. and 0.250% vol., the dependence of concentration on viscoelastic response was removed through colloidal scaling; this revealed insight into the network development through mastercurves. Over the range of concentrations from 0.0030% vol. to 0.010% vol., the dispersions behaved as a viscous liquid. Studying the reduced complex viscosity, non-Brownian behavior was observed in response to applied shear stresses, as predicted by the rotational Peclet number.

For dilute dispersions of single-walled carbon nanotubes (0.0050% vol.), low shear rate induced aggregation phenomena was observed. The aggregation driving force was determined to be chemical in nature. Surface analysis indicated aggregation was avoided in the presence of hydroxyl/phenolic functionalities, as these groups could hydrogen bond with the isophthalic polyester. However, no sample dispersions were found to be thermodynamically stable. This observation was correlated with estimations of the enthalpy of mixing, indicating a positive Gibbs free energy upon mixing.

The potential use of oxidized carbon nanotubes was investigated but unsuccessful for all as-produced samples. The presence of carboxylic acid functionalities was confirmed after these treatments. Acid oxidized nanotubes treated with ethanol did show some degree of mixing, but could not compare in performance to pristine single-walled carbon nanotube dispersions.

Finally, the discovery of a lyophilization based method for creating aligned self-assembled films from aqueous, oxidized nanotube dispersions was reported. The nanotube self-assembly was believed to occur during the freezing step. This method appears to be facile and shows great promise as a significant advancement in the field.

ACKNOWLEDGEMENTS

I would like to thank my committee members for providing both their time and knowledge in the preparation and critical review of this manuscript. Additionally, I would like to thank Dr. Virginia Davis for allowing me to chase my curiosities within this research. Also, thanks are due to Dr. Mark Byrne for often providing advice unrelated to research during my stay in Auburn. I would also like to thank Dr. Steve Duke for providing me with my first opportunity at teaching; a truly invaluable experience.

Acknowledgement and thanks are also extended to Amogh Karwa and Vinod Radhakrishnan for their time on spent on SEM. Additionally, I would like to thank Dr. Michael Bozack, Dr. Ram Gupta, and Dr. Anne Gorden for useful discussions related to this work.

The bibliography was prepared in the style of CARBON. Microsoft Word, Microsoft Excel, Microsoft PowerPoint, and MDL ISIS/DRAW were used to prepare this manuscript.

TABLE OF CONTENTS

LIST OF FIGURES

LIST OF TABLES

1. INTRODUCTION

Since the discovery of carbon nanotubes (CNTs) in the early 1990s there has been a growing interest in nanotube based research as indicated by reported trends in published articles and patents. Recently, a similar trend has been observed for carbon nanotube-polymer composites [1]. Without question, this is a result of the unique combination of physical properties possessed by carbon nanotubes and the desire to translate these characteristics to polymers. Furthermore, the high surface area and large aspect ratio (length to diameter ratio) of this material, along with low mass density, make carbon nanotubes an ideal reinforcement material for composite systems. However, as a result of the nanoscopic dimensions and high aspect ratio of CNTs, deviations from expected physical behavior for traditional composite systems are found. This behavior is indicative of the increased interfacial interaction between nanotubes with themselves as well as the polymer matrix and must be addressed to exploit the full potential of carbon nanocomposite systems [2].

A significant hurdle in the efficient preparation of polymer - carbon nanotube composites lies in effectively dispersing the CNTs throughout the matrix phase. Due to the smooth and highly polarizable sidewalls, single-walled carbon nanotubes (SWNTs) often exist in entangled crystalline ropes or bundles with a characteristic binding energy of ~0.5 eV/nm of parallel contact. Given that nanotube length is often on the order of hundreds to thousands of nanometers, separating nanotubes from bundles is a significant

undertaking. In light of this, a variety of chemical and physical techniques have been employed in the literature to process nanotubes as individuals. Often the successful processing route is material or application dependant with solution based processing being highly effective for thermoset plastics.

In this work, the first detailed study on the shear dispersion of carbon nanotubes into an isophthalic unsaturated polyester resin (UPR) is reported. The effect of incorporating pristine SWNTs, chemically oxidized SWNTS, or vapor grown carbon fibers into UPR was studied. The resulting complex fluid was studied prior to cure as a means of identifying what physical phenomena may influence the final composite properties. Specifically, bulk rheological properties of the system were measured revealing the unique viscoelastic behavior of this new class of material. It was found that the nanotubes formed an elastic network above a critical concentration and show non-Brownian behavior under imposed shear. Additionally, an interesting low shear aggregation phenomena was discovered. Comparative analysis with respect to varying nanotube surface chemistry was performed in order to determine what controlling factors are responsible for dispersion stability.

The results of this work are intended to motivate increased interest and understanding with respect to producing commercially viable carbon nanotube - UPR based composite materials, as well as open the door for possible new material technologies and applications. Also, *en route* to developing unique methods for dispersing chemically oxidized nanotubes a new technique enabling the self - assembly of aligned and transparent nanotube films though lyophilization was discovered.

Finally, this manuscript was prepared with the intention of providing both new and current carbon nanotube-polymer composite researchers with a thorough review of the important underlying fundamental science related to the preparation of nanocomposite systems through solution based methods. To this end, a critical analysis of the current state of nanotube solution theory appearing in the literature was performed.

2. BACKGROUND

Polymers and Their Composites:

Polymers, in general, can be classified into two distinct classes based on their response to heat [3]. Thermoplastic polymers, in the simplest sense, melt when heated and re-solidify when cooled. It is this inherent phase cycle of thermoplastics which allows them to be repeatedly processed and reprocessed. Conversely, thermosetting plastics cure with the onset of heating and therefore do not melt when reheated but significantly degrade. A simple explanation of this phenomenon can be visualized by examining the polymer chain structures in Figure 1.

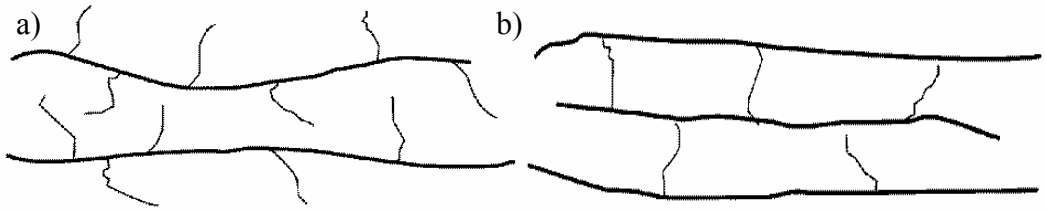

Figure 1: Thermoplastic (a) and thermoset (b) polymer structures. Image reproduced from Kumar and Gupta (2003) [3].

Figure 1a displays a slightly branched thermoplastic structure in which the different polymer molecules associate through secondary associative forces (i.e. van der Waals). When energy is supplied to the structure the secondary forces are overcome and the thermoplastic polymer melts. In contrast, Figure 1b displays a thermoset polymer post-cure. In this structure, the polymer molecules associate into a three-dimensional network supported by covalent bonds or cross-links between chains. As opposed to van der Waals association found in thermoplastics, the energy required to break these covalent cross-links is typically greater then the energy required to degrade the polymer itself [4]. By

this analysis one can argue why thermoset plastics are advantageous for high temperature applications; thermosets hold their shape at temperatures which thermoplastics cannot.

As a result of their high cross-link density thermoset plastics show increased resistance to heat but are typically hard and brittle, limiting their potential for load bearing applications [4]. These shortfalls can be overcome by processing thermoset plastics as composite materials, a technique that has been used in common practice for some time and discussed in later sections. Polymer composites are a class of materials in which some reinforcement with desired properties, for example a fiber, is incorporated into a polymeric matrix. Traditional fiber reinforcement materials include, but are not limited to, glass, carbon, and Kevlar fibers. The properties of the reinforcing material are translated to the matrix material and realized in the resulting composite. Some common examples of mechanical properties that composite processing may enhance include tensile strength, impact strength, and toughness [5].

Polymeric Carbon Nanotube Composites:

In recent years there has been increasing research attention towards processing polymeric nanocomposites [6-8]. Similar to traditional polymer composites, a nanocomposite still comprises of a two-part system of a filler and matrix phase. However, one dimension of the reinforcement material exists between 0.1 – 100 nm, an order of magnitude greater than its atomic constituents. This "nano-size" yields a unique dependence on material properties and high surface areas not found in traditional composite systems [8]. In fact, it is the very high surface area per unit volume ratio that makes nanomaterials such as carbon nanotubes attractive as reinforcement material for

polymer matrices. As the interfacial surface area between the polymer matrix and nanomaterial increases, the macroscale properties of the bulk composite become dominated by the interface [8]. Moreover, since the interfacial area is quite large per unit volume one would expect that low loadings of nanomaterial reinforcement show marked property enhancement. In summary, the exceptionally high aspect ratio, strength, and stiffness of carbon nanotubes, in combination with a low density, make nanotubes an ideal candidate for reinforcement in polymeric materials [9].

While many thermoplastic polymers have been used to construct carbon nanotube-polymer composites, the majority of work with thermoset polymers has largely focused on epoxy based resins [1, 6, 8, 10-13]. However, vinyl ester (VE) resins have recently emerged in growing popularity as nanocomposite matrix polymers [8, 14-16]. VE resins were first commercialized in 1965 by Shell Chemical under the trade name Epocryl and show excellent corrosion resistance [17]. An example synthesis scheme of a VE monomer from an epoxy resin can be found in Thostenson et al. (2008) [15]. Essentially, vinyl esters are methacrylated epoxies which can be cured in the same manner as unsaturated polyester resins (UPR) [18]. Neat unsaturated polyester resins and VE resins are alike in that their high viscosity requires dilution with styrene monomer for processing and cure. But, in contrast to Epoxy and VE resins, unsaturated polyester resins have rarely been used in the literature for nanocomposite research. In fact, Seyhan et al. (2007) claim to be the first to study the processing and properties of CNT-UPR composite systems using an isophthalic polyester resin [19]. Most recently, Battisti et al. (2008) have also studied the "on-line" dispersion of CNT using an isophthalic polyester resin [20]. It is important to note that the common thread between the thermoset research

to date has been the preference of multiwalled carbon nanotubes (MWNTs) in the majority of all work. Presumably this is because of the relative ease of dispersing MWNTs over single-walled carbon nanotubes (SWNTs).

Commercial Applications:

In spite of intense research interest CNT based nanocomposites are just starting to become available commercially [1]. Statically dissipative plastics have been brought to market by Hyperion Catalysis that possess improved toughness while retaining surface appeal. Additionally, Unidym has developed CNT based transparent conductive films for use in touch panel, solar, and display applications. Additionally, in the sporting goods business nanocomposites containing CNT have emerged in several products. For example, Easton has developed a resin containing CNTs for use in the manufacture of bicycle components and baseball bats. The resin is used fill in void spaces between traditional carbon fibers which the company claims has "radically improved strength and toughness" in these areas [21]. Likewise, Babolat has used CNT to stiffen areas of their tennis racquets. The company claims a 20% increase in torsion resistance with more power and stability [22]. Stultz golf has developed golf club shafts using the carbon fiber, CNT, and resin technology as well [23]. It is important to point out that the improvements enjoyed by the consumer in product performance are also supplemented with a reduction in weight, as discussed in later sections.

The promise of producing composite materials with improved performance from lightweight components has potential applications in a variety of industries. Of particular interest is the ground and aerospace transportation industry, as well as applications in

defense. The motivation is simple to understand by considering the work required to propel a jet engine. The force necessary to move the engine over a distance could be directly reduced if the weight of the engine components were reduced. In turn, if the work requirement is reduced the amount of energy needed to propel the jet has decreased leading to an increase in fuel efficiency. A perfect example of the use of composites for aerospace applications is the Boeing 787-3 Dreamliner. This aircraft has a capacity of 290-330 passengers [24]. In order to safely compensate for the weight of this number of passengers lower fuel consumption was required. The only expendable variable was the weight of the airliner components themselves. To this end, Boeing used approximately 50% wt. composite materials in their design [25]. Specifically, 35,000 kg of the traditional carbon fiber reinforced plastic, the primary composite material in the aircraft, was used. With respect to performance this translates to a weight reduction of 30,000-40,000 lbs over the comparably sized Airbus A330-200 and allowing for a 45% wt. increase in cargo carrying capacity. Additionally, a 20% reduction in both fuel consumption and emissions was achieved [24]. The use of composite materials to construct the fuselage allowed the elimination of 1,500 aluminum sheets and 40,000-50,000 fasteners. This reduction and replacement of parts with corrosion resistant materials will improve reliability and maintenance costs in the long run.

Using the 787-3 Dreamliner as an example of how traditional composite materials can enable improved performance in lightweight applications the question remains as to what can be achieved from nanocomposite materials and to what extent the limits of application may be realized. It is for this reason that there is interest in nanocomposite

research, to design the next class high performance materials with the hope of developing enabling technologies yet to be seen.

Materials:

In this research it was desired to study the mechanical property enhancement achieved by the addition of carbon nanocylinders into an unsaturated polyester resin. Specifically, an isophthalic polyester was used in conjunction with two different nanocylinder materials of varying dimension so as to provide a range of material aspect ratios. The carbon nanocylinders used in this work were vapor grown carbon nanofibers (VGCFs) and single-walled carbon nanotubes (SWNTs). The following sections are intended to give an exhaustive description of these materials.

Unsaturated Polyester Resins:

Unsaturated polyester resins (UPRs) are thermoset pre-polymers comprised of linear short chain oligomers. These oligomers are formed from the condensation polymerization of either saturated/unsaturated acids or acid anhydrides with difunctional alcohols or oxides [17]. The result is a viscous liquid or brittle solid depending on the degree of polymerization when initially terminated. Typical UPR molecular weights range from 1,200-3,000 g/mol represented by only a few repeat units (n = 3,4) in Figure 2 [17, 26]. UPR is readily soluble in styrene monomer and can be found in commercial solutions as high as 40% by weight styrene. The styrene serves both to lower the polymer viscosity for processing as well as act as a cross-linking agent between

unsaturation sites on adjacent oligimer chains to form a three-dimensional network structure.

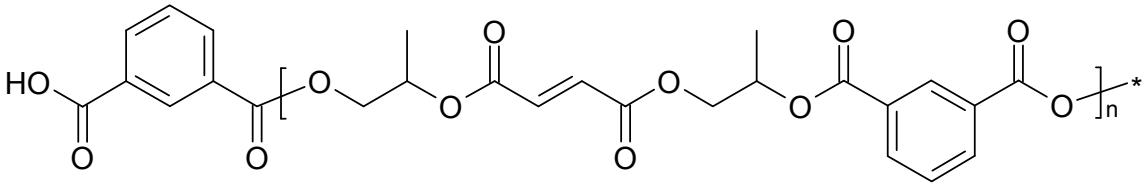

Figure 2: Idealized "baseline" chemical structure of a 1:1 isophthalic polyester constructed from equimolar ratios of isophthalic acid and maleic anhydride. Isophthalic polyesters are known for their corrosion resistance, superior mechanical properties, and higher heat distortion temperatures with respect to other types of thermoset polyester. Reproduced from Mallick (1997) [18].

It is the formation of a network that distinguishes thermoset polyester resins from other linear thermoplastic polyesters such as poly(ethylene terephthalate) [27]. Typical acids used in UPR production are phthalic anhydride, a saturated acid, or an unsaturated dicarboxylic acid such as maleic anhydride. Generally a diol such as propylene glycol or diethylene glycol is also used. Depending on the desired resin properties, the UPR recipe can be adjusted. For example, the addition of a saturated acid, such as isophthalic acid, decreases crosslink density upon cure which also serves to decrease brittleness, increase tensile properties, but lower thermal stability. Figure 3 displays the chemical structure of isophthalic acid. Also, fumaric acid is commonly used in place of maleic acid to increase impact resistance. If the resin is meant to have a shelf life an amount of a free radical scavenging inhibitor such as benzoquinone is added to prevent any premature polymerization. More detailed recipes for tailoring UPR properties can be found in

Mallick (1993) [4]. However, in general UPR can be formulated such that the final product is either hard and brittle or soft and flexible.

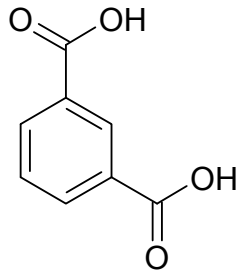

Figure 3: The chemical structure of isophthalic acid. In contrast to other unsaturated acids used in polyesters, there is no anhydride form of isophthalic acid. Reproduced from Mallick (1997) [18].

Curing is initiated by the addition of some type of organic peroxide and crosslinking propagates via a free radical reaction mechanism across the styrene molecule. Generally, the peroxide is cleaved creating a free radical which attacks the unsaturated vinyl-carbon bonds in styrene, whose structure is shown in Figure 4.

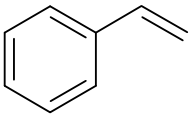

Figure 4: The chemical structure of styrene monomer. Crosslinking between UPR oligomers propagates through the $–CH=CH_2$ "tail."

Styrene radicals, in turn, attack unsaturation sites on the polyester oligomers and crosslink them by forming a bridge between adjacent molecules [4]. Typically for low temperature curing methyl-ethyl-ketone peroxide (MEKP) is used. To help facilitate curing cobalt based accelerator is added which aids in cleavage of the peroxide groups.

The cure time and conditions as well as the mechanical properties of UPRs vary with both the oligomer constituents, the degree of cross-linking, and the amount of condensation product trapped in the polymeric network. The fact that UPR can be cured at room temperature makes its application favorable for manufacture of large parts such as boat hulls or automobile bodies [26].

From a manufacturing standpoint, UPR is advantageous choice for its low viscosity, fast cure time, and low cost. However, its mechanical properties are generally not as favorable as those of epoxy resins. For cast UPR, a tensile strength of 34.5-103.5 MPa is expected with a tensile modulus of 3.1-3.45 GPa. On the other hand, cast epoxy resin can show a tensile strength and modulus as high as 130 MPa and 4.1 GPa, respectively. Conversely, the thermal properties of UPR show better high temperature performance compared to epoxy resins. The continuous working temperature for an epoxy resin is typically 150^{o}C or less. UPR shows heat deflection temperature as high as 205^{o}C making it a better choice for high temperature applications [4]. In addition, the mechanical disadvantages of UPR can be improved upon if processed as a composite material. In practice, the peroxide or curing catalyst is first added to the resin, blended, than the material is processed. Commonly UPR is compression molded into parts but can be resin-transfer molded for intricate geometries which are allowed to cure before removal [27]. If not molded, UPR is typically applied as a glass-fiber laminate. The high strength to weight ratio of polyester-glass laminates, microwave transparency, and corrosion resistance have led to use in many air transport applications [26]. One of the most common polyester laminates goes by the trade name Fiberglas® (Owens Corning). Fiberglas® is a glass-fiber laminate material which became popular in to 1940s and is

widely used in the automotive, marine, construction, and aerospace industries. Fiberglas® found its way as an alternative to heavy porcelain shower stalls and bathtubs but made a memorable impact in the construction of automotive parts when in 1953 Chevrolet produced the first Corvette with a Fiberglas® body [27, 28].

In the year 2000, UPR sales of 681 million kg were reported in the U.S. alone, ranking 3rd among thermoset plastics behind phenolic resins and polyurethane. This was over twice the amount of epoxy resin sold that year but less than 2% of the total market for plastics. It is interesting to note that thermosets were responsible for less than 14% of the total sales of ~42,900 million kg of polymer sold in 2000 [29].

Vapor Grown Carbon Nanofibers:

Vapor grown carbon nanofibers (VGCFs) are hollow shelled carbon fibers having various morphologies and outer diameters typically ranging from 50-200 nm [30]. Lengths of the as grown fibers can range from 10 μm to over 100 μm. The production of VGCFs is commonly a two step process where the fiber is grown catalytically in the axial direction and subsequently thickened by deposition on the outer diameter [31, 32]. Two common morphologies are the "bamboo" and "stacked cup" structured VGCFs as shown in Figure 5. The bamboo structured VGCFs are grown directly on a catalyst particle and show surface defects [33]. Stacked-cup VGCFs consist of truncated conical graphene layers that have a central hollow core. The inner and outer edges of stacked-cup VGCFs consist of exposed reactive graphene layers. The specific surface area of VGCFs is on the order of 10^2 m^2/g [34]. Some commercial available grades of VGCFs have been reported to contain both morphologies [30].

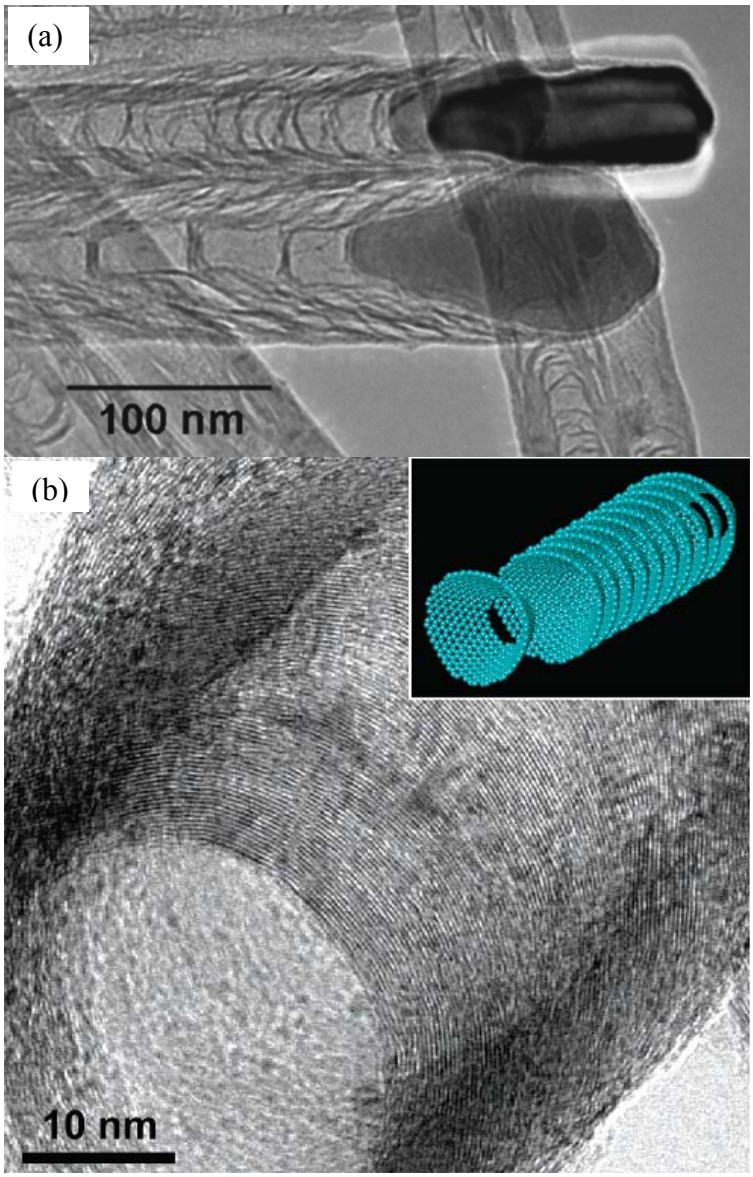

Figure 5: High resolution images of (a) bamboo structured VGCFs and (b) stacked cup structured VGCF. Images reproduced from Merkulov et al. (2000) and Endo et al. (2003), respectively [33, 34].

The tensile strength and tensile modulus of VGCFs has been measured experimentally as 2.92 GPa and 237 GPa, respectively, and are comparable to commercially available poly(acrylonitrile) fibers [35]. However, reported tensile moduli have been wide ranging

in the literature. Uchida et al. (2006) theoretically determined the modulus for the various VGCF morphologies to explain these discrepancies reporting a range starting as low as 50 GPa and as high as 775 GPa [30]. The thermal conductivity of VGCFs has been estimated as 1260 W/m-K [36]. The electrical resistivity of heat treated VGCFs has been reported as low as 0.1-1 μΩ-cm due to crystallization of the tube exterior [37].

Carbon Nanotubes:

Carbon nanotubes were first discovered by Iijima (1991) as needle-like structures deposited on an arc-discharge electrode used for fullerene production [38]. These needles appeared as coaxial tubes of graphite and were actually multiwalled nanotubes (MWNTs). Soon after, Ebbesen and Ajayan (1992) first produced MWNTs in gram quantities [39]. It was not until 1993 that single walled nanotubes (SWNTs) were intentionally produced [40, 41]. Dyke and Tour (2004) have described SWNTs as ladder polymers of carbon where more than one bond needs to be broken to cleave the backbone. However, SWNTs are far superior to typical ladder polymers since approximately 10-20 highly ordered carbon-carbon bonds per repeat unit need be cleaved for tube scission to occur. Since the sp^2 hybridized carbon-carbon bond is among the strongest known it is unlikely that a more robust material will ever be discovered [42].

Characteristics of Carbon Nanotubes:

Molecular Structure:

In general, SWNTs can be considered as seamless hollow cylinders of rolled graphene sheets having a diameter on the order of 1 nm and lengths typically no larger

than a micron. In some cases, isolated SWNTs have been grown as long as 4 cm [43]. Similarly, multi-walled carbon nanotubes (MWNTs) and double-walled carbon nanotubes (DWNTs) consist of coaxially arranged, nested cylinders of graphene. Each concentric layer is spaced 0.34 nm apart and the MWNTs have typical lengths on the order of microns with outer diameters ranging from 2-20 nm [1, 32]. Thus, SWNTs and MWNTs have aspect ratios of approximately 10^2-10^3 [32]. However, these parameters vary within, and between, samples and batches from various laboratories or manufacturers [1]. In absence of defects, the carbon atoms that comprise the graphene sheet are covalently joined to one another via sp^2 hybridized bonds. However, the strain associated with out of plane bending of the surface increases with decreasing tube radius and increases the sp^3 hybrid character of the surface [44-46]. Thus, small diameter CNTs are the most reactive. For this reason the larger diameter MWNTs show weak sp^3 character unless the surfaces are facteted [46].

All known preparations of SWNTs give mixtures of diameters, lengths, and chiralities [42]. The chirality of a CNT refers to the number of ways a graphene sheet may be rolled upon itself. Specifically, tube chirality is identified with a pair of integers (n,m) which in turn define the circumferential chiral vector from which the graphene is rolled upon. Equation 2.1 defines the chiral vector, $\mathbf{C}_h$.

$$\vec{C}_h = n\vec{a}_1 + m\vec{a}_2 \tag{2.1}$$

Figure 6 displays the geometrical constructs of $\mathbf{C}_h$ on a graphene lattice. The length of $\mathbf{C}_h$ is represented by vector **OA**, the nanotube circumference. Orthogonal to $\mathbf{C}_h$ lays the translation vector **T** which serves to define a unit cell. The chiral indices (n,m) describe the number of steps along the hexagonal unit vectors $\boldsymbol{a}_1$ and $\boldsymbol{a}_2$ as displayed by Figure 7.

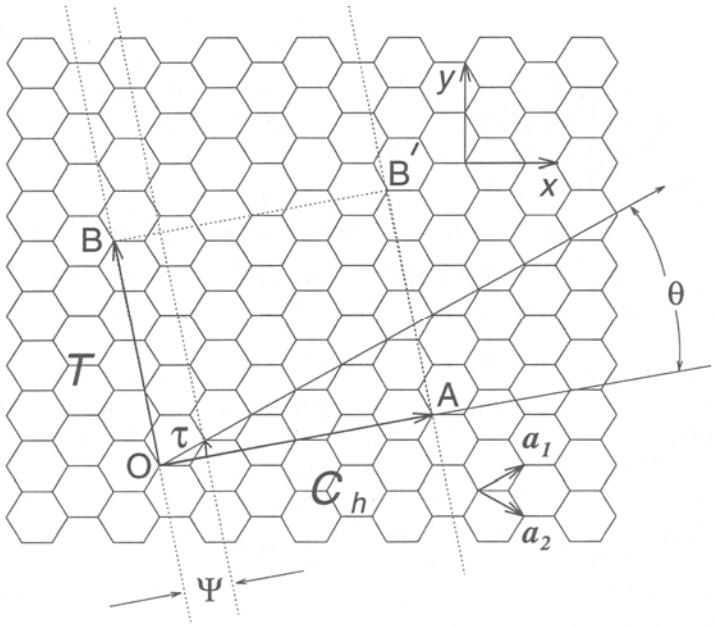

Figure 6: $\mathbf{C}_h$ is defined on the graphene lattice by unit vectors $\boldsymbol{a}_1$ and $\boldsymbol{a}_2$ and the chiral angle θ with respect to the zigzag axis (θ = 0°). The lattice vector of the 1-dimensional unit cell is defined by **T**. The rotation angle ψ and the translation τ constitute the basic symmetry operation $R = (\psi|\ \tau)$ for the carbon nanotube. The diagram is constructed for (n,m) = (4,2). Reproduced from Dresselhaus et al. (1995) [32].

The magnitude of the unit vectors $\boldsymbol{a}_i$ can easily be determined geometrically. The distance between adjacent vertices on a single hexagon is given by the carbon-carbon bond length ($L_{C\text{-}C}$), approximately 1.42 nm for graphite [32]. Considering that a hexagon can be divided into 6 equilateral triangles, each unit vector will bisect two equilateral triangles along a length of distance $\sqrt{3} \times L_{C-C}$, defining the lattice constant (0.246 nm). Likewise, the length of vector $\mathbf{C}_h$ shown by Equation 2.1 can be easily derived from Figure 7 using the lattice constant.

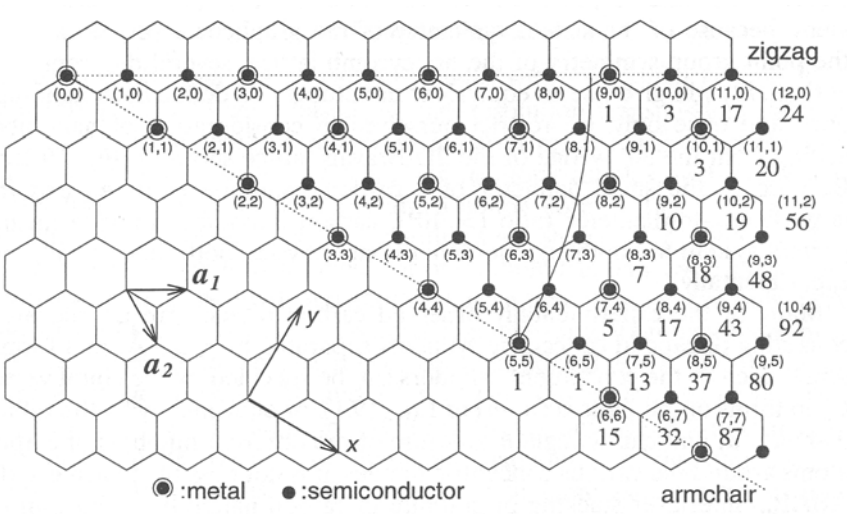

Figure 7: Possible vectors specified by (*n*,*m*) for general CNTs, including zigzag, armchair, and chiral tubes. Below each integer pair is listed the number of distinct caps that can be joined continuously to the CNT denoted by (*n*,*m*). Encircled dots denote metallic structure and small dots are for semiconducting tubes. Reproduced from Dresselhaus et al. (1995) [32].

Equation 2.2 displays this relationship between tube diameter and the magnitude of $\mathbf{C}_h$.

$$d = \frac{\sqrt{3}L_{C-C}\left(m^2 + mn + n^2\right)^{1/2}}{\pi} = \frac{\left|\vec{C}_h\right|}{\pi} \tag{2.2}$$

The division by π is necessary to relate the tube circumference to the diameter. As displayed by Figure 7 the indicies (*n*,*m*) and therefore $\mathbf{C}_h$ determine the tube's electronic structure. Despite the structural similarity to a single sheet of graphite, which is a semiconductor with zero band gap, SWNTs may be either metallic or semiconducting [47]. Specifically, if the difference $n - m$ is nonzero and divisible by three, the nanotube is considered semimetallic (or simply metallic) with a bandgap on the order of meV. If the difference is equal to zero the nanotube is metallic (ballistic conductor) with a bandgap of zero. In all other cases where the difference $n - m$ is nonzero and not

divisible by three the nanotube is semiconducting with a band gap ranging from approximately 0.5 to 1 eV [42]. Structurally the vectors (n,0) and (0,m) denote zig-zag tubes and the vectors having indices that match denote armchair tubes, named by examining a ring of carbon atoms around the circumference. Both armchair and zig-zag tubes are achiral since they have a mirror plane whereas all other vectors where n is not equal to m or zero are chiral (twisted). Figure 8 displays a schematic of each type.

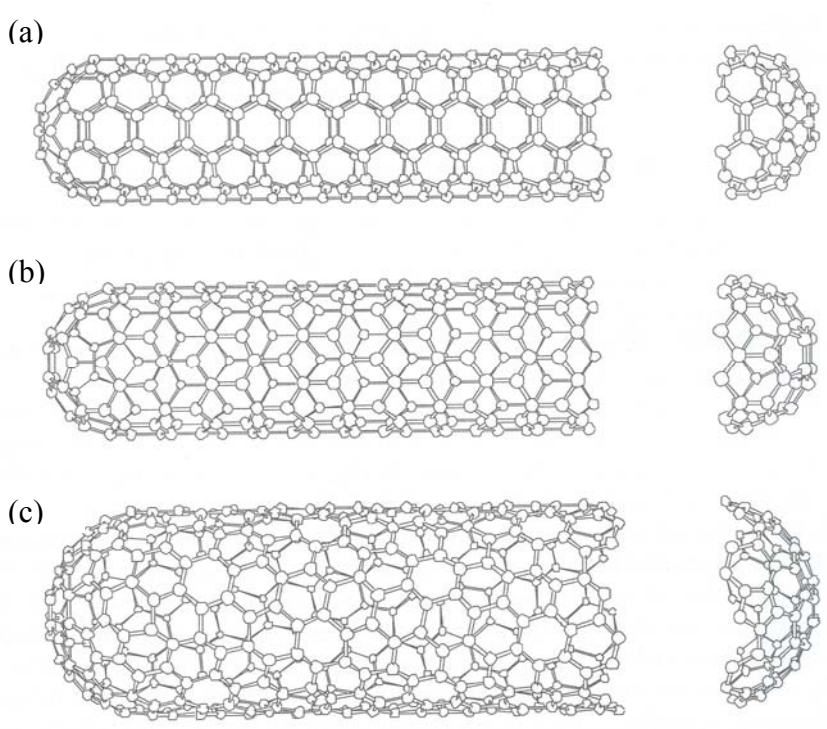

Figure 8: Schematic theoretical model for a SWNT with the tube axis normal to: (a) the $\theta = 30^{o}$ direction with (n,m) = (5,5) (an "armchair" tubule), (b) the $\theta = 0^{o}$ direction with (n,m) = (9,0) (a "zigzag" tubule), and (c) a general direction $0 < \theta < 30^{o}$ with (n,m) = (10,5) (a "chiral" tubule). Reproduced from Dresselhaus et al. (1995) [32].

Mechanical Properties:

The mechanical properties of carbon nanotubes (CNT) have been determined by both experiment and theory. Gao et al. (1998) theoretically determined the Young's modulus of an individual SWNT to be approximately 0.64 TPa [48]. Additionally, average experimental values for individual SWNTs have been reported as 1.25 TPa [49]. This is also consistent with experimental values for SWNT ropes ranging from 0.32-1.47 TPa [50]. Since small diameter SWNT ropes have been extended elastically to approximately 5.8 % the SWNT tensile strength can be calculated as approximately 37 GPa [51]. Taking into account the low density of the hollow carbon shells comprising CNT the modulus and strength can be normalized revealing remarkable comparisons with structural materials. For typical SWNTs the density normalized modulus is approximately 19 times that of steel and 2.4 times that of silicon carbide nanorods. Likewise, the density normalized tensile strength is approximately 56 times that of steel wire and approximately 1.7 times greater than silicon carbide [47]. For these reasons there is great interest in constructing macroscopic CNT materials while retaining the outstanding properties of individual tubes.

Electronic and Thermal Properties:

The electronic properties of MWNTs and SWNTs are quite similar in perfectly structured CNTs [47]. Because of their nearly one-dimensional structure electronic transport occurs ballistically in the axial direction [52]. Therefore high currents can be carried with resistivity on the range of 0.1-200 μΩ-cm [53, 54]. The thermal conductivity for an individual MWNT has been reported in excess of 3000 W/m-K [55]. Likewise, the

thermal conductivity for SWNTs was found to approach or exceed that of diamond, the previous benchmark material [56]. Additionally, superconductivity has been observed in SWNTs at extremely low temperatures [57, 58]. Thermal stability has been reported at temperatures as high as 2800^{o}C in vacuum and 750^{o}C under air [59].

Surface Area:

It is this complement of excellent material properties coupled with low mass density and high aspect ratio (~10^2 - 10^3 for SWNTs) that make nanotubes desirable alternatives for traditional micron to millimeter scale fillers in polymer composite manufacturing [1]. In particular, high aspect ratio nanocylinders are geometrically unique in that their surface area per unit volume provides an enormous means of communication between the polymer matrix and dispersed phase; giving rise to great opportunity for effective load transfer [2]. For comparison to traditional composite systems, reducing the fiber diameter from the order of microns to nanometers increases the surface area per unit volume by three orders of magnitude [8]. Specifically for SWNTs this value is as large as 10^3 - 10^4 m^2/ml [2]. But, in order to take advantage of the excellent properties of CNTs they first must be separated from themselves. It is the poor solubility characteristics of SWNT that have hindered their chemical manipulation and thus their use in applications [60].

Colloidal Interactions:

van der Waals Forces:

The same forces which allow the ladybug to crawl upon ceilings or permit the gecko to scale horizontal walls is also responsible for the binding together of nanotubes in ropes [61]. Indeed, such phenomenon are a result of the same van der Waals force long understood to show negative deviations from Boyle's law of ideal gases. For a closed system, this is interpreted as an attractive force between particles or atoms which reduces the force exerted on the container in a manner inversely proportional to the square of the system volume [62]. These forces allow condensed phases to form and are stronger within solids and liquids than gases. But, what is important to note is that the observance of the van der Waals pressure indicates that even electrically neutral bodies attract [63].

The empty space between two point charges or atoms is actually a constant omni-directional inundation of electromagnetic waves. This is a result of continuous jostling of charges in matter leading to spontaneous and transient electromagnetic fields. Additionally, the charges of matter both influence and respond to other currents and fields. The additive effects of coordinated interactions of electromagnetic stimuli are what create the van der Waals force. Consider an atom surrounded by electromagnetic waves traveling in all directions. Now allow the presence of a neighboring atom to interrupt fluctuations between the two bodies. The net result is that the particles are pushed together. An excellent analogy was given by Parsegian (2005) in which a rowboat on rough water is heading to shore. Once the boat is close enough to the dock to quell the waves between the two, the surrounding wake will push the boat in [63].

In order to extend this idea and describe larger bodies than atoms molecules Hamaker (1937) introduced the concept of pairwise-summation for particles [64]. The coefficient of interaction between objects is known as the Hamaker constant A and is a function of the material. The Hamaker constant is typically on the order of 10^{-19} to 10^{-21} J [64, 65]. Equation 2.3 gives the expression for A.

$$A = \pi^2 C \rho_1 \rho_2 \tag{2.3}$$

Here C is the coefficient in the atom-atom pair potential and ρ_1 is the number of atoms per unit volume in Body 1. The number of atoms per unit volume of Body 2 is represented by ρ_2 [65]. The atom-atom pair potential is given by Equation 2.4.

$$W = \frac{-C}{D^6} \tag{2.4}$$

The potential W is the work required to bring the two atoms from infinite separation to D distance apart and is negative due to the sign convention used for attraction. The treatment and correlation between attractive forces of curved or nonlinear surfaces with planar geometries was handled by Derjaguin (1934) [66]. This idea was termed as the "Derjaguin approximation" and took the attractive potential for planar surfaces and adapted it to describe curved surfaces at small separation. In this research, interactions between cylindrical CNTs are of interest so only these shapes are considered. For the non-retarded van der Waals interaction free energy between parallel cylinders of different radii the interaction potential is described by Equation 2.5 [65].

$$W = \frac{-AL}{12\sqrt{2}D^{3/2}} \left(\frac{R_1 R_2}{R_1 + R_2} \right)^{1/2} \tag{2.5}$$

This expression for parallel cylinders yields the energy per unit length L. The distance of separation between their surfaces is represented by D and the cylinders have radii of R_1 and R_2. The attractive force between the cylinders can be found by taking the derivative of the work with respect to separation distance as shown by Equation 2.6.

$$F = \frac{-dW}{dD} \tag{2.6}$$

In general for parallel cylinders the force is inversely proportional to $D^{5/2}$ power as shown by Equation 2.7, where the terms for the particle size were omitted to highlight the trend.

$$F \propto -ALD^{-5/2} \tag{2.7}$$

If the cylinders are crossed instead of parallel the interaction potential is in purely energetic units with no length dependence. Equation 2.8 gives the interaction energy between perpendicular cylinders.

$$W = \frac{-A\sqrt{R_1 R_2}}{6D} \tag{2.8}$$

Considering the trend with separation the force is inversely proportional to the square of the separation distance as displayed by Equation 2.9.

$$F \propto -AD^{-2} \tag{2.9}$$

In contrast to the treatment of pairwise atom interactions the Hamaker constants are typically determined from experimental data. In this manner, the properties of the bulk material are averaged rather then examining individual constituent atoms or molecules. As a consequence of the empirical determination of A, values appearing in the literature were initially inconsistent in orders of magnitude [63]. This disparity was eventually treated by the introduction of new theories. Regardless of the inconsistency of estimating

A the van der Waals potential functions displayed by Equation 2.5 and 2.8 are useful for examining the attractive potential as a function of the radial dependence and separation distance. Some difficulties arise with determining *A* when using these expressions to describe CNTs as is discussed in later sections.

DLVO Theory:

If van der Waals forces acted alone in Nature one might expect all dispersed particles to crash from solution immediately. Fortunately, this is not the case since particles suspended in media are often charged and stabilized electrostatically [65]. Derjaguin, Landau, Verwey, and Overbeek (DLVO) considered particle and collidal interactions as a function of two separable forces; the long range van der Waals attractive force and the repulsive electrostatic force. The total interaction potential for electrostatically stabilized particles is represented as the sum of the electrostatic repulsive force and van der Waals attractive force. Although the shape of the sum will vary with the magnitude of the contributions, Figure 9 displays one possible net energy curve as a function of interparticle separation. In this representation the total interaction potential shows metastable behavior with a secondary energy minimum (2^o) at intermediate separation and a deep primary minimum (1^o) or energy well at close distances. The shape of the primary minimum is not highlighted by Figure 9 but in general hard sphere behavior is shown at particle contact with the potential energy diverging to infinity consistent with the Pauli exclusion principle for atomic orbitals. The attractive behavior dominates at both small and large distances away from 2^o. On the other hand, at small distances the van der Waals (vdW) attraction must always dominate due to the power law

nature shown by Equation 2.3 which is not matched by any double-layer interaction [63, 65].

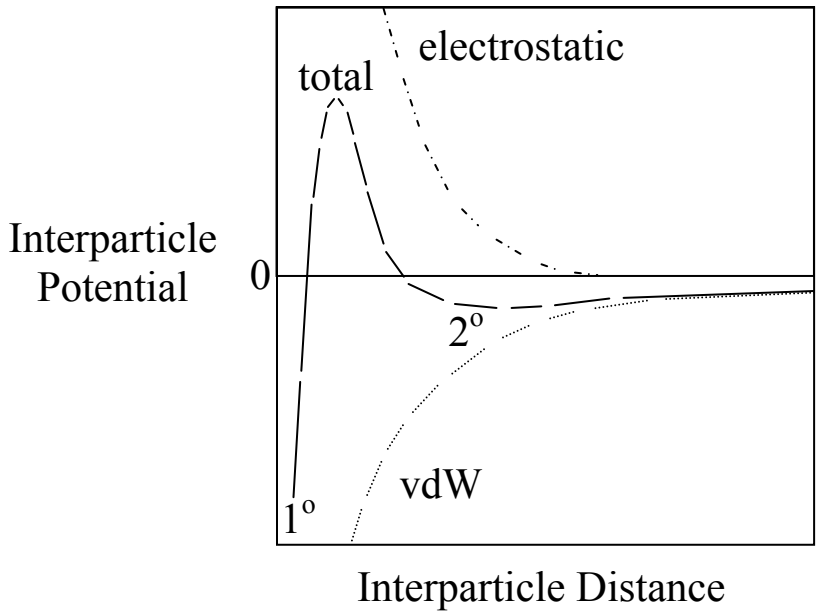

Figure 9: Schematic representation of the interaction potential for dispersion forces (vdW), electrostatic repulsion, and the total interaction potential showing metaseable behavior. The primary (1^o) and secondary (2^o) minima are highlighted.

If 2^o is accompanied by a large enough potential energy barrier (the peak of the total energy curve), particles are kept from falling to 1^o and forming irreversible aggregates. Typically, the energy at 2^o is quite low, estimated as only a few k_BT, and Brownian motion is enough to breakup particle flocculation [67].

The electrostatic force was introduced by the theory of an electric double layer which results from the charging of particle surfaces. Intuitively this repulsive force would explain why all particles in solution did not coagulate and precipitate out. Generally, the charging of a surface results from the adsorption of ions from solution to a

neutral surface or oppositely charged surface or from the ionization/dissociation of surface groups [65]. A common example, and one of specific interest to this research, is the *pH* dependant dissociation of carboxylic groups (–COOH) to a negatively charged carboxylate ions ($–COO^-$). The result of an adsorbed surface charge is an oppositely charged region of counterions around the particle. In close proximity to the surface a narrow layer of bound ions develops known as the Stern layer. Surrounding the Stern layer is an atmosphere of loosely associated ions known as the diffuse double layer. To this end, similarly charged particles or surfaces will repel each other electrostatically in solution.

An additional important type of force that can contribute to suspension stability is that of polymeric or steric forces. These are short range forces produced when polymer layers that have absorbed to the particle surface overlap and avoid mixing. However, if the polymer remains in solution rather than adsorbing to the surface they can induce flocculation instead. If the interparticle separation approaches the dimension of the polymer molecules the space between the particles is depleted of polymer due to entropic effects. Basically, the polymer molecules gain entropy by removing themselves from the constraint of the interparticle dimension. Consequently, the particles are forced together by depletion interactions [67].

Dispersion of Carbon Nanotubes:

Binding Energy of SWNTs:

Thess et al. (1996) showed that in their natural state as produced SWNTs self-organize into crystalline ropes 0.5-20 nm in diameter and tens to hundreds of microns in

length. As shown by Figure 10, the van der Waals intertube bonding holds the individual tubes in a triangular lattice with a lattice constant of 1.7 nm. The parallel alignment seen in Figure 10 is a consequence of the highly polarizable and pristine nature of the sp^2 hybridized carbon interface of SWNTs [68].

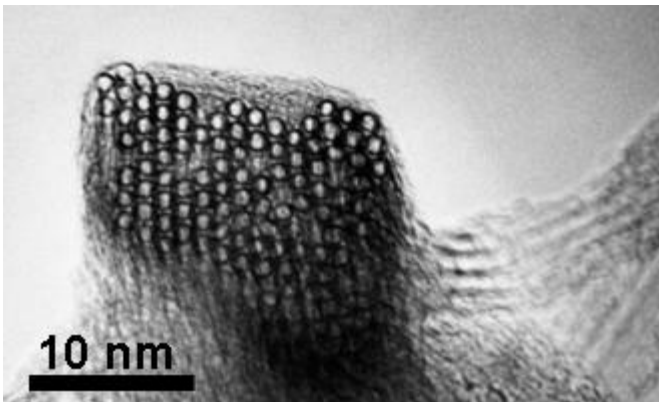

Figure 10: A single SWNT rope made up of ~100 SWNTs as it bends through the image plane of the microscope, showing uniform diameter and triangular packing of the tubes within the rope. The diameter of the individual SWNTs were determined to be ~1.38 nm. Reproduced from Thess et al. (1996) [54].

The pairwise interaction potential has been modeled for parallel carbon nanotubes revealing a deep potential energy well at equilibrium separation on the order of $\sim 10^2$ meV/nm [69, 70]. Due to the high SWNT aspect ratio the van der Waals attractive force becomes the substantial obstacle for achieving stable dispersions as tubes tend to exist in ropes or arrangements of bundles. For tube - tube interactions the binding energy of SWNTs has been commonly accepted on the order of ~ 0.5 eV/nm, making them inherently very difficult to process as individuals [54, 71]. It is important to note that this value is smaller, but on similar order of magnitude, than what is estimated by simulation [69]. This discrepancy is likely due to the unavoidable presence of defects on the

sidewalls of "real" tubes as well as solvent interactions. Additionally, this lower value may have been meant to reflect the peeling of an outermost CNT from a bundle rather then a tube centered in a rope.

In order to calculate the intertube interaction potential, Girifalco et al. (2000) used a continuum approach for nanotube pairs [69]. By this method they determined the interaction energy over an effective area occupied by a carbon atom. The intertube potential for two structures was then calculated by integrating the Lennard-Jones potential over the surface of the tubes [72]. From this model the potential energy well depth was characterized at equilibrium spacing. Considering hexagonal symmetry, the cohesive or binding energy was calculated for a tube centered in a rope interacting with six nearest neighbors as three times the potential energy well depth [73]. From these calculations conclusions can be drawn as to how the van der Waals force in ropes or tube pairs scale with tube diameter. For a (10,10) SWNT with diameter of 1.35 nm the binding energy of a tube centered in a rope (1.67 nm lattice spacing) is ~2.855 eV/nm and the intertube interaction potential is 951.6 meV/nm. Whereas, increasing the tube diameter to 1.89 nm a (28,28) tube in a rope (4.162 nm lattice spacing) has a binding energy of ~4.862 eV/nm and the intertube interaction potential is 1,620.6 meV/nm [69]. The increase in binding energies with increasing diameter and separation distance may seem somewhat counterintuitive from the perspective of colloidal interactions modeled via Hamaker functions. However, it is important to note that the larger diameter tube (28,28) has more carbon atoms interacting per unit length then the (10,10). Thus, even though the separation between the (28,28) tubes (0.3168 nm) is larger that for (10,10) tubes (0.3153 nm) the models by Girifalco et al. account for the presence of more carbon

atoms whose extra pull seems to outweigh the separation. In the same manner, one must also adjust the Hamaker constant to account for this or incorrect conclusions will be drawn. In fact, considering the separation distance, tube radius, and attractive potential for SWNTs modeled by Girifalco et al. the Hamaker constants for parallel alignment can be extracted to be -7.86×10^{-19} J for two (10,10) tubes and -8.05×10^{-19} J for two (28,28) tubes. Therefore, the van der Waals models based on Hamaker are of little utility in comparing interactions between nanotubes of different diameter/chirality *a priori*.

In order to determine in what manner nanotubes can be effectively separated from one another, Coffin et al. (2006) compared two modes of separating individual tubes from ropes; radial displacement (dilation) and array peeling. Through theoretical arguments their results show that peeling of individual tubes from the outer diameter of a rope requires much smaller forces then dilation. Therefore, the likely mode of separation is array peeling as it can be accomplished by delivering much lower intensity energy density to the CNT [72, 74]. For this reason it is assumed that this is the mode likely separating tubes from bundles by high shear. Huang and Terentjev (2008) have confirmed this assumption with both theoretical calculation and experiment [75]. Although not primarily used in this research, the authors also provide detailed analysis on the energetics involved in dispersion by sonication techniques.

Nanotube Dispersion in Polymers:

It is well known that the potential for mechanical property enhancement is determined by both the degree of nanomaterial dispersion throughout the composite system and adhesion between the polymer matrix and dispersed phase [76, 77]. In spite

of this fact, mechanical property improvements have typically been lower than predicted or reported inconsistently in literature with respect to theoretical expectation [9, 78, 79]. This phenomena is not only a consequence of a less than ideal dispersion state, but also the dominance of interfacial interactions as the defining length scales of the filler and polymer converge. Therefore these interactions must be given careful consideration [80]. A truly "ideal dispersion" state is classified by complete exfoliation of the individual CNTs from bundles or clusters, but typically in the literature an "ideal dispersion" is one in which dispersed tubes coexist with small aggregates [81]. Solution based methods followed by in situ polymerization have been favored and effective for achieving this dispersion state. Sandler et al. (1999) developed a pioneering method for dispersion of CNTs in volatile solvents [82]. For typical thermoset systems the nanotubes are first dispersed in a low viscosity solvent and/or surfactant using ultrasonication before magnetically stirring the monomer and hardener in while evaporating the solvent [82-84]. The effectiveness of solution based methods is a result of the low viscosity solutions the CNTs are initially dispersed in. This is in contrast to the high viscosities of the polymer or resin itself. Likewise, solution based methods have been adopted for thermoplastic systems using more exotic solvents capable of dissolving polyolefins and acrylics [85, 86]. It is important to note that these methods typically employ high powered ultrasonication which results in a decrease in the nanotube aspect ratio over long exposure times and therefore limits mechanical property enhancement [71, 87]. However, it was found that first homogenizing the nanotube solutions via high shear reduces the required sonication time and circumvents extreme reduction in length [88].

In addition to solute dispersion, improved performance has been found by using functionalized nanotubes to improve the CNT dispersion state and CNT – polymer interactions [9, 78, 89]. To this end, a variety of methods have been developed to increase nanotube-solvent compatibility including both covalent and non-covalent functionalization techniques. Common non-covalent techniques involve the use of surfactants and biomolecules. The interplay between the quality of the dispersion state and the interfacial interaction between the CNTs and solvent/polymer is a delicate balance. An excellent illustration was seen in the work of Gojny et al. (2004) who studied the performance of nanocomposites fabricated from DWNTs and amine functionalized DWNTs in a epoxy resin matrix [9]. For the purpose of benchmarking performance, the group was able to extract the expected maximum theoretical Young's modulus for mixtures of pure components. Excellent agreement between predicted and experimental Young's modulus were found at low nanotube loadings of 0.1 % wt. using the amine functionalized DWNTs whereas the pristine DWNTs underperformed. This result was an effect of favorable interactions between the amino groups and the epoxy resin/amine hardener. However, deviations were found when the loading was increased by an order of magnitude to 1.0 % wt. as explained by the non-ideal dispersion state not accounted for in the model. Essentially, sample aggregation resulted in a decreased separation distance between MWNTs. For an exhaustive review on CNT functionalization routes the reader should refer to Dyke et al. (2004), Banerjee et al. (2006), and Tasis et al. (2006) [7, 42, 90].

Another common dispersion method for CNT-thermoset polymer systems is the application of high shear. This strategy is favorable since it is generally believed that this

technique can preserve the intrinsic electric and mechanical properties of an isolated CNT [75]. Additionally, a shear based dispersion technique is industrially scaleable. The only fundamental requirement for successful shear dispersion is that the shear energy density be sufficiently high to overcome the van der Waals attractive forces. However, Huang et al (2006) performed a systematic study of the shear dispersion state of MWNTs in viscous poly(dimethylsiloxane) (PDMS) revealing a long characteristic mixing time, on the order of days, required to achieve a well dispersed state [91]. The authors argue that this characteristic time was so extensive that many previous shear based dispersions studies should be revisited. It is likely that this long mixing time is a result of the time required to expose the entire volume of the fluid to the high shear areas of the mixer as well as the slow kinetics required for array peeling to complete.

In spite of the effect of mixing time, a number of groups have used high shear strategies to disperse CNT in polymers. Sandler et al. (2003) recognized the relationship between high matrix viscosity and high shear stresses [92]. To exploit this effect the group mixed MWNTs at high shear (1000 rpm; 2h) using dry ice to lower the viscosity of the epoxy resin [92, 93]. Likewise, Rahatekar et al. (2006) dispersed aligned MWNT carpets using a high shear protocol (1000 rpm, 2h) but noted that the initial aligned state of their tubes made dispersion much easier as compared to highly entangled MWNTs [94]. Gojny et al. (2004) first used a calendaring (three-roll mill) process to homogeneously disperse DWNTs in to an epoxy resin with very short mixing times on the order of minutes [9]. The authors note that this method is an attractive technique that can be readily scaled up in industry since calendaring is a common industrial process. Shortly after, Gojny et al. (2005) used this method to compare the dispersion of various

MWNTs and SWNTs in to an epoxy resin matrix [95]. From this work, two important conclusions were drawn. The first was that while SWNTs possess the highest potential for mechanical property enhancement the resulting nanocomposites could not outperform the amine-functionalized MWNTs due to the poorer SWNT dispersion state. The second conclusion was that the three-roll mill process could not produce composite material with a MWNT loading above 0.3 % wt.. This limitation was later addressed by Wichmann et al. (2006) who developed a post-calendaring method by means of a vacuum dissolver to construct MWNT epoxy composites at loading up to 2 % wt. [96]. Seyhan et al. (2007) achieved dispersion of MWNTs and amine-functionalized MWNTs in a VE/UPR resin at short mixing times by means of a three-roll milling process [14]. Similarly, the technique was later used for processing MWNT-UPR dispersions [19].

Even though the successes of the aforementioned shear techniques are promising for achieving homogenous polymer nanocomposites on an industrial scale they all have an inherent difficulty when processing VE or UPR resins. This difficulty arises from the presence of the volatile styrene monomer required to both lower the viscosity and cure the resin systems. Seyhan et al. (2007) recognized that the milling process essentially casts a thin film over the rollers from which much of the styrene can escape [14]. To bypass this difficulty they obtained a viscous styrene free UPR in which the initial dispersions were blended. After dispersion the group added a VE resin as well as styrene monomer prior to cure. The same conclusion was reached by Thostenson et al (2008) who synthesized a VE resin to have a styrene free starting material [15]. Similarly, the use of three-roll milling with commercial isophthalic UPR failed due to evaporative loss. Additionally, undesired sample polymerization was found to be initiated by the high heat

generation in the mill. As a result Seyhan et al. (2007) were unable to determine the final concentration of their dispersion and instead switched to a styrene free UPR [19]. Most recently, a clever combination of shear mixing and horn ultrasonication was employed by Battisti et al. (2008) to disperse MWNTs in a commercial UPR. Recognizing the problems associated with the heat generated during sonication and subsequent styrene evaporation the group affixed a condenser to the vessel. On a separate note, another difficulty was encountered by Gojny et al. (2004) who discovered the initial CNT-polymer solution was too thin to cling to the rollers [9]. Therefore, a viscosity modifier had to be added pre-calendering to prevent this effect.

Methods for Probing Dispersion State:

It would be beneficial to be able to probe the nanotube dispersion state directly as a means of monitoring composite processing in situ. MWNT suspensions have been studied using optical methods as well as light scattering techniques to probe aggregation modes [94, 97, 98]. However, problems arise due to the high optical absorbance of CNTs. Therefore, the applicability of small-angle light scattering (SALS) is limited to dilute regimes and moderate length scales [99, 100]. Difficulties are further exacerbated when working with SWNTs due to their inherently small size. Thus, the applicability of optical microscopy is removed and smaller incident scattering wavelengths are required. In this manner, small-angle X-ray scattering (SAXS) has been used to study clusters or aggregates of tubes [101]. Likewise, small-angle neutron scattering (SANS) has been used to resolve these objects further and even resolve scattering from individual tubes revealing various power-law scattering profiles from fractals [102]. What is apparent is

that as the dispersion state of the CNT is improved towards individuals the ability to observe the sample optically tends to rely on more complex techniques. In general, all optical methods are ineffective below a length scale of ~ 0.2 - 0.5 μm and electron microscopy techniques are limited to the sample surface. Furthermore, the small wavelength techniques suffer from the unavoidable difficulty of working in reciprocal space and the difficulty associated with data analysis [91]. An excellent alternative to monitoring dispersion state optically is to monitor its rheological response. Thus, rheological techniques have emerged as an efficient and promising method for probing and monitoring the dispersion state and microstructure of carbon nanotube composites and dispersions.

If efficient and economically viable bulk processing of nanotube-polymer composites is to be realized, a well developed understanding of responses to simple steady-state shear flow is required [91]. Furthermore, from processing and application points of view, the mechanical and rheological properties of nanocomposites are very important. These properties are related to the material microstructure, the state of nanotube dispersion, the aspect ratio and orientation of nanotubes, and the interactions between nanotubes and polymer chains [103]. The rheological response of CNT has been studied both in polymer solutions, melts, and solvents. In spite of the differences in the solvent type used remarkable parallel behavior has been seen. Davis et al. (2004) observed Brownian rigid-rod behavior for highly individualized SWNT dispersions using sidewall protonation via superacids revealing a shear viscosity dependence on aspect ratio [104]. Rai et al. (2007) studied the effect of functionalization on SWNT-superacid solubility which unveiled rheological dependence on CNT dispersion states [105].

Hough et al (2004) studied concentrated surfactant stabilized suspensions under oscillatory flow displaying the viscoelastic nature of associating, rigid-rod SWNT networks [106]. The rheological behavior of the dispersions used in the aforementioned studies serve as a benchmark to which less than ideal dispersion states can be compared.

Less than ideal polymer solvents have also been studied rheologically to reveal unique behavior in their own. Hobbie et al. (2007) examined non-Brownian MWNT-poly(isobutylene) suspensions were under the influence of shear flow and stress. This type of fluid was found to exhibit yielding behavior manifested via an elastic network. Interestingly, both linear and non-linear responses showed a concentration dependant scaling [107]. Huang et al. (2006) systematically studied dispersions of MWNTs in viscous poly(dimethylsiloxane) to reveal the dependence of shear mixing time on the emergence of network elasticity; this work identified a long characteristic mixing time for a well dispersed state [91]. Similar elasticity was discovered by Kinloch et al. (2002) in which concentrated and entangled oxidized MWNT aqueous suspensions showed Bingham behavior [108]. Fan et al. (2007) produced a detailed study regarding MWNT-epoxy suspensions which revealed the variation in rheological behavior upon loading, aspect ratio, and initial dispersion quality supporting the utility of oscillatory shear for probing dispersion state [81]. Similarly, direct connections were made by Rahatekar et al. (2006) between rheological response and microstucture for MWNT-epoxy suspensions by optical observation under shear [94].

In contrast to epoxy resin, only limited rheological data has been reported in the literature for UPR matrix dispersions. Seyhan et al. (2007) have studied the response of MWNT and amine-functionalized MWNT dispersions to both oscillatory non-linear

shear [14]. However, their data suggests a poor dispersion state for multiple reasons. First, the amine-functionalized MWNTs showed lower degree of mechanical property enhancement as compared to pristine MWNTs in the low angular frequency regime. Of course, this could also be a result of less favorable interactions after functionalization. However, the authors report an increase in the glass transition temperature for the functionalized tubes. This is an indication of the CNTs successfully impeding polymer motion. Additionally, by comparison of measurements reported by Fan et al. (2006) who used MWNTs almost five times shorter (10 - 15 μm) than what Seyhan et al (2007) used (50 μm), while having similar matrix viscosities, obvious discrepancies can be observed. The response of the MWNT-epoxy dispersions reported by Fan et al. (2006) is almost independent of frequency at concentrations of 0.2% wt. whereas at 0.3% wt. elastic behavior was just beginning to be seen in the dispersions of MWNT-UPR. This would most likely indicate a less than ideal dispersion state and undeveloped network in this work.

Battisti et al. (2008) have only reported the non-linear viscosity of MWNT-UPR dispersions at 0.25% wt. [20]. However, their results show improved steady-shear viscosity enhancement over the 0.3% wt. dispersions constructed by Seyhan et al (2007). Thus, there is opportunity for a detailed study of CNT-UPR dispersions available in the literature. Furthermore, a strategy able to process commercial grade UPR would be beneficial industrially. Specifically, it would be advantageous if the final CNT loading was repeatable and controlled after processing so that "on-line" monitoring techniques such as bulk rheological characterization of the sample could be used.

Shear Aggregation in CNT Dispersions:

Schueler et al. (1997) first studied the shear induced agglomeration of carbon black dispersed in an epoxy resin [109]. They argued that the particles were stable in absence of shear but formed aggregates under certain conditions. This was attributed to the dispersion existing in a metastable state where a potential energy barrier existed providing kinetic stability from the aggregated state. The barrier could be surmounted by external shear forces or by increasing the ionic concentration resulting in an aggregated state which was concluded to be energetically more favorable than the dispersed state. Similarly, Martin et al. (2004) observed shear aggregation in MWNT-epoxy dispersions but only after the addition of the amine based hardener [93]. Their dispersions were created by high shear and were stable for months in storage. The samples were found to be electrostatically stable in this state due to the electric double-layer. The repulsive potential V between spheres was approximated using Equation 2.10.

$$V \propto \exp(-\kappa D) \tag{2.10}$$

Here, D is the interparticle distance and κ is the Debye screening length. Since the screening length is proportional to the ionic conductivity the screening length decreases with increasing ionic concentration in the dispersion. This, in turn, results in a reduction in the stability. Thus, the authors concluded that while high shear forces can create a homogeneous dispersion, the addition of the amine hardener, the application of small shear, and an increase in temperature for curing promoted aggregation by a reduction in the mutual repulsion between the tubes. The high temperature was determined to increase the particle mobility by reducing the resin viscosity. Likewise, the use of shorter nanotubes was found to increase the rate of agglomeration due to their increased mobility

compared to longer MWNTs. However, both samples were found to agglomerate after the addition of the hardener and application of low shear.

Shear aggregation has also been identified through rheological response coupled with optical imaging. Lin-Gibson et al. (2004) studied the flow-induced clustering of semi-dilute non-Brownian MWNT-poly(isobutylene) suspensions [84]. The samples were primarily prepared at 0.17% vol. and measurements were made at constant shear with a variable gap height between the parallel plates. Samples were found to associate into diffuse networks after the application of low shear (0.03 s^{-1}) for ~ 30 min with a 50 μm sample gap. The gap size was observed to dictate the length scale of cluster growth from confined to bulk areas. The MWNTs could be redispersed by application of a shear rate of 10 s^{-1} and oriented with the flow. Over long steady shearing of ~ 24 hours the samples were found to "quench" under the weak shear. This aggregation behavior was identified by means of a unique rheological signature where the shear viscosity exhibits a maximum after approximately one hour of shearing and decays thereafter. Tracking the first-normal stress difference over this period showed that a negative value was observed at the viscosity maxima which trended down with the viscosity curve. The negative first-normal stress difference was concluded to result from compressibility of the clusters where the contracting aggregate domains exhibit a collective pull on the parallel plates.

It is important to note that not all observed shear aggregation is a result of interparticle attractive forces. In absence of interparticle attraction Schmid et al. (2000) showed through simulation that flow-induced aggregation can occur in non-Brownian fiber suspensions as a result of fiber friction alone [110]. Specifically, low concentrations of particles having high stiffness flocculated under the application of low

shear stress. The strongest flocculation was found to occur in suspension of stiff fibers with irregular shapes. The flocs were predicted to have at least three or more contact points and were held together by stored elastic energy in the fibers.

Finally, shear induced aggregation has also been linked to the non-linear rheological response of fluids. Rahatekar et al. (2006) optically observed low shear aggregation in MWNT-epoxy suspensions under a confined sample gap of 0.3 mm [94]. They found that the aggregate size in the dispersions was sensitive to the shear rate applied and a high shear rate could readily homogenize the dispersion. This phenomena was concluded to be the origin of shear thinning in the sample. The application of a low shear rate caused a buildup of aggregates that persisted after cessation of flow. However, at low concentrations macroscopic aggregates did not form and bulk viscosity enhancement was not seen below 0.1% wt.. It was concluded that the high viscosity of the epoxy (10 Pa-s) limited the diffusion of the MWNTs through the samples at low concentrations where particles were further apart. Thus, it was concluded that above a certain loading of MWNTs the low shear viscosity enhancement was a result of "mechanical" aggregate formation. Brownian motion was found to play little to no part in the dynamics of aggregation.

In summary, it is important to realize that the shear induced aggregation of particles or fibers can have different origins between samples. Aggregation has been found to be a result of dispersion destabilization, an increase in mobility, and interparticle friction alone.

Modifying the Nanotube Interface via Oxidation:

Introduction:

Oxidation of carbon nanotubes is a common means of chemical modification as it provides a precursor for many further functionalization reactions. These include but are not limited to amidation reactions, esterfication reactions, biomolecular attachment, polymer grafting, and coordination chemistry [7, 90]. Additionally, oxidation reactions typically produce a wide range of functionalities such as carboxylic acids, alcohols, aldehydes, ethers, lactones, and epoxides depending on the type of nanotube and oxidizing agent used [111]. However, the most synthetically useful group is the carboxylic acid as not only can it participate in many subsequent reactions but it serves to increase hydrophilicity. Furthermore, the introduction of functionalities serves to interrupt the van der Waals attractive forces between nanotubes. Common purification techniques that use acid oxidation remove tube endcaps and introduce holes into the tube sidewalls. Typically, the tube ends and, depending on the strength of the oxidizing agent used, the sidewalls are decorated with predominately carbonyl and carboxylic groups [7]. Figure 11 displays a SWNT after oxidative treatment. Although this treatment can increase dispersion properties in aqueous solvents the length is often reduced to submicron dimensions and the π–π conjugated structure is damaged affecting the mechanical and electrical properties [7, 112].

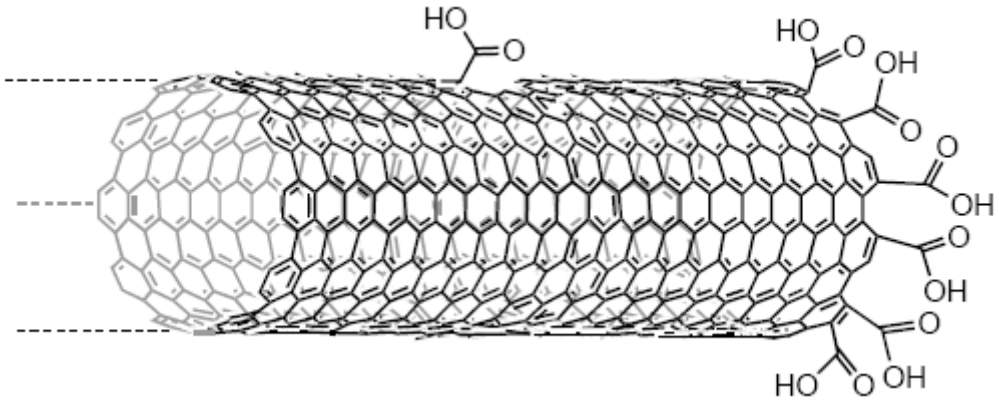

Figure 11: Schematic of an oxidized SWNT. Carboxylic groups can be seen terminating the tube end and on sidewall defect site. The presence of the acidic hydrogen is indicative of low *pH* conditions. Image reproduced from Hirsch et al (2002) [113].

In general, it is believed that chemical attack on CNT originates at end caps and defect sites where sp^3 character may be present in contrast to the sp^2 conjugated carbons of the pristine sidewall. The curvature of the endcaps leaves them unstable and strained resulting in a higher reactivity [46, 114]. Additionally, the sidewalls contain defect sites such as pentagon-heptagon pairs (Stone-Wales defects), sp^3 hybridized defects, and lattice vacancies [90]. Such defect sites are chemically active due to disruption of the delocalized electron density [46]. Interestingly, even localized bending or twisting of the CNT renders them more susceptible to chemical attack. Furthermore, under certain oxidative conditions additional defect sites are created by attack on the graphene sidewalls and subsequently oxidized [114].

Theory of Organic Acids:

The dissociation of an organic acid follows a reversible reaction scheme dictated by the value of its acid dissociation constant K_a. A larger value of K_a is indicative of a stronger acid. However, it is more practical to describe the extent of dissociation on a logarithmic scale, and in this manner the pK_a is expressed by Equation 2.11.

$$pK_a = -\log K_a \tag{2.11}$$

By this convention a smaller pK_a value indicates a stronger acid and is typically determined using water as the base. Its interpretation is meant to indicate how readily a compound gives up a proton whereas the *pH* indicates the acidity of a solution. Carboxylic acids have *pKa* values ranging from 2.5 to 5 and therefore are considered moderately strong acids [112, 115]. Figure 12 displays what is referred to as a carboxylic (carboxyl) functional group.

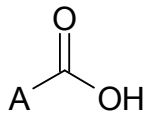

Figure 12: Generic depiction of a carboxyl functional group. The atom A is a general representation but typically signifies an aromatic or amorphous carbon in this work.

In a carboxylic acid or carboxyl group, the oxygen atom in the C=O bond is electronegative and pulls the electrons bonded in the -OH group (hydroxyl) away from the proton. Thus, the proton is easier to donate as indicated by the relatively low *pKa* for carboxylic acids. Additionally, the conjugate base of the carboxylic acid (carboxylate

ion) is resonance stabilized sharing the delocalized electrons between oxygen atoms [115].

Whether or not a compound will exist in its acidic form or as a conjugate base is dependant on both the *pKa* of the acid and the *pH* of the solution. These two quantities are related by means of Equation 2.12, commonly known as the Henderson-Hasselbalch equation.

$$pK_a = pH + \log\frac{[base]}{[acid]} \tag{2.12}$$

Here [base] represents the molarity of the compound in its conjugate form and [acid] represents the molarity of the compound in its acidic form. As indicated by the logarithmic component of Equation 2.12, the acid and conjugate base coexist in various proportions over a range of *pH*. Generally, compounds exist in their acidic form in solutions with *pH* lower than the compound's *pKa* and vice versa.

As the *pH* is raised above *pKa* the carboxylic acid dissociates into the carboxylate ion ($-COO^-$). Basically, the carboxyl group depicted in Figure 12 loses a proton (hydrogen atom) leaving behind a negative charge. This effect can induce electrostatic repulsion to disperse particles, such as CNTs, and keep them stable in suspension. However, it is not recommended to neutralize the *pH* with caustic salts as the ions in solution will compress the thickness of the electrical double layer and eventually may cause the particles to crash out of solution [99, 112].

Oxidative Treatment of Nanotubes:

Although various accounts in the literature claim to be the first to treat CNTs with a mixture of concentrated nitric and sulfuric acids the initial report was actually made by Esumi et al (1994). The mixture of strong acids used in this experiment was originally found to intercalate and swell graphite [116]. Esumi et al. refluxed (140^{o}C) MWNTs in a 3:1 mixture of concentrated sulfuric to nitric acid (1g MWNT/40 mL) and found that the concentration of acidic sites was greater after only 20 min of exposure than when the same MWNTs were refluxed for 4 h in concentrated nitric acid alone. It was concluded that the effect of concentrated nitric treatment was less pronounced then the acid mixture due to the difference in oxidative power between the two methods. Additionally, a negative zeta potential was found to trend with increasing pH confirming the presence of acid sites and their increasing occurrence with acid exposure time [117]. For point of reference, the nitric acid treatment used by Esumi et al. was originally developed to open the endcaps of CNTs for filling of metal oxides by Tsang et al (1994) [118]. Subsequently, Lago et al. (1995) adopted this nitric acid treatment for intertube insertion of palladium and were the first to suggest the introduction of predominately carboxylic (–COOH) and phenolic (-OH) groups to the MWNTs by means of titration to identify acidic site concentration [119]. Additionally, Lago et al. were the first to report that the use of high energy ultrasound (sonication) readily creates local defects in, or destroys, CNTs and the number of acidic sites introduced to the tubes can be increased with ultrasonic pretreatment.

Similar chemical treatments used for MWNTs were successfully performed with SWNTs soon after their discovery. Liu et al. (1998) were the first to study the ability of

the sulfuric/nitric acid mixture to cut highly tangled SWNT ropes into short "fullerene pipes." [120]. The cut tubes were found to have a length of approximately 300 nm. By their method a 3:1 mixture of 98% sulfuric to 70% nitric acid (10 mg SWNT/40 mL) was bath sonicated for 24 h at 35 - 40^{o}C, diluted, collected via filtration, and washed with 10M NaOH. To remove amorphous carbon generated by the cutting the final product was then polished in a 4:1 ratio of 98% sulfuric and a 30% aqueous hydrogen peroxide solution (piranha) at 70^{o}C for 30 min. The open tube ends were assumed to be terminated with many carboxylic groups. However, they found that the final product readily flocculated in aqueous solution and had to be suspended with aid of a surfactant. The instability of these solutions was addressed by Shaffer and Windle (1998) who used the method developed by Esumi et al. to oxidize MWNTs. Fourier transform infrared spectroscopy (FTIR) showed the oxidative treatment introduces oxygen rich surface groups that were predominately phenol, carboxyl, or lactone functionalities. The author's note that the addition of ions destabilizes the suspension in accordance with a reduction in the Debye screening length. Thus, the solutions were not neutralized with a strong base like NaOH and after dilution the nanotubes formed a well dispersed, electrostatically stabilized colloid in water [99]. This was a result of the ionization of the acidic groups present on the MWNT surface.

The use of nitric acid alone was also found to be effective to oxidize CNTs. Jia et al. (1999) created short and straight MWNTs from an entangled starting material by oxidation in boiling concentrated nitric acid. The authors suggested the final nanotube length was inversely related to the treatment time. FTIR spectroscopy was used to identify functional groups present. Because of the presence of many -OH, –COOH, and

C=O groups the pH of the final solution could not approach 7 upon washing. The oxidized tubes were assumed to be attracted to water molecules by hydrogen bonds between -OH groups on the nanotube surface and the water molecules [121]. Similar conclusions were made by Saito et al. who used 22 h bath sonication (50^{o}C) to create shortened oxidized MWNTs by sulfuric/nitric treatment (1 mg MWNT/2 mL) [122]. The final product was found to have a length of ~338 nm. The original length was not determined but was shown to be noticeably longer.

CNT oxidation has also been found to serve in disentangling the nanotubes and increasing their mobility. Wang et al (2003) showed that while physical separation methods such as ball milling, shearing, and ultrasonication can break down large agglomerates of MWNTs into smaller clusters only treatment with sulfuric/nitric acids (140^{o}C, 0.5 h) could disentangle the tubes. This was achieved by effectively severing the entanglements and therefore damage was unavoidable. However, if the tubes were first annealed at high temperature the defects introduced to the tube walls could be decreased and this method was suitable for purification [123]. Rosca et al. (2005) dispersed MWNTs in nitric acid by bath sonication (30 min) followed by reflux for up to 48 h [124]. As shown by Figure 13, after 24 h of treatment time the MWNT alignment has significantly increased. This alignment was thought to be a result of tube disentanglement and the increase in mobility as a result of the functionalization. Continued treatment can increase the cutting and these smaller fragments can align themselves further as seen after 48 h of treatment. Benefits from oxidation on mechanical properties of CNT films have also been reported.

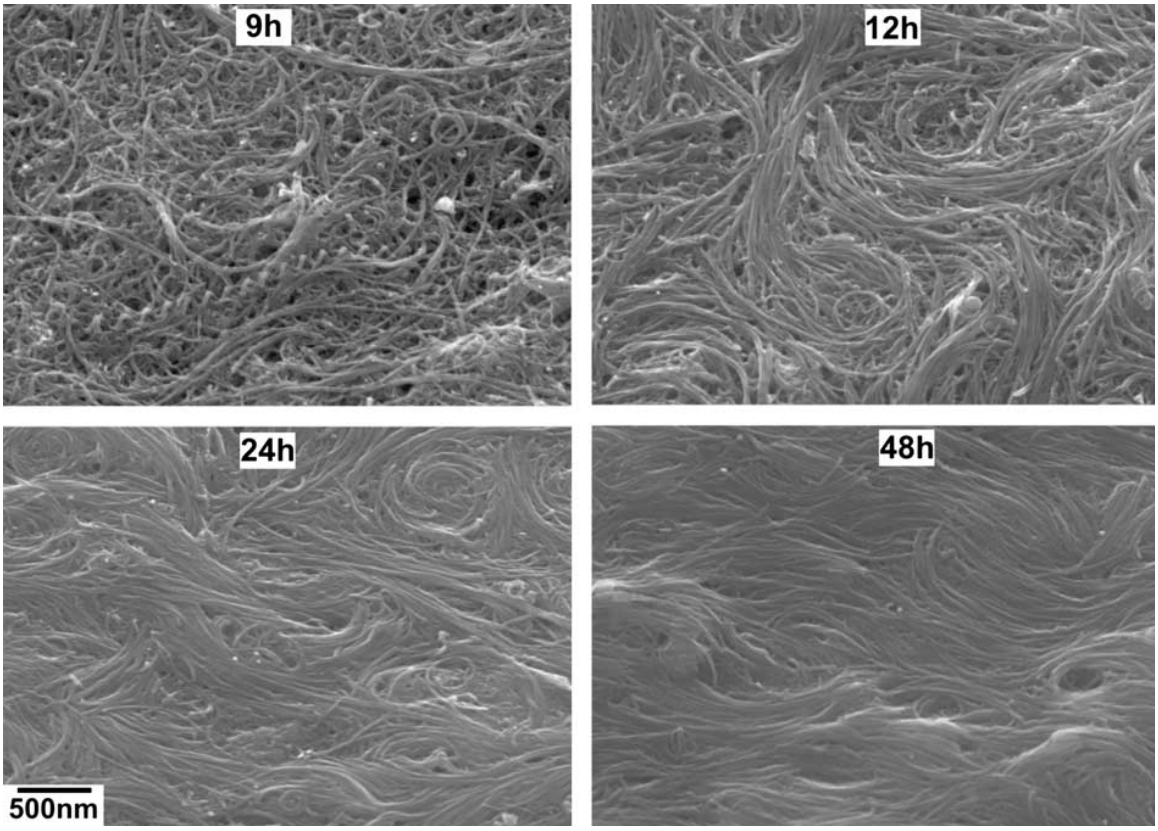

Figure 13: The evolution of MWNT alignment during the oxidation process. Here 10 mg MWNT/mL of 60% nitric acid was used. Image taken from Rosca et al. (2005) [124].

Zhang et al. (2004) compared the mechanical strength of buckypapers produced from various concentrated (3,6,10 M) of nitric acid solutions by sonication (2 h) and refluxing (2 h) [125]. Selective degradation of small diameter tubes was confirmed via Raman spectroscopy. This resulted in a narrower tube diameter distribution, which increased the shear modulus of the tube bundles, resulting in higher film modulus while the degradation product can fill voids [126]. The mechanical properties of the films approached that of engineering plastics with those treated by 10 M acid showing the strongest mechanical properties.

Recently, Rasheed et al. (2007) critically compared the performance of some of the more common oxidation methods on VGCFs [111]. The sulfuric/nitric acid mix (50 mg VGCF/150 mL) was found to be the most severe treatment (24 h sonication at 45^{o}C) and generated the most amorphous carbon. Treatment with RuO_4 and $KMnO_4$ were compared with a nitric acid (200 mg VGCF/40 mL) reflux at 120^{o}C for 20 h. The group was able to determine that treatment by sulfuric/nitric acid produced an order of magnitude higher functional groups (1.05×10^{21} acidic sites/g VGCF) than the other treatments. In addition, they found that the nitric acid was least severe but provided the lowest amount functional groups.

Although the focus thus far has been on acid oxidation methods other methods have been successfully performed. By treatment with sec-butyllithium and carbon dioxide both alkyl and carboxyl groups were introduced to the sidewalls of SWNTs [127]. Additionally, a variety of strong oxidants such as $K_2Cr_2O_7$, $KMnO_4$, H_2O_2, $OsCl_3$, $RuCl_3$ were studied by Hwang (1995) for their ability to open nanotube endcaps [128]. Similarly, Hernadi et al. (2001) studied $KMnO_4$, H_2O_2, $HClO_4$, and O_3 to gauge their effectiveness in removing amorphous carbon by oxidation [129]. Interestingly, no correlation was found by this group between the oxidation rate and electrochemical oxidation potential.

Mechanism of Oxidation:

As previously mentioned, Lago et al. were the first to report that the use of high energy ultrasound (sonication) readily creates local defects in, or destroys, CNT [119]. Additionally, they noted that the number of acidic sites introduced to the tubes can be

increased with ultrasonic pretreatment. Liu et al. (1998) argued that simultaneous exposure of CNTs to oxidizing agents and ultrasonication is an effective way to etch the CNTs. Under the influence of ultrasonication microscopic high temperature domains are created by the collapse of cavitation of bubbles. These hot areas induce attack the surface of SWNTs leaving a hole in the sidewall. Subsequent attack by strong oxidants quickly cuts this area completely cleaving the CNT. Because of the moderate temperatures the open tube ends were assumed to be continuously etched away in a time-linear fashion (fuse burning) by the oxidizing agent unless quenched [120]. Essentially this is a two step process of introducing defects then cutting the sites. Their results show that the mixture of sulfuric and nitric acids can complete both steps. Ziegler et al. (2005), on the other hand, used hot piranha to complete the cutting step because they found it was less destructive to the sidewalls. Basically, they concluded that if the cutting was by "fuse burning" from the ends much of the nanotube material is wasted in etching to a desired length. The authors circumvent this with the piranha, only cutting at defect sites already created and thus preserving electrical properties of the sidewall [130]. Likewise, over time SWNT exposed to Piranha solutions were found to be stable against damaging the tube structure [131].

A mechanism for the oxidation of SWNTs was proposed by Zhang et al. (2003) who systematically investigated the effect of sulfuric/nitric (60 mg SWNT/50 mL), 2.6 M nitric, and $KMnO_4$ oxidants on the structure of SWNTs [114]. They concluded that the oxidation process begins by attacking defect sites already present from CNT production and is additionally accompanied by a two step process. First, in a defect-generating step the oxidants attack the graphene structure via electrophilic addition and

generate -OH and C=O groups. For various treatments, the effectiveness of this step depends on the oxidants ability to generate the –OH groups initially and transform them to C=O. Specifically, for the sulfuric/nitric acid mixture evolves very aggressive NO_2^+ ions which attack the graphene structure to generate active sites. Similarly, OH^+ ions are generated in piranha. Next, during the defect consuming step the graphene structure is destroyed by oxidation of the active sites generated previously. This extent of this step depends on the ability of the oxidant to etch the graphite like structure around the already generated C=O and neighboring groups. It was found that dilute nitric could purify tubes by etching carbonaceous particles but not generate abundant functional groups. FTIR spectroscopy indicated that even at treatment times up to 96 h dilute nitric could not generate new –COOH groups. Instead, it consumed already existent defects but could not etch into the aromatic rings to generate more defect sites. Similarly, $KMnO_4$ treatment was ineffective in the defect consuming step.

Etching Mode and Rate:

Generally, there are two proposed mechanisms for the shortening of carbon nanotubes as a result of oxidation. The first is "fuse burning" taking place form the tube ends and the second is the cutting at induced defect sites in the nanotube walls. Of course, these modes can operate simultaneously as well. Early descriptions of tube etching under sonication in sulfuric/nitric acids described the mechanism where cut and open tube ends were slowly etched away by the "fuse burning" process [120]. Ziegler et al. (2005) also agreed that "fuse burning" was to blame for etching in sulfuric/nitric acid mixtures seen previously but argued that was not so in Piranah solution [130]. Marshall

et al. (2006) later correlated the treatment/sonication time with the degree of cutting and oxidation (2 mg SWNT/1 mL) after exposure from 2 h to 14 h [132]. This group concluded that two hours of treatment increases the acidic group content by 1%. Additionally, the found that at short time scales the amount of observed length reduction indicated that "fuse burning" alone could not account for this. Furthermore, the substantial increase in carboxylic acid groups even at shorter times indicates that cutting at sidewalls is necessary. Additionally, a nonlinear increase in acidic sites was seen by Zhang et al. (2003). Finally, Forrest and Alexander (2007) developed a working relationship between oxidation time and nanotube length for SWNT in nitric and sulfuric acid showing the nonlinear relationship that could not be explained by "fuse burning" alone [133].

Fourier Transform Infrared Spectroscopy of Oxidized CNTs:

Fourier transform infrared spectroscopy has been the most widely used technique for identifying oxidation products [99, 111, 114, 121, 122, 125, 134, 135]. In the infrared region the energy levels involved in the transitions of molecules are typically a result of vibration and rotation. To this end, identification by means of characteristic group frequencies have been successful in identifying surface functionalities. For an exhaustive source of tabulated spectra for both IR and Raman refer to Socrates (2004) [136]. However, several groups have had difficulties directly resolving any differences between the spectra of the starting material and treated samples. Attempts by Rasheed et al. to observe carboxylic functionalities were unsuccessful by FTIR unless the product was further derivatized with octadecylamine. The authors hypothesize that low

concentrations of acidic sites may be the cause of this. Likewise, to examine their oxidation product Saito et al. treated the cut tubes with alkyldiamines prior to FTIR analysis [122]. Additionally, difficulties have been identified with detection and contamination. Li et al. (2007) were unable to detect carboxylic groups on MWNTs after treatment with hydrogen peroxide. This group found difficulties with contamination by absorbed water manifested by peaks at 3444 cm^{-1} and 1636 cm^{-1} [112]. Similar artifacts were found previously by Shaffer et al. (1998) as well [99].

Although a few studies have indicated the presence of ether functionalities in the oxidized tubes using various X-ray techniques, these functional groups have generally not been observed via FTIR [137, 138]. Likewise, Wang et al. (2005) used a microwave reactor to carboxylate SWNTs in a sulfuric/nitric acid mixture and discovered various sulfonate functionalities were present that have not been identified elsewhere [139]. Therefore, it is unlikely that ether or sulfonate groups typically are produced by oxidation. In fact, Zhang et al. (2003) have performed theoretical calculations and molecular simulation to conclude that after strong oxidative treatment only –COOH, -OH, and C=O functionalities can arise. Additionally, they concluded that all groups must be directly connected with the aromatic rings of the CNT while C=O can only lie in the plane of the ring or on the bridging carbon atom of intersected rings [114].

Tzavalas et al. (2006) treated MWNTs with the sulfuric/nitric acid mix (1g MWNT/40 mL) by reflux at 140^{o}C for 0.5, 2, and 4 h. Although they note that the C=O stretch was hard to resolve in some cases, the C=O stretch of carboxylic acids was identified at 1717-1723 cm^{-1}. Additionally, a peak between 1354 - 1366 cm^{-1} was assigned to the -OH deformation mode. Finally, the -OH stretch of carboxylic acid

monomer was found at 3180 cm^{-1} and between 3329 - 3335 cm^{-1} for hydrogen bonded carboxylic acids. The authors note that due to high symmetry of C-C bonds in the tubes themselves they are generally inactive in the infrared [134]. Similar carboxylic peaks were identified by Zhang et al. (2003) for SWNT treated by the sulfuric/nitric acid mix. A peak at approximately 1735 cm^{-1} was assigned to the C=O stretching mode in the –COOH group of carboxylic acid. The authors note that carboxylic peaks at 1740 cm^{-1} are generally assigned to –COOH in the free state. This peak shifted from 1737 cm^{-1} to 1720 cm^{-1} as treatment time progressed suggesting the presence of carboxylic groups not only increases with time but the hydrogen bonding between the groups become more effective. After treatment with NaOH peak at 1540 - 1615 cm^{-1} for the carboxylate ion appeared which is proof of $–COO^-$ charging.

Raman Spectroscopy of SWNTs:

Despite probing a similar range of incident wavenumbers, the origin of Raman spectra is different than that of FTIR. FTIR measures the adsorption or transmission of IR light by the sample as a function of frequency. On the other hand, with Raman Spectroscopy the sample irritated by intense UV-visible lasers and the scattered light is collected. Raman excites the molecule to what is known as a "virtual state;" called so because it is not a true quantum state rather a short lived distortion of the electron cloud [140]. A sample is IR-active if the molecular vibration changes its dipole moment and Raman-active only if the molecular vibration changes the polarizability [141]. For example, in a C=C bond the polarization changes significantly with a vibration associated with a C=C stretch. As a result, a C=C vibration is strong toward Raman scattering

whereas a C=O stretch is not [140]. Thus, Raman has the capability to measure more of the molecular backbone of CNTs whereas FTIR readily measures the functional groups.

The Raman scattered light consists of two parts; the Rayleigh scattering (elastic) of the same frequency as incident laser and the Raman scattering (inelastic) of weak intensity and probability. The Raman scattering is shifted at a frequency plus (anti-Stokes) or minus (Stokes) the vibrational frequency of the sample molecule. Since, the Stokes side of the spectrum is much stronger (it gains energy from the shift) this is measured [141]. As a result of this phenomenon, the vibrational frequency of the molecule is measured as a "Raman shift" from the incident beam.

Raman Features of SWNTs:

Typically the strongest features in SWNT Raman spectra are the 1st order features of the G-band at ~1580 cm^{-1} (E_g mode) and the low frequency radial breathing modes (RBMs). In fact, with respect to other graphitic materials the RBMs (A_g mode) are unique to SWNTs and provide direct evidence for their presence [142, 143]. The RBMs are located from approximately 100 - 500 cm^{-1} and are a result of out of plane bond-stretching where all the atoms radially move coherently. Essentially, the stretching is along the tube diameter equally in all directions. The frequency of these peaks are inversely proportional to the tube diameter but the exact relationship varies between individuals and bundles. In general, at lower Raman frequencies the vibrations can only serve as a probe of the nanotube surface and at higher frequencies reflect the local sp^2 bond structure for graphite [143]. The G-band feature in SWNTs has two main components; G^+ peaks at ~1590 cm^{-1} and G^- at ~1570 cm^{-1}. The G^+ vibration is

associated with carbon vibrations along the nanotube axis and its frequency upshifts and downshifts with charge transfer from dopant additions. For example, Davis observed that SWNTs in superacids showed an upshift as a result of protonation [144]. G^- is associated with vibrations of carbon atoms along the circumferential direction of the tube and its frequency and lineshape are dependant on diameter and the electronic structure (metallic or semiconducting). Figure 14 displays a schematic of the various atomic vibrations associated with the 1st order Raman modes.

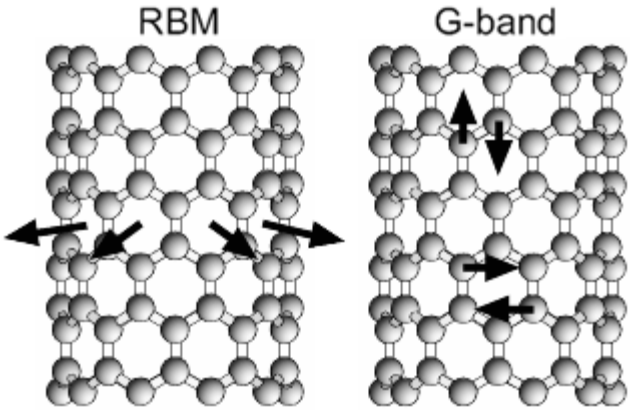

Figure 14: Schematic representation of the RBM showing vibration of the carbon atoms is in the radial direction as if the tube were "breathing" and the G-band showing tangential vibration in the circumferential direction and atomic displacements along the axial direction. Image taken from Jorio et al (2003) [145].

Two 2nd order Raman scattering features are also present in SWNT spectra, the D and G' band. These features are present in graphite as well. The D-band is located at ~ 1350 cm^{-1} and is dispersive; it shifts with the incident laser energy. The G' band is located at approximately 2700 cm^{-1} and is an overtone of the D mode. This peak is highly dispersive [146]. The D-band stems from the disorder induced mode in graphite with the

same name [142]. It origin is a result of scattering from a defect that breaks the basic symmetry of a graphene sheet and thus it is observed in sp^2 carbons containing vacancies, impurities, or other symmetry-breaking defects [146]. Ferrari and Robertson (2000) showed a relationship between the G-peak position, the ratio of D to G peak intensity (I(D)/I(G)), and sp^3 carbon (amorphous) content [147]. In general, a large I(D) with respect to I(G) in SWNT bundles usually indicated the presence of amorphous carbon [145]. Additionally, the relative intensity of the D-mode can provide direct evidence of covalent modification to the nanotube framework [148, 149]. Broadening of the D-band has been previously observed as a result sidewall functionalization by means of ozone oxidation in absence of significant amorphous carbon generation [150]. Thus, the observation of the D-band is related to either the presence of defects in the tube walls (vacancies, 7-5 pairs, dopants, tube ends) or to the presence of amorphous carbon material in the sample [151]. Furthermore, the D to G peak intensity ratio can also be correlated with tube length at certain wavelengths [152]. For shorter tubes the end effects become more important and therefore the intensity ratio was found to be higher. But, this ratio did not approach zero for longer tubes. Instead, finite residual values for I(D)/I(G) were observed as a result of defect induced scattering within the tube walls, confirming the dual nature of the existence of D-band scattering.

X-ray Photoelectron Spectroscopy of CNTs:

X-ray photoelectron spectroscopy (XPS) measures the emission and energy of core level photoelectrons from a solid surface resulting from an incident X-ray beam. Depending on the size of the material under study the surface atoms may be in small

proportion and therefore detection must be both sensitive and free of atmospheric interference. Thus, XPS analysis is conducted under ultra-high vacuum. The observed photoelectrons are often described by means of their quantum numbers and have characteristic energies which reflect the atomic binding energy. The intensity at a certain observed binding energy indicates the concentration present of a certain bonding type. The binding energy is simply the incident X-ray energy less both the kinetic energy of the ejected electron and the work function of the instrument. The binding energy identifies the electron specifically and is a function of the imposed X-ray energy ($h\upsilon$), the kinetic energy of the ejected electron E_k, and the spectrometer work function. What is recorded experimentally is the photoelectron spectrum as intensity vs. binding energy and this accurately represents the quantum electronic structure of the material. Essentially, the photoelectrons have a kinetic energy distribution which represents the shell form of the electronic structure [153]. Only excited photoelectrons that are elastically scattered contribute peaks in the spectrum. Once a photoelectron is emitted the ionized atom must relax by emission (fluorescence) of an X-ray photon [154]. Since the electrons in the sample may be loosely bound or tightly bound, when excited with the same energy, the photoelectrons produced may be of various kinetic energies. Thus, even though the incident radiation may be monochromatic the observed spectrum will yield a polychromatic photoemission [153]. The depth of analysis will vary with the kinetic energy of the incident beam, but it is generally only a few nanometers. This is dependant not on the sample penetration which is actually deeper but rather the depth from which photoelectrons can escape of approximately 2 nm [153].

High Resolution Analysis of CNTs:

For typical carbon based materials the main peaks present on the surface spectra result from the photoemission of electrons from the carbon 1s core orbital (C1s) at ~284.6 eV and the 1s core orbital of oxygen (O1s) at ~531 eV [155]. Within high resolution C1s analysis characteristic binding energies are representative of a graphitic peak (aromatic and aliphatic) at 284.6 - 285 eV and four main oxide peaks. The exact location of the oxide peaks vary slightly in the literature and are found at ~286.1 - 286.3 eV for –C-OH (hydroxyl, phenol and enol-keto) and –C-O-C– (ether); 287.3 - 287.7 eV for –C=O (carbonyl and quinone); 289.1 - 289.4 eV for –COOH and –COOR (carboxyl), and 290.6 eV for –COO– (carbonate and/or absorbed CO, CO_2) and π-π^* shake up satellite peaks [155-159]. The shake-up satellite peaks are a result of π-π^* transitions in aromatic rings [160]. For SWNTs specifically binding energies for the carboxylic groups have been fit as low as 288.6 - 288.8 eV and as high as 289.54 eV [161-163].

Thermodynamics of SWNT Solutions:

Introduction:

Rigorous thermodynamic analysis of SWNT dispersions and solutions are still rare in the literature. To date, currently only two exhaustive studies exist that attempt to describe the free energy of mixing with each work taking a different approach. The first thermodynamic description of nanotube solutions was treated by Sabba and Thomas [164]. Specifically, an approach based on Onsager's theory for anisotropic particles was used to describe the Hemholtz energy of mixing. The authors conclude that due to the large van der Waals attraction and poor solvents generally available for dispersion, a

negative value for the free energy of mixing may only be obtained at low nanotube number density. Therefore, according to their analysis only extremely dilute solutions of nanotubes are thermodynamically favorable.

A later attempt was made by Bergin et al. who first formulated an appropriate description for the Gibbs free energy of mixing and then attempted to justify their theoretical treatment by experimentally measuring individual thermodynamic variables in a "good" solvent [165]. A "good" solvent is considered as one in which there is no enthalpy of mixing. Solutions with zero enthalpy of mixing are considered athermal and therefore there is no liberation of absorption of heat between components. An approach similar to that of Bergin et al. is taken in this section to describe the important thermodynamic aspects of CNT solutions and draw general conclusions based on these arguments.

Motivation for Rod-like Particle Theory:

Flory (1955) was the first to consider that the role of polymer chain inflexibility or stiffness plays an integral part in polymer crystallization [166]. In motivating this idea the filling of given volume with a large fraction of disordered chains that resist bending was considered. It was argued that if one were to imagine placing long inflexible molecules one at a time (while preserving disorder) into the volume after a certain fraction was added it would be impossible to find space for additional molecules without relaxing the previous requirement for chain stiffness. By this reasoning it was hypothesized that only through the development of order (parallel alignment of chains) could the remaining, or additional, molecules be inserted. It is important to note that no

weight has yet been given to the intermolecular forces that may be present in formulating this idea. Similar conclusions have also been made previously by Onsager (1949) and Isihara (1951) who theoretically argued that separation of an ordered phase highly asymmetric particles will occur even in the absence of repulsive intermolecular forces [167-169]. However, Flory was critical of the applicability to these theories outside of low particle concentration; a criticism Flory would later addressed by extending his theory for semi-flexible polymers to rod-like particles [170]. On the other hand, it has been argued that Flory's lattice approach suffers when describing liquid-crystalline ordering due to restrictions placed on the chain flexibility. In general, Onsager's theory is more appropriate for studying liquid-crystalline order while Flory's theory is more useful for describing concentrated solutions and melts [171].

Flory's semi-flexible model considered polymer chains having many segments arranged on a two-dimensional lattice. As a result of the constraint of chain stiffness chain segments had to placed co-lineary with adjacent segments of the molecule. Also, the chains are assumed to exist in a configurational arrangement that is energetically favorable over others, for example the trans isomer of polymethylene ($-CH_2-$), but in a discrete manner defined by the lattice. This treatment restricts the placement of subsequent chain segments. With the geometrical constructs in place and considering j molecules already inserted into the lattice the next step was to estimate the expected number of vacant sites accessible as the first segment of the $j+1$ chain was added. Such an exercise in combinatory mathematics was independently developed by Flory and Huggins for a two component liquid mixture of polymeric solute in solvent assuming no change in volume upon mixing [166, 170, 172, 173]. Flory then extended

this treatment for semi-flexible polymers by including the degree of chain bending, f. The result was an expression for total number of possible lattice configurations and subsequently the partition function.

To address the issue of the solute behaving as a rigid-rod ($f = 0$) with no preferred orientation, the semiflexible model's partition function was modified by taking the flexibility and interaction parameters to zero. The partition function for athermal solutions of rigid rods at two extremes was then extracted. At one extreme the system existed in complete disorder and the other in the rods existed in parallel arrangement. However, neither expression was thought appropriate to describe intermediate arrangements with the isotropic extreme found to be only appropriate in the dilute regime or for short rods. What was needed was an intermediate expression that would expand the theory past what was done previously for highly asymmetric particles.

Theory of Solutions for Rod-like Particles:

In developing the expectation for the intermediate orientations a new approach was adopted to the lattice model to overcome its inability to accommodate a rod in a continuously varying range of orientations [170]. Figure 15 displays molecule i inclined at an angle Θ_i with respect to the horizontal axis of orientation, the principal axis of the lattice [170]. Instead of treatment as a continuous rod as shown by Figure 15, Flory divided each molecule into a series of submolecules having parallel arranged segments in a manner consistent with Figure 16 [174, 175].

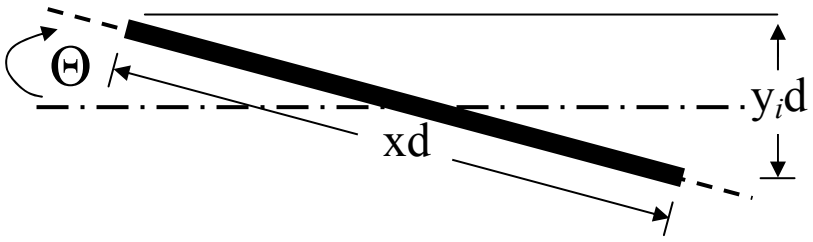

Figure 15: A rigid-rod in the Flory lattice tilted at angle Θ to the director. The rod length is taken to be xd so that x plays the role of the aspect ratio where d is the characteristic dimension of the cubic lattice cell. Reproduced from Beris and Edwards (1994), Cifferi (1994), & Wang and Zhou (2004) [171, 174, 175].

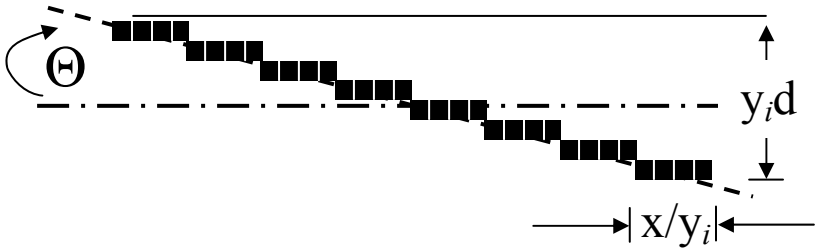

Figure 16: A rod divided into y_i submolecules having x/ y_i segments per submolecule and tilted at angle Θ to the director. The term y_id represents the height with respect to the director with units of lattice cell number. Reproduced from Beris and Edwards (1994), Cifferi (1994), & Wang and Zhou (2004) [171, 174, 175].

Introduction of a new parameter y_i known as the disorder index was defined by Equation 2.13.

$$y_i = x\sin(\Theta) \tag{2.13}$$

For Equation 2.13 to be valid it is required to take x as the rod aspect ratio with a diameter equivalent to the lattice size. Therefore, a total of y_i submolecules were taken to have x/y_i segments per submolecule, aligned along the principal axis with each

submolecule occupying one lattice site. The omission of the index on the rod length of x indicates that all solute molecules are taken to be of uniform length. In this case, with j molecules already in place, the number of situations accessible to an additional $j+1$ rod inserted into the lattice must be considered along with its orientation of Θ_{j+1}. This was achieved by estimating the probability of finding a vacant lattice site while inserting each of the $xsin\Theta_{j+1}$ submolecules one at a time, row by row. A conditional probability allowing for the necessary lattice sites in adjacent rows, a result of the inflexibility, must also be upheld. What results is the partition function for disordered rods in an athermal solution with the solvent. Both extremes of Flory's semi-flexible theory can also be recovered from this treatment. In perfect alignment the angle of inclination would disappear and there would be only one submolecule per rod. In other words, for perfect order the disorder index is unity and approaches x for complete disorder. The partition function (Z) for rods of random disorder is displayed by Equation 2.14 where Stirling's approximation has been used to treat the logarithm of combinatory factorials [171].

$$-\ln Z = n_s \ln v_s + n_x \ln\left(v_x / x\right) + n_x(x-1) - n_x \ln\sigma \tag{2.14}$$

In Equation 2.14 n_s and n_x represent the number of solvent and solute molecules with v_s and v_x represent the volume fraction of solvent and solute molecules, respectively. The rod aspect ratio is taken to be x and σ manifests itself as the rotational degeneracy factor, an arbitrary constant.

Entropy of Mixing:

Equation 2.14 can be related to the nanotube-solvent system by using more convenient factors suitable for experiment. The nanotube loading is an independent variable defined by the volume fraction, ϕ, and the aspect ratio is taken as α. With these conventions, and combining like terms, Equation 2.14 can be written in a more useful form as show by Equation 2.15.

$$-\ln Z = n_s \ln(1-\phi) + n_{NT} \ln\left(\phi/\sigma\alpha\right) + n_{NT}(\alpha - 1) \tag{2.15}$$

This expression in itself contains the statistical configuration information for the isotropic array of nanotubes approximated as a rigid-rods in an athermal solution. The change in entropy upon mixing ΔS_{mix} can then be obtained by invoking the Boltzman' relation as shown by Equation 2.16 [27].

$$\Delta S_{mix} = k_B \ln Z = -k\left[n_s \ln(1-\phi) + n_{NT} \ln\left(\phi/\sigma\alpha\right) + n_{NT}(\alpha - 1)\right] \tag{2.16}$$

Here, k_B represents Boltzmann's constant.

Enthalpy of Mixing:

In describing the enthalpy of mixing it is first necessary to consider the existence of nanotubes in their natural state. Evidence of crystalline nanotube ropes was shown by Thess et al. with hexagonal close packing [54]. Taking nanotubes having density ρ_{NT} existing in bundles of radius R_1 and length L_1 the number of bundles N_1 in a fixed mass of nanotubes can be defined by Equation 2.17.

$$N_1 = \frac{m_{NT}}{\rho_{NT} \pi R_1^2 L_1} \tag{2.17}$$

Bergin et al. considered such a system and determined the enthalpy of mixing for a solvent-nanotube dispersion by calculating the energy required to separate all molecules to infinity less the energy required to bring them back arranged in a dispersed phase [165, 176]. Here a dispersed phase is considered one in which the final solute bundle size has been reduced with respect to the bulk starting material. This was treated by dividing the contributions into five energetic components. The first component being the energy required to create the surfaces associated with the individual nanotubes, E_1^{NT}. This is a direct function of the intertube attractive potential (energy per surface area). A second enthaplic component was derived considering the energy required to remove all solvent molecules to infinity, E_1^{Sol}. This was taken as the difference between the solvent energy of cohesion (per volume) less the solvent interfacial surface energy and is by definition a function of the pure solvent only. In order to arrange the nanotubes in a dispersed state in the solvent a second term E_2^{NT} was used in the exact same fashion as E_1^{NT} but differing in the bundle final size, R_2. Presumably R_2 will be much smaller than the original bundle size. The fourth term E_2^{Sol} takes the solvent molecules from infinite separation to a molecular packing appropriate for the liquid state specific volume while leaving voids for the newly dispersed nanotube bundles. This term E_2^{Sol} is identical to E_1^{Sol} less the solvent interfacial surface energy interacting with the surface of the dispersed bundles. Finally the interfacial energy associated with placing the nanotubes in the voids E_2^{NT-Sol} is

estimated as twice the solvent-nanotube binding energy per surface area E_{Inter}^{NT-Sol}. Combining all equations and rearranging like terms yields Equation 2.18 [176].

$$\Delta H_{mix} = E_1^{NT} + E_1^{Sol} - (E_2^{NT} + E_2^{Sol} + E_2^{NT-Sol}) \tag{2.18}$$

In this analysis, the magnitude of attraction was taken to be positive by convention. Bergin et al. then assumed the solvent external surface area was the same before and after mixing and that the bundle size was much reduced compared to the original state leading to an approximate solution as displayed by Equation 2.19 [165, 176].

$$\Delta H_{mix} \approx 2\frac{m_{NT}}{R_2 \rho_{NT}}\left[E_{Sur}^{NT} + E_{Sur}^{Sol} - E_{Inter}^{NT-Sol}\right] \tag{2.19}$$

Rigorous derivation of Equation 2.19 using identical assumptions can be found in Appendix A1. Next, the solute-solvent binding energy can be approximated by Equation 2.20 with the identity of Equation 2.21 [176].

$$E_{Inter}^{NT-Sol} \approx \left(E_{Sur}^{NT} E_{Sur}^{Sol}\right)^{1/2} \tag{2.20}$$

$$\delta_i \approx \left(E_{Sur}^{i}\right)^{1/2} \tag{2.21}$$

By relating the nanotube loading to the total solution volume V_{Mix} by Equation 2.22 the energy of mixing can be made of further experimental utility as displayed by Equation 2.23 [176].

$$\phi = \frac{m_{NT}}{\rho_{NT} V_{Mix}} \tag{2.22}$$

$$\frac{\Delta H_{mix}}{V_{Mix}} \approx 2\frac{\phi}{R_2}\left(\delta_{NT} - \delta_{Sol}\right)^2 \tag{2.23}$$

According to Equation 2.23, in order to minimize the heat of mixing the surface solvent parameters for the nanotubes and solvent should match. The origin of R_2 in the

denominator is a result of estimating the tube/bundle number density N_2 in the final state from the SWNT tube density and bundle size (see Appendix A1). It is important to note that these parameters are not identical to the regular solubility parameters used in the well known Scratchard-Hildebrand solution theory. In Equation 2.23 the solute and solvent parameters are a function of the surface energy whereas Scratchard-Hildebrand uses the cohesive energy density [62]. Hence, from here on the parameters defined by Equation 2.21 are referred to as "surface-solubility" parameters. It is important to point out that approximation introduced by Equation 2.20 allows the surface solubility parameters δ_i to be estimated from the pure component interaction energy using Equation 2.21, as discussed in Chapter 4. For the nanotube "surface solubility" parameter δ_{NT} both experiment and theory have produced approximate values for the intertube attractive potential E_{Sur}^{NT}. Additionally, the pure solvent surface energy has been shown to be related to the readily measurable solvent surface tension. To this end, a surface tension criterion for minimizing the enthalpy of mixing has been estimated for solvent as ~40 mJm^{-2} by screening several common nanotube solvents [165].

Alternatively, the enthalpy of mixing can be defined using the Flory-Huggins parameter, χ. The Flory interaction parameter is dimensionless and describes the interaction energy between solute-solute, solute-solvent segment, and solvent-solvent segments [62]. For ideal solutions χ is zero and can take positive or negative values for real solutions. For chemically similar mixtures χ is small compared to unity [62]. Additionally, χ is inversely related to the temperature but independent of solute concentration [27, 177]. Equation 2.24 expresses the enthalpy of mixing as a function of

χ [27]. This expression was originally adapted from the van Laar heat of mixing by Flory [177].

$$\Delta H_{mix} = \chi RTn_s\phi \tag{2.24}$$

In the case for the nanotube-solvent system it is more useful to write n_1 in terms of the solvent volume fraction. Equation 2.25 introduces the solvent molar volume $\overline{V}_s$ to link these terms.

$$n_s = \frac{(1-\phi)V_{Mix}}{\overline{V}_s} \tag{2.25}$$

Inserting the expression for n_s into Equation 2.24 yields Equation 2.26 upon subsequent rearrangement.

$$\frac{\Delta H_{mix}}{V_{Mix}} = \chi \frac{RT}{\overline{V}_s}\phi(1-\phi) \tag{2.26}$$

By taking advantage of Equation 2.26 the heat mixing can be measured more accurately than by Equation 2.23 and this was used by Bergin et al. to validate the estimation for the enthalpy of mixing [165]. In order to minimize the enthalpy of mixing χ should be small or negative [62]. Additionally, χ can be directly related to the solubility parameters and the solvent molar volume by Equation 2.27 [62].

$$\chi = \frac{v_1}{RT}\left(\delta_{NT} - \delta_{Sol}\right)^2 \tag{2.27}$$

Equation 2.27 again supports the minimization of χ, and therefore ΔH_{Mix}, by matching δ_i for the solute and solvent which agrees with the theory behind Equation 2.23. However, the form of Equation 2.23, Equation 2.27, and any solubility parameter based expression contains a shortcoming for estimating the heat of mixing in a "real" solution. The square

of the difference in these equations cannot yield a heat of mixing less than zero [27]. Thus, exothermic mixing cannot be effectively predicted or described.

Finally, in absence of tabulated data the estimation of the enthalpy of mixing using the Flory-Huggins parameter can be achieved via the second viral coefficient. By differentiating the free energy of mixing with respect to solution volume Bergin et al. related the osmotic pressure to the second virial coefficient using a virial expansion based off the nanotube density [165, 176]. Subsequently, the osmotic pressure was related to the Rayleigh ratio via light scattering which therefore enabled the determination of the virial coefficient, and finally χ [176].

Free Energy of Mixing:

The driving force behind dissolution of a solute into a solvent can be defined by the Gibbs free energy. Equation 2.28 gives the free energy of mixing at constant temperature and pressure [3, 27].

$$\Delta G_{Mix} = \Delta H_{Mix} - T\Delta S_{Mix} \tag{2.28}$$

In the absence of metastabilities, dissolution into a single phase occurs only if the change in free energy upon mixing ΔG_{Mix} can be decreased. Criteria for dissolution can be displayed by Equation 2.29.

$$\Delta G_{Mix} = \Delta H_{Mix} - T\Delta S_{Mix} < 0 \tag{2.29}$$

In the same manner, dissolution can be viewed as competition between the enthalpy and entropy of mixing as shown by Equation 2.30 [165].

$$\Delta H_{Mix} < T\Delta S_{Mix} \tag{2.30}$$

From Equation 2.30 it can be deduced that at constant temperature and pressure minimizing ΔH_{Mix} and maximizing ΔS_{Mix} will help drive solute solubility. For typical small molecule solutions the enthalpy of mixing, ΔH_{Mix}, is small and positive whereas the entropy of mixing, ΔS_{Mix}, is of a large magnitude resulting in an overall negative free energy of mixing, driving dissolution in the solvent. As a result of their inherent properties and structure, carbon nanotubes behave differently than such an ideal small molecule system. It has been generalized that in most polymer-nanotube mixtures the large intertube van der Waals potential is expected to result a positive enthalpy of mixing [165]. This is manifested in a contribution to ΔH_{Mix} via the E_2^{NT} term of Equation 2.18 (E_{Sur}^{NT} in Equation 2.16 holds the same meaning). Furthermore, the nanotube stiffness and high molecular weight generally results in small, positive entropy of mixing [165]. By comparison, Flory-Huggins theory for a system of low molecular weight solute (small α) and solvent to that of a low molecular weight solvent and high molecular weight polymer (large α) one finds the entropy of mixing has become smaller as the solute aspect ratio increases (Equation 2.16). This is a result of the loss in conformational entropy resulting from the linked repeat units in a polymer chain compared to the less ordered and unassociated low molecular weight solute-solvent system [27]. Examining the dependence of ΔS_{Mix} (Equation 2.16) variables α and n_{NT} supports this argument for nanotube-solvent systems. Therefore, a positive free energy of mixing results in nanotube-polymer systems, preventing spontaneous dissolution. Bergin et al. confirm this hypothesis by demonstrating that the solvent N-methyl-pyrrolidone provides an enthalpy of mixing of approximately zero. The calculated result was a negative free

energy of mixing and this was confirmed by the spontaneous exfoliation of nanotubes in solution, leading to a dynamic equilibrium between individual tubes and small bundles.

Rheology Theory and Measurements:

Introduction:

In general, rheology is the field of science that studies the flow and deformation of matter [178]. Of particular interest to rheologists is the study of complex fluids. These types of fluids show mechanical behavior intermediate between classical solids and liquids. Classical fluids show what is termed prototypical "liquid-like" and "solid-like" behavior, as will be discussed in later sections. For point of reference, a classical solid will maintain its shape indefinitely whereas a classical liquid will take the shape of its container [179]. Commonly, many complex fluids will show intermediate behavior in that they will maintain their shape for a certain time and eventually flow. A fluid of this type is termed viscoelastic as it behaves like an elastic solid over short timescales and a viscous liquid over long timescales. Interestingly, a material does not have to be out of the ordinary to be considered complex. In fact, many complex fluids and materials are used everyday. Common examples of everyday complex fluids are mayonnaise and ice cream (emulsions), biological fluids like blood (suspensions), and molten plastics (polymers). Often consumer products are engineered to have complex rheological behavior such as the yield stress of toothpaste or ketchup [179].

A variety of instruments are available to measure rheological properties of fluids. Commonplace to industry and quality control are simple flow indexers or capillary viscometers. On the other hand, research grade rotational rheometers are available

capable of measuring both steady-state and transient flow properties of materials under controlled stresses and/or strains. Additionally, temperature and pressure controlling capabilities are available on many instruments [178].

Linear Viscoelasticity:

A classic example illustrating how the behavior of complex and ideal fluids differ in response under applied strain is stress relaxation. The shear strain (or simply strain) is a measure of the sample deformation due to an applied force, F. Figure 17 illustrates a sliding plate model where the sample is placed between the gap of distance h apart [180].

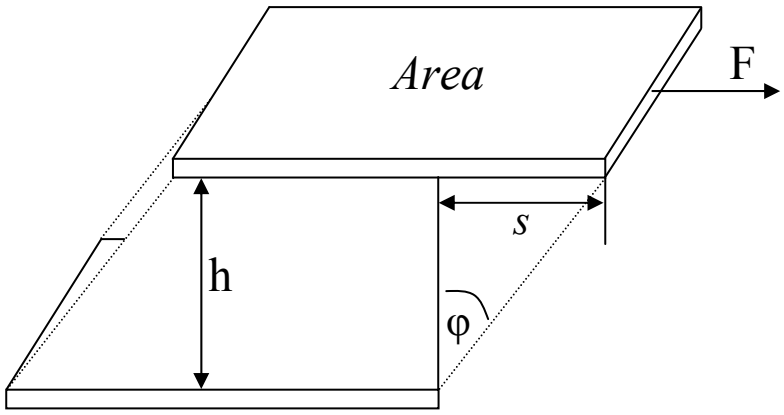

Figure 17: Illustration of important terms used in describing the shear strain of a fluid between two parallel sliding plates. Reproduced from Mezger (2002) [180].

In Figure 17 the lower plate is stationary and the deflection of the upper plate is shown by the distance *s*. Equation 2.31 defines the strain as a ratio of distances.

$$\gamma = \frac{s}{h} \tag{2.31}$$

The shear strain is a dimensionless quantity by definition and is equivalent to the tangent of the deflection angle φ. For point of reference a deflection angle of 45^{o} (π/4 radians) corresponds to a strain of 1 (100%). Often the strain set-points are quite small (< 5%) and therefore the deflection is measured in units of milliradians. While operating the rheometer in strain controlled mode the user sets the strain and therefore the deflection angle. The deflection angle is then fixed by the instrument throughout the test.

Figure 18 illustrates various response types when a step increase in strain γ is imposed on a fluid and the dissipation or relaxation of the stress τ is measured.

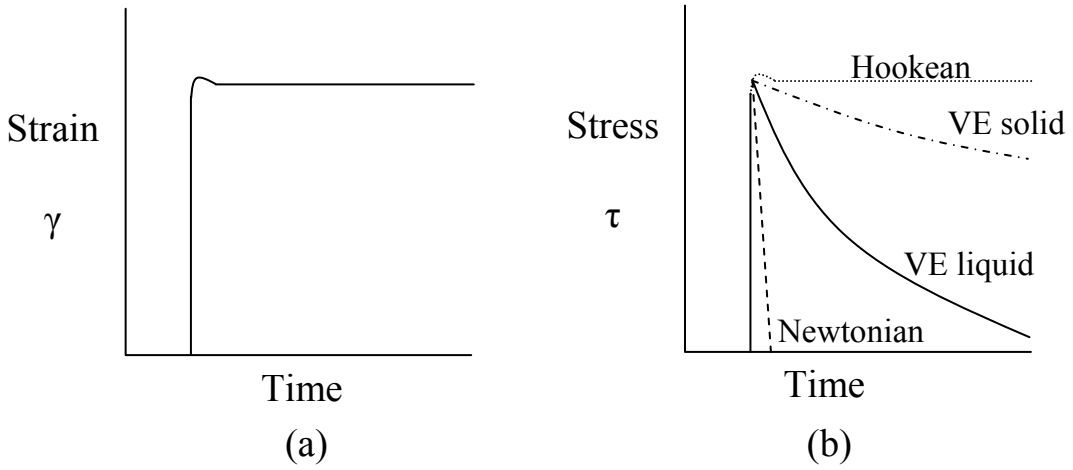

Figure 18: Illustration of a stress relaxation experiment. (a) The step increase in strain and (b) the stress vs. time response (relaxation) of various fluid types. Reproduced from Macosko (1994) [67].

Figure 18a shows the step strain imposed on the fluids. Figure 18b shows the typical response for various types of fluids. The Newtonian fluid relaxes as soon as the strain reaches a constant value characteristic of a prototypical viscous liquid. Conversely, the

Hookean solid shows prototypical elastic behavior with no stress relaxation. Intermediate behavior is seen for both the viscoelastic liquid (VE Liquid) and solid (VE Solid) where the stress relaxes over some time. The difference being the VE liquid will eventually relax to zero stress whereas the solid approaches an equilibrium value [67].

The stress relaxation data can be easily converted into a modulus by taking the stress to strain ratio. In this manner the stress relaxation modulus is defined by Equation 2.32.

$$G(t,\gamma) = \frac{\tau(t,\gamma)}{\gamma} \tag{2.32}$$

Typically, for imposed step strains larger than unity the stress is both a function of time and the imposed strain. This behavior is known as nonlinear viscoelasticity. On the other hand, for small strains, typically less than unity, log-log plots of the stress relaxation modulus superimpose. This region of strain showing independent stress modulus is known as the linear viscoelastic regime. Equation 2.33 defines the linear relaxation modulus.

$$G(t) = \frac{\tau(t)}{\gamma} \tag{2.33}$$

Both G and τ are only functions of time in the linear viscoelastic regime. This is a fundamental observation and can be exploited to further characterize the material.

Oscillatory Flow:

In the linear viscoelastic regime all measurements made at small strains less than the critical strain γ_c of that material are related to one another through Equation 2.34. To this end small-amplitude oscillatory shear measurements provide important structural

information without significantly deforming the fluid's microstructure. Furthermore, by changing the frequency of strain one can vary the timescale of observation. Typically a sinusoidal wave in stress or strain is imposed on the fluid with the frequency measured in cycles per second or commonly as angular frequency, ω, in units of radians per second. The strain can then be represented by equation 2.34 where γ_0 represents the strain amplitude.

$$\gamma = \gamma_0 \sin \omega t \tag{2.34}$$

Additionally, the strain rate is found by taking the time-derivative of Equation 2.34, the result displayed by Equation 2.35.

$$\dot{\gamma} = \omega \gamma_0 \cos \omega t \tag{2.35}$$

At steady state the stress will also oscillate sinusoidally with the same frequency but shifted by phase angle δ in regards to the strain wave, shown in Equation 2.36 [67].

$$\tau = \tau_0 \sin(\omega t + \delta) \tag{2.36}$$

Figure 19 displays the applied strain and resulting stress wave, graphically. The stress will be out of phase with the strain rate unless the fluid is Newtonian. In that case δ will shift the stress by π/4 rad and the trigonometric functions will be of equal value.

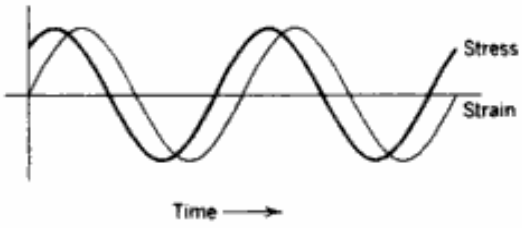

Figure 19: The imposed strain wave and resulting steady-state stress wave under simple shear flow. The stress wave is in frequency with the strain but shifted in phase by angle δ. Reproduced from Ferry (1980) [181].

The stress wave can be decomposed further by applying the sum-difference identity leading to Equation 2.37.

$$\tau_0 \sin(\omega t + \delta) = \tau_0 (\cos\delta \sin\omega t + \sin\delta \cos\omega t) \tag{2.37}$$

The first term in Equation 2.37 represents the stress component in phase with the strain wave (sin ωt) and the second represents the stress component out of phase with the strain (cos ωt). Both components oscillate on the same frequency but do not necessarily have to be of the same magnitude. Equation 2.37 holds true regardless of the deformation mode (e.g. shear, extension, flexure) provided that the strain amplitude does not exceed the linear viscoelastic threshold [178]. Graphically the components are displayed by Figure 20.

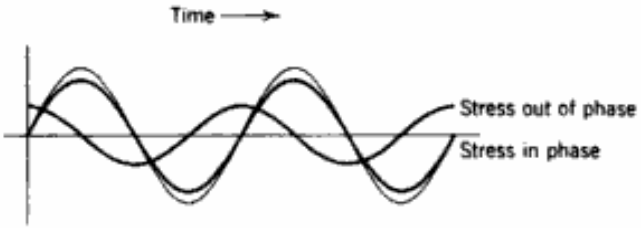

Figure 20: Trigonometric deconvolution of the steady-state stress wave in to its in-phase and out-of-phase components. Reproduced from Ferry (1980) [181].

Taking the ratio of Equation 2.37 to the strain amplitude, two independent moduli can than be defined by Equation 2.38 and Equation 2.39 [181].

$$G' = \left(\frac{\tau_0}{\gamma_0}\right)\cos\delta \tag{2.38}$$

$$G'' = \left(\frac{\tau_0}{\gamma_0}\right)\sin\delta \tag{2.39}$$

Equation 2.38 displays the in-phase modulus, commonly referred to as the storage modulus, representing the storage of elastic energy in the sample. Equation 2.39 describes the out-of-phase, viscous, or what is commonly referred to as the loss modulus. The loss modulus represents the viscous dissipation of energy through the sample [179]. For a perfectly elastic solid, the phase angle is close to zero radians and all energy is stored in the material as indicated by G" having no value. For a perfectly viscous liquid, the phase lag is close to $\pi/4$ radians and all energy is dissipated through the sample as heat with G' having magnitude of zero. Figure 21a displays the linear viscoelastic response of a prototypical "solid-like" fluid and Figure 21b shows the response of a prototypical "liquid-like" fluid.

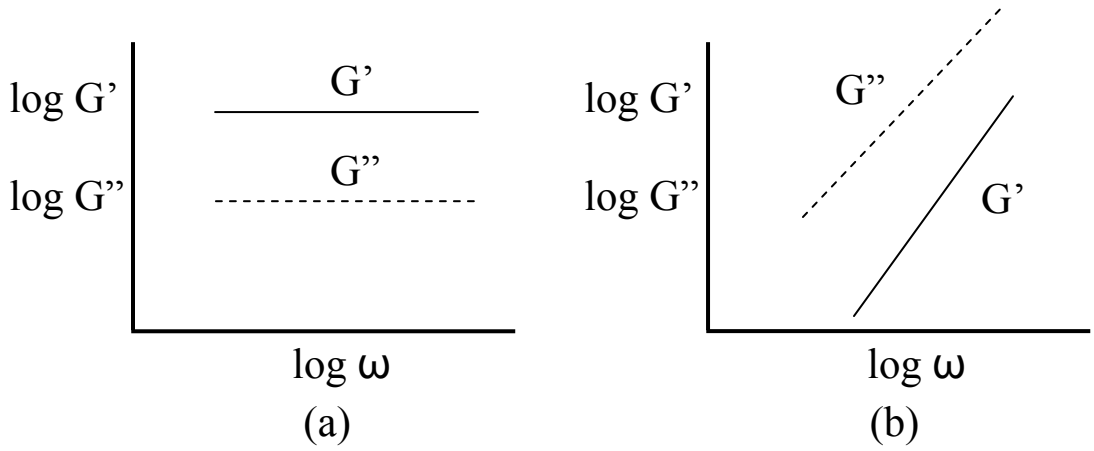

Figure 21: The prototypical linear viscoelastic response in terms of frequency dependent storage and loss moduli G' and G" for (a) a "solid-like" fluid and (b) a "liquid-like" fluid. Adapted from Larson (1998) [179].

For the "solid-like" response in Figure 21a, G' is much greater than G" in magnitude and G' is also nearly or completely frequency independent. G" does not necessarily have to

be frequency independent and may show some upturn at low frequency as a result of aging, as predicted for glassy substances [182]. For the "liquid-like" response shown in Figure 21b G" dominates in magnitude and both moduli scale with frequency in a power-law fashion. As mentioned previously, real complex fluids are expected to show some behavior intermediate to these two ideal responses.

Taking advantage of Equation 2.38 and Equation 2.39 the expression for the stress wave (Equation 2.37) can be written in the more convenient form given by Equation 2.40.

$$\tau = \gamma_0 \left[G' \sin(\omega t) + G'' \cos(\omega t) \right] \tag{2.40}$$

Another useful parameter is defined by taking the ratio of the loss modulus to the storage modulus as displayed by Equation 2.41.

$$\tan \delta = \frac{G''}{G'} \tag{2.41}$$

The result is referred to as the loss tangent, damping factor, or by "tan delta." Its magnitude is greater than unity for samples behaving "liquid-like" and less than unity for "solid-like" samples. Alternatively, liquid or solid behavior can be inferred by what modulus is dominant in magnitude at a given frequency. Tan delta is simply another means to measure energy dissipation in viscoelastic materials [178].

The complex modulus G^* is defined by considering the amplitude of the stress waveform as a whole and taking its ratio to the strain amplitude [179]. Its magnitude is defined by Equation 2.42.

$$\left| G^* \right| = \left(G'^2 + G''^2 \right)^{1/2} = \frac{\tau_0}{\gamma_0} \tag{2.42}$$

The magnitude of G^* can be interpreted as a measure of the overall resistance to deformation. This measurement takes no consideration in to the how the energy is dissipated via G' and G" individually. Finally, dividing the complex modulus by the angular frequency gives the magnitude of the complex viscosity η^* as displayed by Equation 2.43.

$$\left|\eta^*\right| = \frac{\left|G^*\right|}{\omega} = \left[\left(\frac{G'}{\omega}\right)^2 + \left(\frac{G''}{\omega}\right)^2\right]^{1/2} \tag{2.43}$$

The complex viscosity is a measure of the fluid's resistance to flow under oscillatory shear.

The complex viscosity can be related to the shear or apparent viscosity by means of the "Cox-Merz rule." This relationship is strictly empirical but often holds true at high shear rates. Cox-Merz simply states that shear viscosity of a fluid at steady state is equivalent to the complex viscosity of that fluid in the linear viscoelastic regime provided that they are measured at equivalent magnitudes of rotational shear rate and angular frequency [67]. Mathematically this can be expressed by Equation 2.44 with the condition of Equation 2.45.

$$\eta(\dot{\gamma}) = \left|\eta^*(\omega)\right| \tag{2.44}$$

$$\dot{\gamma} = \omega \tag{2.45}$$

Again, Equation 2.44 holds true only if the conditions of matching shear rate and angular frequency shown by Equation 2.45 are met. It is important to note that $\dot{\gamma}$ used in Equation 2.45 is intended to represent the shear rate but its meaning still holds true as the rate of deformation. The difference being that under steady rotational shear the shear strain and

therefore shear rate is held constant whereas under oscillatory flow it remains a function of time.

Simple Shear:

Although the geometries of various rheological measuring systems may vary all are similar in that they impose a drag flow by controlled motion along a system boundary. For point of reference, refer to Figure 22 showing a simple sliding plate geometry. All motion is along one coordinate direction (x_1) with velocity varying in a second coordinate (x_2) orthogonal to the shear geometry [178]. This type of flow is called viscometric flow.

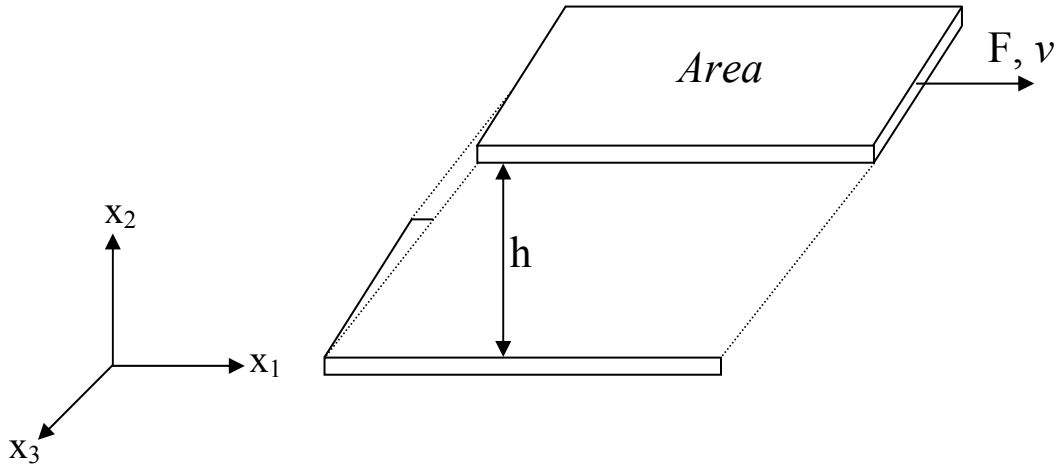

Figure 22: The sliding plate model and relative coordinate system for simple shear. Adapted from Gupta (2000) and Mezger (2002) [178, 180].

The upper plate in Figure 22 moves along the positive x_1 direction with velocity *v* while the sample remains between the gap of distance h. Mathematically viscometric flow

translates to there being only one non-zero velocity component v_1 and therefore one non-zero component to the velocity gradient tensor [67]. This non-diminishing component is known as the shear rate $\dot{\gamma}$ and can be represented by Equation 2.46.

$$\dot{\gamma} \equiv \frac{\partial v_1}{\partial x_2} \tag{2.46}$$

It is noteworthy to indicate that the shear rate is simply the velocity gradient and is often alternatively referred to as rate of deformation or strain rate as will be discussed in later sections. For sliding-plate type geometries the magnitude of the shear rate is simply the velocity divided by the gap as shown by Equation 2.47.

$$\dot{\gamma} = \frac{v}{h} \tag{2.47}$$

The force that the flowing fluid is exerting on the surface, per unit area of that surface, in the direction parallel to flow is known as the shear stress, τ. After imposing a steady shear to a fluid from a state of rest the shear stress does not reach steady state immediately. Rather, the stress goes through a transient start-up period where it varies with time. The ratio of the instantaneous stress $\tau(\dot{\gamma}, t)$ to the imposed steady shear rate gives the transient start-up viscosity $\eta(\dot{\gamma}, t)$ as shown by Equation 2.48.

$$\eta(\dot{\gamma}, t) = \frac{\tau(\dot{\gamma}, t)}{\dot{\gamma}} \tag{2.48}$$

After a period of time has elapsed in which a steady shear has been applied the shear stress often comes to a steady state. Thus, the shear stress is no longer a function of time and the shear viscosity is defined by Equation 2.49.

$$\eta(\dot{\gamma}) = \frac{\tau(\dot{\gamma})}{\dot{\gamma}} \tag{2.49}$$

The behavior of the shear stress as a function of various shear rates is one way to define the type of fluid. The simplest response is that of a Newtonian fluid in which the shear stress is directly proportional (linear) to the shear rate and the viscosity is therefore constant. Deviation from this behavior indicates a shear rate dependence on viscosity and materials exhibiting this type of response are classified as non-Newtonian.

A common phenomena seen with some complex fluids is that of a yield stress. Often fluids with some "solid-like" character will not initially flow upon the inception of shear. Instead the stress grows linearly with shear rate up to a critical value above which the material "yields" or flows at a constant shear stress. It is noteworthy to point out that yielding is often indicated by the absence of flow but this term is truly intended to describe the point at which flow begins not resists; this is a common point of confusion [179].

In general, a fluid is a material that cannot support a shear stress without flowing [67]. Consider the fluid element displayed by Figure 23. If at rest, all surface stresses on that element act orthogonal to the surface (normal stresses) and are not only equal in magnitude but independent of orientation of the element. This type of normal stress is known as the hydrostatic pressure and is compressive in nature. The absence of motion within the element also implies the absence of shear stresses. Thus, for a fluid in motion it follows that their must be either shear stresses present or normal stresses that are unequal. These shear stresses are known as viscous or extra stresses because they act on a fluid in addition to the fluid pressure.

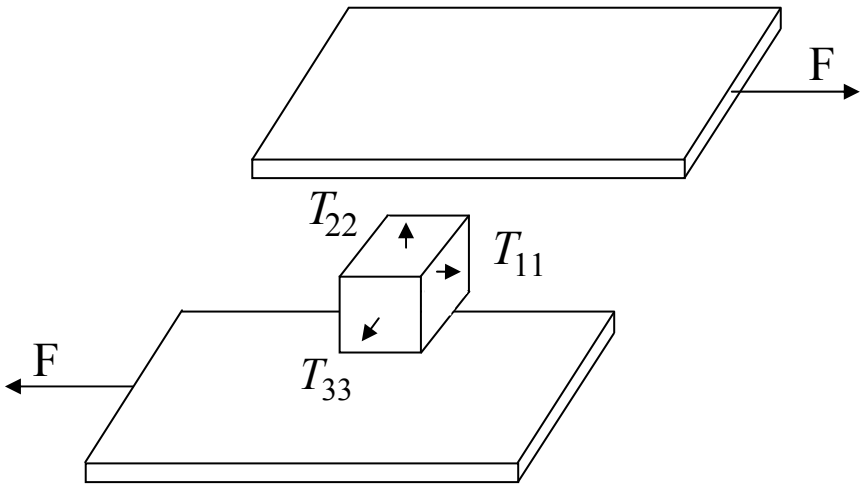

Figure 23: Schematic diagram showing the notation for normal stresses in a shear field. Adapted from Gupta (2000) [178].

The tensor T_{ii} contains the contributions of the pressure and the extra stress as shown by Equation 2.50.

$$T_{ii} = -p + \tau_{ii} \tag{2.50}$$

As a consequence of most liquids being considered incompressible the application of equal normal stresses (pressure) along the three coordinate directions shown in Figure 23 does not lead to deformation or a change in volume. Therefore, it is only unequal normal stresses that may cause motion or strain in liquids. This means that one cannot determine the absolute value of the normal stresses from controlled strain experiments but only normal stress differences because the value of p alone is indeterminate. Equation 2.51 gives the expression for the first normal stress difference N_1 and Equation 2.52 gives the expression for N_2.

$$N_1 = T_{11} - T_{22} = \tau_{11} - \tau_{22} \tag{2.51}$$

$$N_2 = T_{22} - T_{33} = \tau_{22} - \tau_{33} \tag{2.52}$$

Subtraction of normal stresses eliminates the pressure term leaving only the difference between the extra stress. A negative first normal stress difference tends to force the plates together and the positive first normal stress difference tends to push them apart. For a detailed explanation see Kumar and Gupta (2003) [3]. On the other hand the second normal stress difference tends to bulge the fluid at the edge of the plates. The most common instance of a positive first normal stress difference is the die swell experienced by a melt extruded polymer emerging into the atmosphere. But in general, if the fluid being sheared is polymeric the normal stresses become unequal in magnitude and if the fluid is Newtonian their magnitude remains the same [178].

Cone and Plate Rheometer:

The geometrical features of the cone and plate rheometer is displayed by Figure 24 utilizing a spherical coordinate system (r, θ, ϕ). A flat, circular plate of radius R is opposed by a linearly concentric upper cone. The tip of the cone is truncated so that no physical contact is made with the lower plate. The cone angle α is typically only a few degrees and the cone is rotated at an angular speed of Ω. Rigorous derivation for the velocity profile, shear stress, first normal stress, and finally the torque can be found in Macosko (1994) starting from the equations of motion in spherical coordinates [67, 183].

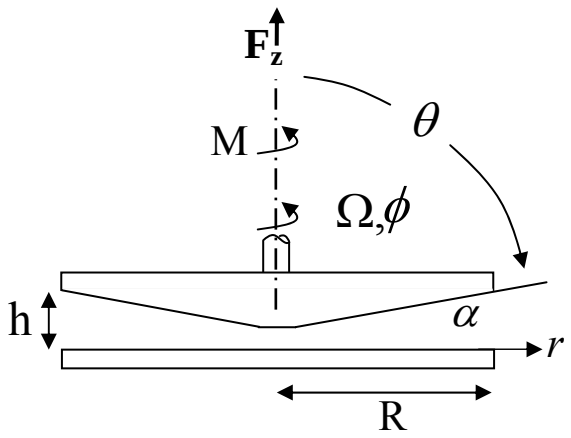

Figure 24: Coordinate system and geometric parameters used to describe the cone and plate measuring geometry. Adapted from Macosko (1994) [67].

Assuming that the velocity is a function of r and θ only and the only non-diminishing component is in the ϕ direction (v_ϕ) the shear stress can be measured from the raw torque by Equation 2.53.

$$\tau = \frac{3M}{2\pi R^3} \tag{2.53}$$

During an experiment the rheometer measures the raw torque, from a torque transducer, required to maintain the set test variable which is commonly the shear rate or the angular frequency at set strain amplitude. By means of Equation 2.54 the shear stress is calculated and vice versa for stress controlled measurements. It is important to note that there is no θ angular dependence on the shear stress due to the small magnitude of α. Thus, the shear stress imposed on the fluid is essentially constant and uniform and therefore the shear strain and shear rate are uniform as well [67]. Analogous to Equation 2.31 for the sliding plate, the shear strain in cone and plate geometry is measured by

introducing the angular displacement θ_d. Equation 2.54 represents the angular displacement under steady shear.

$$\theta_d = \Omega t \tag{2.54}$$

By this definition the shear strain is displayed by Equation 2.55.

$$\gamma = \frac{\theta}{\alpha} \tag{2.55}$$

Likewise, the equivalent expression to Equation 2.47 for the shear rate in a cone and plate geometry is given by Equation 2.56.

$$\dot{\gamma} = \frac{\Omega R}{h} = \frac{\Omega}{\tan\alpha} \approx \frac{\Omega}{\alpha} \tag{2.56}$$

Here the angular speed of the cone is given by Ω and the cone angle is represented by α. The product of the angular speed and the radius R gives the tangential velocity at the edge. The first normal stress difference is measured directly in cone and plate geometry by the total thrust on the plate. Equation 2.57 gives the value of N_1 as well as its interpretation.

$$N_1 = T_{\phi\phi} - T_{\theta\theta} = \frac{2F_z}{\pi R^2} \tag{2.57}$$

Here N_1 is taken to be the difference between the normal stress in the direction of flow and the direction orthogonal to the lower plate. The quantity F_z is the normal force measured by the rheometer force transducer taken to be the force required to hold the apex of the cone at the center of the lower plate [178, 179]. Similar expressions for Equation 2.57 can be found in various textbooks with all measuring the downward force [67, 178, 179]. As displayed by Figure 24, the rheometer used in this study measures the

normal force in the opposite direction. Thus, the magnitude of Equation 2.57 must be adjusted for the coordinate system as displayed by Equation 2.58.

$$N_1 = \frac{-2F_z}{\pi R^2} \tag{2.58}$$

Parallel Plate Rheometer:

Given that the cone and plate rheometer provides a uniform stress it is the preferred geometry for many rheologists. However, if suspensions of particles or filled polymer melts have dimensions comparable to the small gap between the cone and plate a parallel plate geometry must be used. In many ways these two devices are similar with the striking difference being that the flow between the parallel plates is not homogeneous but a function of the radius *r*. Figure 25 displays the geometrical constructs parallel plate rheometer. A cylindrical coordinate system (r, θ, z) has been used to describe the plates. Two identical and coaxial flat parallel disks are rotated to impose flow. Typically the upper plate is rotated with an angular speed of Ω in the direction of θ. The gap between the plates h is held constant and can be adjusted throughout testing. An adjustable gap is advantageous for correcting sample edge defects or checking for sample slip whereas with the cone and plate rheometer the gap is fixed and requires reloading upon edge failure. Rigorous derivation for the velocity profile, shear stress, first normal stress, and finally the torque can be found in Macosko (1994) starting from the equations of motion in cylindrical coordinates [67, 183].

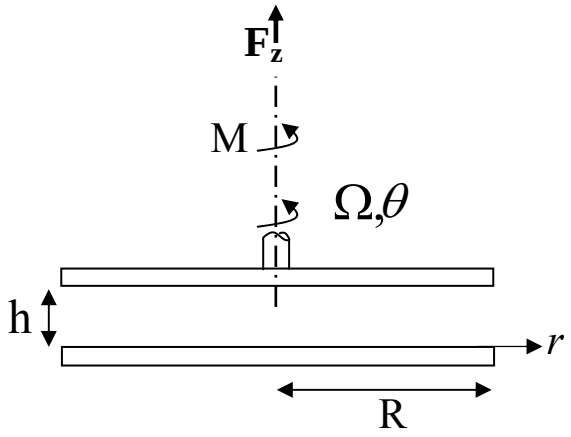

Figure 25: Coordinate system and geometric parameters used to describe the parallel plate measuring geometry. Adapted from Macosko (1994) [67].

Assuming that the velocity is a function of r and z only and the only non-diminishing component is in the θ direction (v_θ) the shear stress can be measured from the raw torque by Equation 2.59.

$$\tau(r) = \frac{M}{2\pi R^3}\left[3 + \frac{d\ln M}{d\ln \dot{\gamma}_R}\right] \tag{2.59}$$

Examining 2.59 it should be apparent that the derivative of the natural log of the torque with respect to the natural log of the plate edge shear rate $\dot{\gamma}_R$ cannot be determined accurately without sufficient data to correlate the two variables. However, if the fluid is Newtonian the derivative equals unity and the shear stress is defined as the apparent shear stress τ_a. Equation 2.60 gives the expression for the apparent shear stress.

$$\tau_a(r) = \frac{2M}{\pi R^3} \tag{2.60}$$

Often the apparent shear stress is simply used to calculate an apparent viscosity since only the raw torque measurement is required. Obvious inaccuracy may be contained within measurements but this if often not addressed in the literature. However, in the case of sinusoidal varying measurements within the linear viscoelastic regime the derivative in Equation 2.59 also diminishes to unity and the apparent stress given by Equation 2.60 is exact [67]. In both cases Equation 2.59 and Equation 2.60 are function of the radius of observation. This is a result of the shear rate being a function of the angular speed which varies with radial distance from the center of the plate. Equation 2.61 displays the shear rate for the parallel plate geometry.

$$\dot{\gamma}(r) = \frac{r\Omega}{h} \tag{2.61}$$

For sake of completeness the shear rate at the plate edge introduced previously is defined by Equation 2.62.

$$\dot{\gamma}_R = \frac{R\Omega}{h} \tag{2.62}$$

Likewise the shear strain also varies with radial position and can be calculated from Equation 2.63.

$$\gamma(r) = \frac{r\theta_d}{h} \tag{2.63}$$

The angular displacement θ_d was introduced previously by Equation 2.54. To evaluate visoelastic moduli the strain should be measured at the plate edge. Equation 2.64 gives the expression for the edge strain.

$$\gamma_R = \frac{R\theta_d}{h} \tag{2.64}$$

In contrast to the cone and plate rheometer the first normal stress difference cannot be measured alone for a parallel plate system. Instead what is obtained is the difference between the first and second normal stress differences as shown by Equation 2.65.

$$\left(N_1 - N_2\right)\Big|_{\dot{\gamma}_R} = \frac{F_z}{\pi R^2}\left[2 + \frac{d\ln F_z}{d\ln \dot{\gamma}_R}\right] \tag{2.65}$$

The normal force is represented by F_z and is taken to be positive consistent with Figure 25. Again if one were to compute Equation 2.65, consideration for the coordinate system of the instrument must be accounted for. In order to completely decompose the difference between N_1 and N_2 measurements must be made in both parallel and cone and plate geometries and compared. Since N_2 is often of little magnitude the parallel plate is commonly used alone to estimate N_1.

Rheology of Particulate Suspensions:

Suspensions consist of discrete particles dispersed in a liquid medium [67]. The hydrodynamic disturbance resulting from the presence of particles was first determined by Einstein (1906 & 1911). The presence of particulates can not only drastically change the measured viscosity but can also introduce non-Newtonian behavior to the fluid under study. Essentially, the particle will modify the velocity distribution in a flowing liquid. Extra energy dissipation will arise because of this and will be reflected in a proportional increase in viscosity. The stability of these types of fluids are of primary concern if one is to measure the rheological properties of the dispersion. An exhaustive list of important assumption and criteria that need be met for accurate rheological measurements can be

found in the classic text by Macosko [67]. In general, for reproducible results the fluid structure or dispersion state should not change over the duration of the experiment.

Particle settling is the primary cause for concern as particles larger than approximately 1 μm tend to settle under the influence of gravity alone [179]. This can be circumvented by either matching the density of the suspending medium to that of the particle or by using a medium that is very viscous. By matching the densities of the particles and fluid the buoyant force can be exploited to support particles in suspension. Likewise, if the particles are Brownian, the ratio of gravitational to Brownian forces should be less than unity indicating stability from thermal motion. Brownian motion is the name given to the irregular movement of pollen in water as observed by Robert Brown (1827) [184]. If the particle dimensions are small (generally sub-micron) then the random thermal motions of solvent molecules can transfer momentum to the particle. By this analysis a density difference of approximately 1 g/mL leads to settling of particles bigger than 2 μm in diameter [179]. On the other hand, if the medium is viscous the rate of particle sedimentation can be slowed. Depending on the viscosity of the solvent this effect may be enough to allow for stable measurements to be taken over the duration of the rheological testing. An approximate criterion for neglecting the effect of settling in spherical particles can be obtained from Stoke's law as shown by Macosko (1994) [67].

Rheology of Nonspherical Particle Suspensions:

Generally, the rheology of nonspherical suspensions depend on the particle loading, the aspect ratio and its distribution, as well as the rheology of the suspending fluid [178]. To begin to understand how elongated particles flow single non-interacting

particles in dilute suspensions were considered. At these conditions the suspension can be essentially thought of under the constraints of an ideal gas. Jeffery (1922) considered non-interacting particles dispersed in a Newtonian fluid in the absence of Brownian motion. Solving the appropriate equations of motion he concluded that axisymmetric non-Brownian particles (rods, prolate spheroids) not only translate but rotate indefinitely under the influence of a shearing flow [178, 179]. Interestingly the rotation was discovered to be periodic with time in what is now known as a "Jeffery Orbit." Particles with large aspect ratios were predicted to rotate rapidly when their longest dimension was orthogonal to flow and very slowly when parallel. The consequence of this type of behavior is that the viscosity, which depends on the dispersion microstructure, is also periodic and cycles with time [178].

If Brownian motion cannot be neglected stochastic deviations from the Jeffery Orbits for particles is observed and must be dealt with probabilistically. In absence of flow an important Brownian phenomena known as the dilute-solution rotary diffusivity D_{r0} can be estimated. The rotary diffusivity is simple a measure of the rate at which a particle reorients by Brownian motion. For rods of length L and diameter d, D_{r0} can be estimated from the theory of Doi and Edwards and that of Kirkwood and Auer [179, 185, 186]. Equation 2.66 gives the expression for the rotary diffusivity.

$$D_{r0} = \frac{3k_B T\left(\ln\left(L/d\right) - 0.8\right)}{\pi \eta_s L^3} \tag{2.66}$$

From Equation 2.66 one can see the logarithmic dependence on the length to diameter ratio known as the aspect ratio of the rods. The viscosity of the suspending fluid or solvent is represented by η_s, the temperature T, and Boltzmann's constant by k_B. If the

solvent is non-Newtonian the viscosity should be taken in the limit of zero-shear as η_0. The rotary diffusivity at higher concentrations has also been predicted by Doi and Edwards but is not discussed here [185].

Under the application of shear the crossover from Brownian to non-Brownian behavior for a flowing suspension can be calculated by the magnitude of the rotational Peclet number [179]. Equation 2.67 displays the dimensionless Peclet number Pe as a ratio of what is essentially two independent shear rates.

$$Pe \equiv \frac{\dot{\gamma}}{D_r} \tag{2.67}$$

The shear rate in the numerator should be taken as the lowest value imposed in experiment in order to characterize the lower limit of the transition. Likewise the rotary diffusivity in the denominator can then be taken as the dilute-solution rotary diffusivity. A value of Pe greater then unity indicates a dominating contribution by the imposed shear rate and thus non-Brownian behavior. On the contrary, a value of Pe less than unity indicates that the rotary diffusivity dominates and thus Brownian motion is relevant in the imposed flow field. Identifying Brownian and non-Brownian behavior is important for computational modeling and interpretation of particle dispersions as the stress tensor contains an elastic contribution from Brownian motion [179]. In absence of Brownian motion this contribution is simply neglected.

Relaxing the criteria for dilute dispersions brings in some additional considerations in describing particulate suspensions. To this end the rheology of rodlike particles is defined by unique concentration regimes as displayed by Figure 26.

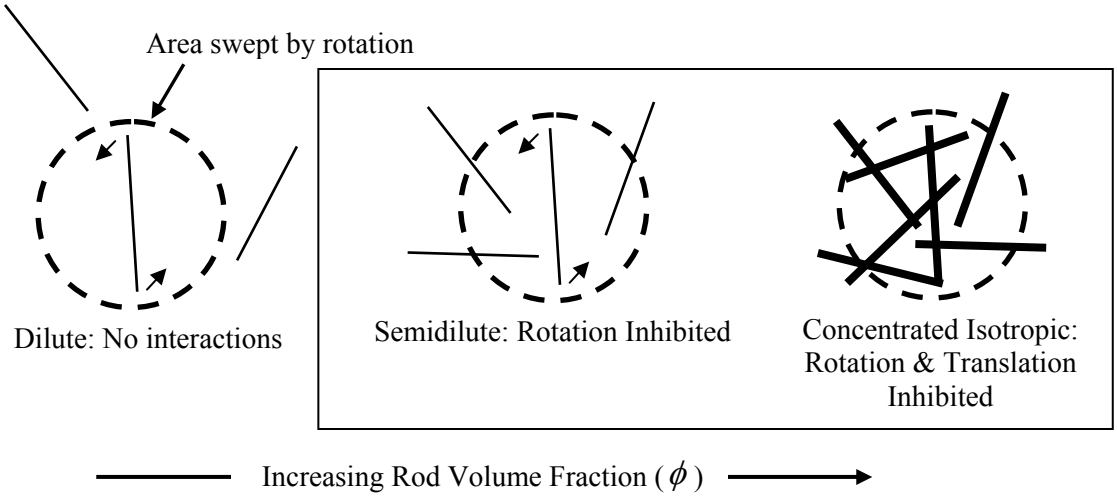

Figure 26: Concentration regimes used to describe rod-like particles. Adapted from Larson (1999) & Doi and Edwards (1986) [179, 185].

Here, the major assumption is that the rods are rigid and inflexible with the absence of attractive interactions [185]. In the dilute regime the rods are able to rotate freely without interacting with neighboring rods. Considering a rod of length L rotating about its center of mass there is a volume of approximately L^3 that must be free of nearest neighbors. Equation 2.68 introduces the relationship between the number concentration υ and volume fraction ϕ of rods.

$$\phi = \frac{\pi d^2 L \upsilon}{4} \tag{2.68}$$

From Equation 2.68 one can define transitions between each regime. Intuitively rod-rod interactions can be assumed to occur when the number density approaches L^{-3} but experiment has shown disagreement with this prediction. The volume fraction which delineates semidilute from dilute behavior is approximated by Equation 2.69.

$$\phi_0 \approx 24\left(\frac{d}{L}\right)^2 \tag{2.69}$$

As shown by Figure 26 the semidilute regime is characterized by having neighboring rods impeding the rotation of one another but still allowing translation through the suspending fluid. Therefore at rod concentrations somewhat above ϕ_0 a rod may be inserted with negligible probability of intersecting another and therefore excluded volume is not a factor [179]. The effect of the rod volume is indicated in Figure 26 by the size of the lines used to represent each rod. Increasing concentration in the semidilute regime there lays a point in which the rods have trouble isotropically arranging themselves due to excluded volume interactions. This condition delineates the semidilute from the concentrated isotropic regime as approximated by Equation 2.70.

$$\phi_0^{'} \approx \frac{\pi d}{4L} \tag{2.70}$$

In practice, for both rigid and flexible rod-like particles or polymers, these naming conventions for various concentration regimes are used. The logic being that in the case of flexibility the swept area would be smaller. Therefore, the transitions predicted for rigid rods would be conservative estimates on the higher end of each concentration regime. For non-Brownian rods the interpretation of when the crossover from dilute to semidilute occurs is physically taken to be the point when the rods begin to influence each other hydrodynamically. It is important to note that this crossover is not necessarily at the same concentration that Brownian motion of one rod would be affected by its nearest neighbors [179].

Other deviations between Brownian and non-Brownian behavior can be seen in the shear viscosity of suspensions. At low shear rates the theory of Doi and Edwards predicts a large increase and domination of the stress contribution from Brownian motion as the concentration is taken from dilute to semidilute [179]. However in non-Brownian solutions this is not the case and the same dramatic viscosity increase in not expected. The modest particle contribution to the viscosity was experimentally and theoretically confirmed even for fibers with large aspect ratios by Yamane et al. (1994) and Bibbo (1987) [187, 188]. This occurs because in absence of Brownian motion the fibers readily rotate to align with the shear flow contributing little to the shear viscosity which is especially true at large Pe. Hence, the shear history must be considered when measuring the rheological properties of non-Brownian suspensions and is of utmost importance for reproducible results. It may also be necessary to allow sheared suspensions to relax back to isotropic orientation before characterization.

As the concentration of the particles is increased through the semidilute regime there is a critical point where three-dimensional network formation occurs known as percolation. This onset of network formation is interpreted differently depending on the mode of percolation. Rheological percolation occurs when the particle network is sufficient to impede the motion of the solvent. If the solvent is a high molecular weight polymer percolation occurs when the size of the polymer chain is large compared to the separation between the rods or particles [189]. Depending on the length of the polymer percolation may be a result of entanglement instead of intertube contacts. This is initially characterized by a "solid-like" viscoelastic response over short timescales. A second mode of percolation exists in which electrical conductivity can be realized. However, the

formation of conductive networks occurs on a different length scale. It has been shown that physical contact does not need occur in nanotube systems since the intertube distances only need be close enough for elections to "hop" from one tube to another. This distance has been estimated to be less then ~5 nm [103, 189]. Being that CNTs are comprised of some non-metallic tubes not all particles contribute to network conductivity. Thus, in CNT systems electrical percolation can be assumed to occur at higher loading than rheological percolation. Furthermore, CNT with sidewall defects contribute little to the conductivity. This has been shown experimentally by Hu et al. (2006) for MWNTs in poly(ethylene terephthalate) where "solid-like" viscoelasticity was found at 0.6 % wt. loading followed by the onset of electrical conductivity at 0.9 % wt. [189]. Likewise, Du et al. found rheological percolation at 0.12 % wt. and electrical percolation at 0.39% wt. for SWNT-poly(methyl methacrylate) composites [103]. These results are consistent with theory modeling the geometrical percolation for overlapping needles (no excluded volume) with aspect ratios from 10^2-10^3 to be in the range of 0.1-1% vol. [190]. Differences between the results of Hu et al. and Du et al. can be attributed to differences in aspect ratio and dispersion state between the two composite systems. For this reason the percolation threshold for high viscosity thermoplastic melts can be expected to be larger than that of low viscosity thermoset solutions [189]. In general, the greater the aspect ratio, the less the packing density of the particles and the lower one would expect to find the critical volume concentration [191].

Evidence of fiber interactions can also be seen from the fact that a steady state is ever reached in steady shearing flow. In the absence of such interactions the original fiber orientation would be revisited continuously over a period consistent to that

predicted by Jeffery. In fact, even very weak hydrodynamic interactions incurred in the semidilute regime are enough to disturb the Jeffery orbits and produce a steady-state distribution of orientations such that the viscosity reaches a steady value [179].

3. EXPERIMENTAL DETAILS

Microscopy:

Scanning Electron Microscopy:

In order to characterize sample surface morphology SEM images were taken. Samples were prepared by applying double sided carbon tape to a JEOL Specimen Mount (Ted Pella, Inc.). Materials of interest were then pressed on the surface of the carbon tape and examined using a JEOL 7000-F Field Emission-Scanning Electron Microscope.

Transmission Electron Microscopy:

Samples were prepared for TEM by first diluting the SWNT-UPR dispersion in acetone directly in the shear mixer. Only low shear was applied so as to wash the sample but not further separate the SWNTs. This solution was then dropped onto a 30 mesh copper grid coated with a formvar carbon support film (Electron Microscopy Sciences). After air dying the grid was dried under vacuum at ~105^{o}C to remove residual solvents. A Zeiss EM 10C 10CR Transmission Electron Microscope was used to study the samples.

Optical Microscopy:

At various points in the mixing process dispersions were characterized by optical microscopy using a Nikon (Melville, NY) Eclipse 80*i* optical microscope. Samples were

illuminated by either transmission or reflected light and images were recorded digitally. Both 10x (0.3 NA) and 20x (0.45 NA) "Luminous Universal Plan Fluor" Nikon objectives were used without oil immersion. For high magnification optical images a Nikon 60x (1.40 NA) "Plan Apo VC" oil immersion objective was used. Either 1x or 2x magnification was also applied before the camera giving a maximum effective magnification of 120x. Images were collected and processed in both Nikon Elements and Nikon ImagePro software. Scalebars were calibrated and applied by means of a manufacturer supplied optical micrometer.

Raw Materials:

Unsaturated Polyester Resin:

Polylite® X31003-00 base resin (Lot# 4508-38) was used as-received from Reichhold (Research Triangle Park, NC). This resin is classified as an isophthalic base resin having 40% wt. styrene monomer and 60 % wt. proprietary polyester resin. This resin contained no additional additives or catalyst.

Vapor Grown Carbon Fiber:

Pyrograf III grade PR-19 (PR-19 XT PS LD) was obtained from Applied Sciences Inc. (Cedarville, OH) and used as-received. Figure 27 displays a SEM micrograph showing the morphology and fiber diameter of the VGCFs. Lengths of the VGCFs range from 10 μm to over 100 μm, as indicated by the manufacturer.

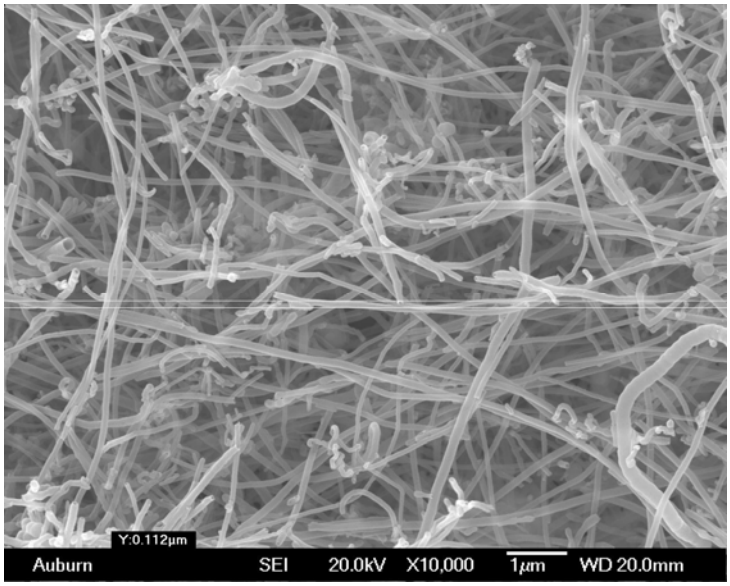

Figure 27: SEM Image of the as-received VGCF. The measured fiber diameter is approximately 110 nm across. A loose network structure can be seen from this image.

Single-walled Carbon Nanotubes, Batch 183.6:

SWNTs (Batch 183.6) produced by the high-pressure carbon monoxide (HiPco) process were received from Rice University (Houston, TX) partially purified following a deactivated thermal oxidation process as described by Xu et al. (2005) [192]. The following images show the overall sample morphology and network structure for both the as-received (183.6 Unpure) and purified (183.6 Pure) sample. Figure 28 shows both low and high magnification SEM images of the as-received SWNT 183.6. Likewise, Figure 29 shows the structure of the sample after purification. At low magnification both materials appear to have a similar overall morphology of aggregates and some ribbon-like structure. But, the high magnification image of the 183.6 Pure shows an increase in rope size. These ropes also appear very uniform and defect free as compared to the high

magnification image of the 183.6 Unpure sample. This is likely a result of the removal of both residual catalyst and amorphous carbon from the as-received material.

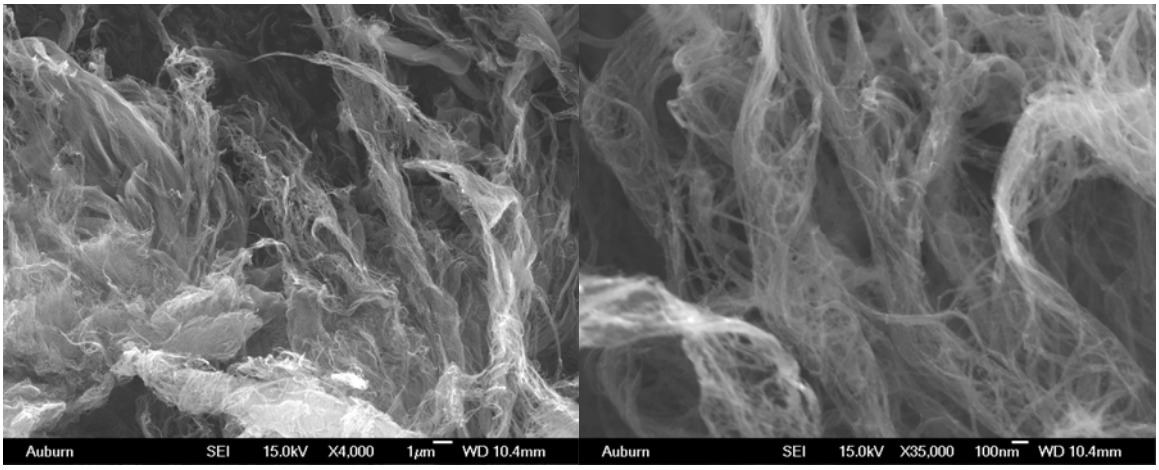

Figure 28: SEM images showing the morphology of the as-received (un-purified) SWNT 183.6 imaged at (left) 4,000x magnification and (right) 35,000x magnification.

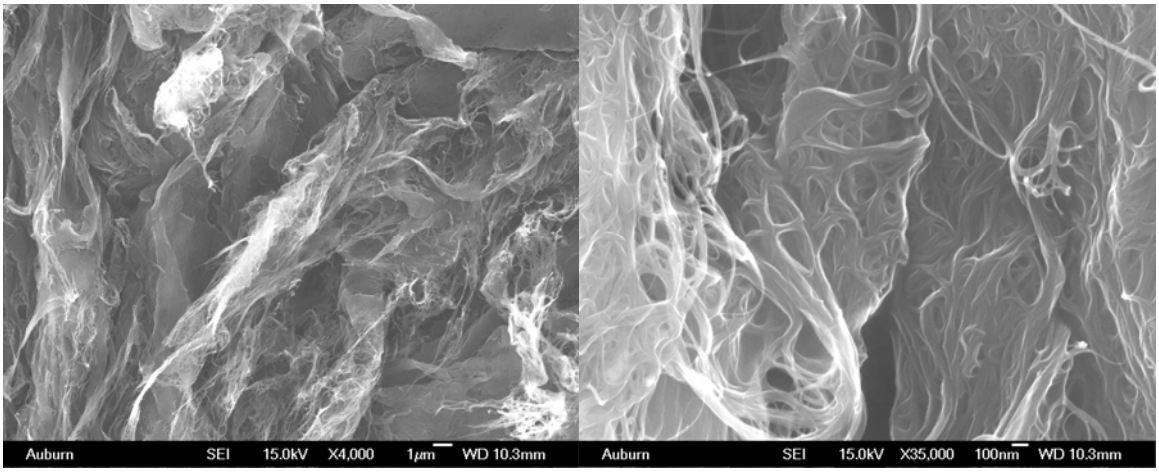

Figure 29: SEM images showing the morphology of the SWNT 183.6 Pure imaged at (left) 4,000x magnification and (right) 35,000x magnification.

Single-walled Carbon Nanotubes, Batch 187.3:

SWNTs (Batch 187.3) produced by the high-pressure carbon monoxide (HiPco) process were received from Rice University (Houston, TX) fully purified and used as-

received. Figure 30 shows the overall sample morphology under low magnification and network structure under high magnification. At low magnification the bulk sample appears in aggregate form. Higher magnification images reveal non-uniform and loosely packed, entangled ropes or bundles.

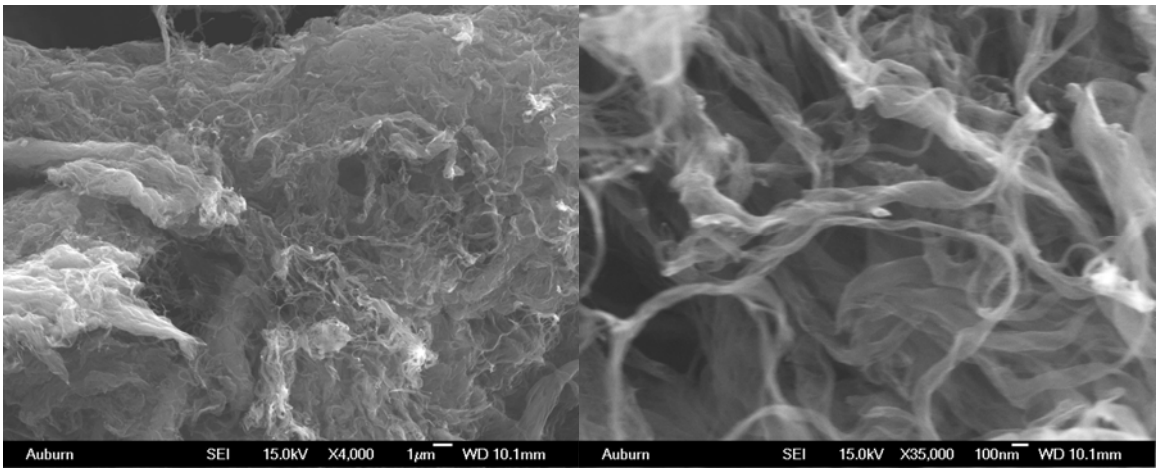

Figure 30: SEM images showing the morphology of the SWNT 187.3 imaged at (left) 4,000x magnification and (right) 35,000x magnification.

Single-walled Carbon Nanotubes, Unidym:

SWNTs (Lot # PO355) produced by the high-pressure carbon monoxide (HiPco) process were used as-received from Unidym, Inc. (Menlo Park, CA). This sample is referred to as SWNT Unidym throughout this work. Figure 31 shows SEM images of the overall sample morphology and network structure, respectively. The sample has the largest bulk density of all the SWNTs as can be seen from the tight and aggregated network structure in both images. This was apparent when weighing out a certain amount of the tubes relative to the other batches (i.e. the Unidym batch appeared to have less volume for a given weight).

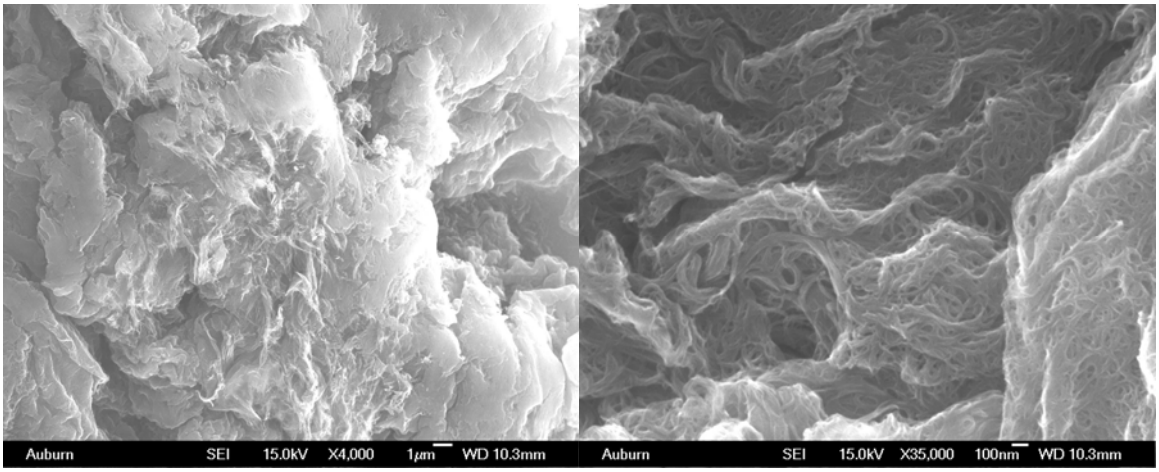

Figure 31: SEM images showing the morphology of the Unidym SWNTs imaged at (left) 4,000x magnification and (right) 35,000x magnification.

SWNT Purification:

SWNTs (Batch 183.6) produced by the high-pressure carbon monoxide (HiPco) process were received from Rice University (Houston, TX) partially purified following a deactivated thermal oxidation process as described by Xu et al. (2005) [192]. This process exposed the iron catalyst used to produce the SWNTs and deactivated the metal oxide to a metal fluoride so as to not further oxidize the SWNT upon furnace treatment. Figure 32 shows a TEM image of the as received SWNTs where the presence of residual catalyst can be clearly seen.

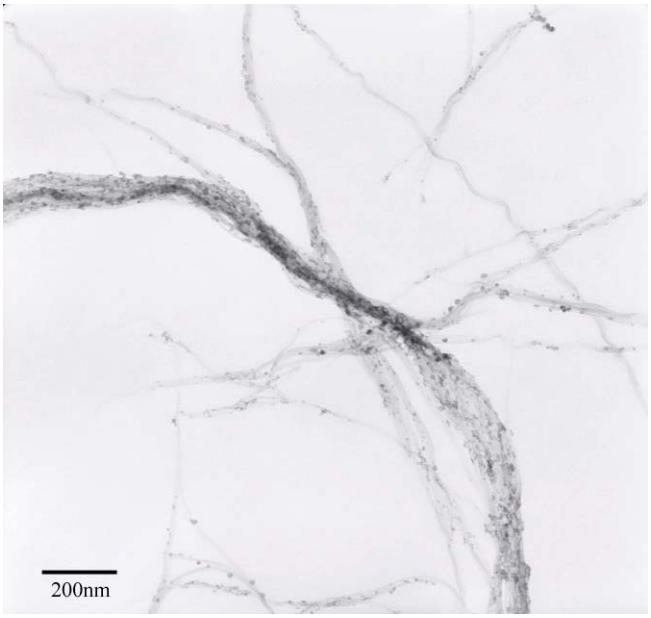

Figure 32: TEM Image of SWNT batch 183.6 Unpure as-received from Rice University. The dark sports are residual catalyst particles. The scale bar is 200 nm in this image.

The as-received tubes were then further processed in our lab to remove the exposed iron fluorides (catalyst) by two main steps; an HCl soak and a Soxhlet extraction. The HCl soak was done in 200 mg batches of SWNTs. In a typical batch, 160 ml of a 50% vol. aqueous solution of concentrated HCl acid was added to 200 mg of as received SWNT. This was heated just below 100^{o}C and magnetically stirred overnight. The solution was then transferred to a separation funnel and extracted with 5 ml of hexane. The aqueous phase was drained and washings were repeated with deionized water approximately three times. Next, the sample was transferred to a glass thimble and placed in the Soxhlet extractor. Figure 33 displays the Soxhlet apparatus used in this process.

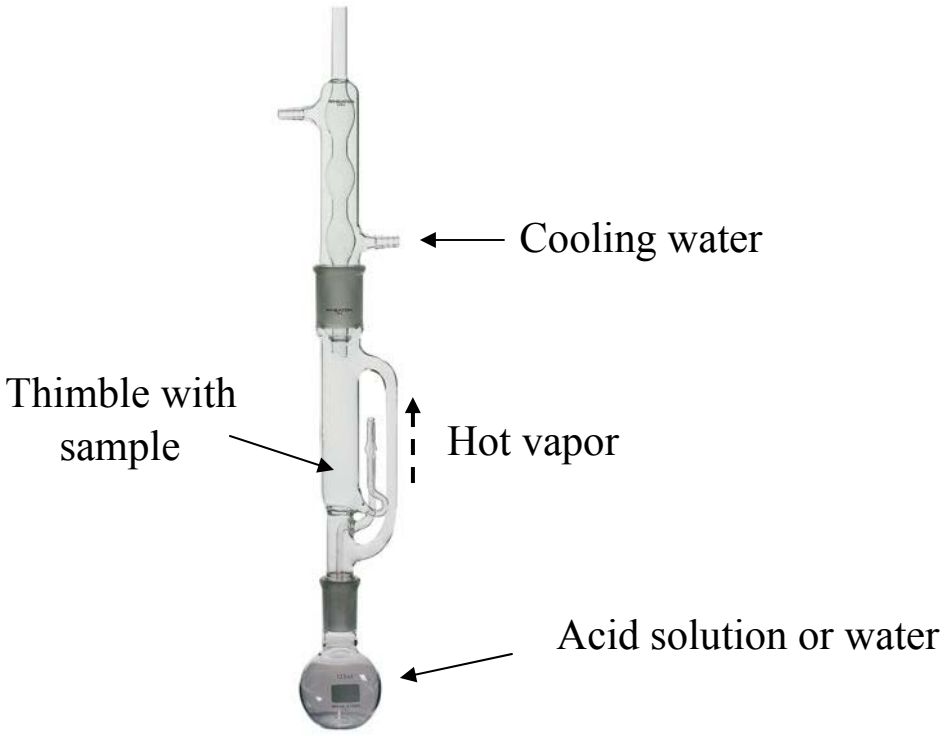

Figure 33: Soxhlet extraction apparatus used to purify the as-received SWNT 183.6 to high purity.

A 40 ml aqueous solution of 50% vol. concentrated HCl acid was added to the Soxhlet flask. This was heated to 90^{o}C and cool tap water was passed through the condenser tube. The Soxhlet is designed such that hot vapor exits the flask and bypasses the thimble. The vapor then condenses and falls onto the sample. After a certain amount of time, enough condensate collects in the thimble, building hydrostatic pressure, to drain out of the elevated exit tube in turn creating a siphon effect an draining the thimble. A total of three 12 h cycles were completed with the HCl solution and two 12 h cycles with deionized water. Finally, the acidic product was placed in a separation funnel and extracted one last time with hexane followed by subsequent washings with water as

previously stated. The final neutral, washed product was then dried at 100°C under vacuum for 24 h. Figure 34 shows the final purified SWNT product.

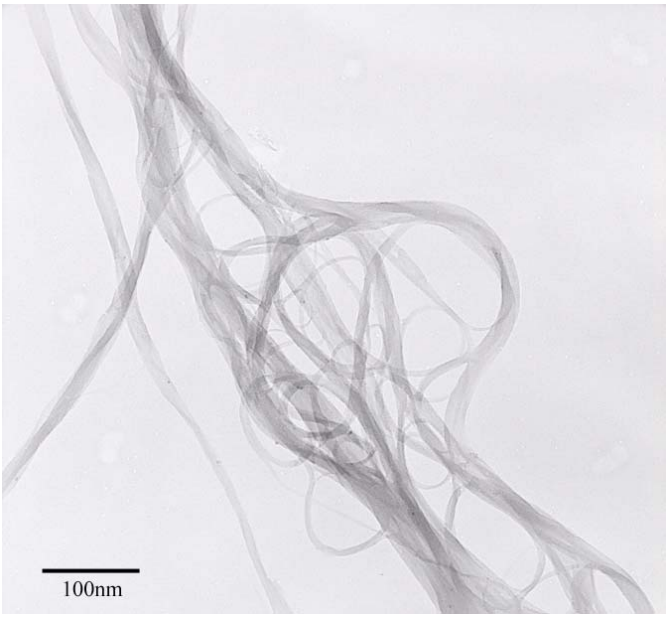

Figure 34: TEM Image of SWNT 183.6 Pure after Soxhlet extraction.

In contrast to Figure 32 showing the as received SWNTs, no catalyst can be seen after Soxhlet treatment in Figure 34. The extent of the purification was further examined by thermal gravimetric analysis.

Thermal Gravimetric Analysis:

Nanotube purity was measured using a TA Instruments (New Castle, DE) Q500 Thermal Gravimetric Analyzer (TGA). Only samples vacuum dried overnight in an oven were used. Samples were loaded into a tared platinum weigh pan and the sample chamber was purged with compressed air at a constant flow rate of 60 cm^3/min. The temperature was then held at 120°C for 15 - 20 minutes to drive off residual water. Next,

the temperature was ramped at a rate of 10°C/min until a temperature of 800°C was reached. Finally, the temperature was held constant for 45 minutes so a constant final weight could be reached. Figure 35 shows the thermal stability of the primary SWNTs used in this research.

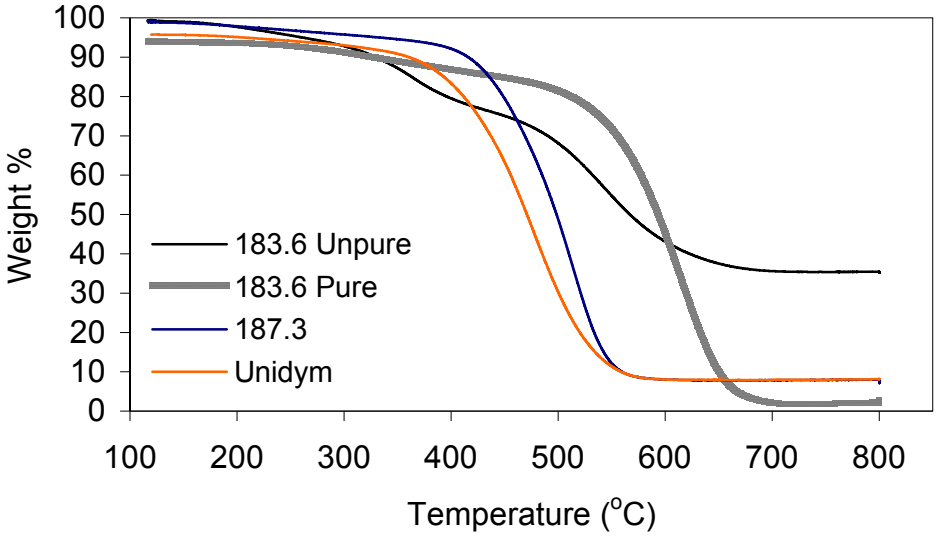

Figure 35: TGA curves for the primary SWNTs used in this research. The oven atmosphere was compressed air.

The final weight W_f was compared to the starting sample weight W_s after the 120°C hold and a residual mass fraction W_c of catalyst was determined by Equation 3.1.

$$W_c\% = \frac{W_f}{W_s} \times 100 \tag{3.1}$$

The CNT purity was then taken as the balance of $W_c\%$. Table 1 summarizes the purity of the SWNTs under air. Residual impurities were assumed to be catalyst particles.

SWNT Batch	SWNT Purity (% wt.)
183.6 Unpure	65 %
183.6 Pure	98 - 99 %
187.3	92 - 93 %
Unidym	91 - 92 %

Table 1: Purity of the SWNT samples as determined by TGA residual weight.

Methods of Nanotube Oxidation:

Oxidiation by Acid Mixture:

In a typical experiment, an amount of SWNT 183.6 Pure was added to a 125 mL Erlenmeyer flask at a ratio of 1 mg SWNT per 1.5 - 2.0 mL of concentrated acid solution. The acid solution was carefully constructed using a 3:1 (vol.) mixture of concentrated sulfuric (98% vol.) to nitric acid (70% vol.), respectively. The flask was then sealed with a few layers of laboratory film and suspended over a Cole Parmer ultrasonic cleaner (15 W, 55 kHz) so as to not contact the bottom. The experiment start time was taken to be the moment the bath sonicator was switched on. Approximately 1 - 2 times an hour the flask was removed from the bath and manually swirled to put any noticeable aggregates back into solution. After 1.5 h of treatment time, the acid-SWNT solution was diluted by a factor of 10 using deionized water. A stirbar was added and the solution was covered while allowed to mix for 45 min. This solution was then transferred to a

vacuum filtration apparatus and allowed to collect on a pre-wetted (organic solvent) 0.2 μm PTFE coated (Whatman, polypropylene backed) 47 mm membrane filter. Figure 36 shows a typical apparatus used in this step. When the acid-water solution was almost completely drained vacuum was released and 500 mL of deionized water was added to further wash the filtrate. The vacuum was released leaving a moist black filtrate of oxidized nanotubes. The final product was left on the filter paper as a cake and set aside to air dry. The resulting air-dried sample was in the form of an entangled bucky paper and placed into a dessicator overnight. The sample was then peeled from the filter paper and placed into a glass scintillation vial covered with pierced aluminum foil followed by overnight drying in a vacuum oven at ~105^{o}C. Samples prepared using this treatment are referred to as SWNT-Ox.

Figure 36: Typical vacuum filtration apparatus used in this research.

Oxidation with Ethanol Finish:

The method described previously for producing SWNT-Ox was followed through to the point of filtration and washing. In this treatment when the acid-water solution was almost completely drained vacuum was released and 500 mL of deionized water was added to further wash the filtrate. When the water was almost completely drained the sample was then washed with approximately 100 mL of ethanol. The vacuum was released leaving a moist black filtrate of ethanol finished oxidized nanotubes (SWNT-Ox Film). The sample was then scraped from the filter paper and rinsed into a 20 mL scintillation vial with more ethanol, capped, and bath sonicated for approximately 30 min to disperse. The image on the left of Figure 37 shows the sample after this step.

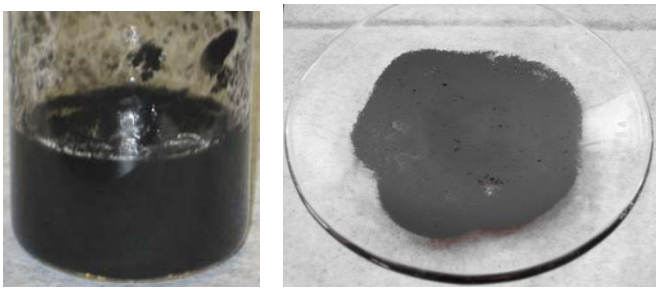

Figure 37: (left) Acid oxidized SWNT (SWNT-Ox) dispersed in ethanol (right) and the resulting film (SWNT-Ox Film) cast from an ethanol dispersion.

After re-dispersion was complete the sample was transferred to a watch glass and allowed to air-dry. After a uniform film was cast on the glass, the sample was scraped off with a spatula leaving ribbons of oxidized SWNT film. The image on the right of Figure 37 displays a typical dry film while still attached to the watch glass. These ribbons were placed into a glass scintillation vial and covered with pierced aluminum foil. The vial

was then placed in a dessicator overnight or was dried overnight under vacuum at ~105^{o}C.

Nitric Acid Oxidized SWNT Films:

To produce oxidized SWNT films the method developed by Zhang et al. (2004) was modified [125]. Approximately 27 mg of SWNT 183.6 Pure was added to 40 mL of 10M nitric acid and bath sonicated until well dispersed (~3 h). The sample was then covered and heated on a hot plate to 70^{o}C for one hour followed by a second hour at 90^{o}C. The hot solution was then bath sonicated for 1h to break up any remaining aggregates. The sample was left overnight (~18 h) to cool and sonicated for an additional hour before dilution with 100 mL of deionized water. This solution was then transferred to a vacuum filtration apparatus and allowed to collect on a pre-wetted (organic solvent) 0.2 μm PTFE coated (Whatman, polypropylene backed) 47mm membrane filter. When the nitric acid-water solution was almost completely drained vacuum was released and 500 mL of deionized water was added to wash the filtrate. This was allowed to pull through the filter under vacuum followed by a second 500 mL washing. The vacuum was released leaving a moist black filtrate of which was scraped from the filter paper while still wet and transferred to a 20 mL glass scintillation vial. Approximately 5 mL of deionized water was added and the capped sample was bath sonicated for 5 minutes in a Cole Parmer ultrasonic cleaner (15 W, 55 kHz). This solution was allowed to air dry and subsequently covered with pierced aluminum foil followed by overnight drying in a vacuum oven at ~105^{o}C. The increased amount of bath sonication in this method was required to break up and aggregates present in the raw material. This was a result of the

inability of the nitric acid to intercalate the SWNTs which, in turn, required the addition of additional energy by sonication with respect to the acid mixture.

Dilute Nitric Acid Reflux:

To produce oxidized SWNTs using a dilute nitric acid reflux approximately 6 mg of SWNT 183.6 Pure was added to 20 mL of 2.6 M nitric acid in a round bottom three-neck flask. The original concentrated of nitric acid (70%, 15.8 M) was diluted with deionized water to 2.6 M. This solution was then suspended over a Cole Parmer ultrasonic cleaner (15 W, 55 kHz) so as to not contact the bottom and sonicated for approximately 1 hour to break up large aggregates. During this time a silicone oil bath was prepared to an internal temperature of 125^{o}C into which the round bottom flask was securely lowered. A reflux condenser was added to the center flask neck and securely clamped in place. The side flask ports were plugged and sealed. The top of the reflux condenser was plugged but not sealed in case of over-pressurization. With all components safely in place the cooling water was slowly switched on from outside the lab hood in case of water-oil contact. It is important to note that at high temperatures the heating oil will react violently when exposed to cooling water. The solution was then allowed to reflux for 24 h. After which another 20 ml of 2.6 M nitric acid make-up was added and allowed to reflux for another 24 h. After 48 h total time the oil bath was removed and the sample was allowed to cool. The SWNT-dilute acid solution was then quenched by dilution in 200 mL of deionized water. This solution was then transferred to a vacuum filtration apparatus and allowed to collect on a pre-wetted (organic solvent) 0.2 μm PTFE coated (Whatman, polypropylene backed) 47 mm membrane filter. When

the acid-water solution was almost completely drained vacuum was released and 500 mL of deionized water was added to further wash the filtrate. This was allowed to pull through the filter under vacuum followed by a second 500 mL washing. When the water was almost completely drained the vacuum was released leaving a moist black filtrate of oxidized nanotubes. The final product was left on the filter paper and set aside to air dry. The resulting entangled bucky paper was placed into a dessicator overnight. The sample was then peeled from the filter paper and placed into a glass scintillation vial covered with pierced aluminum foil followed by overnight drying in a vacuum oven at ~105^{o}C.

Hot Acid Mixture Reflux:

The method of Esumi et al. (1996) was strictly followed [117]. Approximately 100 mg of SWNT 186.6 was lightly ground in mortar and pestle and refluxed at 140^{o}C in a 3:1 (vol) mixture of concentrated sulfuric (98%) to nitric acid (70%). The sample was treated for 1.5 h over which all tubes appeared to be completely digested.

Lypholization Following Oxidation of SWNTs:

In order to examine the effect of final sample morphology after oxidative treatment samples were oxidized, washed, dispersed in water, and lyophilized (freeze-dried) to prevent sample aggregation. The method used in this treatment was developed specifically for this research. In a typical experiment an amount of SWNT 183.6 was added to a 125 mL Erlenmeyer flask at a ratio of 1 mg SWNT/4 mL concentrated acid solution. The acid solution was carefully measured in a 3:1 (vol.) ratio of sulfuric acid (98% vol.) to nitric acid (70% vol., 15.8 M), respectively. The flask was then sealed with

a few layers of laboratory film and suspended over a Cole Parmer ultrasonic cleaner (15 W, 55 kHz) so as to not contact the bottom. The experiment start time was taken to be the moment the bath sonicator was switched on. Approximately 1 - 2 times an hour the flask was removed from the bath and manually swirled to put any noticeable aggregates back into solution. During the bath sonication the temperature of the SWNT-acid solution was ~50^{o}C. At the end of the desired treatment time the acid-SWNT solution was diluted by a factor of 10 using deionized water. The image on the left of Figure 38 shows the diluted acid-nanotube solution. A stirbar was added and the solution was covered while allowed to mix overnight (typically 18 h). The resulting suspension appeared homogeneously black with no phase separation and qualitatively confirmed oxidation via water solubility. This mixture was then transferred to a vacuum filtration apparatus and allowed to collect on a pre-wetted (organic solvent) 0.2 μm PTFE coated (Whatman, polypropylene backed) 47 mm membrane filter. When the acid-water solution was almost completely drained vacuum was released and 500 mL of deionized water was added to further wash the filtrate. This was allowed to pull through the filter under vacuum followed by a second 500 mL washing. If the pressure drop was too high the sample was washed from the filter and a new membrane was used. When the water was almost completely drained the vacuum was released leaving a moist black filtrate of oxidized nanotubes. The removal of the oxidized SWNTs from the paper was achieved by removing the filtration funnel and base from the filtration flask and washing the sample into a beaker with a deionized water bottle. Again, the resulting solution should be a homogeneously black aqueous dispersion (typically ~20 mL) at almost neutral pH showing no phase separation. The solution was then transferred to a 20 mL scintillation

vial, capped, and bath sonicated for 30 min. The image on the right of Figure 38 shows the sample at this point in the process. The sonicated nanotube solution was then transferred to a 50 mL disposable polypropylene centrifuge tube, capped, and placed in a freezer. The resulting frozen dispersion was then placed inside a lypholization apparatus (cap replaced with pierced laboratory film) and pumped down for at least 24 h. Due to the very low bulk density of the product care should be taken when handling the freeze-dried oxidized SWNTs to prevent accidental exposure from the airborne sample. In a final step the centrifuge tube was placed inside a dessicator overnight and transferred to a large glass vial covered with pierced aluminum foil followed by overnight drying in a vacuum oven at ~105^{o}C.

Figure 38: Qualitative proof of successful oxidation. (left) The lack of phase separation in absence of stirring is indication of a stable colloidal suspension. (right) Final aqueous dispersion of neutral, acid oxidized SWNTs. The sample shows excellent dispersion after washing.

Spectroscopy:

UV-visible Spectroscopy:

A Varian Cary 3E UV-Vis spectrophotometer was used to probe pH dependant dispersion fluorescence of the acid oxidized and lyophilized SWNTs. Samples were placed in a Starna semi-micro quartz cell and compared to a background of pure water. Typical scans were taken over a range on wavelengths from 800 - 200 nm. A saturated solution of 6h acid oxidized and lyophilized SWNTs was created by dissolving the CNT in water using bath sonication and centrifuging the dispersion at 17,000 x g for 1.5 hours. The supernatant was then collected for analysis at its natural pH of ~6. A dilute solution of NaOH (~0.1 - 1.0 M) was added dropwise to raise the pH to 10.

Fourier Transform Infrared Spectroscopy:

In order to identify surface functional groups after oxidation infrared spectra were collected. A Perkin Elmer (Waltham, MA) Spectrum 2000 FTIR Spectrometer was used in conjunction with a liquid nitrogen cooled MCT detector. A 15-bounce zinc selenide attenuated total reflectance (ATR) crystal was used to analyze the sample. Measurements were carried out at room temperature over a wavenumber range of 4000 - 600 cm^{-1} having a 4 cm^{-1} resolution with 1,024 total scans.

The 6 h acid oxidized lyophilized sample was dispersed to saturation in water using bath sonication and dropped on the crystal. The crystal was then held under vacuum at 60^{o}C to cast a thin film. This process was repeated and the spectrum was checked until no change in absorbance was seen indicating that only the SWNT and not the atmosphere above the crystal was being sampled.

SWNT 187.3 was dispersed in 1,2-dichlorobenzene by means of bath sonication and deposited on the ATR crystal. The crystal was held at ~100^{o}C under vacuum to remove the solvent.

Raman Spectroscopy:

To characterize the extent of sidewall damage on the various SWNT samples Raman spectra were obtained using a Renishaw (Hoffman Estates, IL) inVia Raman microscope and a Leica (Wetzlar, Germany) optical microscope used to focus on the surface of interest. Figure 39 shows the instrument used for all experiments.

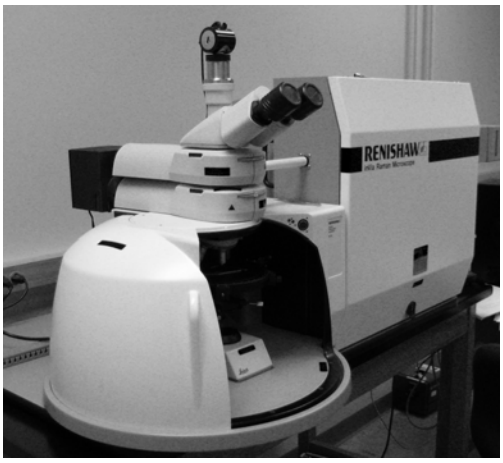

Figure 39: Image of the Renishaw inVia Raman microscope used in this research.

A Leica 50x (0.75 NA) "N-plan" objective was always used for measurements. For 514 nm wavelength irradiation a Spectra-Physics (Irvine, CA) 263C air-cooled ion laser was used. For 785 nm irradiation an SDL (San Jose, Ca) 8530 high power laser was used. The laser spot areas were 0.548 μm^2 and 1.28 μm^2 for the 514 nm and 785 nm lasers, respectively. All measurements were taken under ambient conditions. A total of 10

scans from a Raman shift of 3200 - 100 cm^{-1} were collected with a 10 sec sample exposure time. The incident laser beams were polarized by the microscope.

X-ray Photoelectron Spectroscopy:

The identification and quantification of surface functional groups was obtained via XPS. For XPS analysis the SWNT samples were first placed into an acetone rinsed 8 mL scintillation vial, covered with pierced aluminum foil, and dried for 18 h under vacuum at ~105^{o}C. The dry sample was then allowed to cool under vacuum before being capped, sealed, and stored in a dessicator. Samples were pressed into an adhesive carbon tape using stereo microscopy to ensure complete surface coverage by the SWNTs. Photoemission experiments were performed in a custom Kratos Analytical XSAM 800 surface analysis system using unmonochromatized MgKα (1253.6 eV) x-ray radiation and a hemispherical energy analyzer. The base pressure of the system was $1x10^{-10}$ torr. An exhaustive list of calibration and XPS analyzer details for the exact instrument used in this research can be found in Bozack (1993) and Bozack et al. (1994) [193, 194]. The analyzer was operated such that electrons were collected from a 5 mm^2 sample area. Due to specimen charging during x-ray irradiation of the powdered organic specimens, the energy axis of each XPS spectra was shifted to make the C1s binding energy line equal to the standard hydrocarbon energy (C-H and C-C bonds) of 284.6 eV. The uncertainty of the recorded binding energies was +/- 0.1 eV.

All specimens were first examined by means of an overall scan of binding energies from 0 - 600 eV. This was done to identify the elements present on the surface as well as calculate the surface composition (atom %). These compositions were

calculated using peak backgrounds determined by the iterative Shirley technique and instrument specific corrections were applied. Next, high resolution scans over the C1s and O1s regions were performed to yield the overall line shapes of these areas. C1s peaks were further deconvoluted in accordance with reported binding energies for oxidized SWNTs. From this analysis surface composition of functional groups covalently bonded to the SWNT sample was relatively determined.

Dispersion Preparation:

CNT-UPR dispersions were constructed by mass fraction based on actual measured component weights but converted to volume fraction using the specific material density. The UPR was taken to have a density of 1.09 g/mL as provided by the manufacturer. All SWNTs were assumed to have a mass density of 1.45 g/mL. VGCFs were assumed to have a density of 1.95 g/mL as provided by the manufacturer. The volume fraction ϕ can be calculated from the mass fraction of the nanotubes ω_{CNT} by means of Equation 3.2.

$$\phi = \frac{\rho_{relative}(\omega_{NT})}{1+(\rho_{relative}-1)\omega_{NT}} \tag{3.2}$$

Here, the relative density is defined as the ratio of the solvent density to that of the nanotubes. Alternatively, the volume fraction can be determined directly from the component mass used to construct the samples.

In order to develop a reproducible mixing protocol dispersions of VGCFs were constructed at 0.100% vol., corresponding to 0.1788% wt. loading. The volume and mass concentrations of the SWNT dispersions used in this research are given in Table 2.

Volume Percent (%)	Mass Percent (%)
0.2500	0.3323
0.2000	0.2659
0.1825	0.2426
0.1472	0.1957
0.1000	0.1330
0.0500	0.0665
0.0250	0.0330
0.0100	0.0133
0.0075	0.0100
0.0050	0.0067
0.0030	0.0040

Table 2: Volume percentages and the corresponding mass percentages for the SWNT 183.6 Pure-UPR dispersions.

Dispersion Techniques:

Bath Sonication:

The effectiveness of bath sonication alone on dispersing SWNTs directly into UPR was determined by optical microscopy. A 0.100% vol. SWNT 183.6 Pure-UPR mixture was placed into a 20 mL scintillation vial and processed for 24 h using a Cole Parmer ultrasonic cleaner (15 W, 55 kHz).

Syringe Dispersion:

A controlled amount of shear can be applied to the entire sample using a syringe dispersion method. To this end, syringe dispersion has been used previously in the literature to successfully disperse MWNTs [195]. In this research, this technique was used to study the transition of a raw CNT-UPR mixture to a dispersed state. Two disposable 10 mL BD syringes (Franklin Lakes, OH) were used with the appropriate amount of each material weighed into the cavity of one syringe. The Luer-Lok threaded syringe tips were removed using a razor and a short section of 1/8" inner diameter Nalgene® PVC tubing was used to connect the syringes. After inserting the plunger into the syringe containing the sample and removing excess air the syringes were interconnected tip to tip. The material was then forced to the adjacent syringe by depressing the plunger and this was counted as one cycle. Samples were removed after 100, 250, and 400 cycles and characterized by optical microscopy and oscillatory rheology. A time-sweep test was conducted on the samples using a 50 mm diameter cone and plate measuring geometry described in subsequent sections. Controlled frequency (10 s^{-1}) and strain measurements were taken and both the storage and loss moduli were measured as a function of time. In order to not disturb the sample a small strain of 0.1% was imposed on the sample throughout the test. Well not determined beforehand, it was assumed that this small strain would not exceed the linear viscoelastic strain for the sample.

High Shear Mixer Design:

Shear mixer components were purchased from Ace Glass (Vineland, NJ). The flask head used in this work featured three top joints for access to the flask contents and a Teflon coated lower joint. The flask bottom was a round bottom type with a capacity of 50 mL. A 10 mm Trubore glass bearing and a 10 mm diameter Trubore Teflon coated, steel stirring shaft was used. A stock 48 mm wide Teflon stirring blade was purchased (Ace Glass) and hand cut to size. This was then affixed to the shaft using nylon hardware and offset with the center of the shaft. The offset geometry prevented settling on the bottom of the flask and provided sufficient "pumping" as to apply shear to the entire sample over time. Additionally, a "paddle-fan" shaped mixing impeller was purchased and used as received. The stirring shaft was driven using a ¼ hp solid state laboratory stirrer (Ace Glass) with a maximum output speed of 4,000 rpm. The motor was mounted upside down and connected to a 36" flexible stirring shaft linked via a nylon chuck. In a typical mixer loading, the CNTs were measured and carefully added to the flask. However, in the case of SWNT 183.6 Pure the sample was always first placed in a vial and lightly ground by hand using a stainless steel spatula to facilitate better mixing. The flask was then tared and the appropriate mass of resin was added. The mixer was then assembled and purged with ultra high purity Argon (Airgas) before being sealed to prevent humidity from interfering with the sample. Alignment between the bearing and shaft was ensured before sealing in order to prevent damaging the components. Misalignment of the components often generated excess friction and subsequently failed the 20A fuse filament. A final adjustment was made to the mixing shaft after alignment where the chuck was loosened and a downward force was applied so

that contact between the mixing blade and flask sidewall was maintained. The flask and contents were then submerged in a room temperature water bath with volume approximately 8 - 10 times the sample volume. This was simply used to absorb excess heat although its effect was not studied. Typically, the mixer was run at approximately 500 - 1,000 rpm for 72 hours with intermittent stops (approximately 3) to allow the sample to settle off the flask wall. Figure 40 shows an image of the assembled mixing flask, stir shaft, and impeller.

Figure 40: Image of the mixing vessel used in this research.

Sample Extraction and Loading:

Above a CNT loading of 0.010% vol. aliquots of the sample were extracted using a bulb and pipette having a wide inner diameter of 7 mm. This wide cross section was necessary in order to prevent shear aligning the CNT and preserve isotropic orientation. Dilute samples of approximately 0.01% vol. and below were drawn using a 12 gauge

syringe (Sigma-Aldrich). The 10" syringe was cut to a length of approximately 7.5" and had an inner diameter of 2.159 mm. Small air bubbles could be observed within the dilute samples as a result of the intense shear mixing. The syringe was used not only to ensure solvent evaporation was avoided but to degas the dilute samples as well. Syringe extracted samples were always placed in a vial and allowed to relax for 12 - 18 hours.

Rheology:

All rheological experiments were performed using a Anton Paar (GmbH) Physica MCR 301 series rheometer displayed by Figure 41.

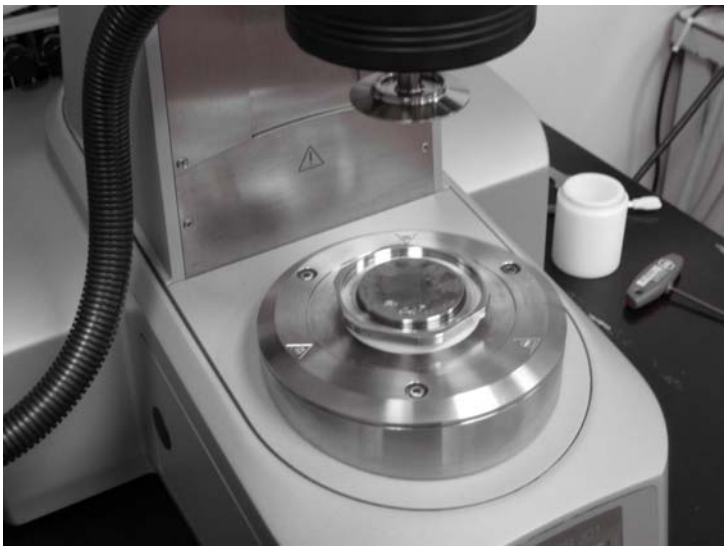

Figure 41: Image of the Anton Paar Physica MCR 301 rheometer with the parallel plate measuring geometry affixed to the P-PTD200 device and the H-PTD200 peltier controlled upper oven in place.

This model rheometer can operate in controlled stress (CSS), controlled shear rate (CSR), or controlled shear strain (CSD) mode. The motor is driven using a permanent magnet

synchronous drive operating on an air bearing. The torque range for this instrument is from 0.1 μNm to 200 mNm with a torque resolution down to 0.001 μNm. Normal force is measured using a capacitive probe with a range of -50 N to +50 N and a sensitivity of 0.002 N. The sign convention for a positive normal force was taken by the manufacturer to be exerted in the direction of the upper plate.

When measuring in cone and plate geometry the temperature was controlled using the P-PTD200 peltier temperature control device located below the lower shear plate. Surrounding the upper plate and the sample was the H-PTD200 peltier controlled upper oven. For a detailed explanation on the principle of operation see Sato and Breedveld (2005) [196]. This allowed for controlled atmospheric temperature as well as introduction of inert gas. The temperature range for both peltier devices was from -40^{o}C to +200^{o}C. Both peltier controlled devices were counter cooled with a Julabo F12 (GmbH) water recirculation bath maintained at +20^{o}C. This was plumbed in series starting with the H-PTD200 and passing through the P-PTD200 before emptying to the bath.

For cone and plate rheometry the Anton Paar CP50-2 fixture was used. Unless otherwise noted the cone radius used in all experiments was 24.9985 mm with a cone angle α of 2.018^{o}. The cone truncation and distance between the center of the upper and lower surfaces was constant at 52 μm for all measurements. At these distances the required sample volume was 1.14 mL and the gap distance at the edge h was calculated to be 0.933 mm.

In order to monitor the fluid structure optically rheological measurements were also taken using the Anton Paar small angle light scattering (SALS) system. This measuring system was of parallel plate geometry constructed out of transparent quartz

glass. The SALS setup was used simple to observe the sample optically and no scattering experiments were conducted. Unless otherwise noted the plate radius used in all experiments was 21.4600 mm with construction of transparent quartz glass. The gap h was set between 0.4 and 1.0 mm for all measurements. At a gap of 1.0 mm the required sample volume was 1.5 mL. The SALS system is not equipped with any temperature controlling device except that of the cooling water circulation. However, the water temperature at the device inlet was monitored via the SALS system.

All rheology measurements were taken just below room temperature at 20^{o}C in order to limit styrene evaporation. To load the instrument an appropriate volume of sample was placed on the lower plate and the upper measuring surface was lowered to the proper gap. The gap-setting velocity of the upper plate while was set to 500 μm/s on close approach so as to not destroy the sample structure. If necessary, excess sample was trimmed from the edge using a rubber policeman in order to eliminate error from edge effects. After which the normal force was zeroed and the sample was given 10 min to achieve thermal equilibrium.

In order to characterize the flow regime in these experiments the Reynolds number *Re* was estimated as shown by Equation 3.18.

$$\mathrm{Re} = \frac{\dot{\gamma} z^2 \rho}{\eta_s} \tag{3.18}$$

Here, the strain rate is represented by $\dot{\gamma}$ and z is the average distance between the plates. The solvent mass density and viscosity are shown by ρ and η_s ,respectively [91, 107]. Re was less than unity for all experiments indicating that assumptions for viscometric flow were valid.

Amplitude Sweep Test:

Amplitude sweep tests (AS) were first performed to probe the structural stability of the sample and the range of linear viscoelastic strain. A controlled strain was imposed on the sample at a fixed frequency of 10 s^{-1} (rad/s) and the resulting storage and loss moduli were measured. When the storage modulus showed nonlinear behavior the test was stopped and repeated to ensure the critical strain was correctly identified. Typically the strain ranged from 0.01 - 100% but the maximum strain was often reduced to 10% so as to not destroy the structure of the samples.

Frequency Sweep Test:

Frequency sweep (FS) experiments were conducted at controlled strain but variable angular frequency. The strain set point was determined from an AS test and chosen to be inside the linear viscoelastic regime. The typical measured frequency range was from 100 - 0.01 rad/s. For efficiency all FS experiments were run from high to low frequency so that the long measuring times associated with the lowest frequencies could be terminated if the data was outside the measurable range of the torque transducer. As a rule of thumb the time required to acquire a steady state data point is inversely proportional to the shear frequency.

Step Rate Test:

The start-up of flow was characterized by conducting step-rate tests. Here a fixed shear rate was set and the time of observation was varied logarithmically. From this experiment the time required to achieve steady-state flow can be determined.

Surface Tension:

For thermodynamic analysis the surface tension of UPR was measured using a KSV Instruments (Finland) Sigma702 Tensiometer. A DuNoy ring was physically immersed and extracted from the sample to collect experimental data. This instrument had a tension resolution of 0.001 mN/m. A total of 10 runs were collected and both the average surface tension and standard deviation was reported.

4. RESULTS AND DISCUSSION

Characterization of Dispersion Methods:

Syringe Dispersion:

In order to estimate the magnitude of the shear stress applied to the sample the pressure drop across the syringe tip was calculated. A syringe was filled with water, evacuated of excess air, and connected to a Psitronix (Tulane, CA) digital gauge. The syringe plunger was depressed manually in the same fashion as used dispersion experiments and a pressure of approximately 25 - 30 psi (172 - 207 kPa) was observed. Taking this to be the pressure drop over the tip p_c the tip wall shear stress τ_w was estimated using a model developed for a capillary viscometer [67]. Equation 3.3 displays the wall shear stress as a function of nozzle radius r and length L.

$$\tau_w = \frac{p_c r}{2L} \tag{3.3}$$

The geometry of the syringe was taken to have an internal tip radius of 0.875 mm and length of approximately 1 mm. This resulted in an estimated shear stress of 10^4 Pa and was most likely conservatively large based on the assumption for the tip pressure drop. Chen et al. (2000) have used the same model for a time-pressure fluid dispensing process as well as developed a rigorous model for the frictional pressure drop by considering the conservation of mechanical energy [197].

The dispersion of VGCFs into UPR at a loading 0.100% vol. was studied by the syringe extrusion method with the intention of characterizing the transition to a well dispersed state. Figure 42 shows the response of the fluid under small strain oscillatory shear after 100, 250, and 400 syringe cycles.

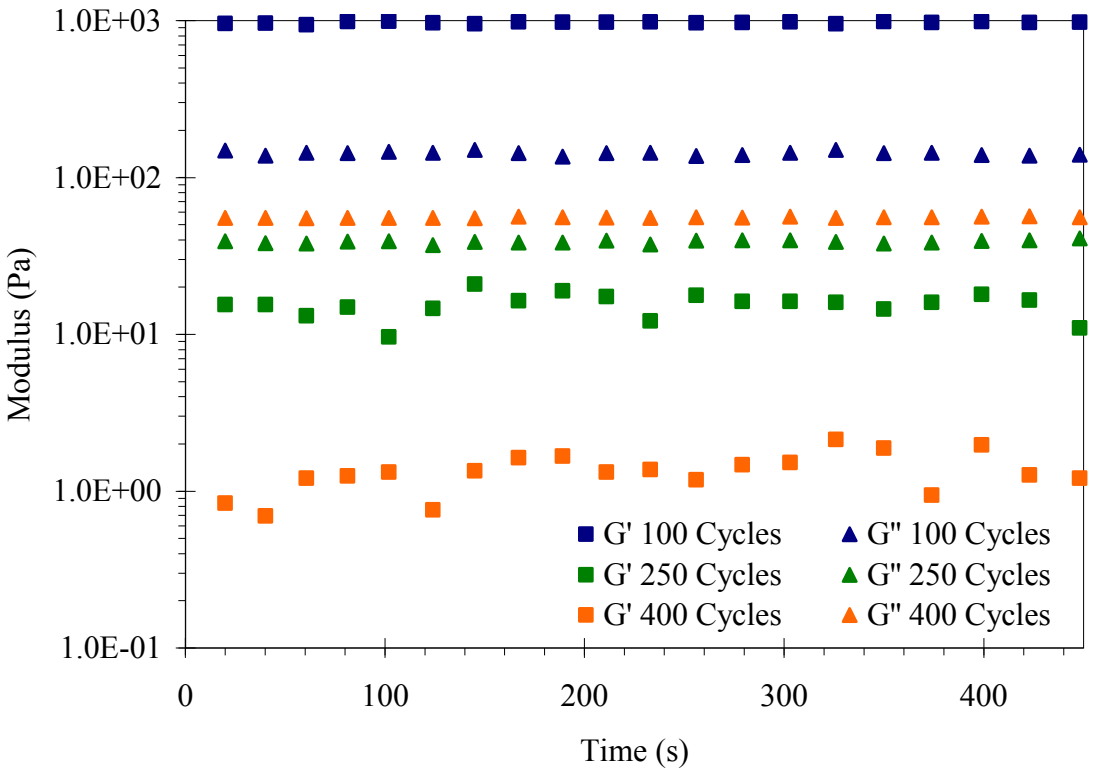

Figure 42: Rheological characterization of the transition to a well dispersed state for 0.100% vol. VGCF in UPR processed by tip-to-tip syringe extrusion.

Examining Figure 42, the response after only 100 cycles shows elastic behavior dominated by G'. Processing the fluid to 250 cycles the sample behavior has transitioned to a viscous liquid dominated by G". After 400 cycles the viscous behavior is more pronounced showing a decrease in G' by an order of magnitude accompanied a slight

increase in G". To understand the physical origin of this transition in rheological behavior optical images were analyzed. Figure 43 shows the sample for 100 cycles.

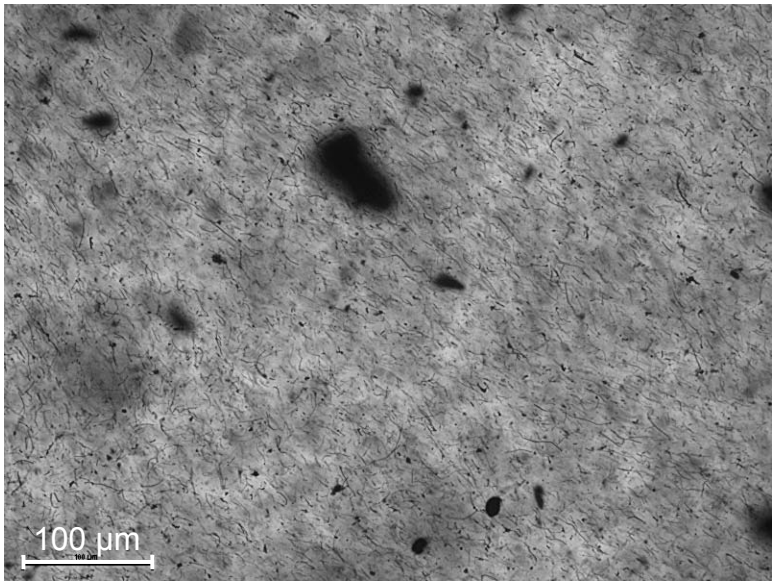

Figure 43: Image of a 0.100% vol. VGCF-UPR dispersion processed at 100 cycles syringe extrusion. The sample was imaged at 20x with no cover glass in place.

The presence of a large aggregate can be seen in Figure 43 on the order of ~50 µm.

It is important to note that this large cluster size is comparable to the 52 µm gap between the cone and plate measuring geometry. For this reason it is believed that the solid-like rheological response seen in Figure 42 was a result of "jamming." Thus, the direct probing of the solid aggregate leads to a false and large magnitude of G' as well as large but inaccurate complex viscosity of the fluid. The observation of a false solid-like response at short mixing times is consistent with the erratic behavior seen by Huang et al. (2006) for MWNT-PDMS dispersions [91]. Figure 44 shows an image of the sample after 400 cycles.

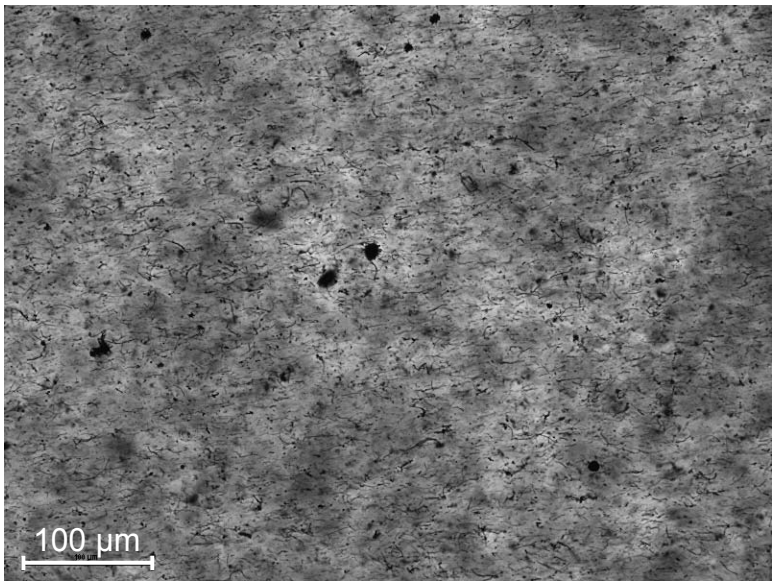

Figure 44: Image of a 0.100% vol. VGCF-UPR dispersion processed at 400 syringe extrusion cycles. The sample was imaged at 20x with no cover glass in place.

The absence of large aggregates in Figure 44 is believed to be the origin of the liquid-like response seen at 250 cycle time in Figure 42. The increase in liquid-like behavior between 250 cycles and 400 cycles is attributed to the development of a homogeneous dispersion state. The development of a well-dispersed state also supports the existence of a minimum critical mixing time similar to that found by Huang et al. previously. Similarly, a transition in rheological response was found in MWNT-Epoxy dispersions by Fan and Advani (2007) [81].

Although syringe dispersion appears to be an excellent means to deliver a controlled stress to the sample it suffers from being both arduous to complete by hand and unreliable due to a weakening of the syringe material over time from exposure to the styrene. Furthermore, as the material becomes better dispersed with each cycle large increases in the viscosity are observed making the extrusion more difficult. However, if

an appropriate apparatus were constructed this method may show promise. Unfortunately, the device used in this preliminary study was unable to successfully disperse SWNTs.

Bath Sonication:

Fan and Advani (2007) created MWNT-Epoxy dispersions by means of bath sonication alone [81]. Specifically, after 24 hours the authors reported no change in rheological response indicative of a "saturated" network structure. Figure 45 displays the morphology of a 0.100% vol. SWNT 183.6 Pure-UPR dispersion.

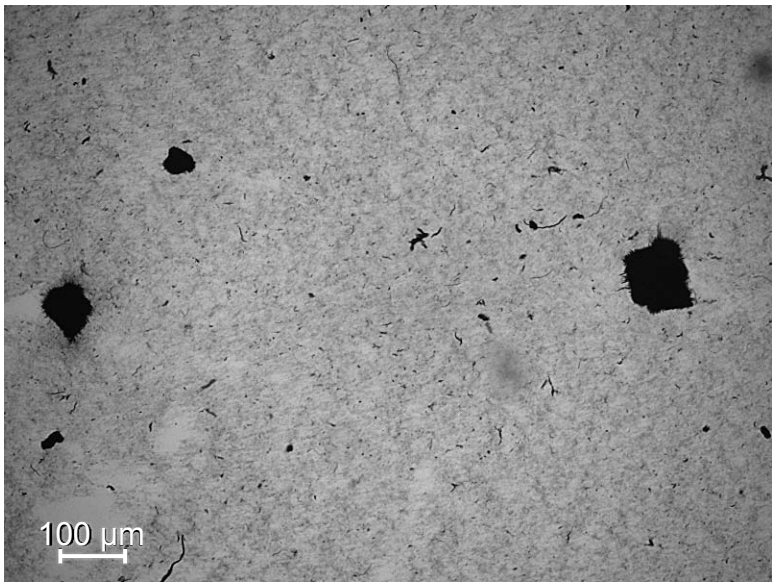

Figure 45: Image (10x) of a 0.100% vol. SWNT-UPR dispersion processed by 24h bath sonication alone.

In contrast to the successful results reported for MWNT-epoxy dispersions large SWNT aggregates persisted in the UPR. This was likely due to the higher viscosity of the neat UPR (2 Pa-s) with respect to the Epoxy (0.59 Pa-s). Furthermore, as the treatment time

progressed the final UPR viscosity increased as a result of styrene evaporation from sample heating. Since it was required that the final dispersions show repeatable rheological behavior methods inducing styrene loss, such as sonication, were not employed.

High Shear Mixing:

In order to approximate the shear stress delivered to the fluid the velocity profile between the annular gap of the stirring blade and the flask wall was derived. The maximum shear stress was assumed to be delivered where the blade tip speed was the greatest. This also happened to be the area where some contact between the impeller and flask wall was made; thus, minimizing the annular gap and maximizing the slope of the velocity profile. Therefore, the area of the blade with the largest radius was used to describe the mixer geometry in estimating the shear as shown by leftmost image in Figure 46. The radius of the impeller r_{min}, measured from the center of the stirring rod to the edge, was taken to be 1.85 cm. The mixer flask radius was measured by water displacement and the flask radius R was taken as the distance from the center-line to the inner wall, measuring 2.13 cm. On the microscale, these geometries were approximated as two small sections of concentric cylinders using the cylindrical coordinate system (r, θ, z) as displayed by Figure 47.

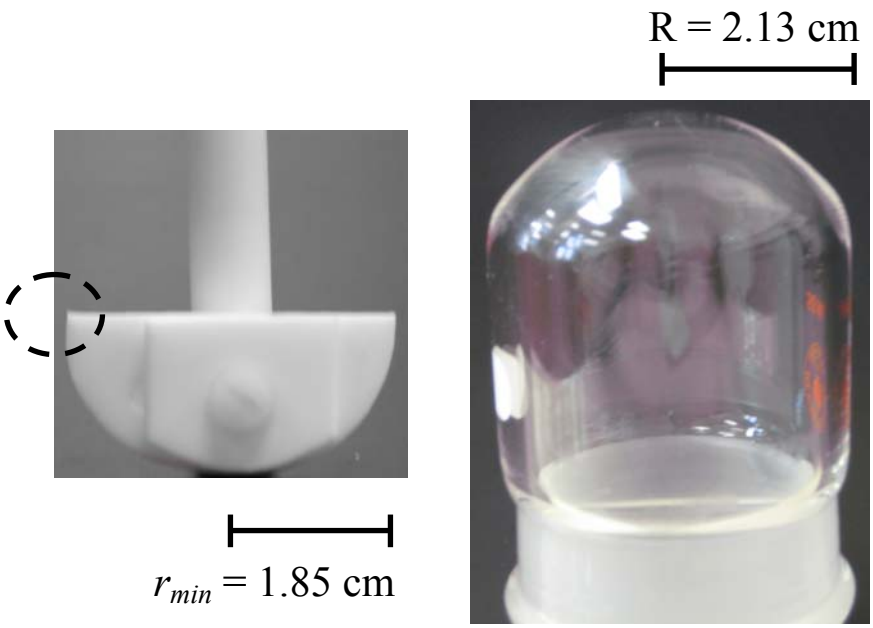

Figure 46: Images and dimensions for the custom shaped mixing impeller (left) and mixer flask (right) used in this work.

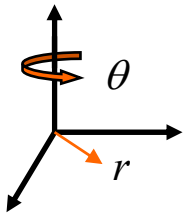

Figure 47: Cylindrical coordinate system used to estimate the shear stress of the mixer.

In this manner the velocity component in the θ-direction was assumed to depend only on the radius of observation, r. This is displayed mathematically by Equation 3.4. Thus, the components in the *r*-direction and z-direction were assumed to be zero as shown by Equation 3.5.

$$\upsilon_\theta = \upsilon_\theta(r) \tag{3.4}$$

$$\upsilon_r = 0 = \upsilon_z \tag{3.5}$$

Assuming the working fluid as the Newtonian UPR with constant mass density the equation of continuity (EOC) reduces in accordance with Equation 3.6.

$$\left(\nabla \cdot \mathbf{v}\right) = 0 \tag{3.6}$$

Specifically, considering the assumptions made by Equations 3.4 and 3.5 we can expand the EOC to yield Equation 3.7.

$$\frac{\partial \upsilon_\theta}{\partial \theta} = 0 \tag{3.7}$$

Equation 3.7 indicates that υ_θ is constant in the direction of flow. Next, the θ-component of the equation of motion was reduced in accordance with Equations 3.4 and 3.5 as well as the assumption of constant density and viscosity as shown by Equation 3.8.

$$0 = \frac{d}{dr}\left(\frac{1}{r}\frac{d}{dr}\left(r\upsilon_\theta\right)\right) \tag{3.8}$$

Since, we have assumed that υ_θ is only a function of r the derivatives in Equation are no longer partial. Equation 3.8 is a 2nd order differential equation but can be separated and integrated twice to yield the velocity profile as shown by Equation 3.9.

$$\upsilon_\theta = \frac{Ar}{2} + \frac{B}{r} \tag{3.9}$$

Here, A and B are simply the constants of integration and can be evaluated with two boundary conditions. In order to reduce the number of independent variables the velocity was evaluated at the flask wall R and at the edge of the impeller κR as displayed by Figure 48.

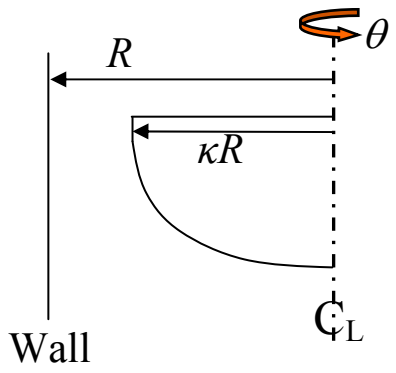

Figure 48: Schematic of the impeller and mixing flask wall with respect to the stirrer center line (C_L). The radial digestion of the mixing flask is represented by R and the dimension of the impeller by κR.

Here, κ is simply the fraction of R occupied by r_{min} and has a magnitude of 0.868 in this mixer. At the flask wall R the velocity is assumed to be zero and at the impeller tip κR the velocity as taken as the product of the radius and the angular frequency Ω. Equation 3.10 and Equation 3.11 show the boundary conditions.

$$\upsilon_\theta(R) = 0 \tag{3.10}$$

$$\upsilon_\theta(\kappa R) = \Omega \kappa R \tag{3.11}$$

Solving for the constants the velocity profile can be represented by Equation 3.12.

$$\upsilon_\theta = \frac{\Omega \kappa R\left[\frac{R}{r} - \frac{r}{R}\right]}{\left(1/\kappa - \kappa\right)} \tag{3.12}$$

In order to relate the velocity profile to the shear stress $\tau_{r\theta}$ Newton's law of viscosity is introduced as shown in Equation 3.13.

$$\tau_{r\theta} = -\mu r \frac{\partial}{\partial r}\left(\frac{\upsilon_\theta}{r}\right) \tag{3.13}$$

By insertion of Equation 3.13, and pulling out constants from the partial derivative, Equation 3.14 can be derived.

$$\tau_{r\theta} = \frac{-\mu r \Omega \kappa R}{\left(1/\kappa - \kappa\right)} \frac{\partial}{\partial r}\left[\frac{R}{r^2} - \frac{1}{R}\right] \tag{3.14}$$

where,

$$\frac{\partial}{\partial r}\left[\frac{R}{r^2} - \frac{1}{R}\right] = -\frac{2R}{r^3} \tag{3.15}$$

Finally, the expression for the shear stress is shown by Equation 3.16.

$$\tau_{r\theta} = \frac{2\mu\Omega\kappa}{\left(1/\kappa - \kappa\right)}\left(\frac{R}{r}\right)^2 \tag{3.16}$$

The resin viscosity was measured to be approximately 2 Pa-s. Equation 3.16 can be further reduced to represent the physical case by introducing the numerical value of κ. Based of the measured mixer component radii κ has a value of ~0.868. One important observation is that as a result of the impeller being mounted offset to the stirring shaft, the manual application of the downward force to the blade, and asymmetry of the flask itself, the impeller actually contacts the flask wall at times. However, this is not accounted for in the model since as κ approaches unity its value increases asymptotically. Furthermore, the proposed boundary conditions would not be valid in this extreme. Equation 3.17 displays the shear stress at the true measured value of κ.

$$\tau_{r\theta,Max} \approx 6\mu\Omega\left(\frac{R}{r}\right)^2 \tag{3.17}$$

Given the dimensions of the mixer when the angular frequency is approximately 100 rad/s (1,000 rpm) the maximum shear stress delivered to the resin is on the order of 2 kPa. This result is in excellent agreement with a similar shear mixer used by Huang et al. (2006) who estimated a shear stress of 3 kPa [75, 91]. However, the estimate is conservative since no estimation has been made for large κ. For point of reference when κ has a value of 0.95 the impeller is approximately 3 mm from the wall and the shear stress approaches a value of 5 kPa. Thus, it can safely be concluded that the original estimate is conservatively low. The critical shear energy required to disperse SWNTs has been roughly estimated on the order of 10^4 J/m^2 (Pa) [91]. Therefore, whether or not the mixer shear stress actually reaches this critical estimate cannot be determined from this analysis.

Attempts at reproducing the well dispersed state achieved by the syringe method were made using the high-shear mixer at 0.100% vol. loading. A paddle-type impeller was first used to process the dispersion. Figure 49 shows an optical image of the resulting mixture after approximately 3 days of processing time. The poor dispersion shown by Figure 49 is believed to be a result of the insufficient "pumping" (convection) of the sample around the mixing flask. This prevented much of the sample from seeing the high shear zones produced by the paddle. Similar to the response after just 100 syringe cycles, samples processed in this manner showed erratic and uncorrelated rheological behavior. Although, longer mixing times beyond three days were studied, this resulted in partial loss of the solvent through evaporation. Therefore, the paddle mixer design was abandoned and a new impeller style was considered. The performance

of the custom cut mixing impeller on processing a 0.100% vol. dispersion is displayed by Figure 50.

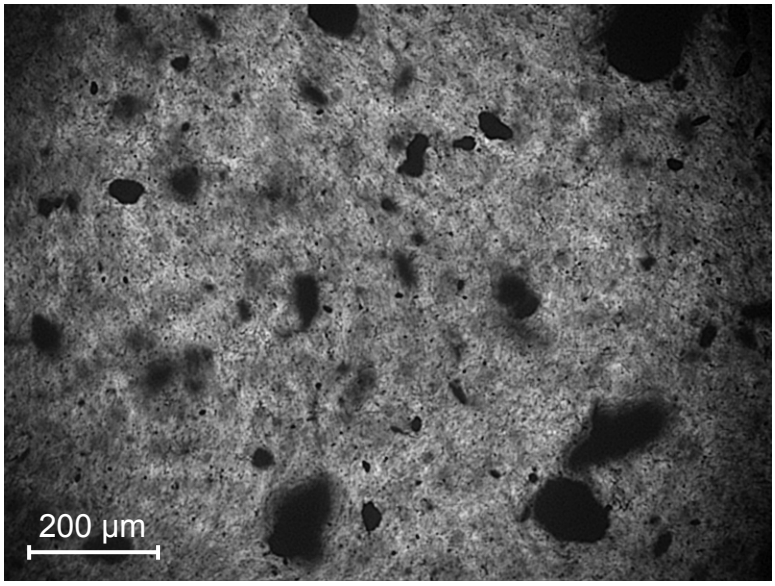

Figure 49: 10x image of a 0.100% vol. VGCF-UPR dispersion processed (~three days) by paddle-type mixing impeller. No cover glass used on sample.

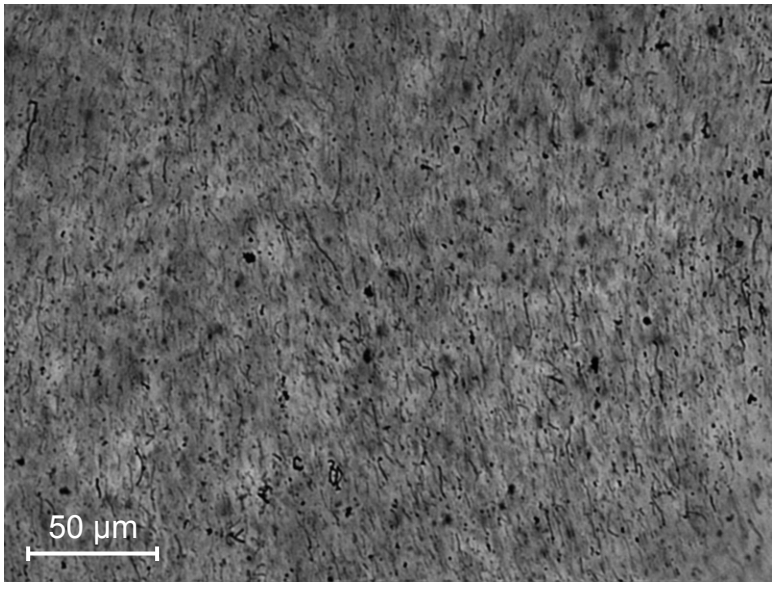

Figure 50: Image of a 0.100% vol. VGCF-UPR dispersion processed (~three days) by the custom cut crescent-type mixing impeller. The sample was imaged at 20x with 2x magnification in front of the camera. No cover glass was used on the sample.

The image was taken after approximately three days mixing time. Here, the visible aggregates have been completely broken down and only fibers and amorphous carbon appear in a homogenously dispersion. The offset impeller blade eliminated "dead-zones" in the mixer and exposed the sample to the high shear areas between the paddle and flask wall. The rheological response was markedly different from the sample processed by the paddle-type impeller. Furthermore, the results were found to be repeatable confirming a successful mixing protocol. In passing it is noteworthy that by studying the rheological response after various mixing times, a unique characteristic showing transition to a dispersed state was found in the linear viscoelastic critical strain. This strain limit was barely existent for samples with large VGCF clusters but widened significantly over poorly dispersed samples.

The three day shear mixing protocol developed for VGCFs was extended for use in SWNT dispersions. Figure 51 displays an optical image under high magnification for a typical SWNT 186.3 Pure dispersion at 0.050% loading. Clearly, only small aggregates and fibers can be seen. Likewise, Figure 52 shows a 0.100% vol. dispersion with the absence of any large aggregates.

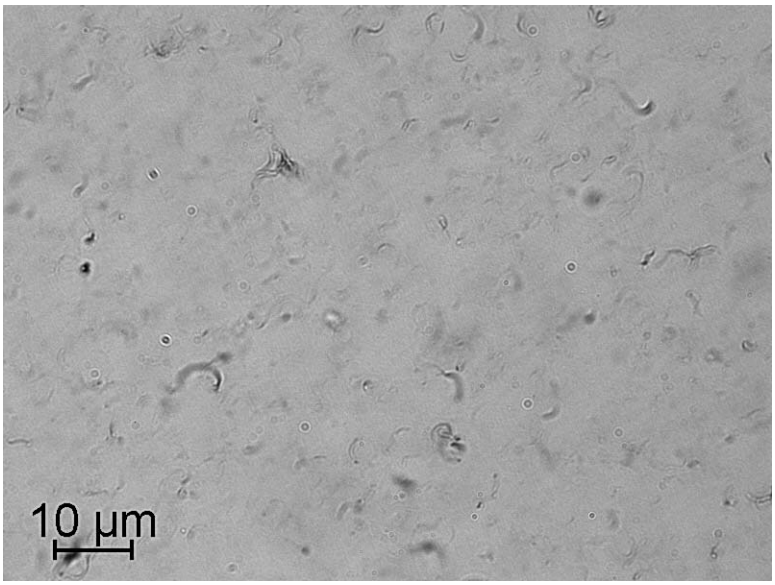

Figure 51: Optical microscopy image a 0.050% vol. dispersion of SWNT in UPR. Image taken through cover slip using an oil immersion 60x (1.4 NA) objective with 2x magnification in front of the camera.

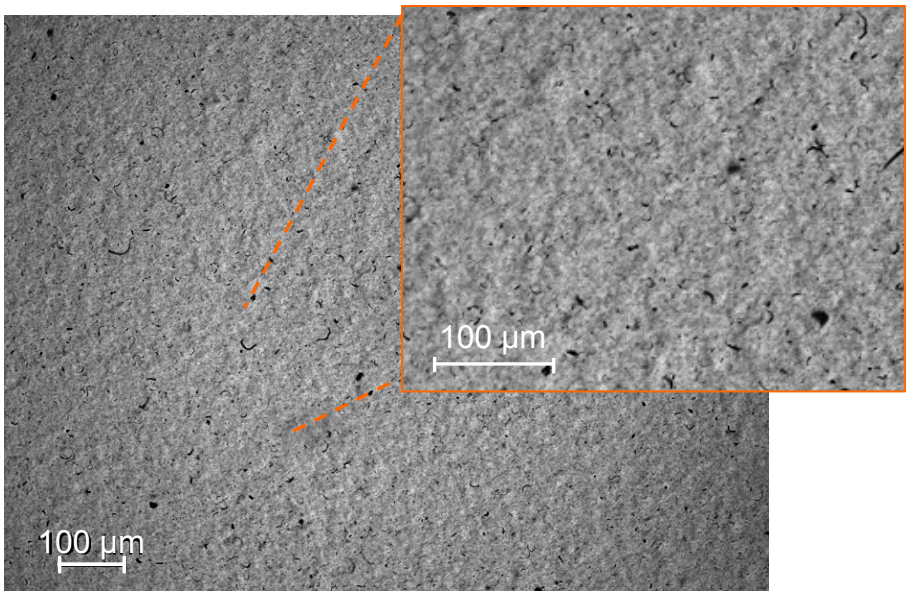

Figure 52: Typical image (10x) of a 0.100% vol. SWNT-UPR dispersion processed by three day high shear mixing. Inset showing 10x2 magnification.

Viscosity of Neat UPR:

The viscosity of the neat UPR used throughout this work was determined from measurement by both oscillatory and steady shear. Figure 53 displays this result.

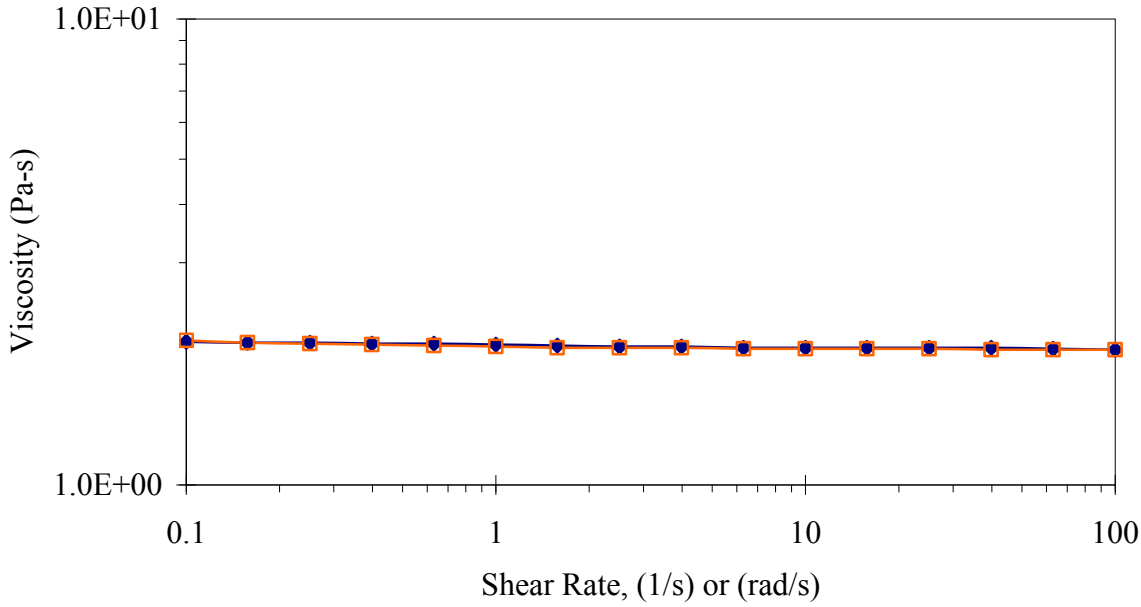

Figure 53: Steady-state viscosity and complex viscosity for neat UPR.

The resin is Newtonian with a viscosity of ~2 Pa-s and adheres to the Cox-Merz rule. The perfect agreement between the two viscosities is characteristic of a Newtonian fluid and a result of negligible phase lag between the viscoelastic moduli. Thus, the response under oscillatory shear has a negligible component of G' and the magnitude of G" is derived only from viscous response of the fluid.

Rheology and Characterization of Acid Oxidized SWNT Dispersions:

A consistent observation throughout this research was the inability of the oxidized nanotubes, from any of the oxidative treatments attempted, to form a dispersion state

comparable to that of the pristine SWNTs. One hypothesis for the origin of this behavior was the final sample morphology after oxidation. Filtered nanotubes often form ropes as a result of the high frequency of collisions encountered as the sample volume is decreased upon filtration [198]. The driving force is enthalpic and barriers preventing a tube from sliding along a rope axially are small, indicating this is a facile process. Figure 54 shows the sample morphology for the nitric acid (10 M) oxidized SWNTs. At low magnification the sample appears in a uniformly aggregated state and under high magnification clear evidence of roping can be seen. These ropes appear to be of smaller diameter and more abundant than present in the SWNT 183.6 Pure starting material.

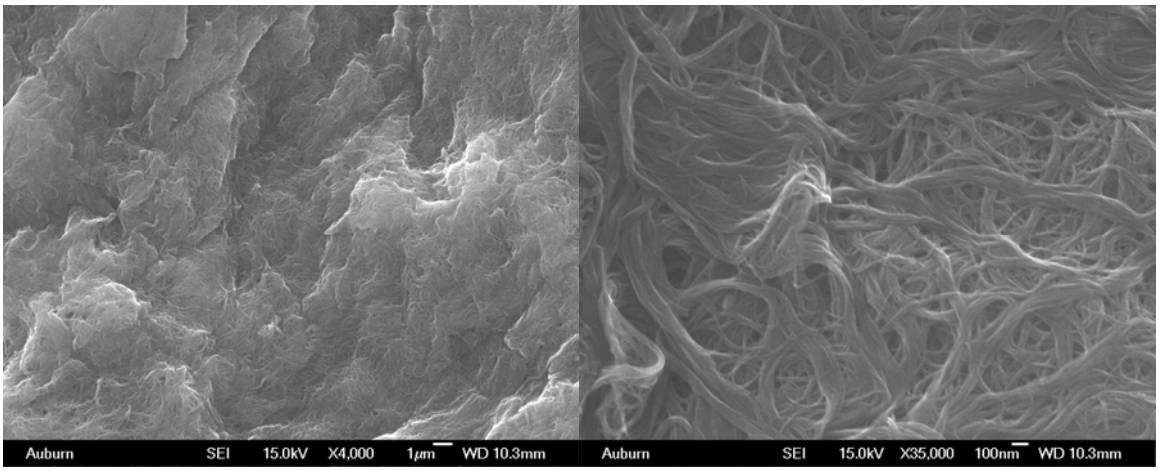

Figure 54: Morphology of the nitric acid oxidized (10M) SWNTs as seen by SEM at (left) 4,000x magnification and (right) 35,000x magnification.

Conversely, Figure 55 shows the morphology of the 48h nitric acid oxidized SWNTs where no sample structure is apparent. Presumably, this is a result of the long oxidation time and generation of a significant amount of amorphous carbon at elevated temperatures. The samples displayed in both Figure 54 and Figure 55 failed to disperse

in UPR. On the other hand, the SWNT-Ox Film sample did show a dispersion of reasonable quality, as shown later in the resin. Figure 56 displays the SWNT-Ox Film sample. Examination of the sample morphology after this treatment shows an intermediate structure from what was seen in Figure 54 and Figure 55. A combination of smooth unstructured material and small ropes can be seen in the high magnification image of Figure 56. Therefore clear no correlation between sample morphology and dispersion ability was apparent for these oxidized samples.

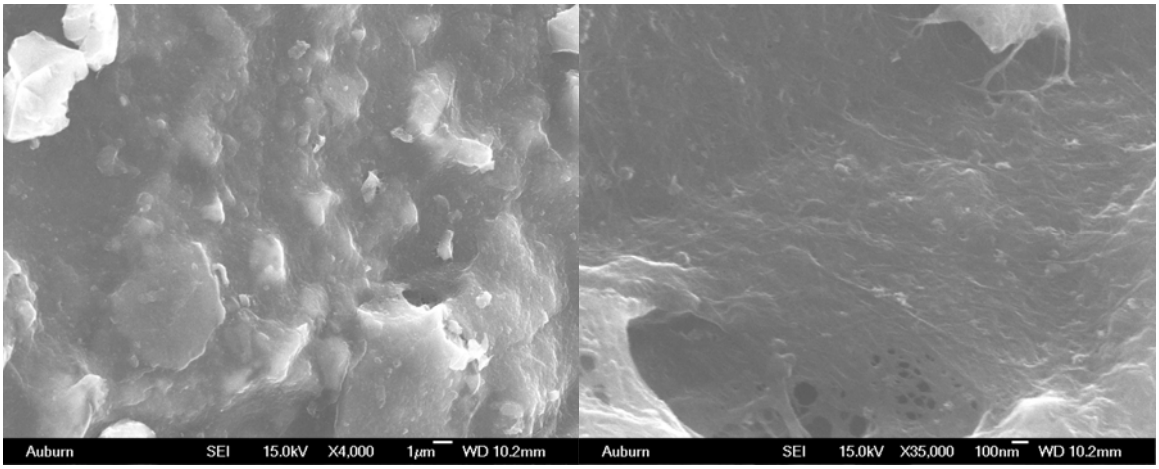

Figure 55: Morphology of the 48h nitric acid (2.6 M) reflux oxidized SWNTs by SEM at (left) 4,000x magnification and (right) 35,000x magnification.

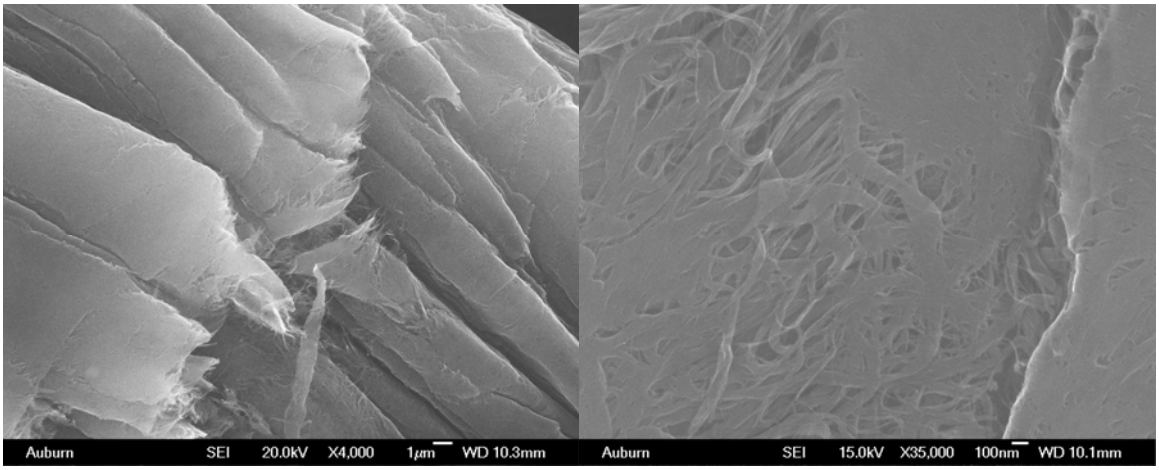

Figure 56: SEM images highlighting the morphology of the SWNT-Ox film SWNTs at (top) 4,000x magnification and (bottom) 35,000x magnification.

The aforementioned success achieved by treatment of the acid oxidized SWNTs with ethanol and casting as a film can be seen below. Figure 57 displays the optical quality of a 0.100% vol. SWNT-Ox Film dispersion.

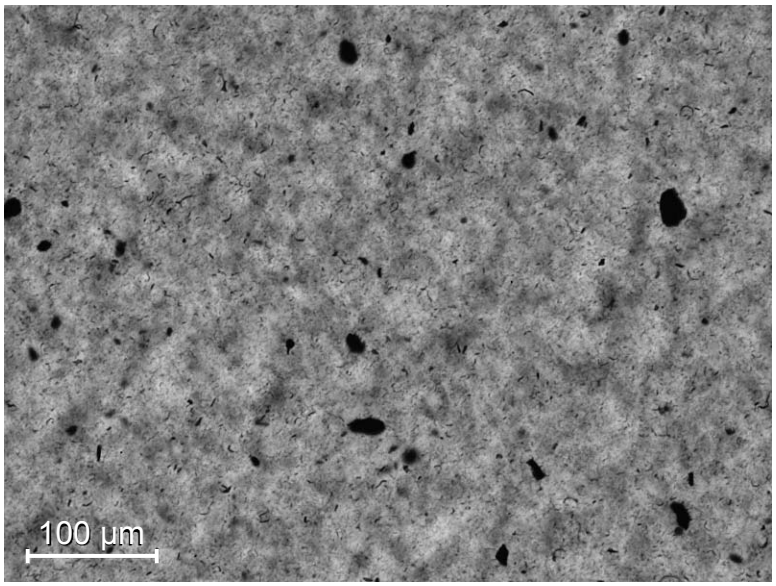

Figure 57: Image (10x2) of the 0.100% vol. SWNT-Ox Film dispersion processed from three day shear mixing.

Compared to the inset image of 0.100% vol. SWNT 183.6 in Figure 52 the dispersion of the oxidized film is poor, consisting of many aggregates. The effect of ethanol treatment was also studied via rheology by comparing dispersions of 1.5 h oxidized SWNTs with (SWNT-Ox Film) and without (SWNT-Ox) ethanol treatment. Figure 58 shows the complex viscosity of these fluids as measured with the 50 mm cone and plate geometry. The complex viscosity of the two samples clearly shows the same trend in behavior but offset vertically in magnitude. To eludicate the origin of this behavior the linear viscoelastic moduli were examined as seen in Figure 59. In Figure 59 both G' and G" were plotted against one another to highlight the increase in magnitude of the oxidized film response as well as the variation in crossover point. The crossover point is defined where G' and G" are of equal magnitude. This behavior is indicative of a viscoelastic fluid since at low frequency the samples resemble an elastic solid and at high frequency viscous liquid response is displayed. In this case, the SWNT-Ox Film displayed both an increased crossover modulus and an increased crossover frequency indicating the greater reinforcing potential of the dispersion state.

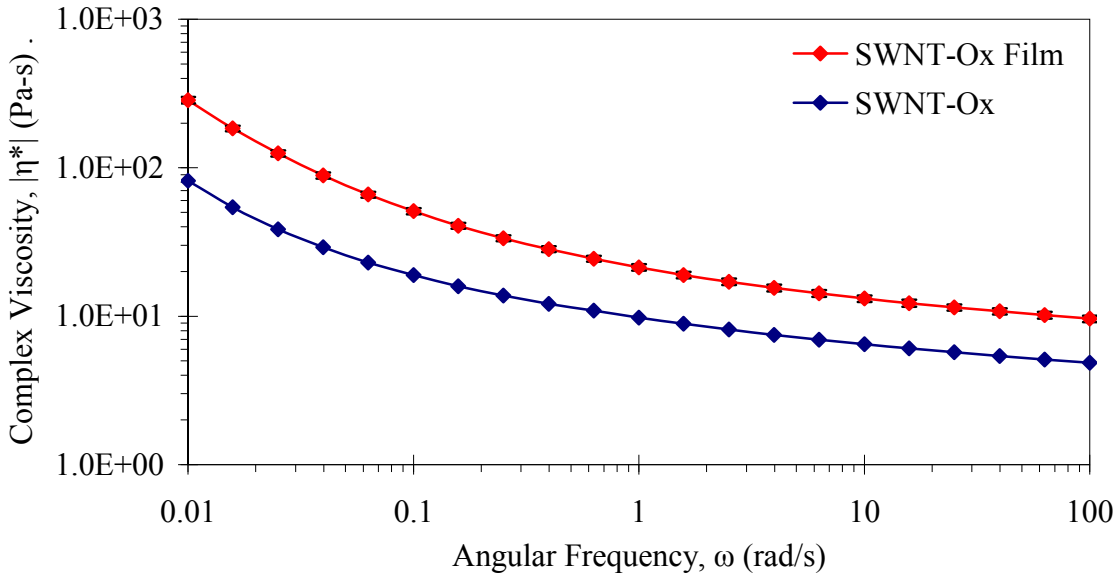

Figure 58: Comparison of the effect of final treatment of oxidized SWNT on dispersion. Both samples were acid oxidized for 1.5 h and dispersed at 0.100% vol. loading.

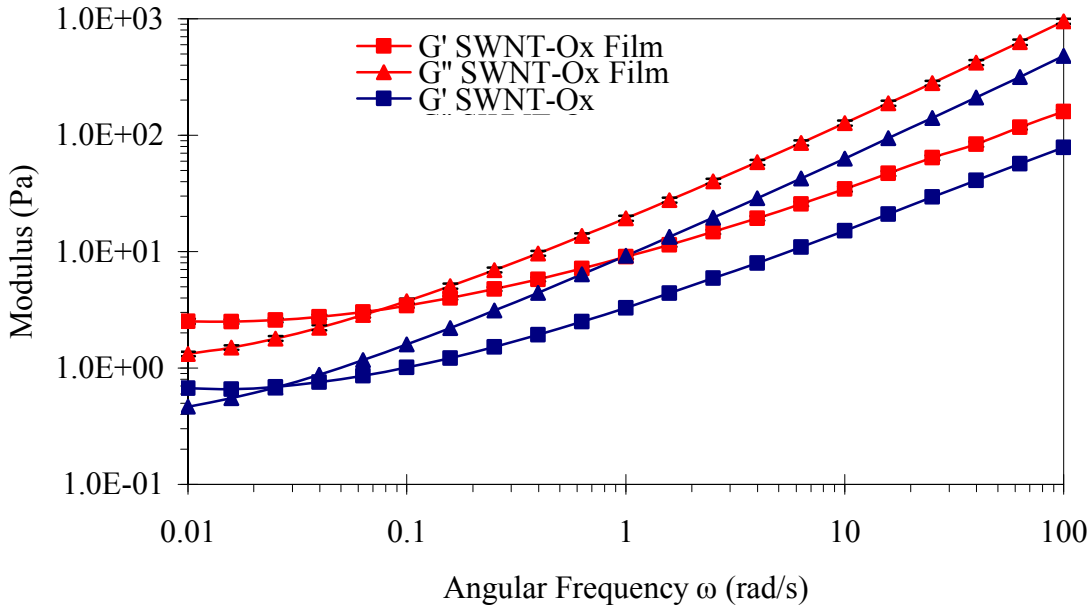

Figure 59: Comparison of the effect of final treatment of oxidized SWNT on dispersion by means of viscoelastic moduli. Both samples are at 0.100% vol. loading.

Qualitative evidence for the lack of dispersion in various oxidized SWNTs can be seen in the following figures. Figure 60 shows a comparison of the 6h acid oxidized and lyophilized SWNTs and a dispersion of SWNT 183.6 Pure. The SWNT 183.6 Pure dispersion is opaque whereas the lyophilized sample is transparent. Figure 61 shows an optical micrograph of the lyophilized dispersion. As can be seen from Figure 61, the dispersion consists of small pieces of the freeze dried film even after intense 3 day shear mixing. Figure 62 shows another poor dispersion consisting of the 48h nitric acid refluxed SWNTs.

Figure 60: Image of (left) lyophilized 6h oxidized SWNT 183.6 in UPR and (right) a SWNT 183.6 Pure dispersion after the same mixing time. Both samples are at 0.005% vol. loading.

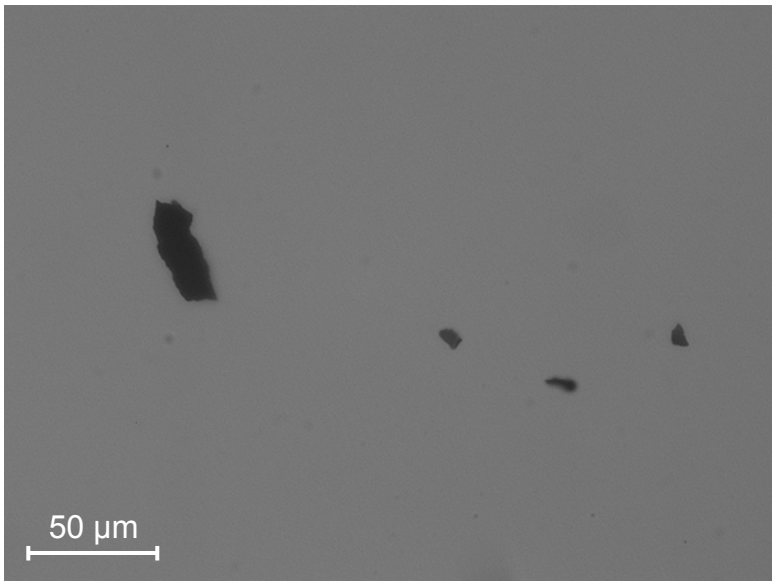

Figure 61: The lack of dispersion in the 0.005% vol. lyophilized 6h acid oxidized SWNTs. Image taken with 20x objective and 2x magnification in front of camera (40x).

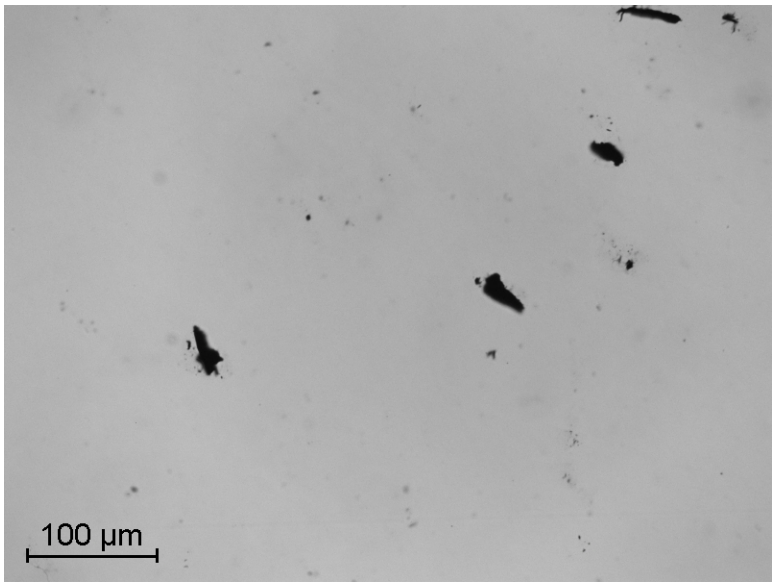

Figure 62: The lack of dispersion in the 0.005% vol. 48 h nitric acid reflux oxidized SWNTs. Image taken with 20x objective.

Even with this extreme 48 h oxidative treatment time the dispersion state is comparable to the 6h lyophilized sample. Out of all the oxidation treatments the two performed on the samples in these images were the most severe and therefore productive at introducing functional surface groups. To confirm that the poor dispersion states are a result of surface chemistry and not a result of entanglement from processing, the surface chemistry of the 6h oxidized and lyophilized sample was rigorously studied. Figure 63 shows the "fluffy" appearance of the lyophilized product. The physical appearance is a result of the low bulk density of the sample after processing. In fact, the same mass of SWNT 183.6 is approximately 5 times more compact.

Figure 63: A 6h oxidized sample as it appeared from the freeze dryer. The sample mass was 15 mg before treatment.

Figure 64 shows the FTIR spectra of a 6h acid oxidized lyophilized SWNT film cast from a reconstituted dispersion in water. In order to remove artifacts from surface bound water or atmosphere the film casting process was repeated, and the spectrum was checked, until

no change in absorbance was observed. This indicated that only the SWNT and not the atmosphere above the crystal was being sampled.

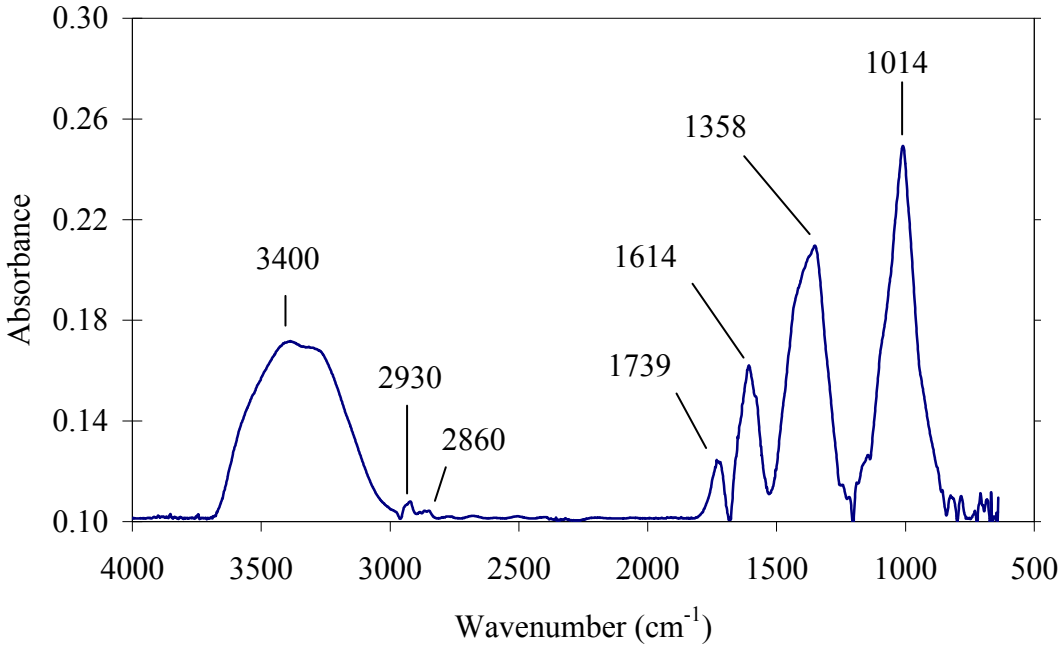

Figure 64: The FTIR spectra 6 h acid oxidized SWNTs (183.6 Pure) after lypholization. The sample was re-dispersed in water to saturation and dropped on a ZnSe ATR crystal. The sample spectra is representative of 5 film layers.

The spectrum shown in Figure 64 is after 5 layers of deposition and one hour under vacuum to remove unbound water. The presence of the peak at 1739 cm^{-1} is a clear indication of carboxyl groups existing in the free state [114]. Unfortunately, spectra of lower wavenumber are multiple overlapping peaks. This is likely a result of the existence of carboxylic acids, carboxylate groups, and bonding. The broad peak at 3400 cm^{-1} is generally indicative of the -OH stretch from a carboxylic acid. The shoulder at lower wavenumber is likely representative the acid monomer and at higher wavenumber for the

hydrogen bonded species. The presence of the shoulder on its peak differentiates this from what would be seen for contaminated water. Furthermore, the absence of a clear water contamination peak at 1636 cm^{-1} supports this argument [99]. The peak at 1358 cm^{-1} represents the -OH bend deformation. At higher wavenumber this peak is broad, suggesting the presence of carboxylate groups. The peak at 1614 cm^{-1} appears to be structured showing the carbonyl groups (C=O) and/or carboxylate ions. The peak at 1014 cm^{-1} is likely a C-O stretch. Finally, the peaks around 2930 cm^{-1} and 2860 cm^{-1} are from sp^2 hybridized carbons, CH_2 and CH, respectively.

The effect of oxidation was also studied by XPS. Figure 65 shows an overall binding energy scan showing relevant atomic oxygen surface composition of 19%. This was a substantial increase from the starting material of SWNT 183.6 Pure which had a surface oxygen content of only 1%, as discussed in later sections. In order to further confirm the functional groups present, high resolution scans of C1s orbital photoelectron emission were recorded. This was further analyzed by peak deconvolution as shown in Figure 66. Peaks were fit at binding energies of 284.6 eV (aromatic carbon), 286.2 eV (hydroxyl or phenolic groups), 287.7 eV (carbonyl carbon), and 289.1 eV (carboxyl groups). In accordance with the FTIR data, the XPS clearly confirms the presence of carboxylic functionalities.

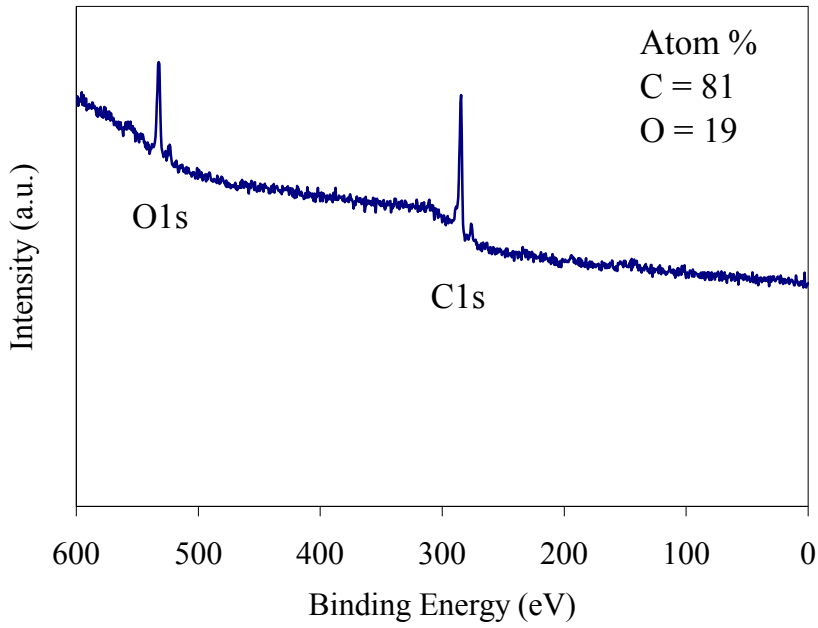

Figure 65: The XPS survey spectrum for 6 h acid oxidized SWNT (183.6 Pure) after lyophilization. The main surface constituents were primarily C and O. Trace amounts of S and Si were observed.

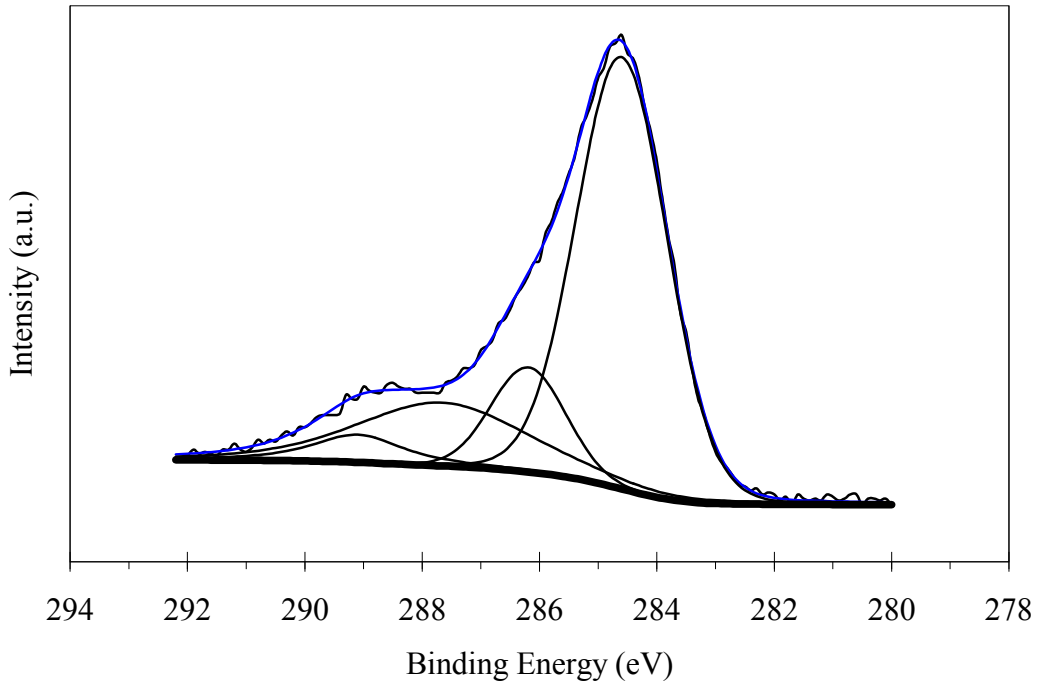

Figure 66: Deconvolution of the high resolution C1s curve for the oxidized SWNT into four separate peaks. The black jagged curve is the raw data and the blue line intersecting this curve represents the sum of the smaller peaks.

Marginal success with the dispersion of oxidized nanotubes was enjoyed only when the sample was post-treated with ethanol. It is important to note that these ethanol treated samples were not oven dried, as will be discussed in detail in later sections. In absence of this ethanol treatment no degree of mixing was observed in oxidized samples. The fact that comparable morphology was seen between oxidized samples, and the fact that dispersion was impossible without the presence of adsorbed solvent, provided compelling evidence to suggest that the effect of surface chemistry is to blame. Thus, it can also be concluded that extreme oxidative treatments were not the correct functionalization route for improving SWNT-UPR dispersions. In fact, examining Figure

60, the oxidative treatment appears to have had a detrimental effect towards creating homogeneous dispersions.

Identifying Experimental Artifacts:

During the processing of some SWNT 183.6 dispersions it was discovered that miniscule air bubbles were incorporated into the sample, effectively creating a "foam" of entrapped air in resin. This was only seen at loadings of 0.025% and below. The elimination of this artifact was studied experimentally by examining various treatments and was essential for understanding a calibrated rheological response for the dispersion state. For point of reference the linear viscoelastic response of the as-produced foam was measured. Additionally, the effectiveness of bath sonication to remove the entrapped air was examined. The agitation and heat produced lowered the sample viscosity and effectively de-gassed the mixture, even after only 5 - 10 min. Finally, extrusion through a long and low gauge syringe was used to remove the air bubbles and the effect of allowing sample relaxation was studied. The large pressure drop across the needle length achieved by means of vacuum driven flow degassed the sample at ambient temperatures. The results of this study are displayed in Figure 67. By comparison, the bath sonicated sample shows the largest increase in complex viscosity whereas the extruded sample shows the lowest enhancement. This is a result of the solvent loss associated with the heating of the sample during sonication but may also indicate an increased dispersion state. The extruded sample, on the other hand, suffers from shear alignment of the SWNT which in turn decreases their contribution to the viscosity. However, if this sample is allowed to relax overnight to an isotropic state the sample shows increased

resistance to flow. It is interesting to note that in the high-shear limit the complex viscosity of the foam was higher than that of the extruded samples.

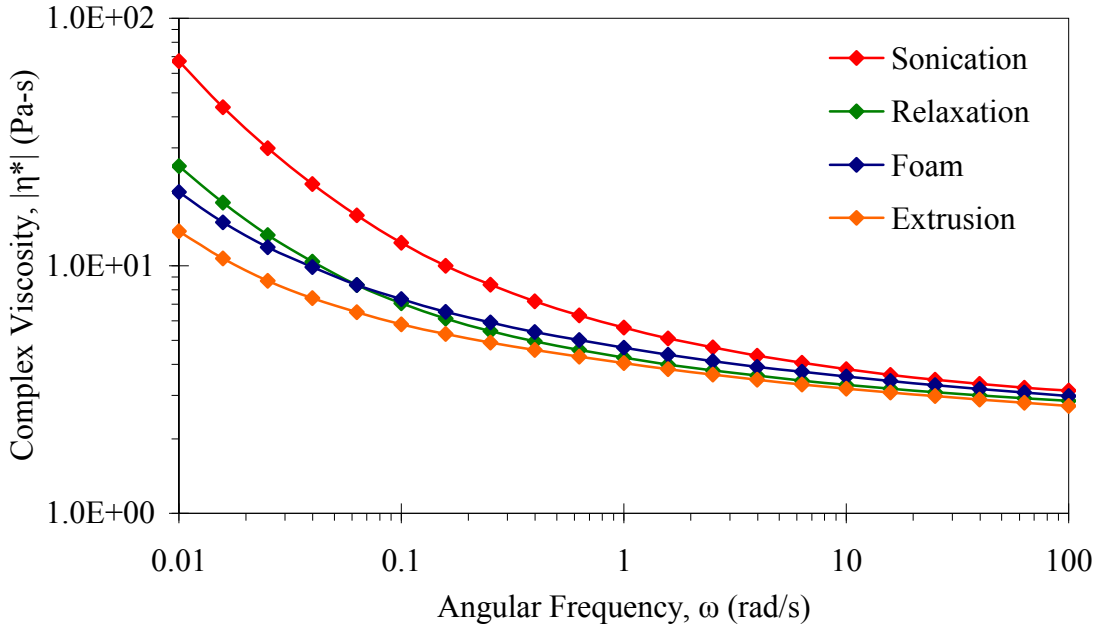

Figure 67: The effect of sample history on the complex viscosity of a 0.025% vol. SWNT 183.6 Pure-UPR dispersion. The 50 mm diameter cone and plate geometry was used.

In order to provide more insight into physical situation the response of G' for these dispersions was also compared. Figure 68 highlights this behavior. Here the two extremes of solvent loss from sonication and shear alignment of the dispersion can be seen. A lower slope can be seen for the sample allowed to relax after extrusion than that of the foam. In the low frequency limit, the inability of the entrapped air to store elastic energy can be seen with respect to the relaxed sample.

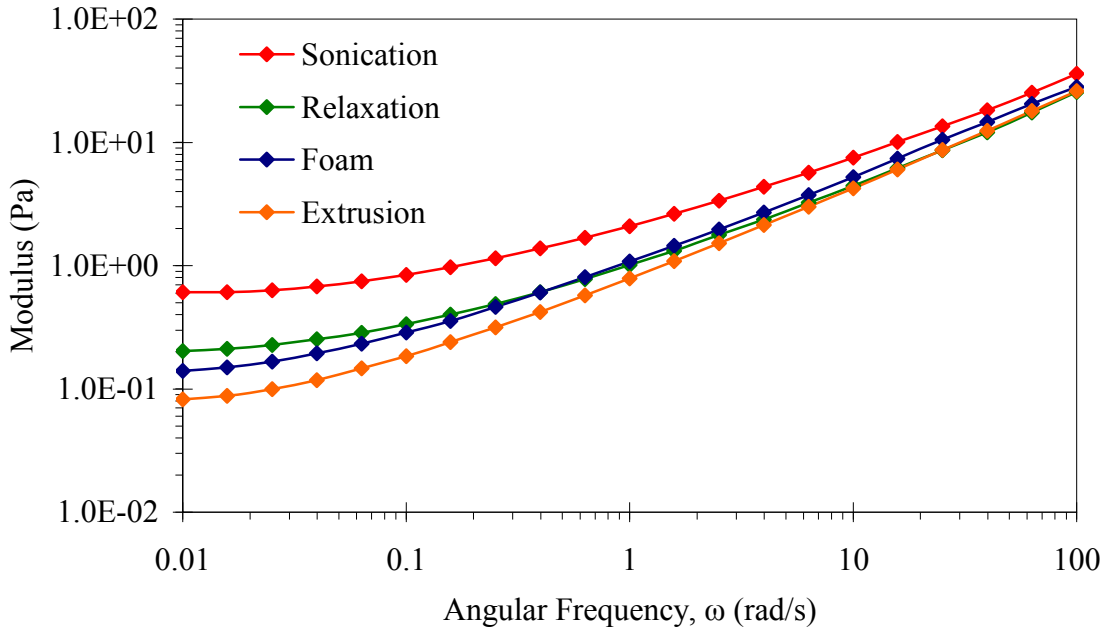

Figure 68: The effect of sample history on the storage modulus of 0.025% vol. SWNT 183.6 Pure-UPR dispersion.

It was assumed that the solvent evaporation was the primary contribution to the high viscosity of the sonicated sample and should be avoided. This was reinforced by the identification of the percolation threshold for SWNT 183.6 Pure dispersions, as discussed in later sections. Essentially, the concentration in the present case is too low to produce an interconnected network without solvent loss which essentially concentrated the sample. Also, allowing the extruded sample to rest overnight recovered the resistance to flow at low shear rates. Therefore, all dilute samples were collected via syringe extrusion and allowed to rest overnight. On a final note, the relaxation of the sample viscosity after resting overnight is good indication that the dispersions of SWNT 183.6 do not settle out of suspension. This serves to validate the measurements made over the experimental duration in this research.

Rheological Behavior of CNTs:

The effect of material type on the mechanical property enhancement was studied at constant a loading of 0.100% vol. of nanotubes. This was measured by the bulk rheological response of the fluid prior to cure. Using the 50 mm cone and plate geometry the behavior of VGCFs, SWNT 183.6 Pure, and ethanol finished acid oxidized SWNTs were compared to neat UPR. The linear viscoelastic response of each material was characterized by an FS test. Figure 69 displays the storage modulus of each dispersion.

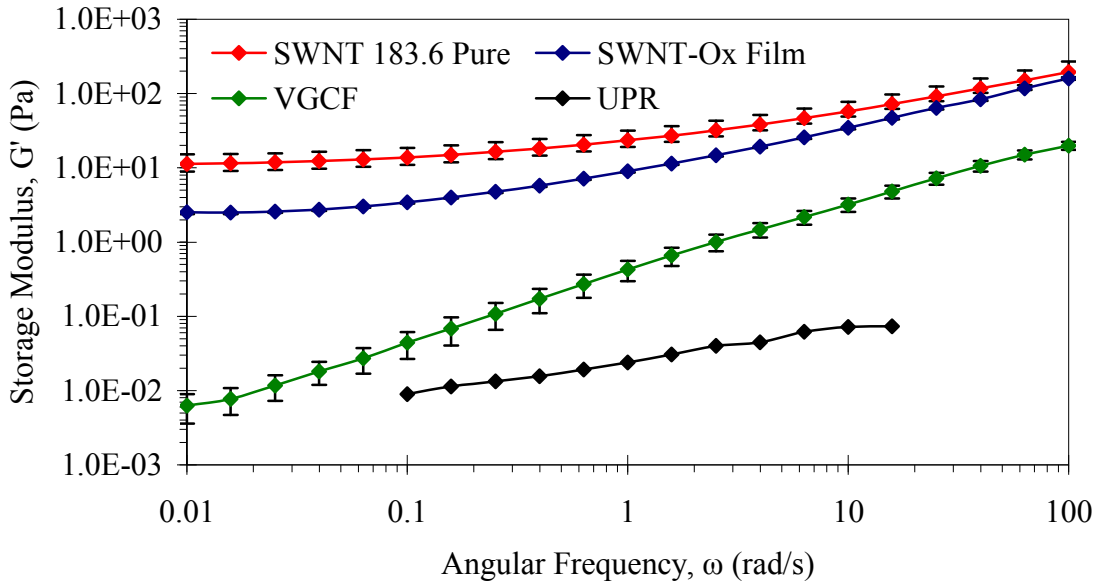

Figure 69: Comparison of material dependant storage moduli at 0.100% vol. loading. The samples were subjected to a controlled linear viscoelastic strain while the angular frequency was varied.

The response of the neat UPR is barely existent at low frequency and not measurable at higher frequencies. This is consistent with a Newtonian fluid where little to no energy is stored in the sample. Below 0.1 s^{-1} the torque falls below instrument sensitivity. In

comparison, an increased slope is seen with the inclusion if VGCFs but the decreasing trend appears consistent with the resin. A markedly different behavior is seen with the SWNT dispersions. For both the pristine and oxidized film samples the value of G' shows development of an elastic behavior where the modulus is nearly independent of frequency at long timescales. Additionally, the value of G' for SWNT 183.6 Pure appears to terminate at almost an order of magnitude higher than the SWNT-Ox Film indicating better reinforcement. The elastic behavior is indicative of SWNT interactions through the formation of a three-dimensional network structure. However, without comparing the effect of concentration no more conclusions can be drawn in regards to the network state. Similarly, the corresponding loss moduli for the 0.100% vol. nanotube dispersion are shown in Figure 70. The behavior of G" for both the neat UPR and the VGCF dispersions are representative of a viscous liquid over all frequencies of observation. In contrast, the SWNT dispersions show deviation from the linear and terminal behavior of the VGCFs at low frequency. Again, this is indicative of SWNT interaction. The variation in the slope of G' for the pristine and oxidized SWNTs indicates a different dispersion state between the samples. From the values of G' and G" the complex viscosity can be determined. As seen in

Figure 71, the viscosity enhancement is minimal for the VGCFs where as a three order of magnitude increase can be seen in the zero-shear viscosity for SWNT 183.6 Pure. In comparison, for the oxidized SWNT sample both a decreased slope and higher infinite shear viscosity can be seen. Examining the dispersion state via microscopy it can be concluded that this type of behavior can be expected for a slightly aggregated vs. homogenous dispersion state.

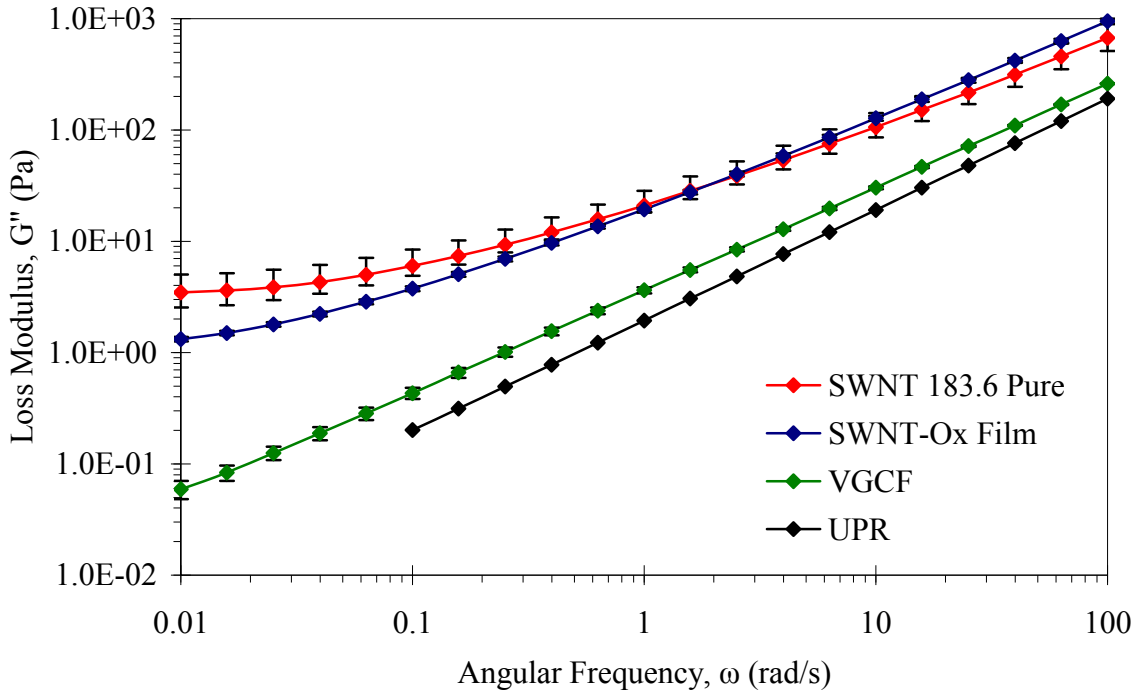

Figure 70: Comparison of material dependant loss moduli at 0.100% vol. loading.

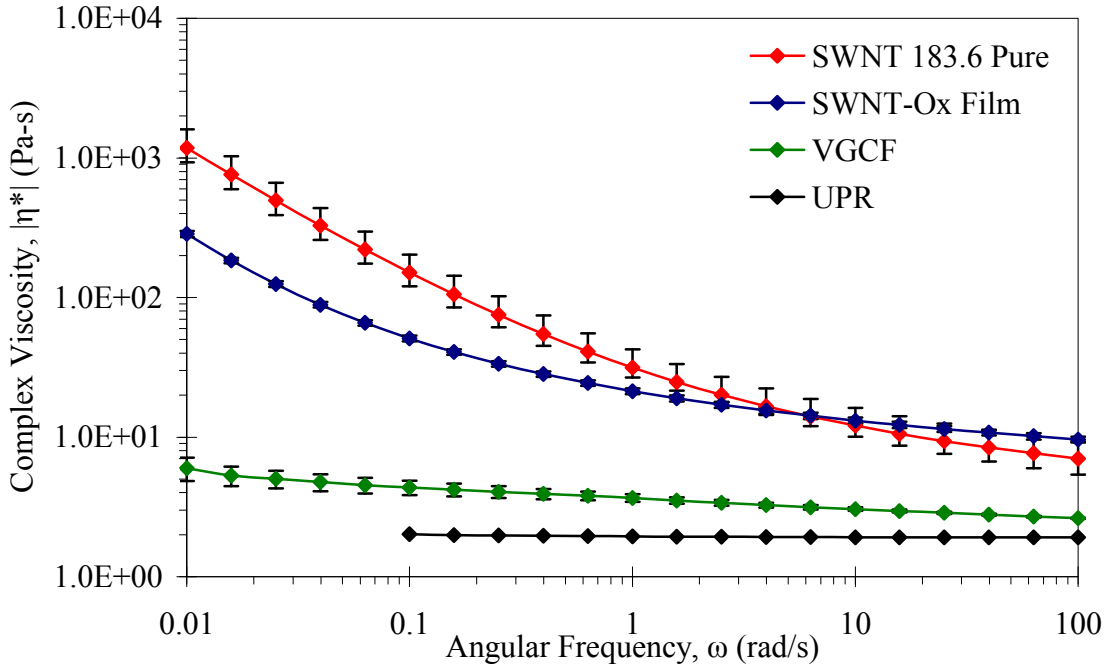

Figure 71: Comparison of material dependant complex viscosity at 0.100% vol. loading.

Finally, the non-linear rheological response of each dispersion to steady shear was characterized as shown in Figure 72. Analogous behavior to the complex viscosity in Figure 71 is seen for all materials. While little viscosity enhancement is seen for VGCFs, nearly a two order of magnitude increase in the low shear viscosity of SWNT 183.6 Pure is observed. Again, the oxidized SWNTs shows less enhancement at low shear rates but has a significantly higher signal in the limit of high shear. This confirms the observation of varying dispersion state between pristine and oxidized SWNTs was not due to experimental artifact. It is noteworthy that the exact mode responsible for shear-thinning behavior observed with the nanotube dispersions has not been fully identified in this work. But, it is assumed that this is a combination of both aggregate breakdown and shear alignment of the nanotube dispersions.

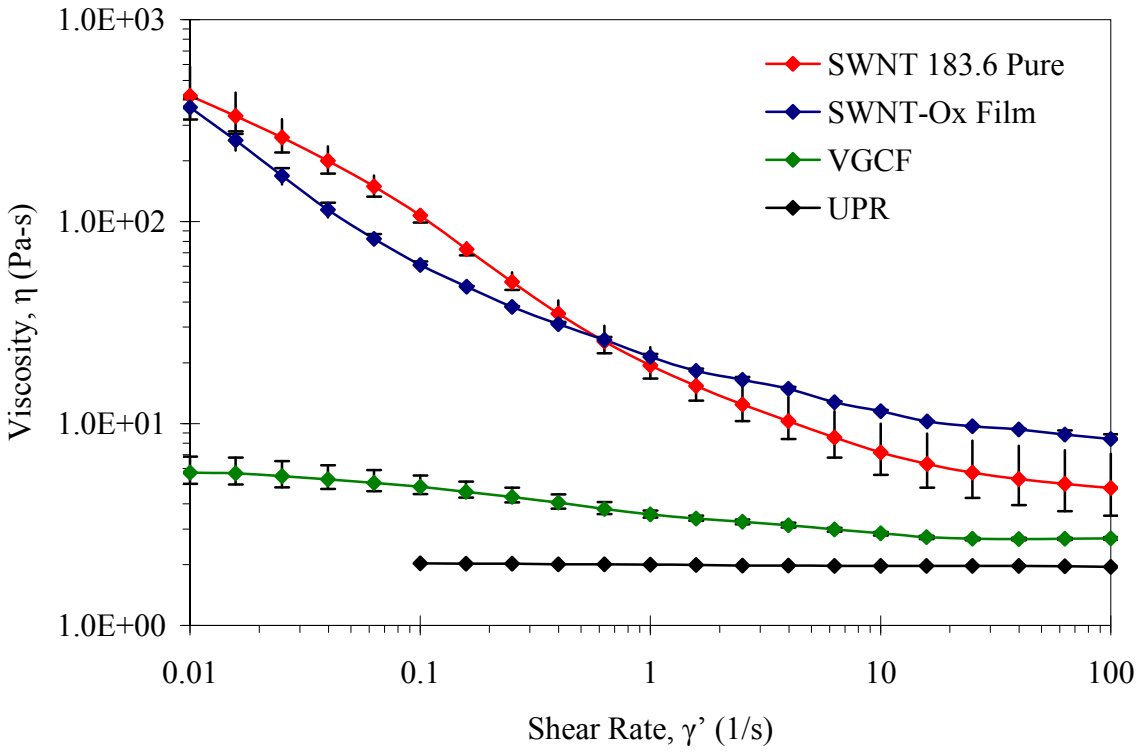

Figure 72: Comparison of material dependant shear viscosity at 0.100% vol. loading.

From this material based study it is clear that the greatest viscosity enhancement was found when the pristine SWNTs were used as the reinforcement material. This is a result of the large aspect ratio, high specific surface area, and strength of association through formation of a three-dimensional network structure in SWNTs. The benefit of using SWNTs over VGCFs is also reflected in the lower mass density of the SWNTs. As a result, great potential exists for producing a lightweight composite materials. However, the effect of SWNT loading on the behavior of these dispersions must still be studied in order to properly characterize this material for processing.

Viscoelasticity of SWNT Dispersions:

The reinforcing potential of SWNT 183.6 Pure was shown to have the greatest promise for property enhancement based on rheological measurements for various materials. But, for efficient processing, the response of the fluid to stress and deformation would be beneficial to characterize. To this end, dispersions were constructed over a range of concentrations spanning almost two orders of magnitude.

The structural stability of the SWNT 183.6 Pure-UPR dispersions was probed by amplitude sweep testing. In this manner the linear viscoelastic regime was characterized and the critical strain was revealed. Figure 73 displays the response of the fluids to controlled frequency, variable strain experiments.

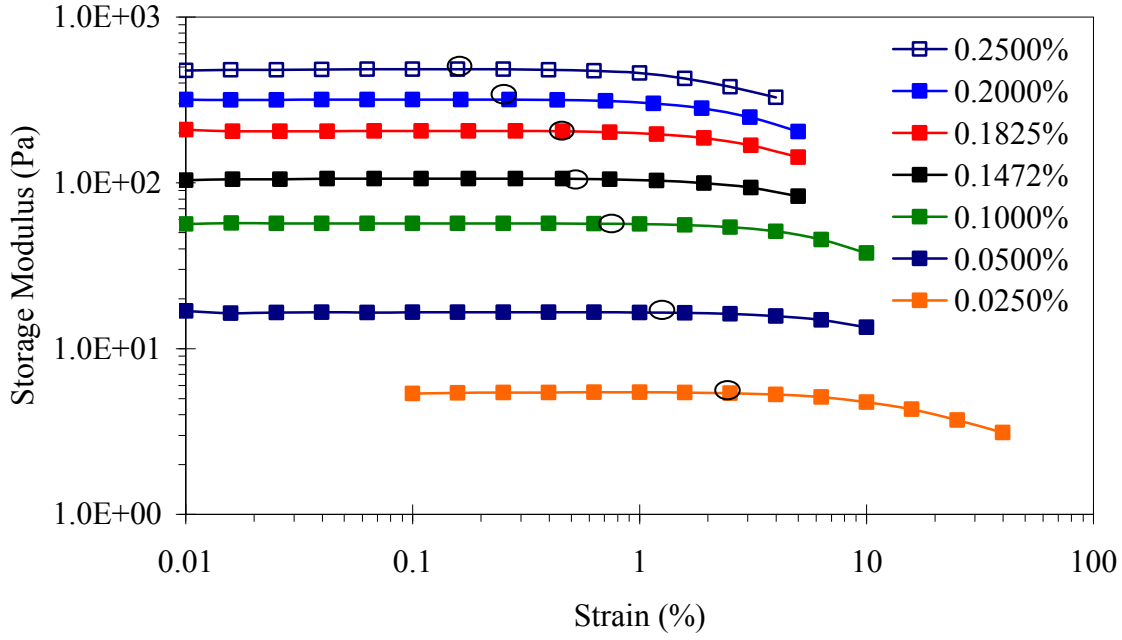

Figure 73: Structural stability of SWNT 183.6 Pure-UPR dispersions as measured by ramping strain amplitude at constant shear frequency. The circles indicate the critical strain at the edge of the linear viscoelastic threshold marked by non-linear response in storage modulus.

The critical strain for the breakdown of linear viscoelasticity is highlighted by the small circles in Figure 73. The value for the critical strain (or stress) decreases with increasing loading reflecting the developing complexity of the network structure, in agreement with Hough et al (2004) [106]. Measurements were halted after the onset of non-linear response so as to preserve the sample structure for FS characterization. Figure 74 shows the behavior over a larger range of strain, moving though the critical linear viscoelastic strain.

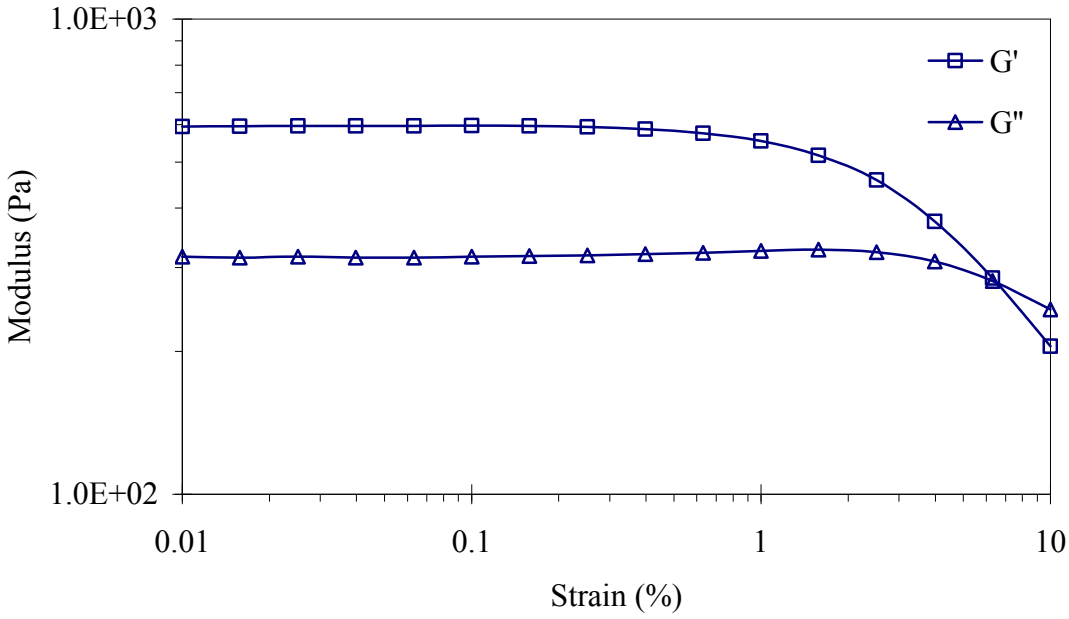

Figure 74: Characterization of the linear viscoelastic regime and transition to non-linear strain response for a 0.250% vol. SWNT dispersion.

As shown in the above figure, the linear response of G' breaks down at approximately 0.15% strain followed by an upturn in G". This behavior is characteristic of strain induced fluidization [106]. The crossover between G' and G" is characteristic of the yield strain. As stated previously, typical measurements were not allowed to progress through the non-linear regime as the time required for the sample to relax was found to be long enough to allow for solvent evaporation. Additionally, the response may not fully recover if aggregates were to form upon fluidization.

Figure 75 highlights the corresponding response in loss modulus to the storage moduli displayed by Figure 73. In contrast to G', the behavior of G" in Figure 75 does not exhibit a drastic non-linear response. This is expected for most fluids as the storage modulus typically is used to characterize the critical strain.

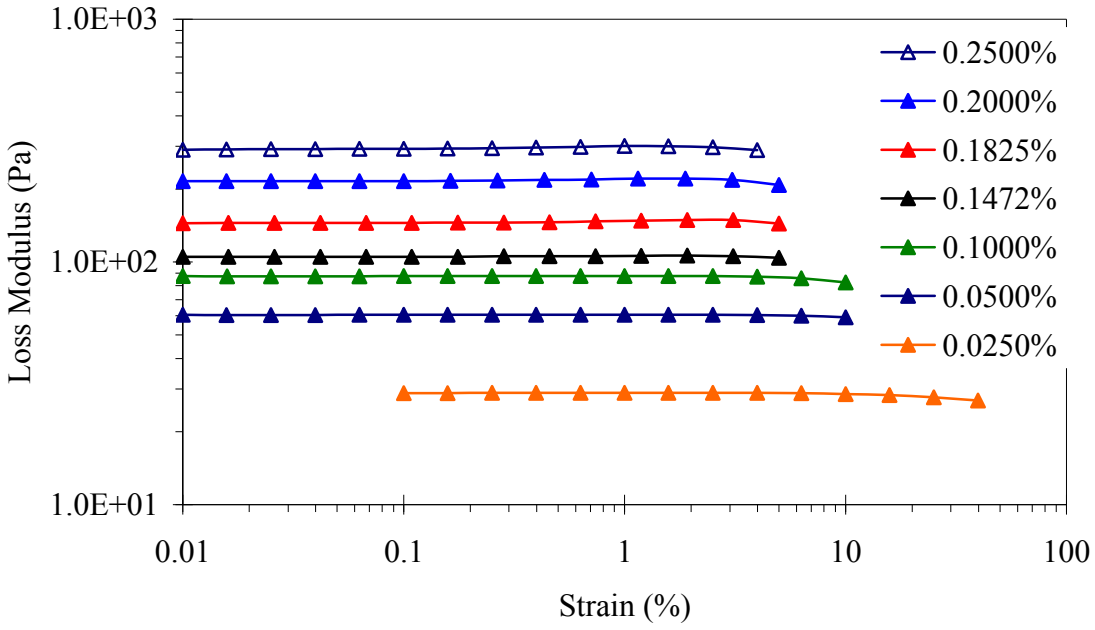

Figure 75: Loss moduli of SWNT 183.6 Pure-UPR dispersions as measured by ramping strain amplitude at constant shear frequency.

With knowledge of the extent of the linear viscoelastic regime for each concentration, the frequency dependent shear moduli were characterized by performing FS testing. Figure 76 displays and overlap of both moduli for each concentration. The purpose of displaying Figure 76 is as a point of reference for applying colloidal scaling theory. It should be pointed out that the both the magnitude of the crossover modulus and the crossover frequency increase with SWNT loading. Trappe and Weitz (2000) proposed a scaling behavior for weakly attractive colloidal particles. This was achieved using the critical crossover parameters to normalize the crossover point to unity in moduli and frequency. Through this technique, the authors suggest the concentration dependence on the viscoelastic moduli can be removed resulting in master curves as displayed by Figure 77

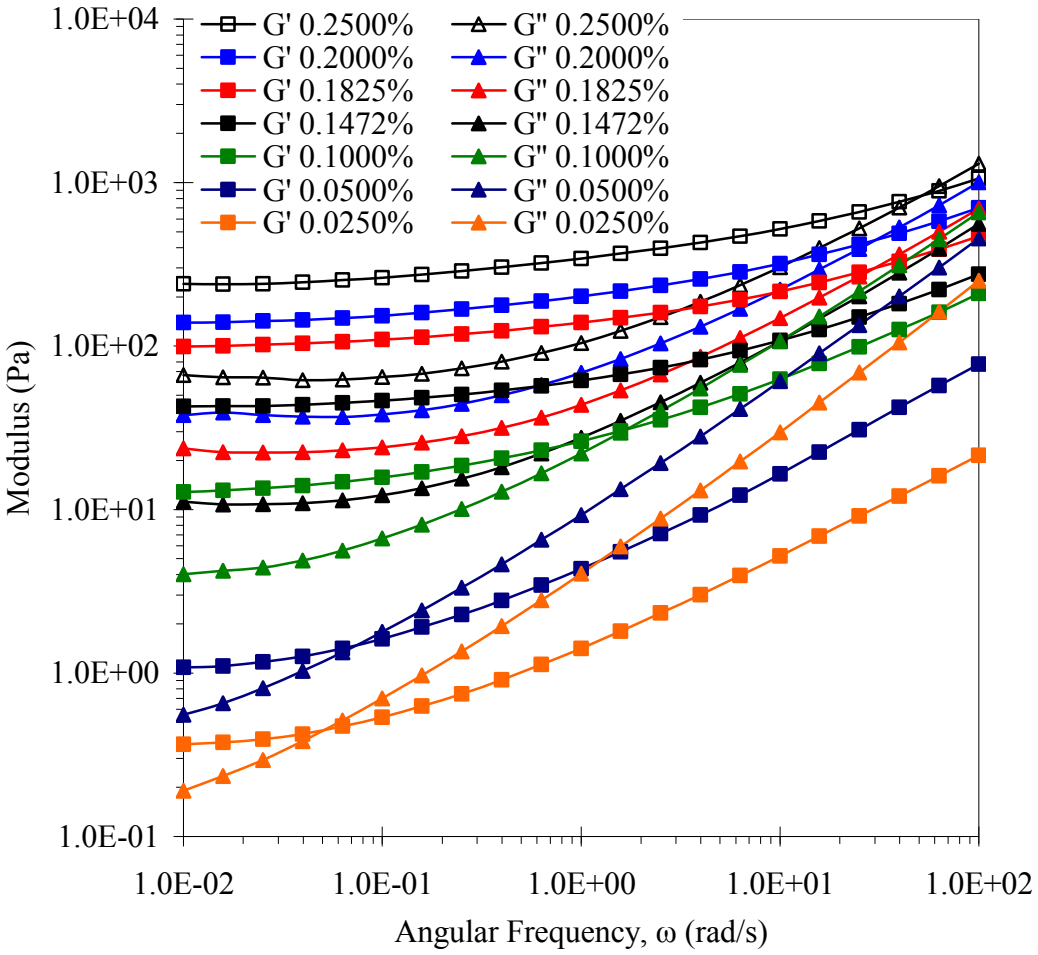

Figure 76: The linear viscoelastic response of the SWNT-UPR dispersions as a function of both SWNT 183.6 Pure loading and the shear frequency. Small square symbols represent G' and small triangle symbols represent G".

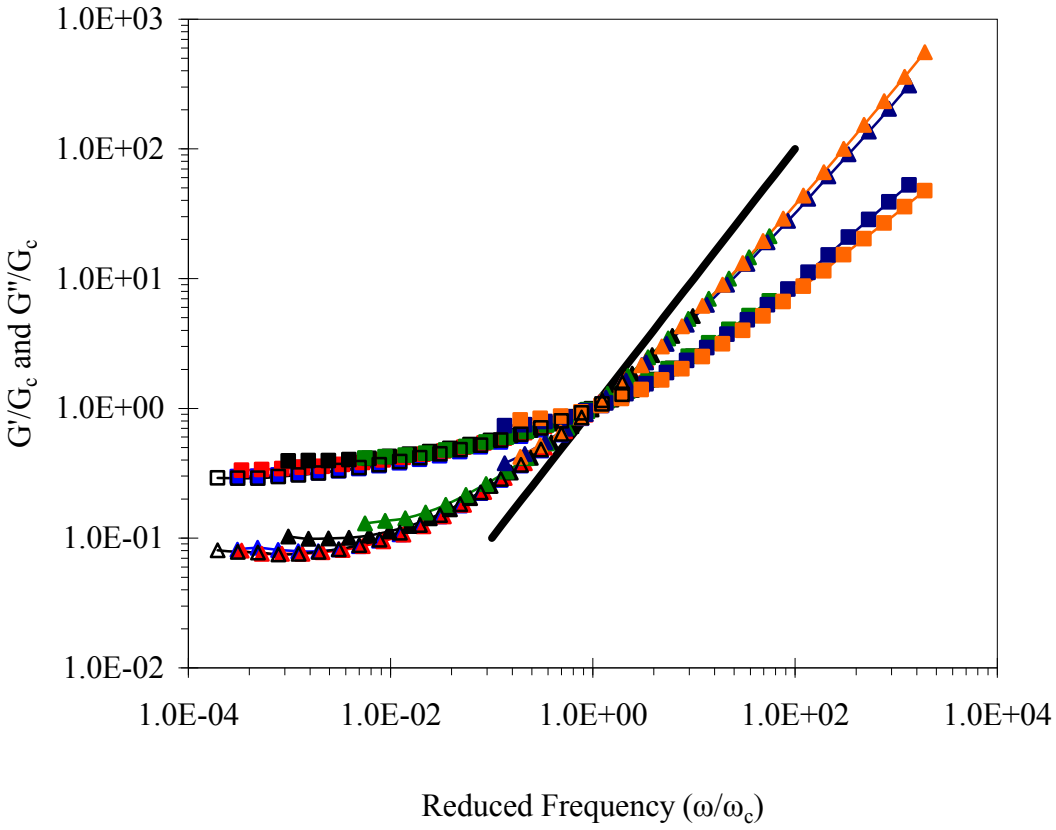

Figure 77: Viscoelastic dependence on concentration removed by means of colloidal scaling [199]. The loss modulus is the raw value of G" for the neat UPR. Its frequency was not shifted.

At high reduced frequency a small discrepancy can be seen between the data corresponding to the lower end of the concentration spectrum. This was predicted by for more dilute loadings as the properties of the solvent are displayed [199]. As a result, the fluid network microstructure is not developed and character resembling the UPR resin is seen by the increase in slope of G"/G_c and the decreased magnitude of G'/G_c (compare orange line to blue line). This observation is feasible since this concentration was found to be well below the percolation threshold, as discussed later. On the other hand, at long reduced timescales slight deviations can be seen in both reduced moduli. The variation

between G'/G_c is attributed to the development of the percolated network structure and its increasing complexity. The upturn in G"/G_c can be expected in accordance with the aging of the network as observed experimentally for laponite suspensions by Baghdedi et al. (2008). Specifically, the upturn in G" arises when local energy barriers become surmountable due to local arrangements throughout the sample allowing for particles to interact [182]. As can be seen for the lowest reduced frequency the behavior converges in G' and G" for concentrations of 0.1825% - 0.2500% vol. indicating the network is self similar at these concentrations. The value of the plateau modulus of G'/G_c at low frequency reflects the elasticity of the network.

Figure 78 shows the crossover modulus, as a function of SWNT loading, used to scale the y-axis in Figure 77. The trend in G_c appears to be linear with SWNT loading even though the scaling plot in Figure 77 indicates deviation from scaling behavior at low loading.

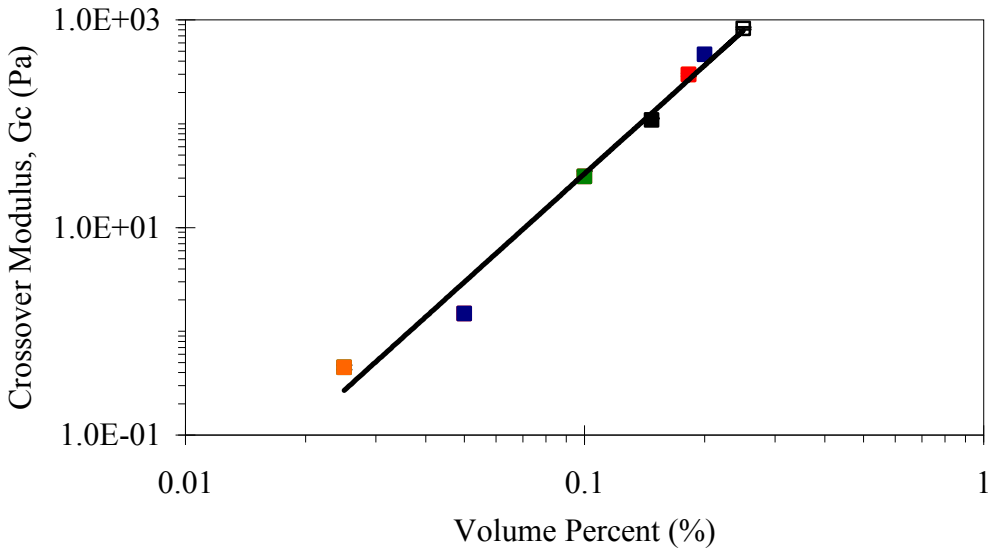

Figure 78: Plot of the parameters used to scale G' and G" to master curves.

By breaking down the viscoelastic response into its separate moduli conclusions on the development of the SWNT network can be drawn. Figure 79 displays the storage modulus as a function of concentration. As the concentration of SWNT is increased the magnitude of G' increases indicative of a more "solid-like" response. Furthermore, the frequency dependence on the magnitude of G' is removed with increasing concentration as indicated by the decrease in G' slope. At highest concentrations the fluid shows response of an elastic solid showing little change in G' with frequency. The apparent jump in low frequency modulus from 0.025% vol. to 0.100% vol. is indicative of a percolation event [103, 106].

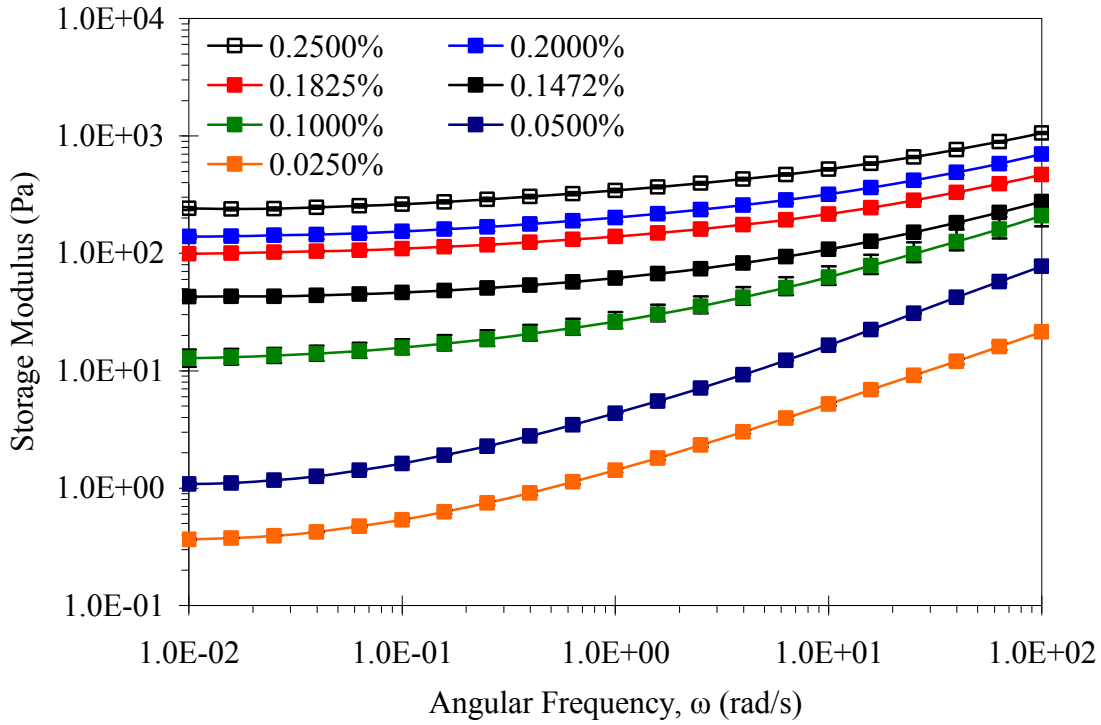

Figure 79: The storage modulus response as a function of angular frequency and increasing nanotube loading for purified SWNT 183.6 dispersed in UPR.

For additional insight into the network development, Figure 80 shows the corresponding loss modulus as a function of SWNT loading. As the concentration of SWNT is raised the magnitude of G" increases and is evidence of increased viscous dissipation of elastic energy. Furthermore, over long timescales the frequency dependence on the magnitude of G" is removed with increasing concentration as indicated by the decrease in G' slope. The fact that the slope in G" is still present at these concentrations indicates that the network structure still may not be fully saturated [81]. Similar to Figure 79 there is an apparent jump in G" from 0.025% vol. to 0.100% vol. at low frequency and this is taken to indicate percolation.

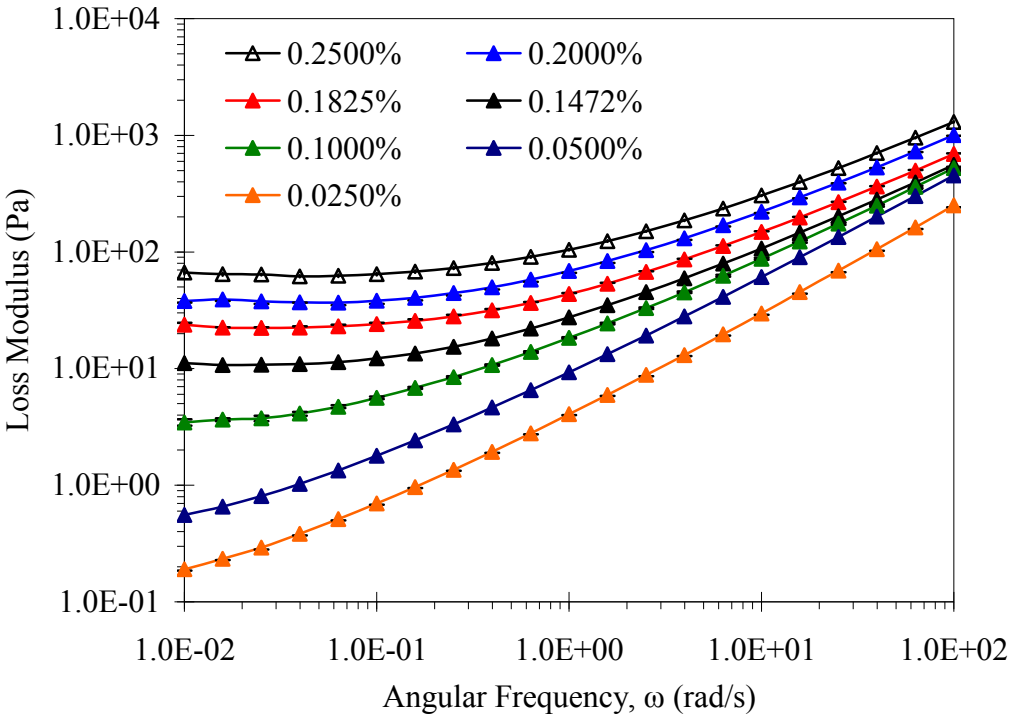

Figure 80: The loss modulus response as a function of angular frequency and increasing nanotube loading for purified SWNT 183.6 dispersed in UPR.

Finally, the over all resistance to flow is shown by the complex viscosity displayed in Figure 81, as a function of SWNT loading. The samples show shear thinning over a wider range of frequencies as the loading is increased, representative of the increasing complexity of the fluid microstructure. In the infinite shear limit the viscosity increases with loading. Between concentrations of 0.025% vol. and 0.100% vol. there is a sudden increase in the degree of shear thinning and a jump in zero shear viscosity. Again, this was taken as an indication of network formation.

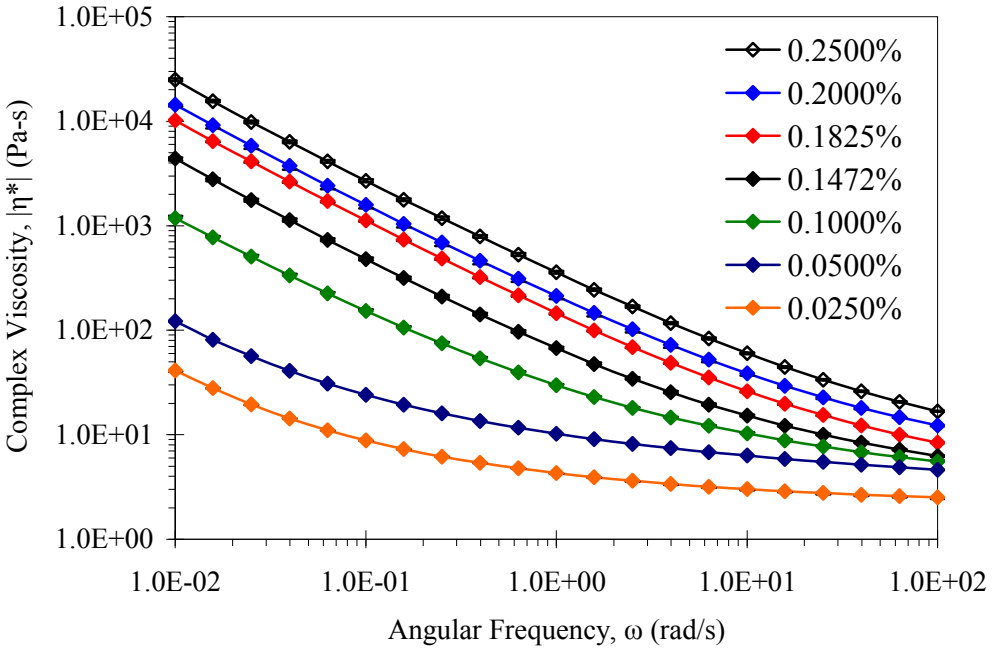

Figure 81: The complex viscosity with increasing nanotube loading for purified SWNT 183.6 dispersed in UPR.

It is important to note that the range of concentrations studied was limited by the method of mixing in this work. Figure 82 shows an image of the highest concentration attempted for dispersion; 0.400% vol. The extremely high viscosity that developed at

this loading prevented sufficient pumping in the mixer leaving large aggregates of SWNT in the sample after processing. Therefore this concentration was not studied.

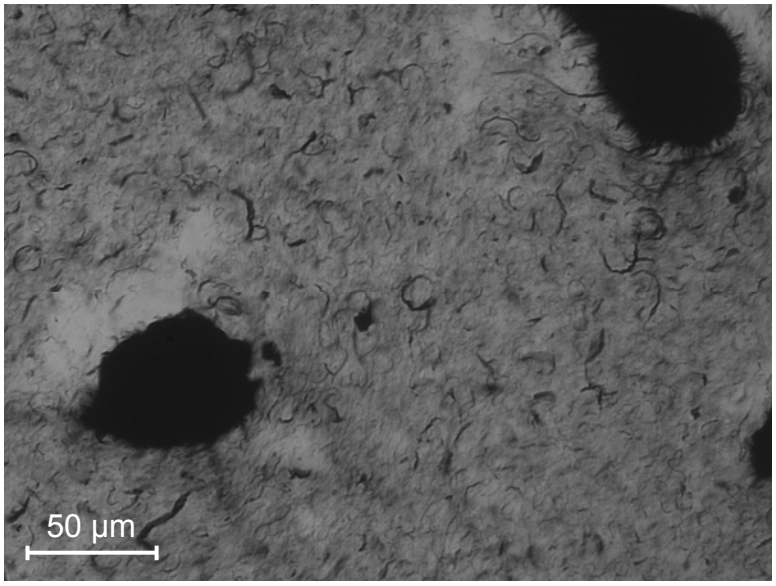

Figure 82: Image (20x2) of a 0.400% vol. SWNT-UPR dispersion processed shear mixing.

Determination of Rheological Percolation:

While linear viscoelastic data suggested network formation, methods exist to extract the onset of percolation and characteristics of the network interaction. Recently, Mitchell and Krishnamoorti used a "divergence" plot to elucidate the evolution of a yield stress in SWNT-poly(ε-caprolactone) dispersions [200]. Figure 83 shows such a plot where the complex viscosity is plotted against the complex modulus. Essentially, this plot displays the resistance to flow vs. the resistance to deformation. The divergent behavior at fixed complex modulus is indicative of a finite yield stress. The vertical arrows show the value of G* as the complex viscosity tends to infinity. Open symbols indicate uncertainty with the divergent behavior as these data points were close to the instrument torque sensitivity on 0.1 µNm. The G* and the corresponding loading can

then be used to correlate rheological percolation. Figure 84 shows such a plot. Linear regression was performed with the set of three, four, and five highest concentrations to determine the x-intercepts (x_{int}). A good linear fit can be seen for the highest 3 - 4 data points. These x-intercepts were taken to be the represent the onset of geometric percolation from approximately 0.12 - 0.13% vol.. Garboczi et al. (1995) calculated the percolation threshold of ellipsoids with no excluded volume interaction as a function of aspect ratio [190]. From this model an effective anisotropy for the dispersion of SWNTs in UPR was found to be ~450 - 470. But, as seen in both Figure 83 and Figure 84 yielding behavior is apparent at 0.100% vol. loading. A linear fit to the five highest concentrations shows a percolation threshold of ~0.100% vol. with L/d of ~550. For comparison, a more classical approach to determining percolation threshold was also performed.

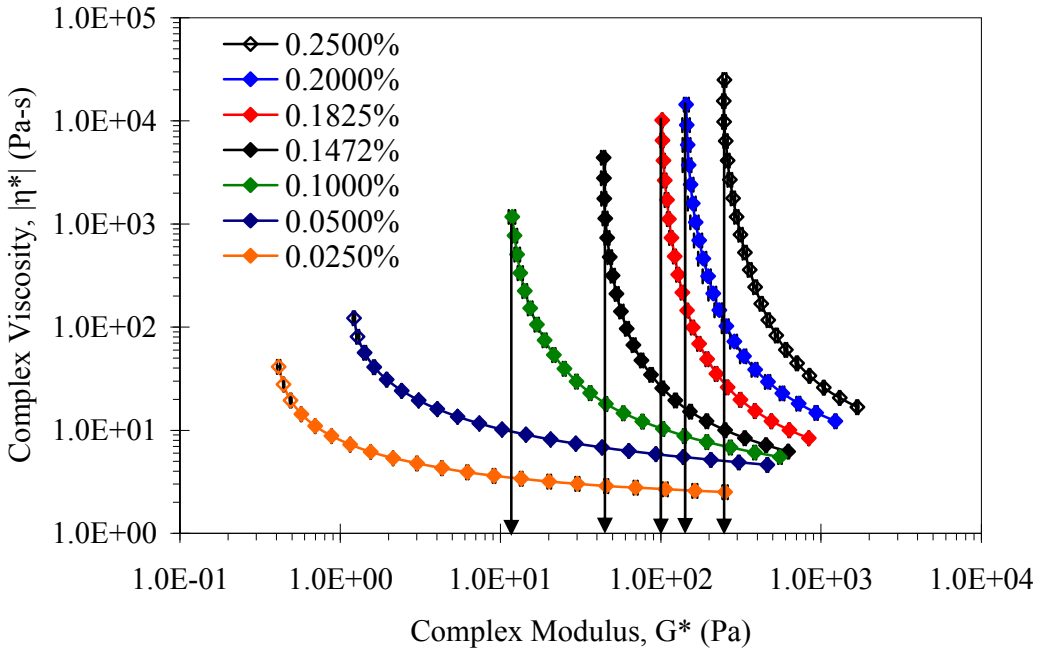

Figure 83: Divergence plot showing the complex viscosity as a function of complex modulus [200]. The arrows point to the value of G* that is taken to be the yield stress.

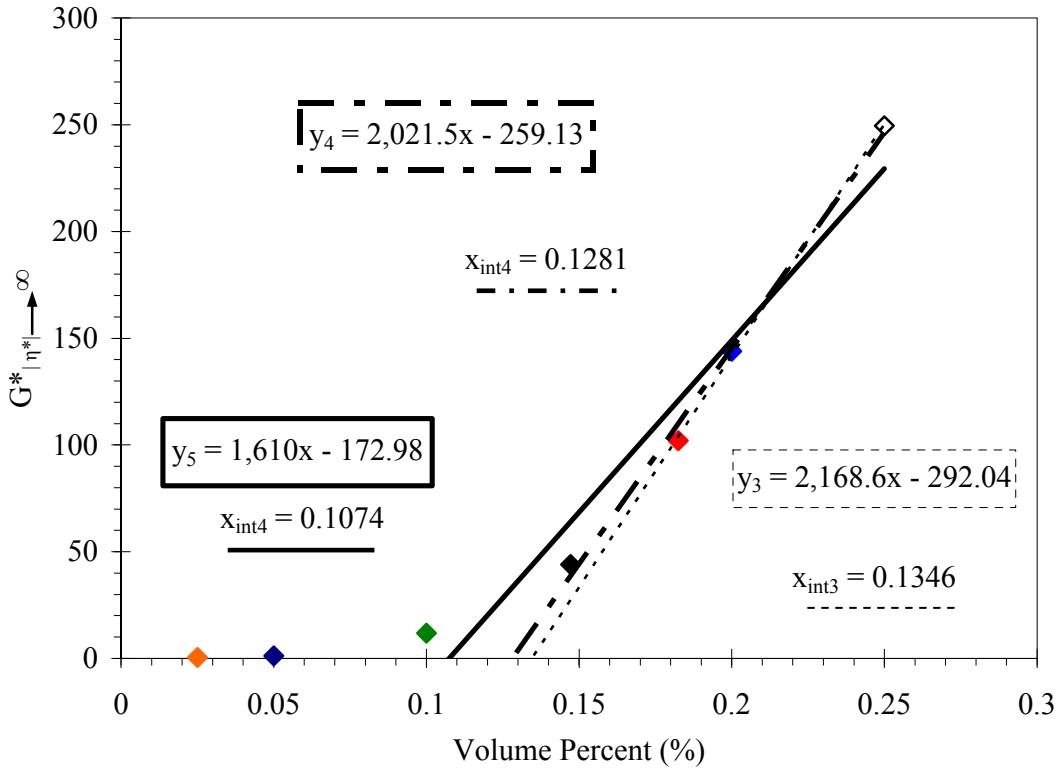

Figure 84: The divergent value of the complex modulus from Figure 85 plotted against its corresponding loading.

Figure 85 displays the trend in low frequency storage modulus, plotted for three constant angular frequencies, as a function of loading. The two order of magnitude jump in G' that occurs between 0.050 % and 0.100 % vol. (gray shading) was interpreted to be an acceptable range for the onset of rheological percolation. A similar plot was used by Hough et al. (2004) used to determine an acceptable range of threshold values. From this data a power-law can be fit and the percolation threshold and scaling exponent can be determined. Figure 86 displays the power-law scaling at 0.1 rad/s. The method of Du et al. (2004) was arbitrarily chosen to render the x-axis of reasonable magnitude, centered around unity.

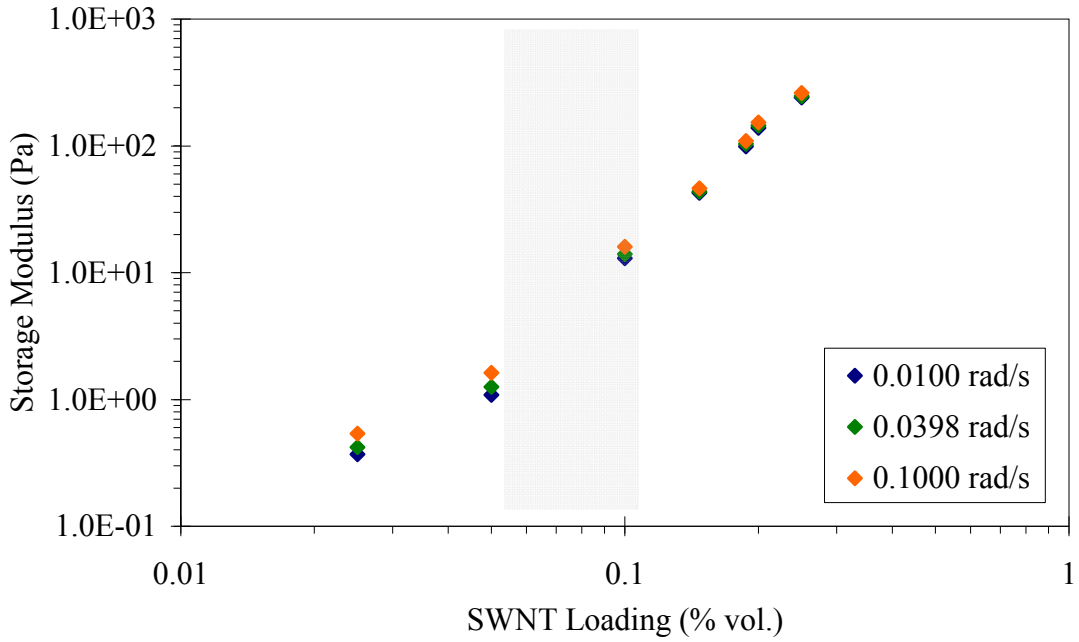

Figure 85: The storage modulus as a function of SWNT loading for fixed angular frequencies on a log-log axis.

The onset of rheological percolation was found to occur at ~0.100% vol. by varying ϕ_c so as to maximize the coefficient of regression (R^2). This is in general agreement, being slightly lower, with the estimation of the percolation threshold from the divergent complex modulus but cannot be assumed to be a measure of individual SWNTs. For point of reference a monodisperse system of individual tubes would show the onset of percolation at the theoretical upper limit for the isotropic concentrated regime. The determined slope (critical exponent) of 1.55 is less than expected for chemical gels, with a predicted value of ~2.1, where bonds resist stretching but are free to rotate under strain [201]. Experimentally, a critical exponent of ~2.3 was extracted by Hough et al. (2004) for aqueous surfactant stabilized individual SWNT suspensions.

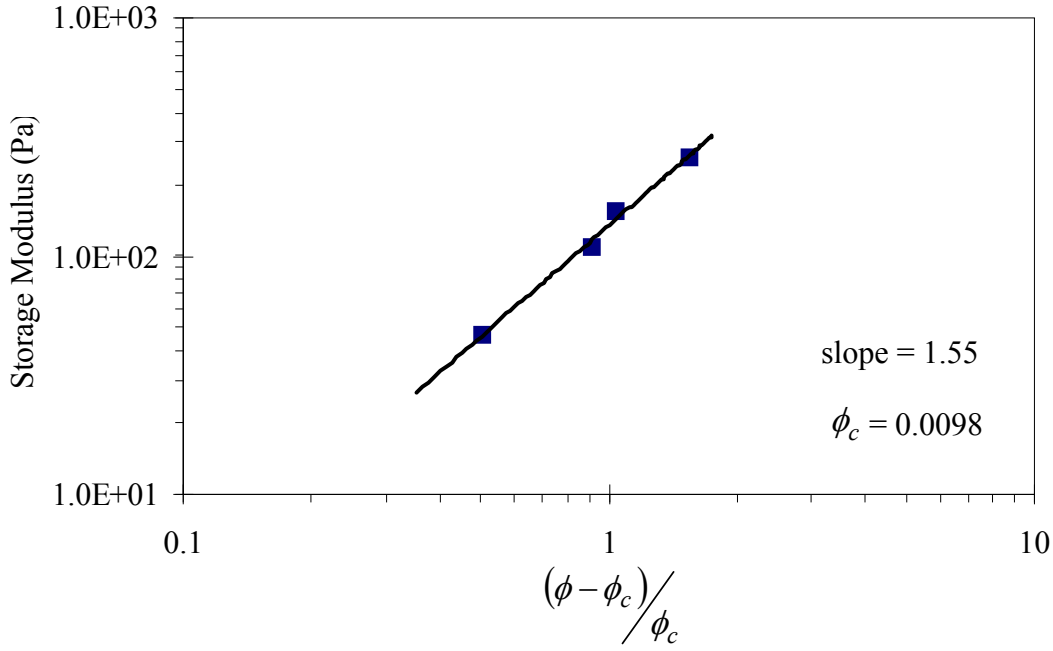

Figure 86: Power law scaling of the storage modulus as a function of the reduced volume fraction at 0.1 rad/s.

This value was interpreted to be a result of central force percolation described previously by Sahimi and Arabi (1993) [201]. Davis (2006) extracted an exponent of ~1.6 for SWNTs in superacid and argued that the lower value was a result of weaker associations between protonated SWNTs than in the surfactant used by Hough et al. [144]. Hu et al. (2006) found a critical exponent of 1.5 in PET-MWNT melts but provided no explanation to the physical origin of this behavior. In the present case, the value of approximately 1.6 is most likely a result of the less than ideal dispersion state and the absence of rigid-rod behavior rather than representative of the tube-tube association at contact points. For sake of repeatability, Figure 87 shows the power-law scaling for data recorded at 0.01 rad/s. Again, similar behavior was found with regard to critical exponent and

concentration. It is noteworthy that upon addition of the 5th lowest concentration point the percolation threshold became non-physical and extended well into the dilute regime.

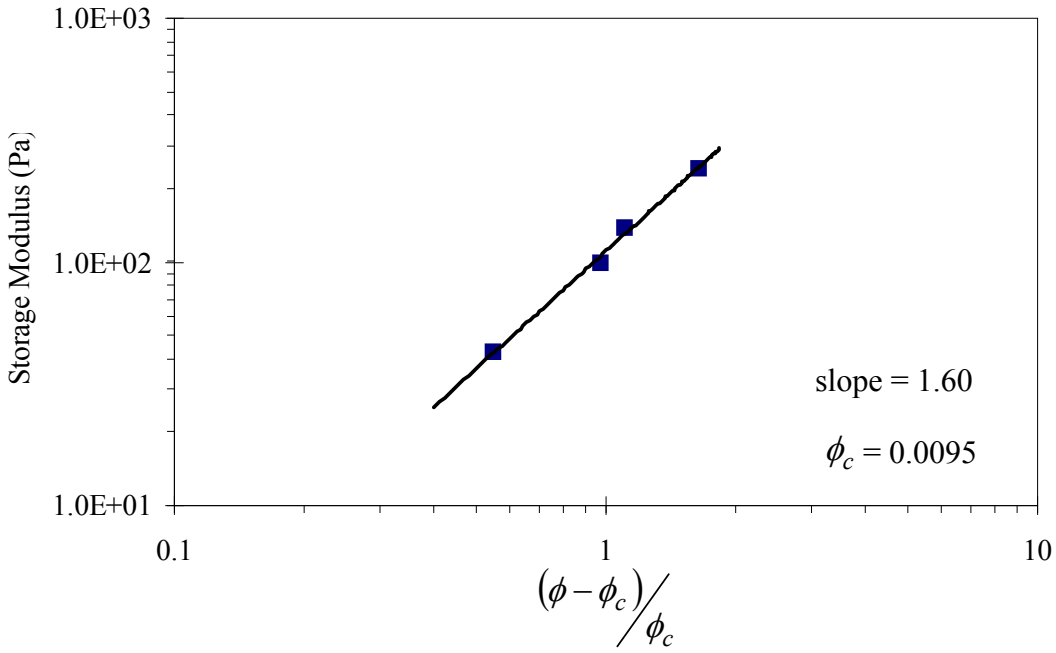

Figure 87: Power law scaling of the storage modulus as a function of the reduced volume fraction at 0.01 rad/s showing similar behavior as the trend at 0.1 rad/s.

Reconsidering the colloidal scaling, the lowest concentration of 0.025% vol. can be removed since this was below the percolation threshold. Figure 88 displays the high frequency behavior of the scaled moduli. The high frequency regions were fit to a power law in order to extract the frequency dependant exponents. According to this trend, $G''/G_c \alpha \omega^{0.85}$ and $G'/G_c \alpha \omega^{0.63}$. For comparison, the reduced loss modulus G''_{sc} was found to scale with a power of 0.75 in filamentous F-actin networks and solution of tightly entangled semiflexible polymers by theory and experiment [202, 203]. Hobbie et al (2007) found power-law scaling of $G''_{sc} \alpha \omega^{0.7}$ and $G'_{sc} \alpha \omega^{0.9}$ for shear aggregated,

fractal MWNT networks [107]. For both reduced moduli the observed behavior for SWNT-UPR dispersions is weaker.

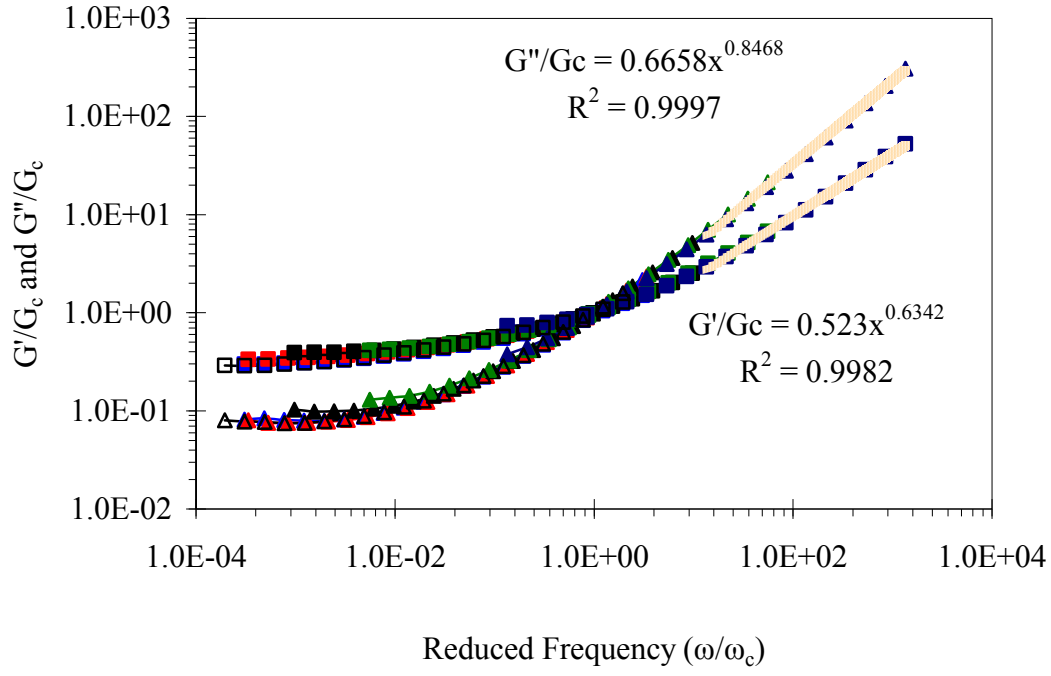

Figure 88: High frequency regression of the scaled moduli after removal of 0.025% vol. data set.

Percolation from Crossover Modulus:

An interesting trend was observed when examining a plot of the crossover parameters shown by Figure 89. There is a similar two order of magnitude increase in the crossover modulus from 0.025% vol. - 0.100% vol. consistent with the data in Figure 85. This behavior can be explained, in part by the fact that the crossover modulus does not differ much from the low viscosity plateau modulus as a result of the frequency independent network elasticity. Additionally, there increasing trend is crossover frequency follows SWNT concentration with the increased reinforcement. Therefore it may be reasonable for one to obtain the same information regarding rheological

percolation at higher torques as compared to a tracking of low angular frequency G'. This would be valuable for researchers studying low viscosity solutions of particles like SWNTs in superacids.

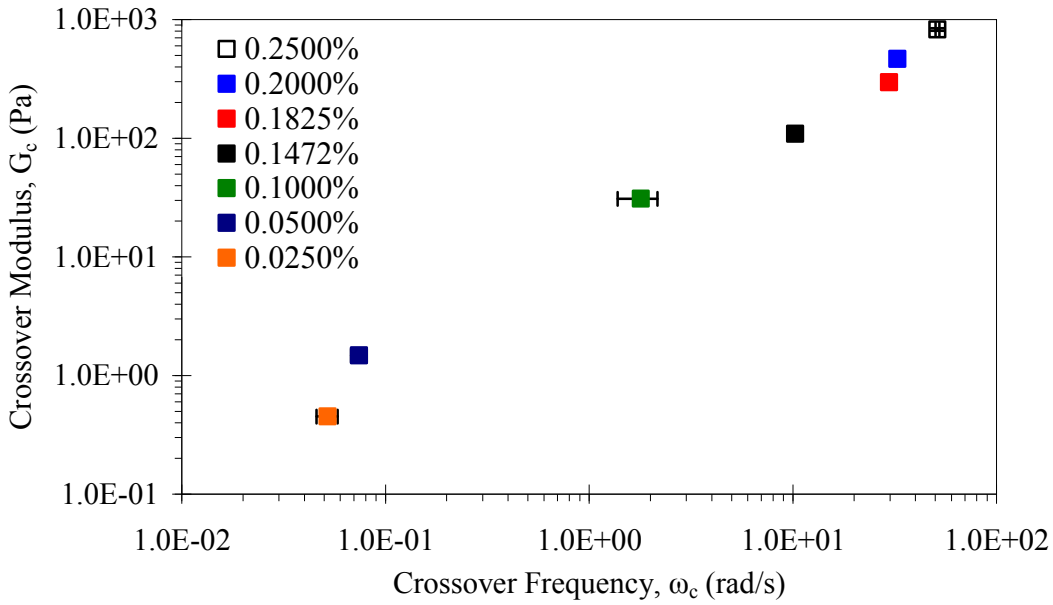

Figure 89: Plot of the crossover modulus and frequency on a log-log axis.

Morphology of SWNT Dispersions:

To address the interpretation of the predicted effective hydrodynamic aspect ratio and the scaling found from the critical exponent, TEM images of the SWNT dispersions were gathered. Figure 90 shows a range of fiber sizes from an acetone washed dispersion. Clearly, by examining the image, the effective aspect ratio of ~450 - 470 reflects the micron length SWNT bundles or fibers instead of individual tubes.

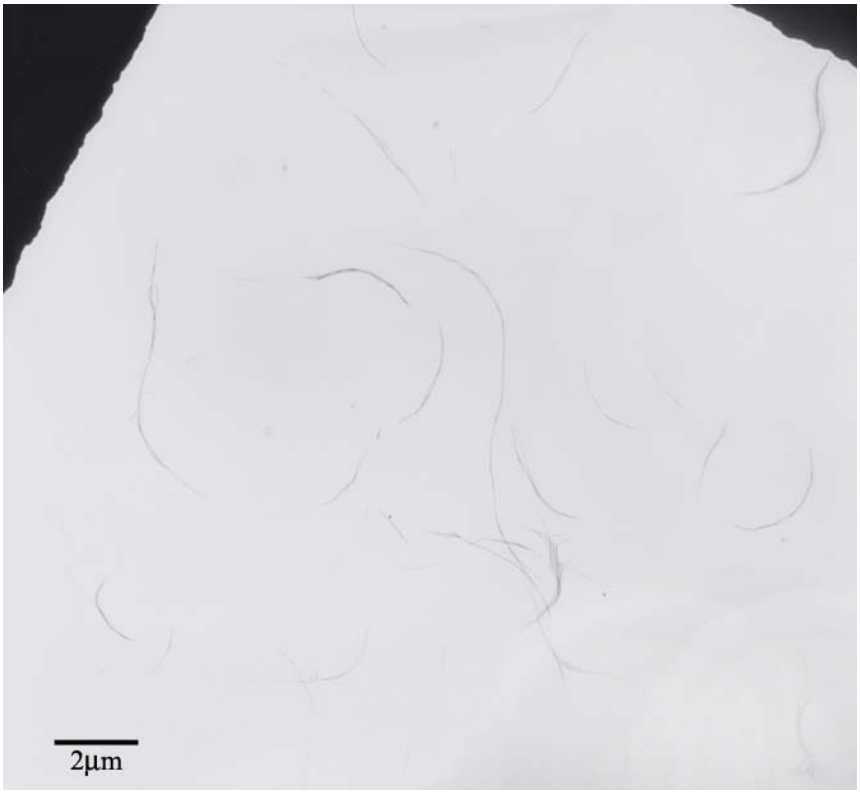

Figure 90: TEM image of the SWNT-UPR dispersion (0.050% vol.) after acetone washing. A mixture of bundled SWNT fibers ranging in lengths and diameters can be seen.

Rheology of Dilute SWNT Dispersions:

Dispersions ranging in concentration from 0.030% vol. - 0.010% vol. were characterized by means of rheology and microscopy through successive dilution experiments. Figure 91 shows a 0.010% vol. image prior to dilution. AS testing was first conducted in order to determine the extent of the linear viscoelastic regime. Figure 92 displays the response of dilute SWNT 183.6 Pure dispersions to shear strain. While both G' and G" increase with loading there is not much variation in the critical linear viscoelastic strain due to the dilute and non-interacting nature at these concentrations. Thus, over the range of concentrations in Figure 92 the fluid behaves as a viscous liquid

at all times. For reference the moduli of neat UPR is shown as well. At low strains G' shows some noise for the neat UPR as it is close to the torque sensitivity of the instrument.

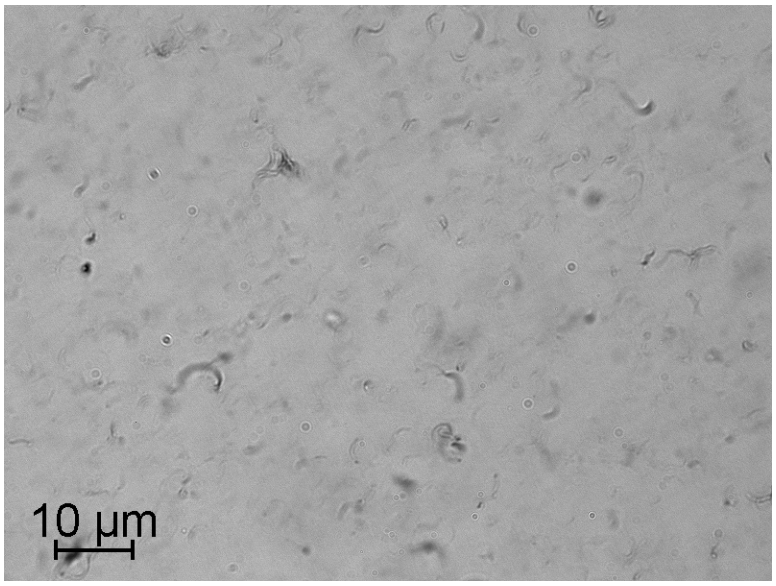

Figure 91: Image of the 0.010% vol. SWNT-UPR dispersion processed shear mixing. The image was taken through cover glass with a 60x oil immersed objective and 2x magnification in from of the camera (120x).

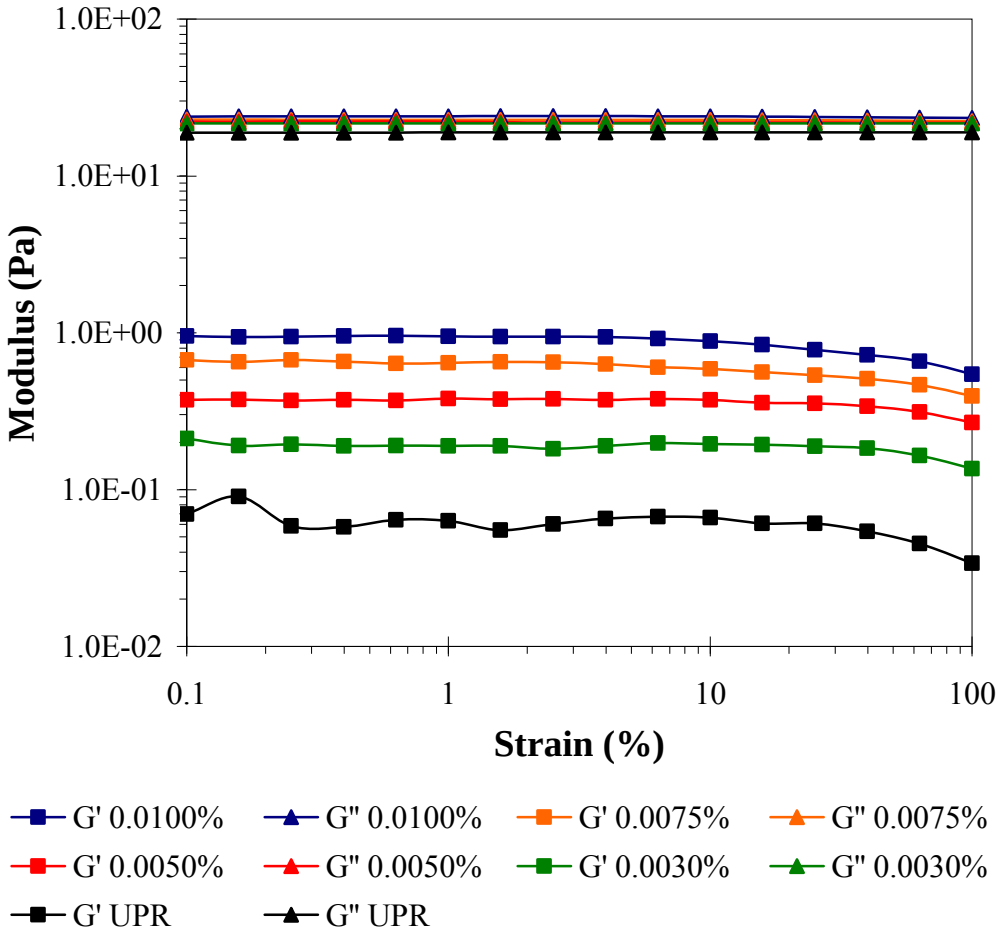

Figure 92: Structural stability of SWNT 183.6 Pure-UPR dispersions following successive dilutions. The moduli were measured by ramping strain amplitude at constant angular frequency of 10 rad/s.

After AS characterization the samples were subjected to FS testing in order to determine the response to controlled strain oscillatory shear. Figure 93 presents the results of this test. The FS data clearly shows the an increase in both moduli with loading but liquid-like behavior was observed for all concentrations. Additionally, Figure 94 shows the corresponding complex viscosity for the dilute SWNT dispersions.

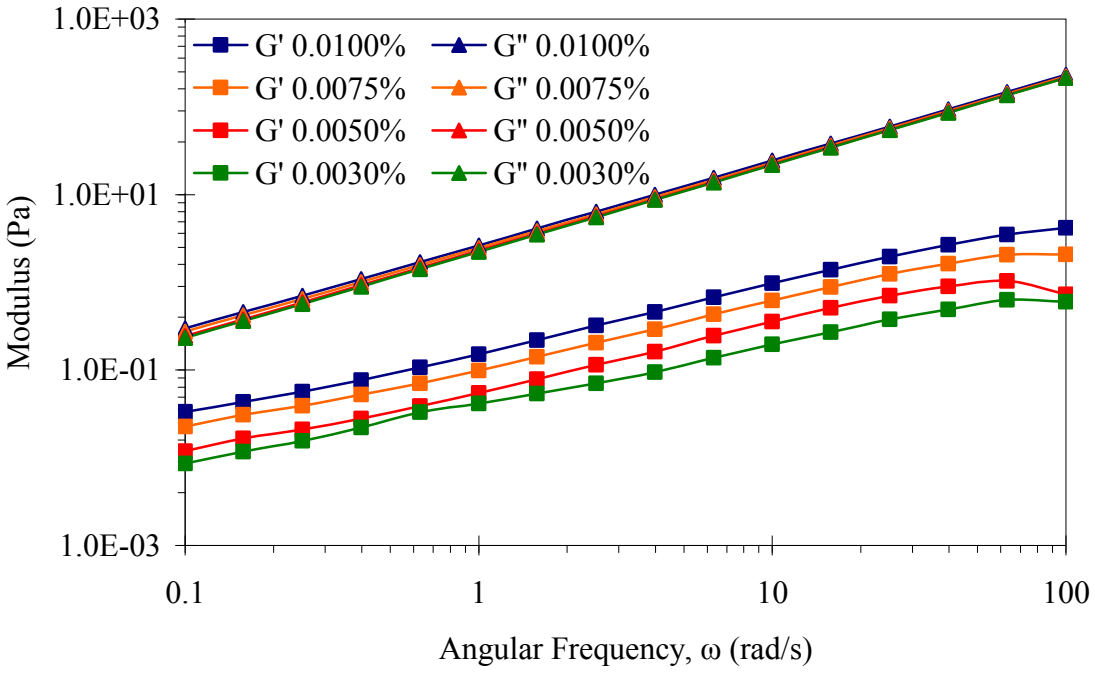

Figure 93: Storage and Loss Moduli from successive dilutions of SWNT 183.6 Pure dispersed in UPR. The magnitude of G' clearly increases over all frequencies with increasing loading.

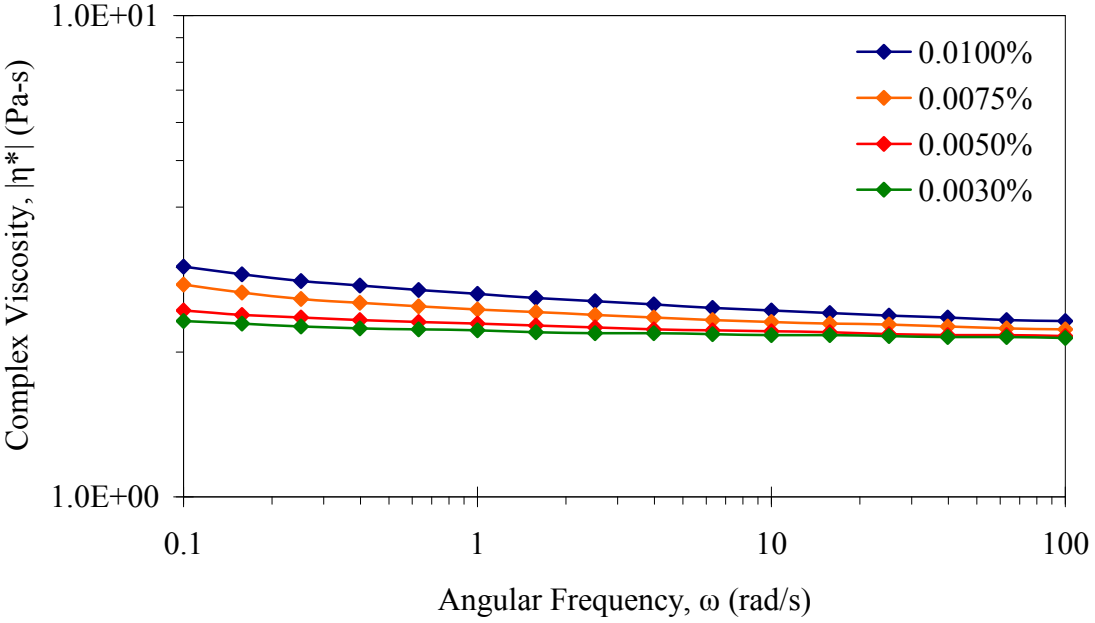

Figure 94: Complex viscosity from successive dilutions of SWNT 183.6 Pure dispersed in UPR.

Similar conclusions to Figure 93 can be drawn. The viscosity enhancement is minimal but consistently increases with SWNT concentration. Since the samples were created in succession their viscosities should be related directly to SWNT concentration. Equation 4.1 defines the reduced complex viscosity, $\left|\eta^*_{red}\right|$.

$$\left|\eta^*_{red}\right| = \frac{\left|\eta^*\right| - \eta_s}{\phi\eta_s} \tag{4.1}$$

Here, the neat solvent viscosity η_s is subtracted from measured complex viscosity $\left|\eta^*\right|$. and this quantity is then divided by the product of the solvent viscosity and volume fraction.

Figure 95 shows the reduced complex viscosity based on the data measured in Figure 94. For all measurements a solvent viscosity of 2 Pa-s was taken.

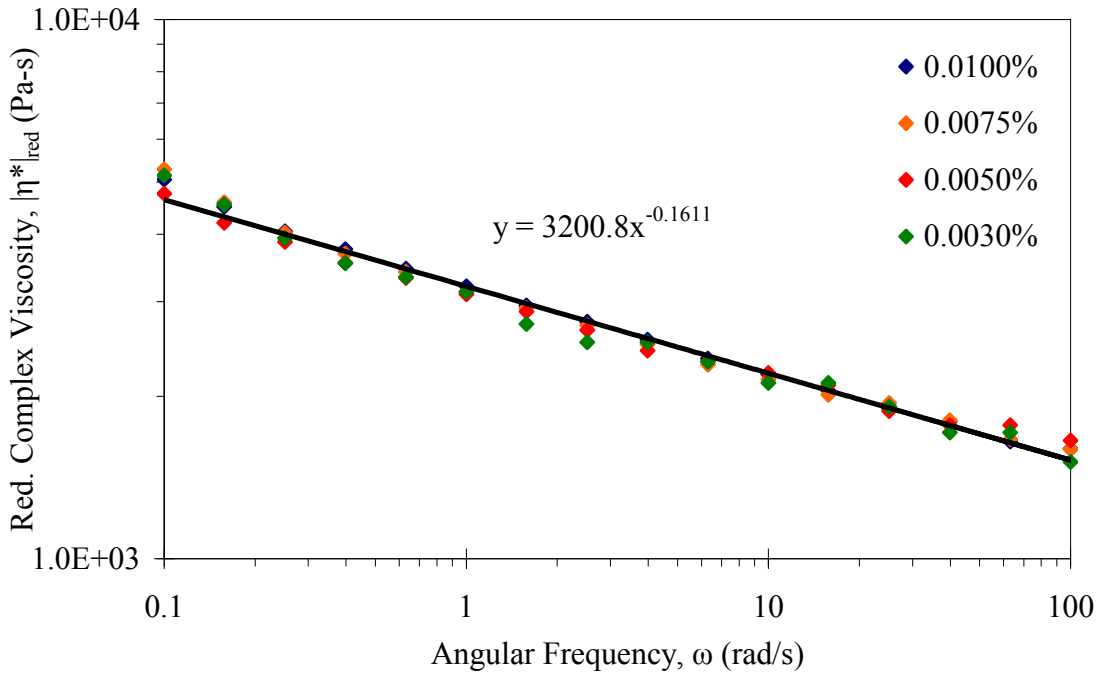

Figure 95: Reduced complex viscosity from successive dilutions of SWNT 183.6 Pure dispersed in UPR.

The slope of the reduced viscosity shown in Figure 95 was fit by regression. The low slope of the line indicates deviation from Brownian rigid-rod behavior [104]. Angular frequencies higher than 100 rad/s and lower than 0.1 rad/s were also examined to ensure that there were no transitions in the slope. Non-Brownian behavior can be confirmed by estimating the magnitude of the rotational Peclet number. Using Equation 2.65 for the dilute rotary diffusivity the Peclet number can be described by Equation 4.2.

$$Pe = \frac{\dot{\gamma}\pi\eta_s L^3}{3k_B T\left(\ln\left(L/d\right) - 0.8\right)} \tag{4.2}$$

Even with a conservatively small estimate for the mean contour length of only 1 μm, and using the hydrodynamic aspect ratio estimated from the divergence plot, the order of *Pe* is on the order of 10^1 at minimum. Thus, the imposed hydrodynamic forces of the rheometer are dominant and the sample shows non-Brownian behavior. This agrees with experimental evidence supporting this claim; ease of fiber shear alignment, long relaxation times, large dependence on sample history.

Shear-induced Aggregation:

It was originally desired to characterize the shear-rate dependent reduced viscosity for the dilute SWNT 183.6 Pure dispersions. However, upon start-up of flow from small shear rates a peculiar rheological response was observed. Figure 96 shows the shear rate dependant start-up curves for a 0.005% vol. dispersion. The viscosity trends up asymptotically when held at a shear rate of 10^{-3} 1/s over long shear duration. As a rule of thumb, the time required for start-up of flow under steady shear is approximately the reciprocal of the shear rate. For 10^{-3} and 10^{-2} 1/s the samples were

found to not reach a steady state over this time period. This behavior was assumed to be a result of sample aggregation. In addition, the application of higher shear rates appeared to breakdown any structure formed in the fluid. The existence of a critical shear rate or corresponding shear stress for dispersion of aggregates has been observed experimentally for a variety of systems. This critical stress is necessary to overcome the effects of both mechanical entanglement and particle attractive forces [107]. Chaouche and Koch (2000) first described this phenomenon in non-Brownian rigid fiber suspensions by means of a characteristic dimensionless number, taking the ratio of the viscous shear force to the adhesive contact force [204]. Indeed, this appears consistent with the current measurements. Additionally, shear aggregation has been seen previously for non-Brownian MWNT dispersions [84, 94].

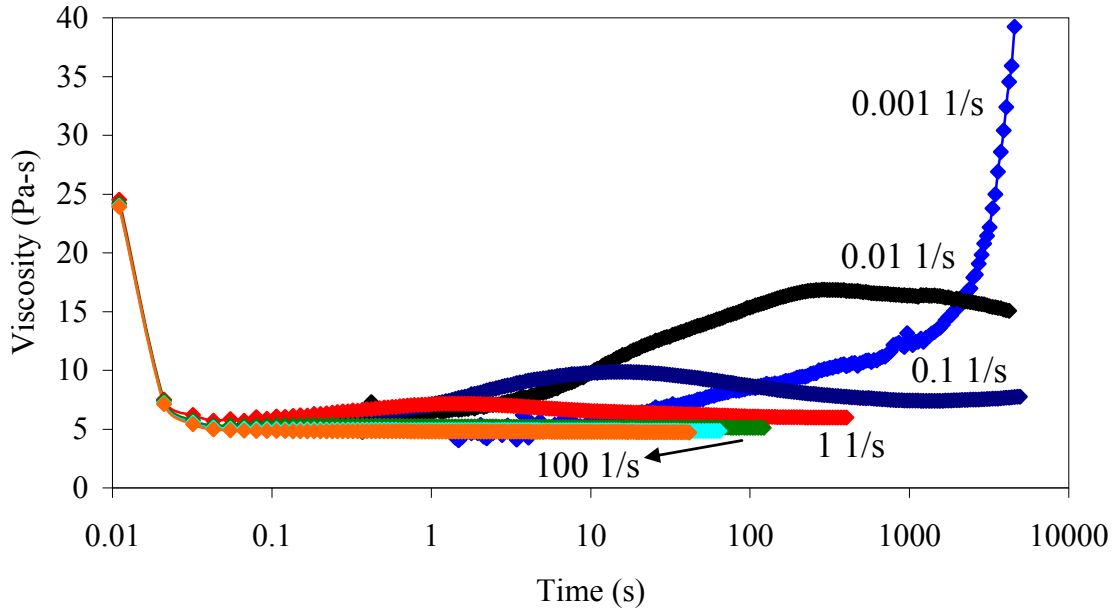

Figure 96: Shear rate dependant start-up of flow behavior for a 0.005% vol. SWNT dispersion.

Figure 97 clearly shows proof of the shear induced aggregation for a SWNT 183.6 Pure dispersion. The fact that this occurs on a length scale able to be seen by the naked eye was impressive. The samples were originally homogeneously black. Sufficient aggregation has occurred to create UPR rich areas. It is interesting to note that this specific sample is stable during storage in absence of shear, as discussed later.

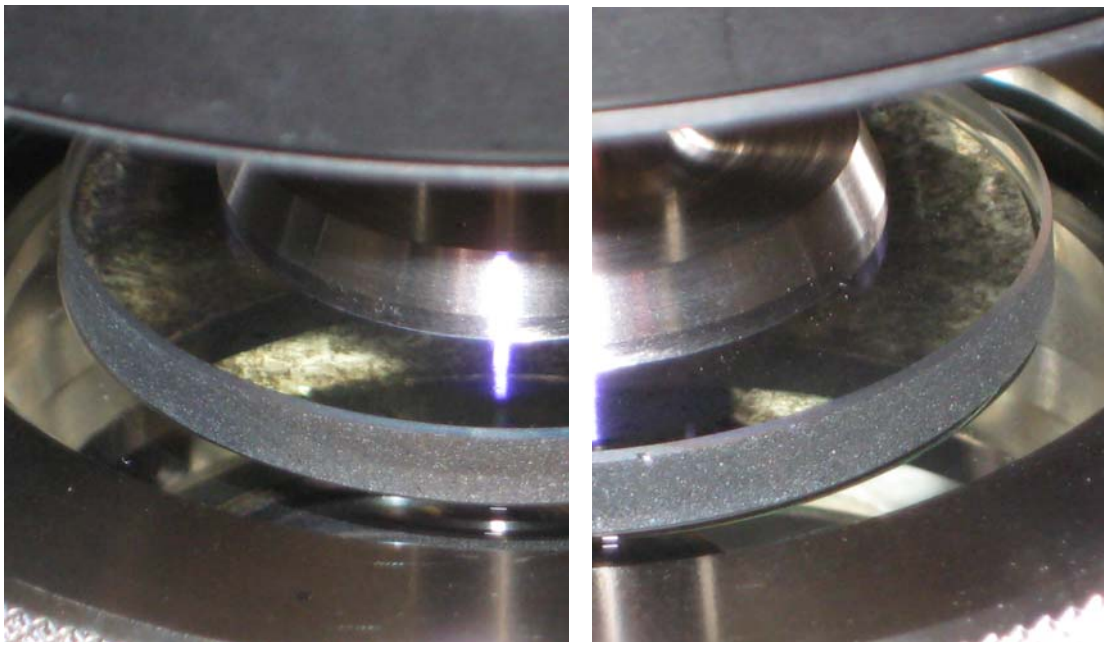

Figure 97: Images showing the transparency of 0.005% vol. purified SWNT 183.6 dispersion after treatment with a steady low shear rate of 0.01 1/s. The sample gap was constant at 0.685 mm.

The samples shown in Figure 97 were carefully extracted so as to not ruin the tenuous structure of the material. These were further characterized by optical microscopy as seen by Figure 98 - Figure 100. The samples show areas of varying concentration in a striated manner. The lighter parts of the image are thought to be SWNT depleted areas.

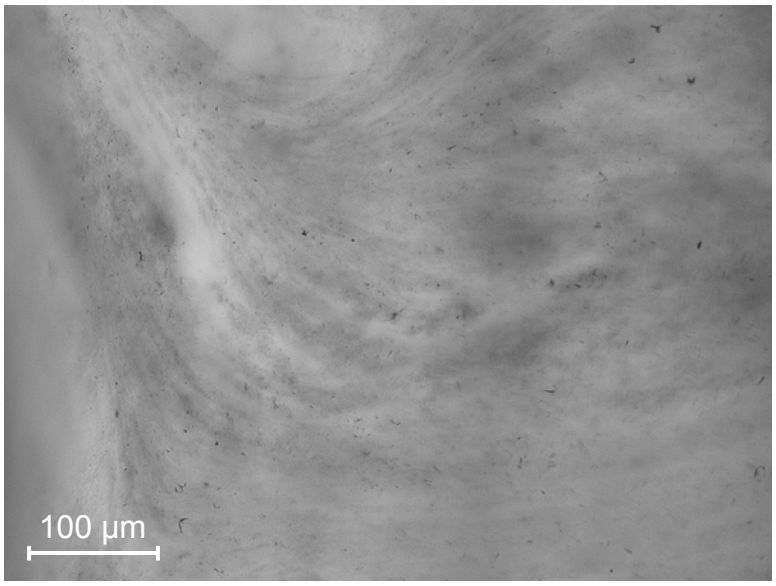

Figure 98: Sample from Figure 99 carefully transferred from the rheometer in its aggregated state to preserve the structure. Image taken with a 10x objective and 2x magnification.

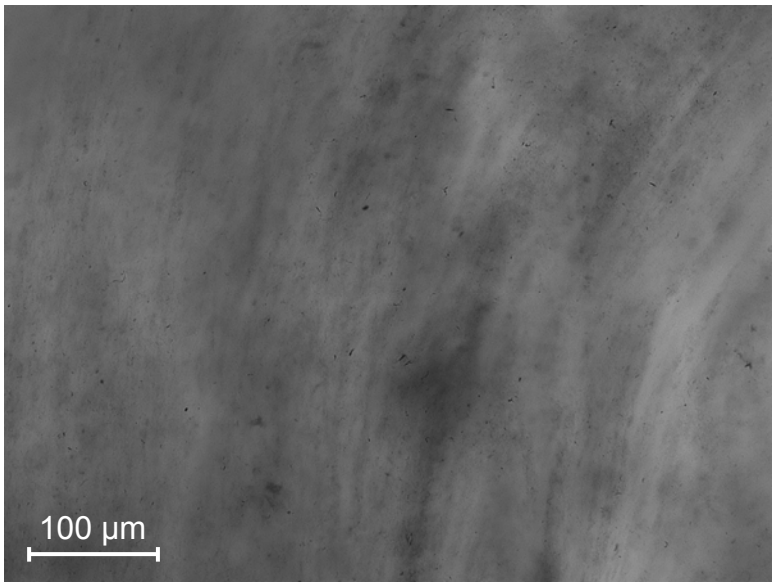

Figure 99: A second image taken at 10x2 magnification showing highly striated structure.

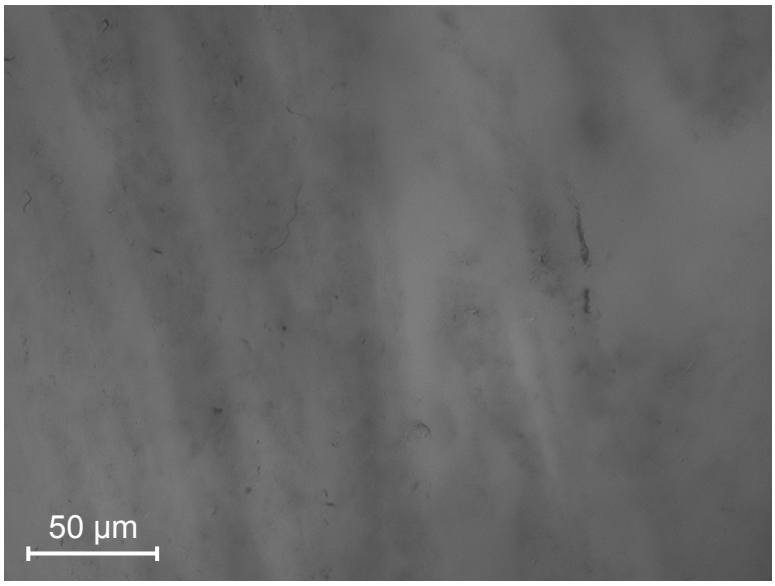

Figure 100: A closer image of the sample showing some diffuse structure. The image was taken with a 20x objective and 2x magnification in front of the camera.

Schmid et al. (2000) showed through simulation that flow-induced aggregation can occur in non-Brownian fiber suspensions as a result of fiber friction alone [110]. In order to determine if shear aggregation was a result of the initial dispersion state alone, the reduced viscosity of a separate SWNT sample was characterized. Figure 101 shows the reduced complex viscosity for a SWNT 187.3 dispersion. In comparison to the SWNT 183.6 Pure reduced complex viscosity shown by Figure 95, shear thinning was slightly less pronounced (lower slope) in this sample. Small discrepancies between the two SWNT dispersions may also be a result of error on initial concentration [104]. Regardless, the behavior of both samples are clearly not drastically different. Again, the data appears not to be in agreement with the theory for Brownian rigid-rods and serves to confirm non-Brownian behavior experimentally. Brownian rods show stronger shear thinning behavior as a result of tube buckling at higher elastic forces [104].

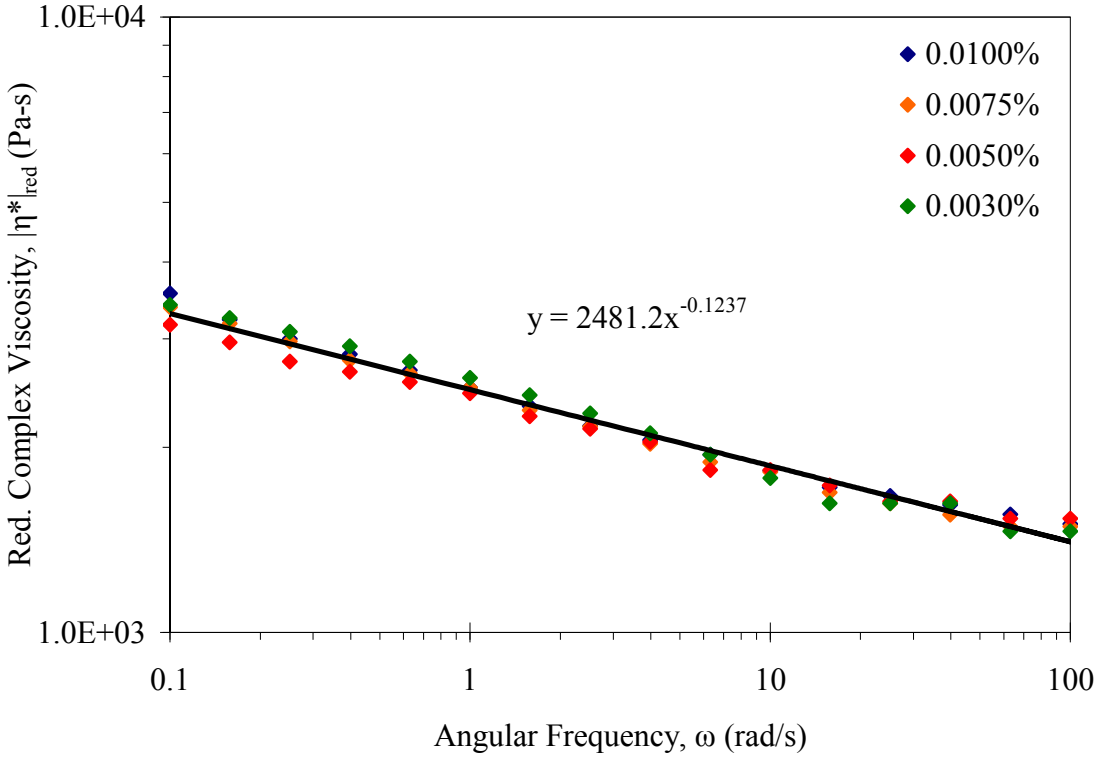

Figure 101: Reduced complex viscosity from successive dilutions of SWNT 187.3 dispersed in UPR.

In order to reveal the nature of the aggregation behavior a variety of SWNTs were studied. Figure 102 shows the start-up of flow for 0.005% dispersions of SWNTs at a constant shear rate of 10^{-2} 1/s. The rheometer geometry for all samples was a 50 mm cone and plate except where indicated for 183.6 Pure (PP43) where a 43 mm parallel plate was used. The sample gap was constant at 0.65 mm in the parallel plate geometry which was larger than the average gap in the cone and plate of 0.493 mm. In the cone and plate geometry both SWNT 183.6 and SWNT Unidym show indication of aggregation behavior. Although the kinetics involved in these two studies appears different a detailed study has not been performed. It is important to note that sample

SWNT 183.6 Unpure and sample SWNT 187.3 show no aggregation behavior. Since the comparison of the reduced complex viscosity failed to show marked differences between a sample which aggregates (183.6 Pure) and one which does not (SWNT 187.3) explanation was sought elsewhere. Specifically, the attention was turned towards characterizing the SWNT surface chemistry in each sample, as discussed in subsequent sections.

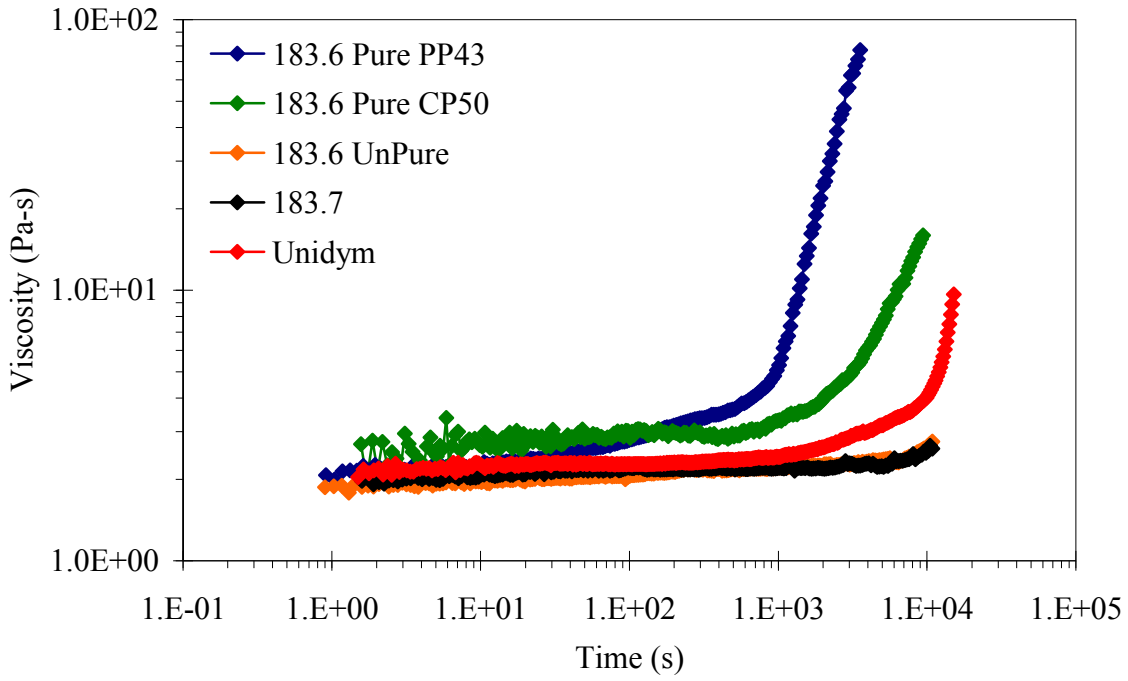

Figure 102: Comparison of start-up flow curves for different dilute CNT samples dispersed in UPR at 0.005% vol. The shear rate was constant at 0.01 1/s for all samples.

Figure 103 shows the effect of sample history on the start-up of flow for SWNT 183.6 Pure dispersions. The tests were run in the cone and plate geometry and the shear rate was carefully increased from low to high. It appears that in all cases the shear stress is below critical shear stress for dispersion of the aggregates since the final viscosity of

the previous run remains. In comparison to Figure 96, viscosity breakdown was seen at 0.1 s^{-1} previously. This is evidence of a "shear annealing" effect on the viscosity which again displays the importance on sample history for these dispersions.

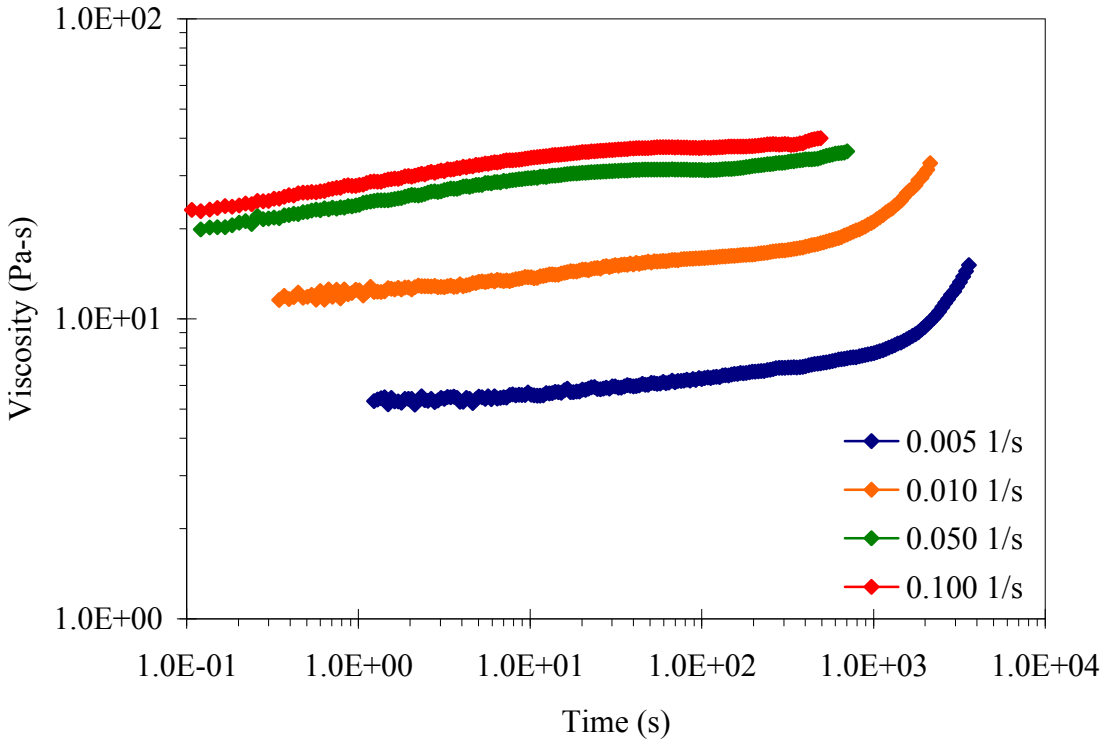

Figure 103: Comparison of start-up flow curves for different shear rates on dilute SWNT 183.6 Pure samples dispersed in UPR at 0.005% vol.

In addition to the cone and plate characterization, the SWNT 183.6 Pure dispersion was studied with variable sample gaps as well. These ranged from 0.674 – 0.344 mm in the SALS unit which has transparent quartz plates. While asymptotic rheological behavior consistent with sample "183.6 Pure PP43" in Figure 102 was observed for all samples, at the smaller gap of 0.344 mm evidence of an aggregated state was not visible with the naked eye. This suggested behavior similar to that of Lin-Gibson

et al. (2003) where the gap size was found to control the sample domain size [84]. Finally, to rule out edge drying as the cause for this viscosity rise a sample was loading at ~1/2 the required volume for the gap size. This prevented any sample from contacting the plate edges, while preserving the air/sample interface, but obviously lowered the measured viscosity signal since not all of the plate surface area was used. Again, the asymptotic behavior was seen consistent with other loadings.

Behavior at Rest:

The four SWNT samples used in Figure 104 were left to rest for weeks with our disturbance. Revisiting the samples showed an interesting behavior. Figure 106 displays an image of the sample vials after this rest period. What appears to be phase separation clearly appeared in three samples. Thus, in absence of shear the samples are only kinetically stable with exception to SWNT 183.6; the sample showing the strongest aggregation behavior. Conversely, and confusingly the two samples showing the most phase separation (183.6 Unpure & 187.3) appeared to be stable under the prolonged application of low shear, as shown by from Figure 102. One possible explanation for the stability of SWNT 183.6 Pure was revealed through TEM. After diluting this dispersion with acetone, applying low shear only, and allowing it to soak for a few days the sample dropped onto a TEM grid. Figure 105 shows a typical image observed. What is shown by the image is a large SWNT bundle coated with UPR even after washing. Therefore, it is possible that through depletion interactions, absorbed surface polymer is acting to keep the SWNT 183.6 sample stable over long time durations in storage. Absorption of

surface polymer is feasible since favorable π- π interactions between SWNTs and unsaturated bonds in UPR may exist.

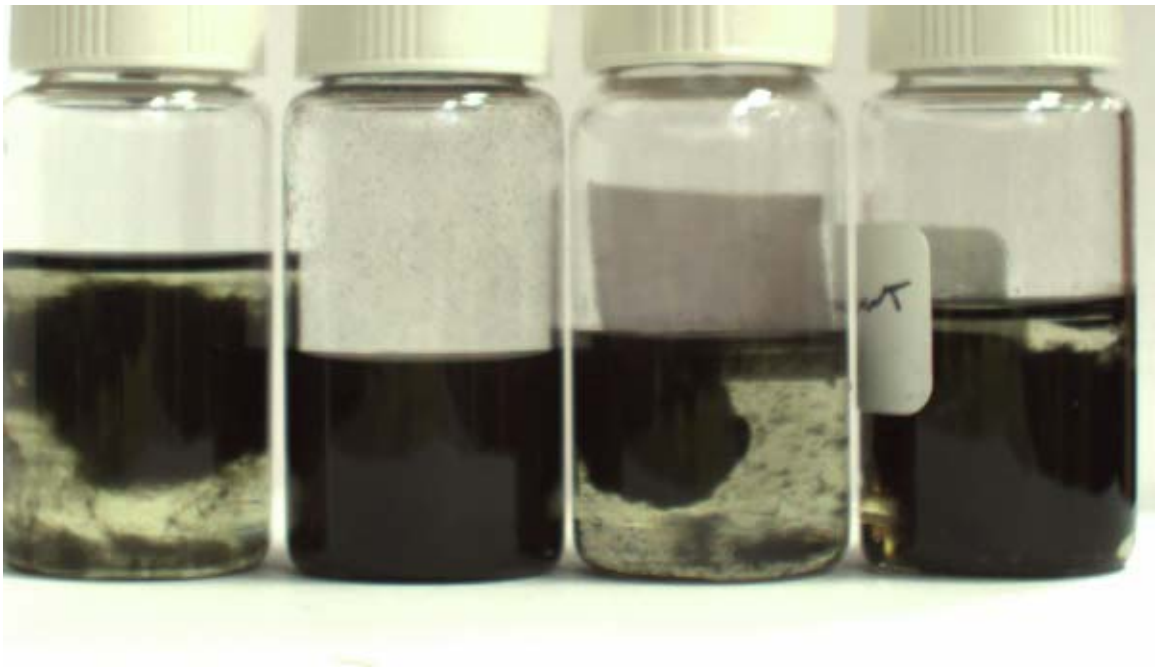

Figure 104: From left to right: 183.6 Unpure, 183.6 Pure, 187.3, and Unidym SWNTs. Only the purified 183.6 SWNT sample did not phase separate when left undisturbed. Timescale of observation was on the order of weeks.

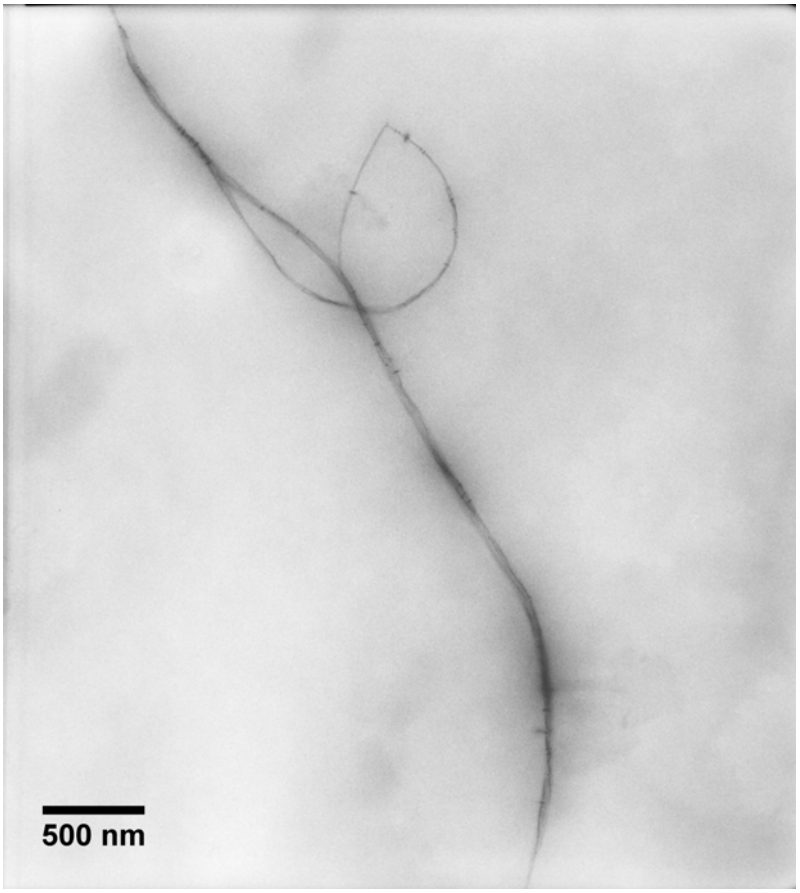

Figure 105: TEM image of a large SWNT bundle taken from a 250 ppm dispersion and diluted many times with acetone. The darker areas and low resolution is a result of adsorbed UPR remaining after the wash.

If, however, the sample was bath sonicated in acetone it was found that the polymer could be removed completely. Figure 106 shows such an image where the interstitial spaces in the SWNT bundles where solvent or polymer may have existed can be seen.

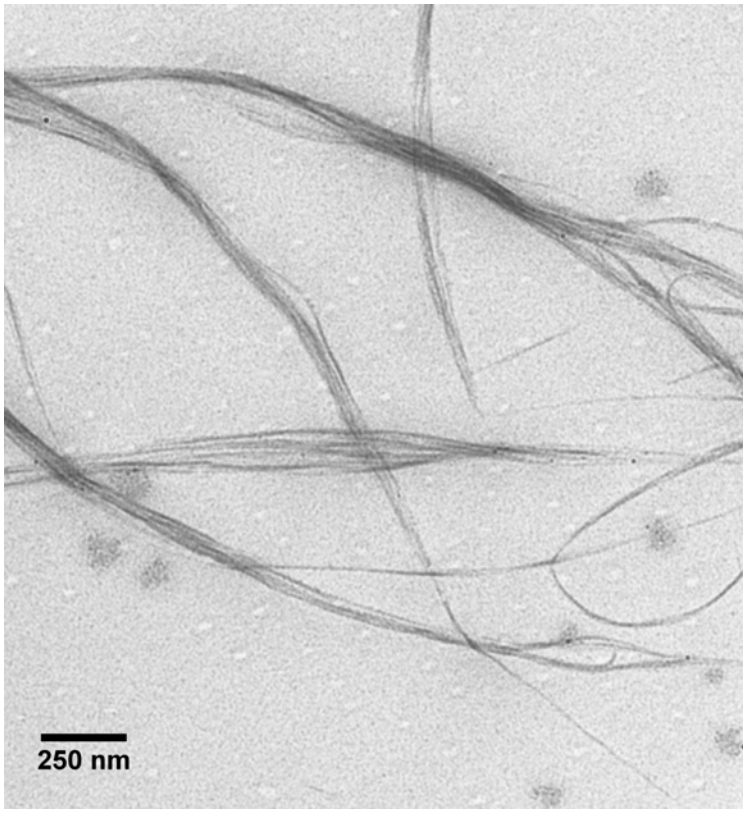

Figure 106: TEM image showing good removal of the UPR from the bundles revealing the interstitial space where solvent may reside. UPR removal was achieved by diluting the sample in acetone followed by 5 min. bath sonication.

Effect of Surface Chemistry:

In order to characterize the surface chemistry of the samples XPS analysis was carried out. Overall binding energy scans were first performed to reveal the relative atomic concentration on the SWNT surfaces. Figure 107 - Figure 110 display the results of these scans for samples 183.6 Pure, 183.6 Unpure, 187.3 and Unidym. All samples showed some trace contaminants such as sulfur, silicon, or tin. These were present in negligible amounts. The results of the overall scans reveal in intriguing trend in surface chemistry with shear aggregation behavior. The two samples which showed significant

aggregation behavior in start-up flow experiments were SWNT 183.6 Pure and SWNT Unidym. Both of these samples showed low surface oxygen content of ~1%. On the other hand, the two samples there were stable under low shear flow were SWNT 187.3 and SWNT 183.6 Unpure. Both samples showed significant surface oxygen content of 5% and 8%, respectively.

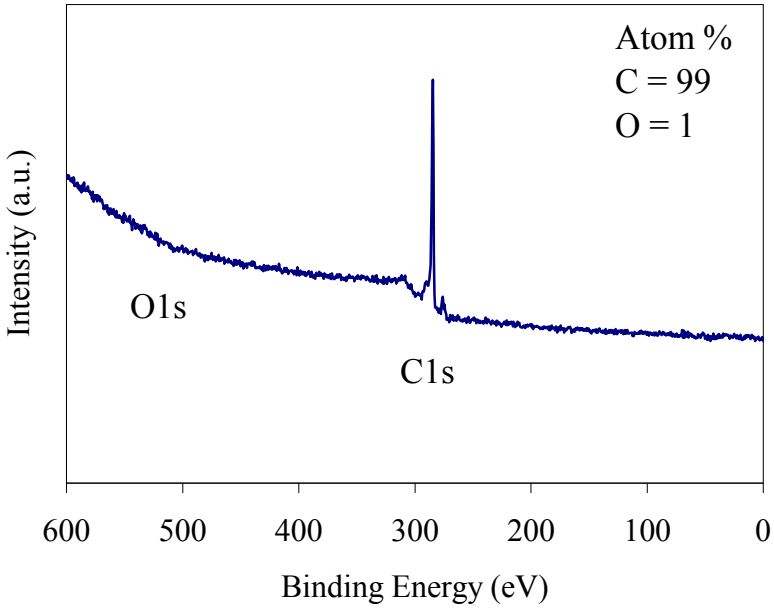

Figure 107: The XPS survey spectrum for SWNT 183.6 Pure. The main surface constituents were primarily C with little O content. Trace amounts of S was also observed.

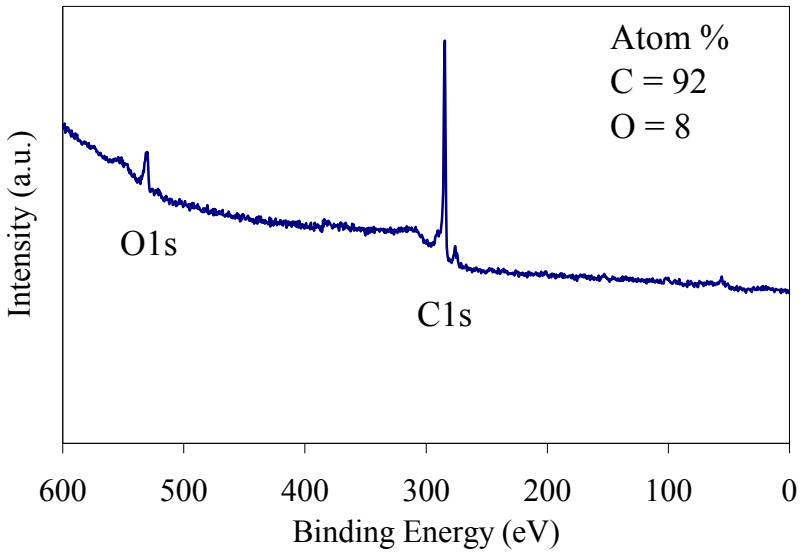

Figure 108: The XPS survey spectrum for the as-received SWNT 183.6 Unpure. The main surface constituents were primarily C and O. Trace amounts of Si was observed.

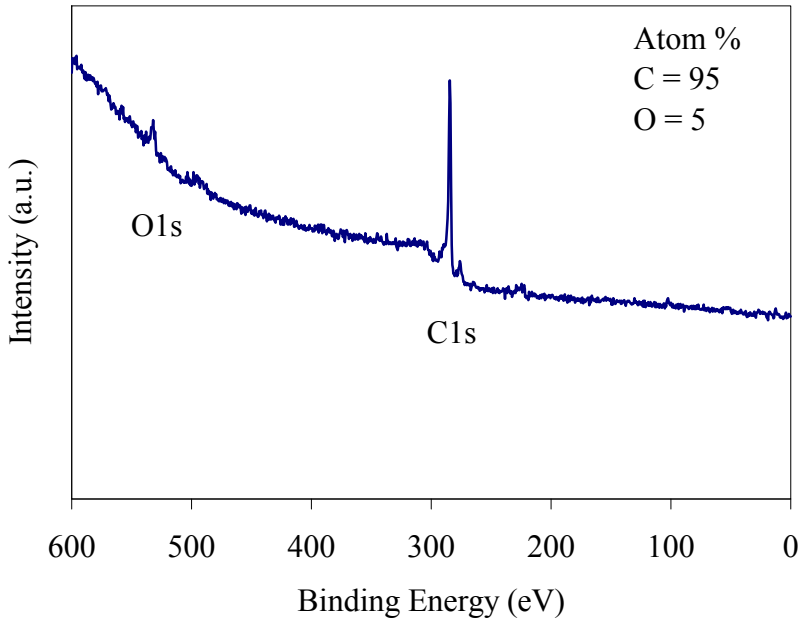

Figure 109: The XPS survey spectrum for SWNT 187.3. The main surface constituents were C and O but trace amounts of the elements Si, S, and Sn were also observed.

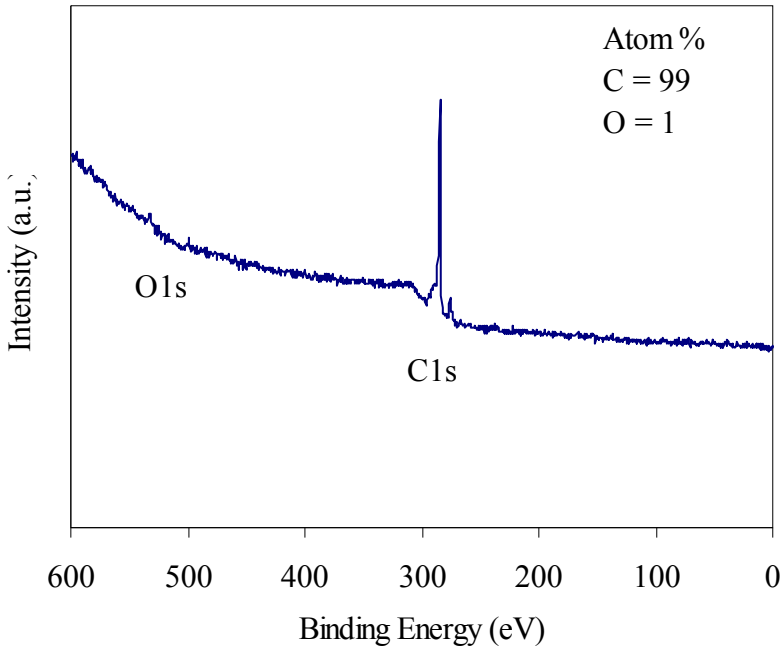

Figure 110: The XPS survey spectrum for Unidym SWNTs. The main surface constituents were primarily C with little O content. Trace amounts of the elements Si, S, and Sn were also observed.

To elucidate more detail about the types of surface functionalities were present in the samples, the high resolution C1s core election photoemission curves were compared. Figure 111 displays the C1s curves for similarly structured materials. Although overall XPS scans indicated sample 183.6 Unpure had a significant amount of surface bound oxygen, the C1s structure on the high energy side of the curve does not reflect this oxygen as bonded to carbon. This can be seen while examining the curves for SWNT 183.6 Pure and Unidym. Thus, it was concluded for SWNT 183.6 Unpure that the majority of the bound oxygen resides on the high percentage of residual catalyst (35% wt.) found in the sample by TGA and TEM experiments, described earlier. All samples could be deconvoluted (not shown in detail) to reveal a major relative concentration of

aromatic or aliphatic carbon at 294.6 eV and a minor peak at 286.3 eV representative of carbon bonded to a singular oxygen atom as in various hydroxl and phenolic groups.

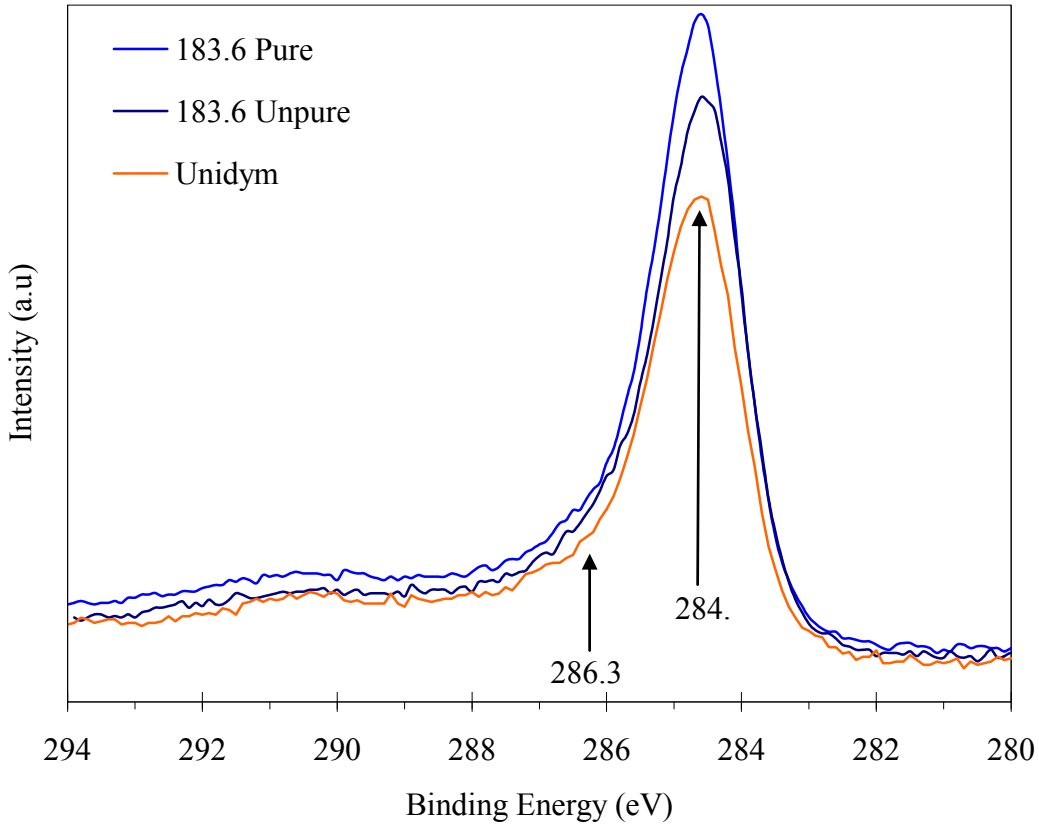

Figure 111: High resolution C1s curves for similar structured SWNTs.

Figure 112 displays the C1s curves for the samples found to have significant surface oxygen functionalities. Additionally, the curve for the 6h acid oxidized and lyophilized SWNTs was shown for contrast. Here, the high energy side (> 284.6 eV) of the C1s curve shows structure representative of oxygen containing functional groups bound to carbon. Both the oxidized SWNT and the as received SWNT 187.3 show hydroxyl and phenol groups (286.3 eV) as well as carbonyl carbons (287.7 eV). Additionally, SWNT 187.3 shows a significant shake-up satellite peak at 290.6 eV and

the oxidixed tubes show carboxylic functionalities at 289.1 eV. On the other hand, the high energy side of the unpurified SWNT shows little structure supporting the previous conclusion of the catalyst bound oxygen. While the purification method used on SWNT 187.3 was unknown, evidence suggests it was treated by a weak oxidizing agent such as nitric acid since hydroxyl and carbonyl groups are present but not carboxylic groups.

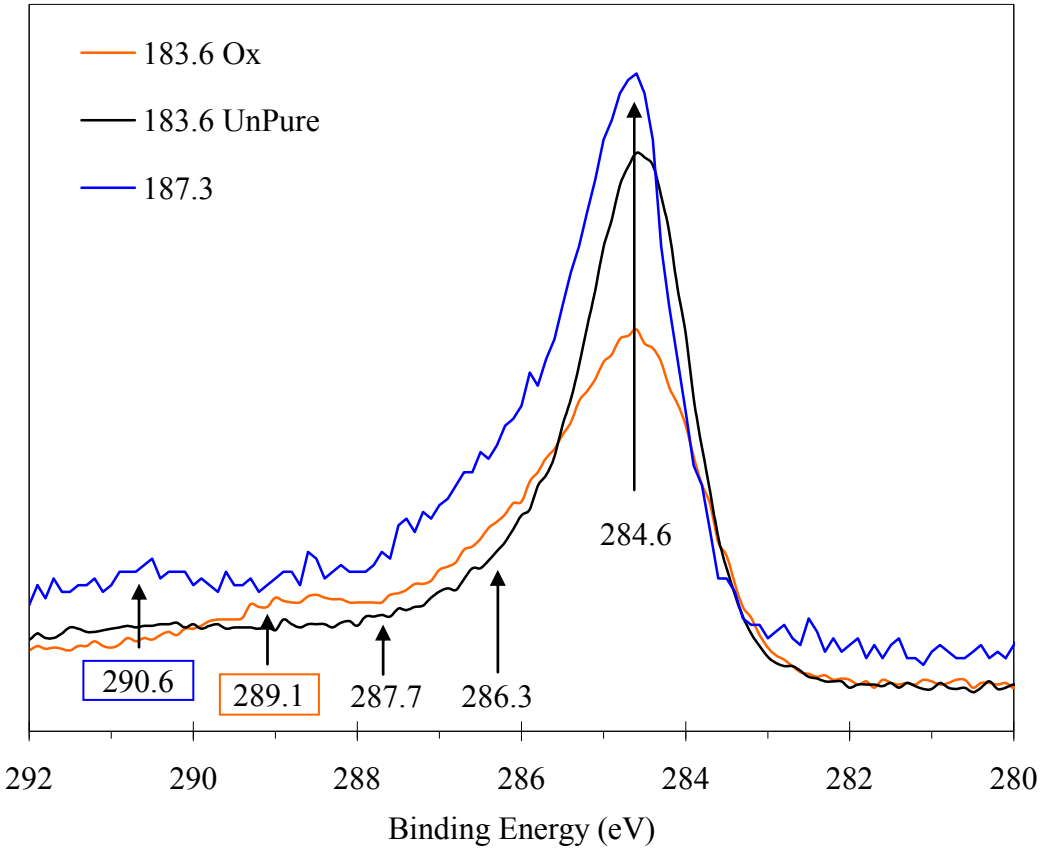

Figure 112: High resolution C1s curves for SWNTs with significant amount of surface bound oxygen as determined from the overall scans.

In summary, the stability of SWNT dispersions to shear aggregation appears to be correlated with the surface chemistry. Specifically, the type of oxygen containing functional groups appears to be important. In absence of significant amounts of surface

oxygen SWNT 183.6 and SWNT Unidym showed strong aggregation behavior. SWNT 183.6 Unpure showed stability but this was not attributed to surface bound SWNT oxygen. Instead, this was attributed to impurities such as residual catalyst and amorphous carbon material in the as-received sample. On the other hand, SWNT 187.3 appeared to benefit from surface bound hydroxyl and phenolic groups. These groups can be singled out because of the failure to form SWNT dispersions with carboxylic functionalized SWNTs shown previously. Additionally, the apparent compatibility of ethanol treated SWNTs with UPR, even in spite of previous oxidative treatment, supports the benefit from singular bound oxygen functionalities.

As a final means of supporting some of these conclusions Raman spectroscopy of the samples was carried out in order to determine the relative D-band to G-band peak intensity, an indication of sidewall defects or amorphous carbon. Figure 113 - Figure 116 display the sample spectra. The value of I(D)/I(G) for each laser wavelength is displayed above each representative laser spectra. From the Raman analysis, the fact that the value of I(D)/I(G) is nearly identical in SWNT 183.6 before and after purification confirms the hypothesis that surface bound oxygen identified in the unpurified sample was not SWNT bound. For the Unidym SWNT significant surface defects are present, but determined from XPS not terminated with oxygen functionalities. It is interesting to note that the magnitude of I(D)/I(G) was comparable between SWNT Unidym and SWNT 187.3, even though the two samples show different shear aggregation behavior. As listed in Table 1, Unidym SWNT showed a purity of 91 - 92% wt. while SWNT 187.3 showed approximately 92 - 93% wt. carbon. Additionally, comparision of the degredation curves in Figure 35 between the samples shows a markedly similar behavior. Therefore, this is

compelling evidence to rule out effects outside of surface chemistry, such as van der Waals retardation, in providing stability from shear aggregation. This also indicates for the Unidym sample, possible aggressive sonication as part of the purification process. On the other hand, for the SWNT 187.3, the value of I(D)/I(G) was supports chemical functionalization proposed previously from XPS analysis.

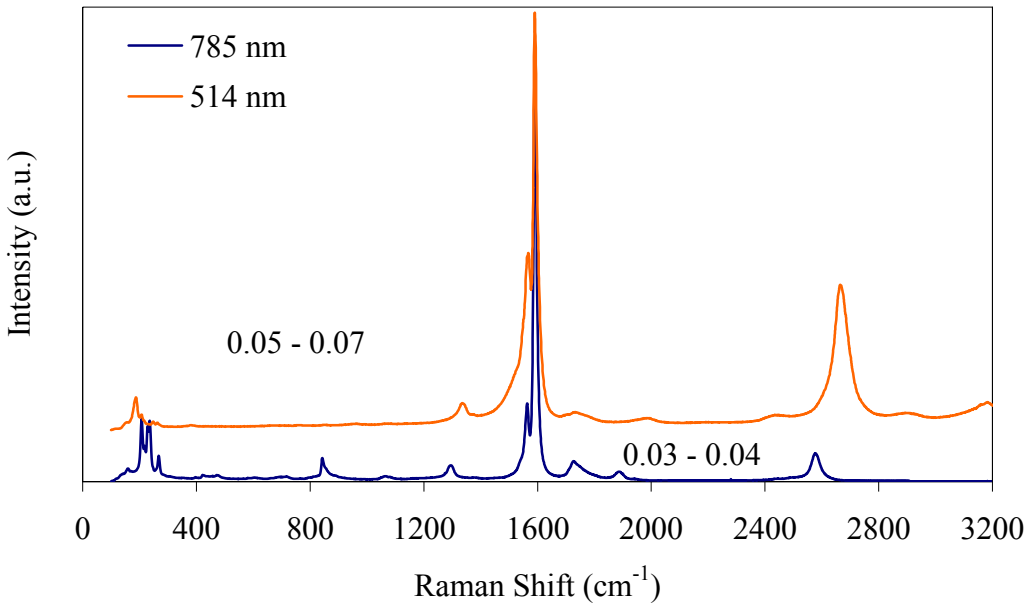

Figure 113: Raman Spectra at 514 nm and 785 nm excitation of the partially purified as-received SWNT 183.6 Unpure.

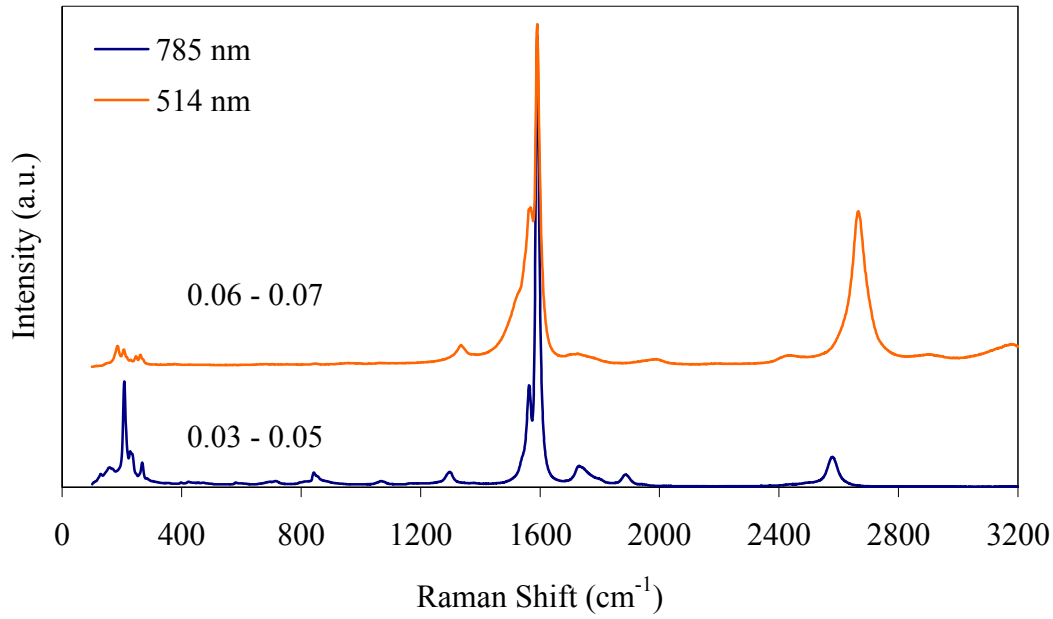

Figure 114: Raman Spectra at 514 nm and 785 nm excitation of the SWNT 183.6 Pure.

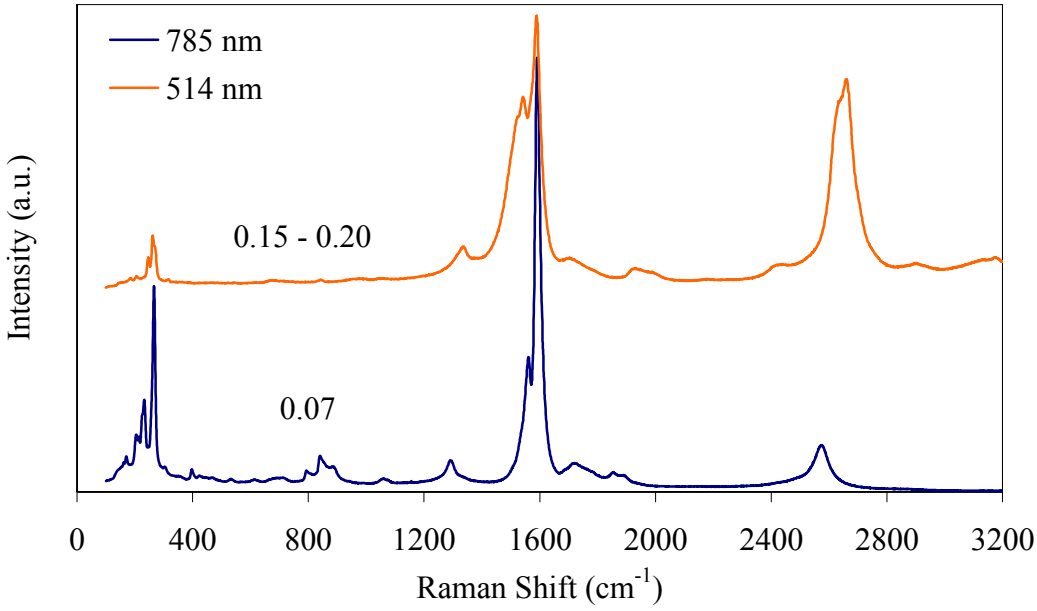

Figure 115: Raman Spectra at 514 nm and 785 nm excitation of as-received Unidym SWNT.

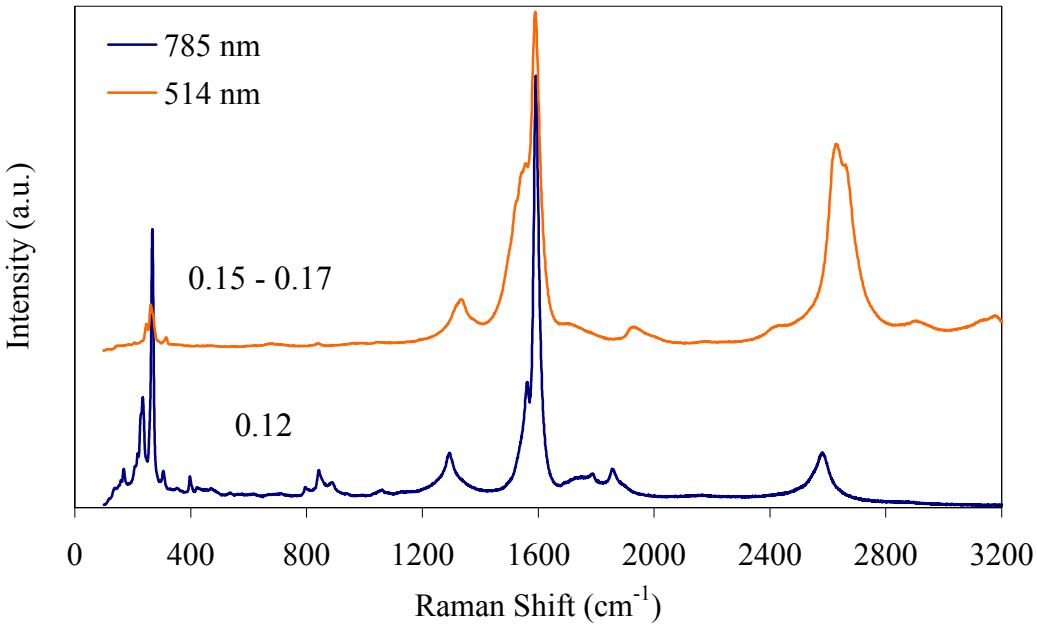

Figure 116: Raman Spectra at 514 nm and 785 nm excitation of as-received SWNT 187.3.

Proposed Chemical Functionalization:

Based on the results of the XPS and Raman studies, as well as on the dispersion behavior of carboxyl terminated SWNTs, a potential future functinalization strategy can be proposed. Figure 117 displays a general schematic for the progressive oxidation of CNTs. In accordance with the chemical analysis for various tubes, a successful oxidative treatment should be one in which significant singular bound oxygen groups are generated such as hydroxyl or phenolic functionalities. Furthermore, the oxidizing agent should not be strong enough to generate new carboxyl groups. Thus, in accordance with the theory of Zhang et al. (2003), the oxidizing agent should be effective in the defect consuming step but not in generation of new structures.

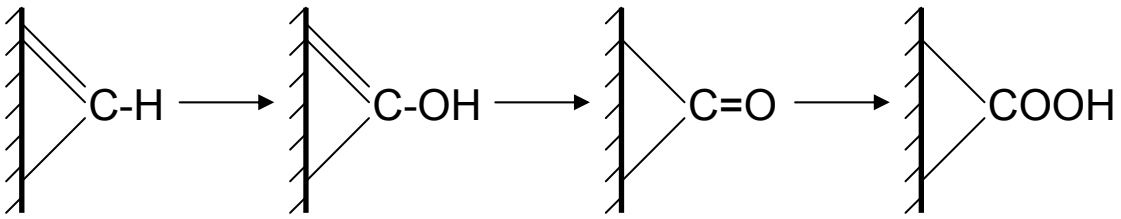

Figure 117: Progression of oxidation reproduced from Yue et. al (1999) [159].

Also, a hypothesis for the physical aggregation behavior between chemical functionalities can be proposed. The inability of the carboxylic terminated SWNTs to form dispersions in UPR is likely a result of the conjugate base lacking the ability to associate with the isophthalic resin backbone through hydrogen bonds. The fact that SWNTs are added in dilute concentrations helps facilitate dissociation of acidic hydrogens to the bulk solvent. Conversely, phenolic and hydroxyl groups retain their acidic hydrogen and may form associative bonds along the isophthalic and ester linkages.

Dispersion Thermodynamics:

In order to determine whether dissolution of SWNTs in UPR is thermodynamically favorable the enthalpy of mixing per unit volume was first estimated ed by Equation 4.3.

$$\frac{\Delta H_{mix}}{V_{Mix}} \approx 2\frac{\phi}{R_2}\left(\delta_{NT} - \delta_{Sol}\right)^2 \tag{4.3}$$

As stated in Chapter 1, the surface solubility parameters are represented by δ_i, the volume fraction of CNT by ϕ, and the bundle radius by R_2. The component surface energy E_{Sur}^i was used to find δ_i, as defined by Equation 4.4.

$$\delta_i \approx \left(E_{Sur}^{i}\right)^{1/2} \tag{4.4}$$

Here the surface interaction energy was approximated by Equation 4.5.

$$E_{Inter}^{NT-Sol} \approx \left(E_{Sur}^{NT} E_{Sur}^{Sol}\right)^{1/2} \tag{4.5}$$

The approximation introduced by Equation 4.5 allows the surface solubility parameters δ_i to be estimated from the pure component interaction energy using Equation 4.5. Specifically this is due to formulating the binomial term of Equation 4.3 which has reduced any dependence on E_{Inter}^{NT-Sol}; an approximation yet to be addressed in literature for nanotube-solvent systems. This is similar to how van Laar and Lorenz (1925) approximated the interaction between dissimilar molecules using the geometric mean. Hildebrand and Scott (1950) subsequently argued that this approximation fails to describe interactions outside of nonpolar molecules [205]. In the present case this introduces serious consequences into the approximation. First, calculating the surface interacting energy by Equation 4.5 results in multiple answers; a positive and negative interaction energy representing an attractive and repulsive term, respectively. However, introduction of Equation 4.4 to calculate the surface solubility parameter requires the attractive (positive) term be chosen as calculation of δ_{NT-Sol} since the repulsive (negative) term is undefined. Taking the attractive term alone, and thus neglecting any repulsive interactions, limits the ability of Equation 4.3 to account for specific interactions between dissimilar molecules. Furthermore, the general form of Equation 4.3 prevents determination of exothermic heats of mixing. Specifically, this neglects the subtle nuances between dissimilar molecules as predicted by what is know as the "Taft and Hamlet" scale for hydrogen bond donor ability [206]. Ausman et al. (2000) have used

the Taft and Hamlet scale to investigate SWNT solvents and concluded that the best solvents for SWNTs are non-hydrogen-bonding Lewis bases [207]. This conclusion indicates that good solvents have the ability to donate an electron pair to the SWNTs but cannot associate through hydrogen bonding; two factors that are entirely dependant on solute–solvent interaction. In this work, the effects of subtle differences in nanotube surface chemistry were also experimentally shown. Thus, the kinetics of the shear aggregation behavior could be correlated with the magnitude of the Gibbs free energy of mixing using this theory. Lastly, it is important to note the original geometric approximation by van Laar was for molecules of comparable size. With a nanotube-solvent system there are certainly many solvent molecules interacting with a single tube.

Neglecting the aforementioned shortcomings, the solvent surface energy E_{Sur}^{Sol} can be related to the solvent surface tension γ by means of Equation 4.6 [208].

$$\gamma = E_{Sur}^{Sol} - TS_{Sur}^{Sol} \tag{4.6}$$

Here the T is the thermodynamic temperature and S_{Sur}^{Sol} represents the solvent surface entropy. It has been argued that the solvent surface entropy is a generic property of liquids and can be approximated as 0.1 mJ/m^2-K [176, 208]. Thus, the value of E_{Sur}^{Sol} can be approximated by Equation 4.6. For UPR the surface tension was directly measured to be 34.85 mJ/m^2. Over a range of temperatures from 293–298 K the value of E_{Sur}^{Sol} for UPR was calculated to be 64.4 mJ/m^2. This is on the same order as the graphitic surface energy estimated to be 70 mJ/m^2 but no criteria has been established as to how closely these values should match in "good" solvents [176]. By means of Equation 4.4 the surface solubility parameter δ_{Sol} can be calculated to be 8.02 mJ$^{1/2}$/m. To calculate the

nanotube surface energy E_{Sur}^{NT} the widely accepted binding energy for "real" SWNTs of ~0.5 eV/nm was used [54, 71]. However, E_{Sur}^{NT} is the binding energy per surface area. An approximation was made to translate the energy acting over a length into the corresponding surface area. Considering the binding energy over a 1.0 nm diameter tube with 1.0 nm length the value of E_{Sur}^{NT} was calculated to be ~51 mJ/m^2. The surface area for only one tube was calculated (1.57x10^{-19} m^2) since the interactions in a bundle have been previously restricted to nearest neighbor interactions [69, 72, 73]. Again, by means of Equation 4.4 the surface solubility parameter for SWNT δ_{NT} was calculated to be 7.14 mJ$^{1/2}$/m. In comparison, if the intertube binding energy theoretically calculated for two (*10*,*10*) tubes of 0.9516 eV/nm is used, the surface solubility parameter δ_{NT} can be as high as 9.84 mJ$^{1/2}$/m [69]. The heat of mixing per unit volume can then be estimated from equation 4.3. To estimate this quantity conservatively the volume fraction was taken as one of the lowest used in experiments, 5.0 x 10^{-5} (0.005 % vol.). The bundle radius R_2 was estimated from TEM images was taken to be on the order of 10^1 nm. Solving Equation 4.3 the heat of mixing per unit volume for SWNTs having a binding energy of ~0.5 eV/nm was approximately +15.5 kJ/m^3. In comparison, Bergin et al. experimentally determined SWNTs in NMP, a "good" solvent, to have a heat of mixing on the order of -1,882 kJ/m^3. It is assumed that with increasing concentration the bundle size will either remain the same or increase, dependant on the mixer. Thus, the enthalpy of mixing will also increase with the same order of magnitude that as an increase in volume fraction. Therefore, at one of the highest volume fraction used in this research of 0.200% vol the heat of mixing can be expected to increase as high as

+620 kJ/m^3. The positive heat of mixing is in agreement with what has been generalized for most polymer-nanotube mixtures [165]. Morawetz (1983) argued that endothermic mixing high molecular weight polymers with solvents is possible only because of the conformational entropy gained by flexible chain molecules in the process of dilution [205]. It can be expected that this statement would be more critical when SWNTs are substituted for polymers since their rigidity decreases chain conformation. The calculated heat of mixing would agree with this statement. Re-examining the criteria for dissolution based on the Gibbs free energy of mixing some insight to the magnitude of the entropy of mixing can be gained. Rearranging Equation 2.29 the criteria for the entropy of mixing upon dissolution is shown by Equation 4.7.

$$\Delta S_{Mix} > \frac{\Delta H_{Mix}}{T} \tag{4.7}$$

For room temperature of approximately 295 K the entropy of mixing at 0.05% vol. must actually be less than 52.5 J/m^3 since experimentally thermodynamic dissolution is not likely to occur. This small positive value for the entropy of mixing is in agreement with experimental dispersion observations and therefore is not large enough to drive dissolution itself. Therefore, although the theory may have made gross assumptions regarding interaction, thermodynamic analysis of SWNT-UPR systems is in agreement with experimental observation. The dissolution of SWNTs into UPR is only kinetically stable with de-mixing driven by the positive Gibbs free energy of mixing. This is a consequence of the dissimilarities in the UPR and SWNT surface energies but can be tuned by adjusting the SWNT interface through functionalization.

Finally, if the heat of mixing is examined without making any assumptions towards the solute-solvent interaction energy some general conclusions about successful solvents can be drawn. Equation 4.8 is displayed below.

$$\Delta H_{mix} \approx 2\frac{m_{NT}}{R_2 \rho_{NT}}\left[E_{Sur}^{NT} + E_{Sur}^{Sol} - E_{Inter}^{NT-Sol}\right] \tag{4.8}$$

Clearly, the heat of mixing can be minimized if the functionalization results in an increased association between the SWNTs and the solvent, which would represent an increased value of E_{Inter}^{NT-Sol}. Also, the effect of functionalization on the intertube van der Waals potential is reflected by E_{Inter}^{NT}. This should be reduced to minimize the heat of mixing. Research in estimating the contribtion of the solute–solvent interaction would be extremely beneficial to the field.

Self-assembly of SWNT Films:

The intent of studying the effect of oxidation and lyophilization on SWNT 183.6 Pure was to eliminate the bundled sample morphology caused by filtration as well as provide a chemically characterized sample. While this technique was successful in satisfying these tasks, the low bulk density shown previously in Figure 63 is misleading if only examined by the naked eye. In fact, when studied under SEM the 6h acid oxidized and lyophilized SWNTs reveal a remarkable aligned morphology. Figure 118 shows a low magnification image of the sample simply collected from the bulk product shown in Figure 63. This sample was not intentionally cast as a film but self–assembled during lyophilization. The film appears to be transparent to electrons. The edge of this film in Figure 118 was further examined under higher magnification to reveal the discovery of a

high degree of nanotube alignment shown in Figure 119. The black arrow is intended to represent the director of alignment. At the film edge bundles or individual SWNTs can be seen extending with the director. What is import to grasp is the order of magnitude this alignment occurs on. According to the scalebar the alignent is on tens of nanometers, which is truly remarkable in comparison to the current state of the art of aligned SNWT films.

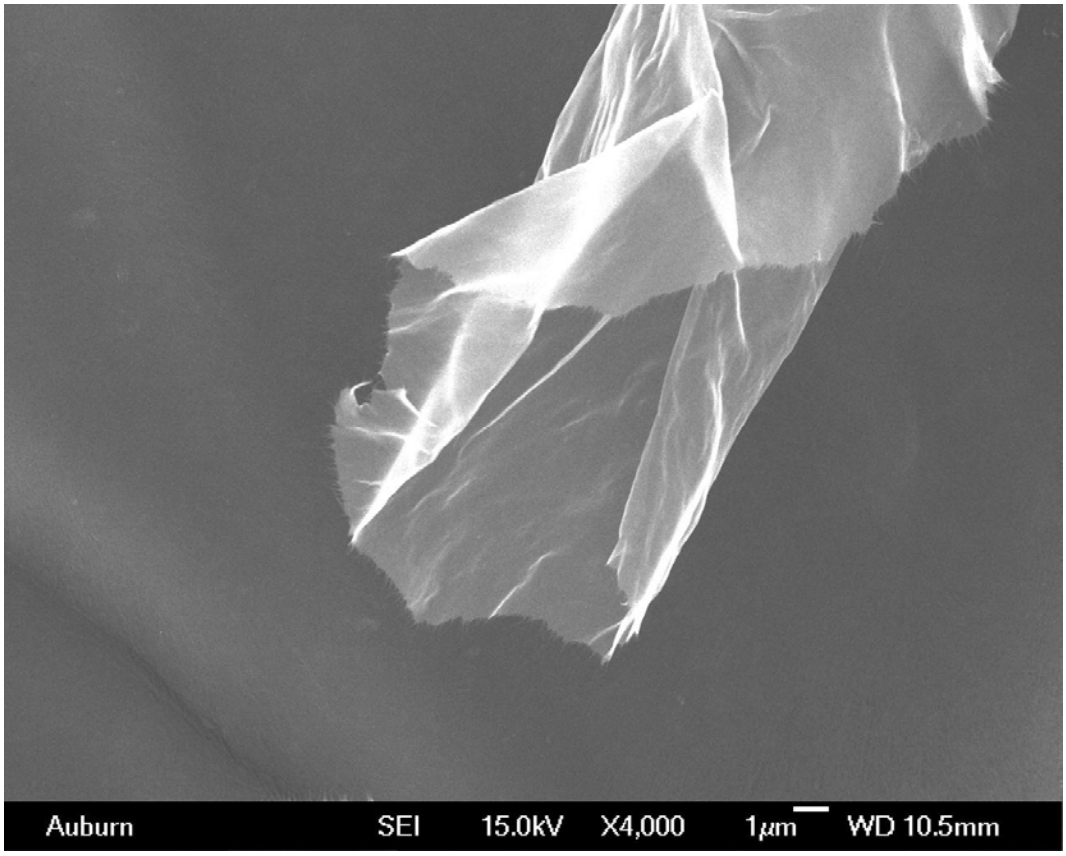

Figure 118: A lyophilized film of the 6h acid oxidized SWNTs.

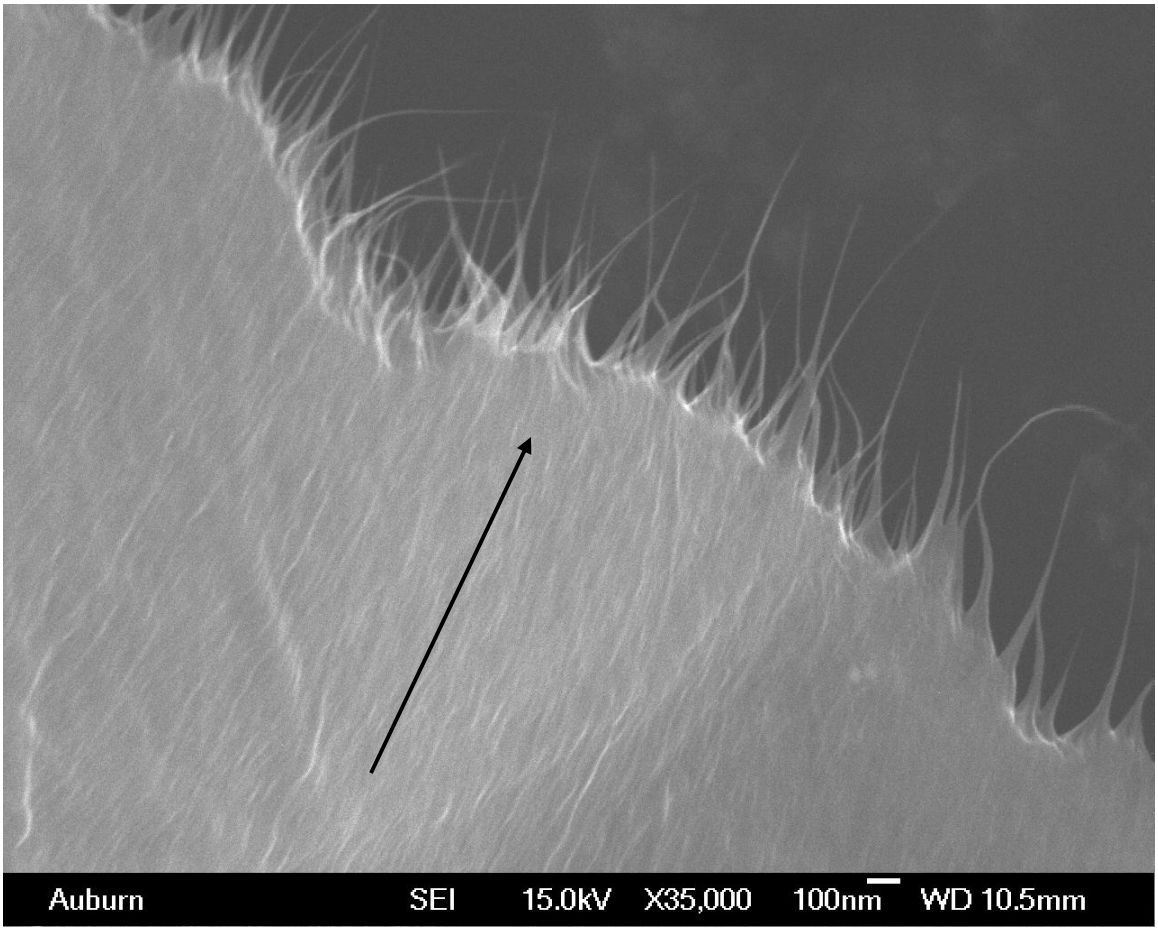

Figure 119: Close up view on the edge of the film shown in Figure 118. A high order of alignment can be seen even on the nanometer scale.

The as-produced films were also examined under optical microscopy indicating their transparency to light. Figure 120 shows a piece of the film where light appears to transmit in certain areas. Examining Figure 121 the ability of the entire film to transmit some light as can be seen by the increase in opacity on the folded corner. It is important to note that no attempt has been made to template these structures.

Figure 120: Optical microscopy image of a piece of lyophilized 6 h acid oxidized SWNT film. The film was held between a cover glass and imaged at 10x magnification.

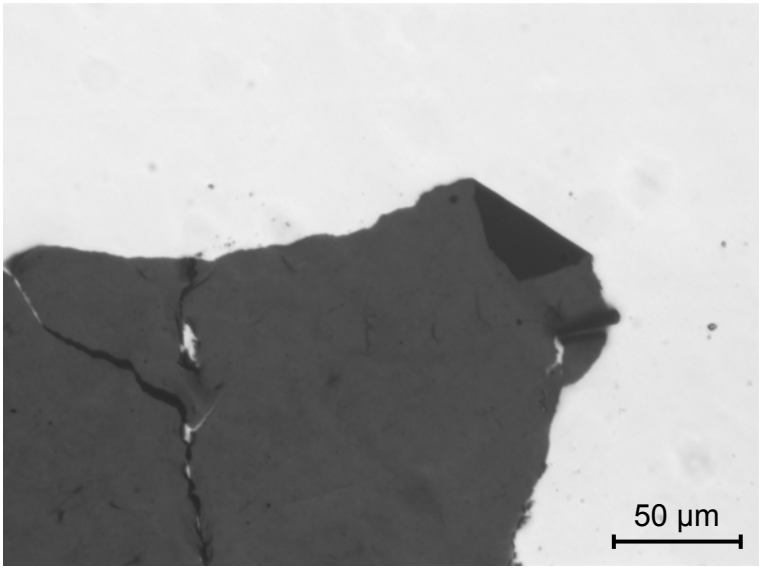

Figure 121: Optical image of a bulk 6 h acid oxidized and lyophilized SWNT film. The sample was affixed to double sided adhesive tape and the image was taken with a 20x objective and 2x magnification in front of the camera.

The effect of oxidation treatment time was also studied. Figure 122 shows the resulting samples after only 2 h of oxidation. Even at low magnification the sample does not appear to be as finely structured as the 6 h treated sample. Figure 123 shows a higher magnification of the film edge displayed in Figure 122. In comparison to the 6 h oxidized sample, the 2 h sample appears highly bundled and isotropic. Furthermore, these bundles exist on approximately an order of magnitude larger length scale than the 6 h sample. A transition from a bundled to a more aligned state was previously described by Rosca et al (2005), as mentioned in Chapter 1 [124]. This was described by an increase in sample mobility by tube disentanglement and cutting, which is also true in the preset case. Additionally, the alignment can be explained by the increase in functional groups over the course of the reaction as well as an increase in mobility from digestion of small diameter tubes.

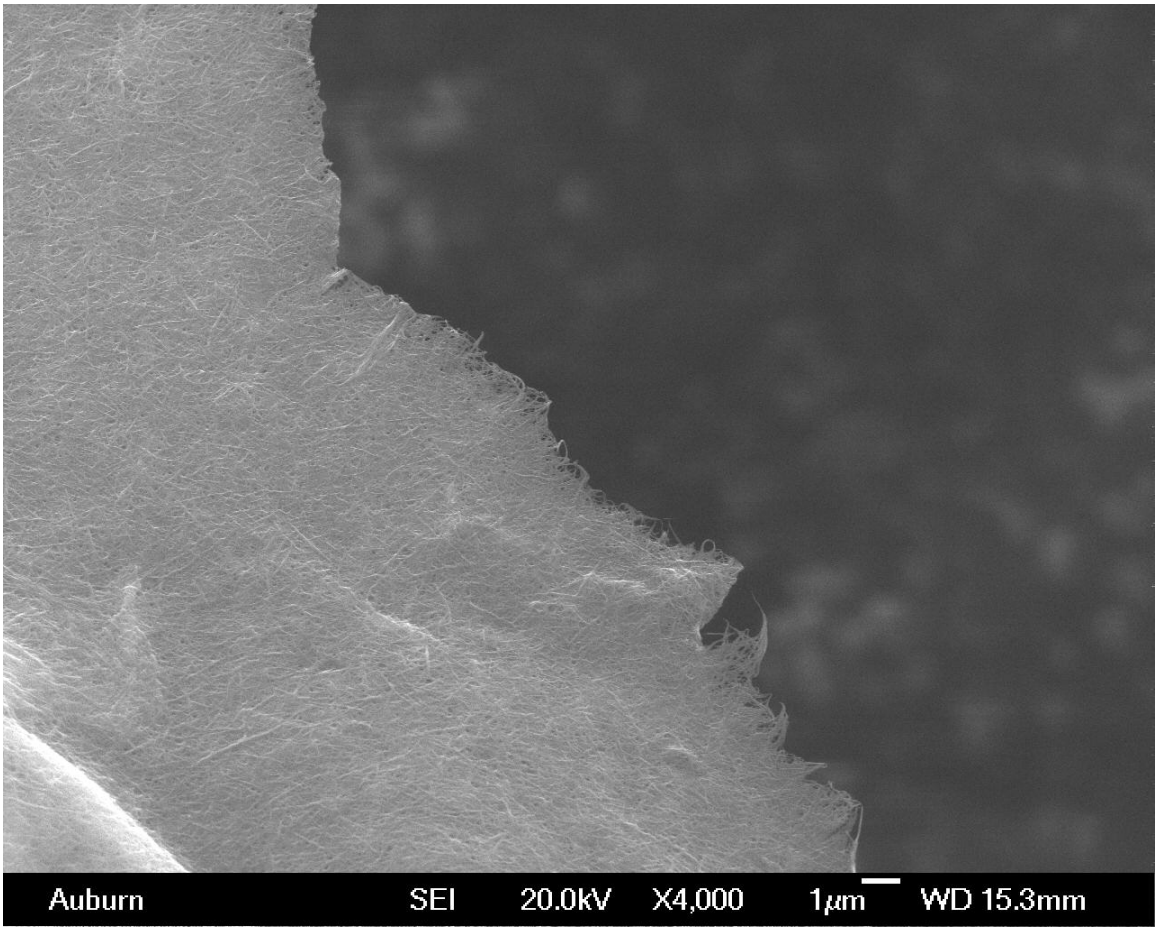

Figure 122 : SEM image of a 2 h acid oxidized SWNTs after lyophilization.

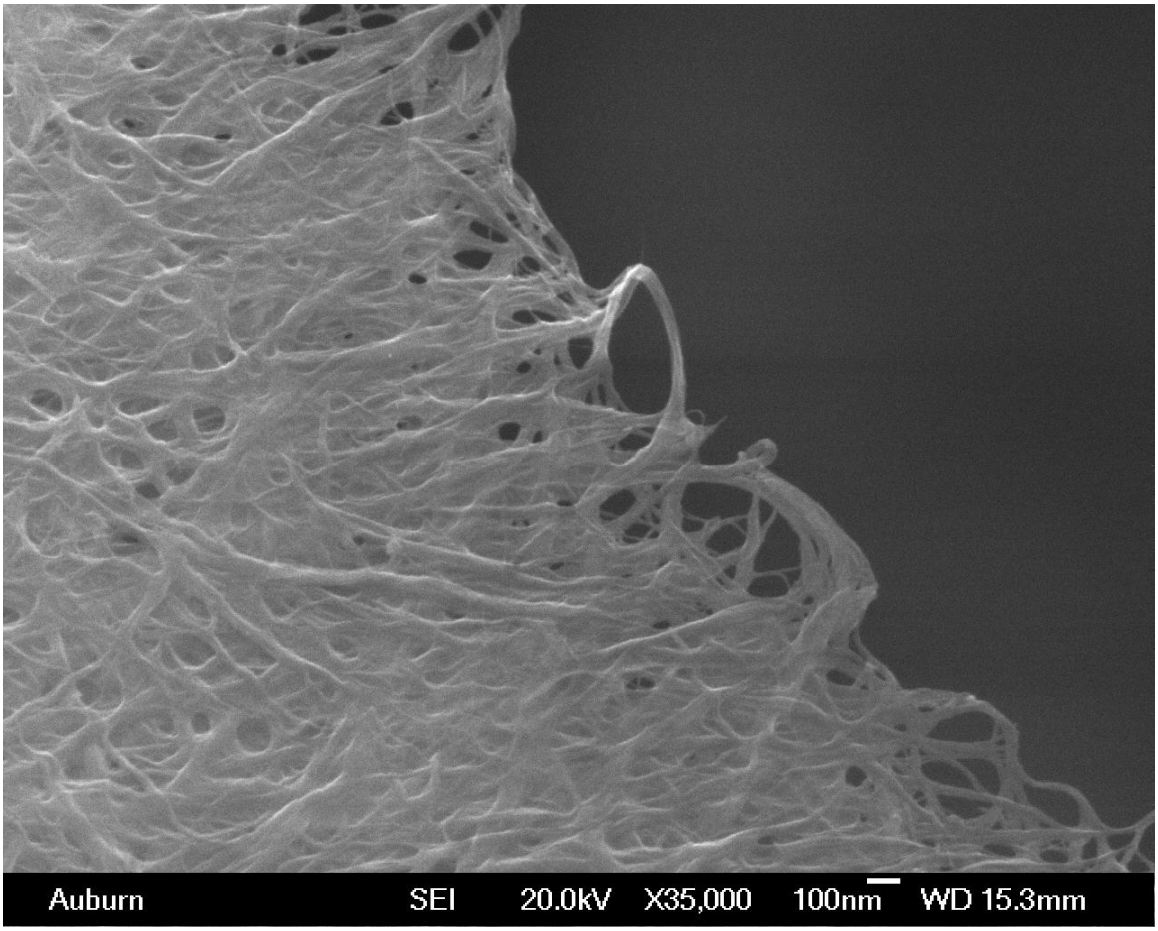

Figure 123: Close up image of the 2 h acid oxidized SWNTs after lyopholization.

To correlate the degree of functionalization and cutting with time, Raman spectroscopy on both samples was carried out as shown by Figure 124 and Figure 125. The results of the Raman study indicate an increase in I(D)/I(G) with treatment time of almost three fold indicating the presence of significant defect generation to the sidewalls, tube end defects, or the generation of amorphous carbon.

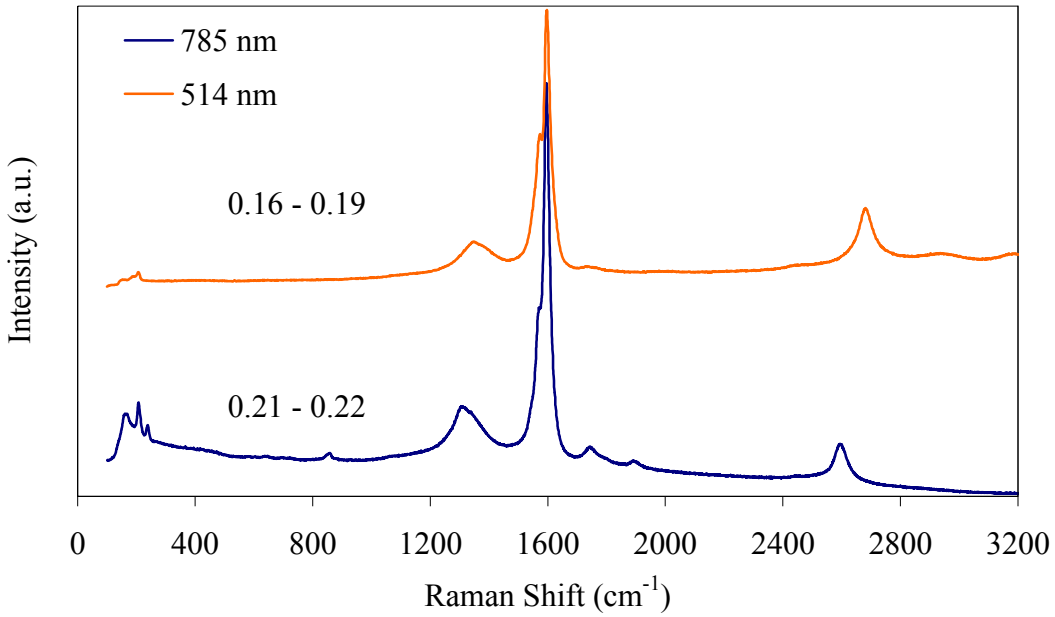

Figure 124: Raman Spectra of SWNTs after 6 h acid oxidation and lyophilization.

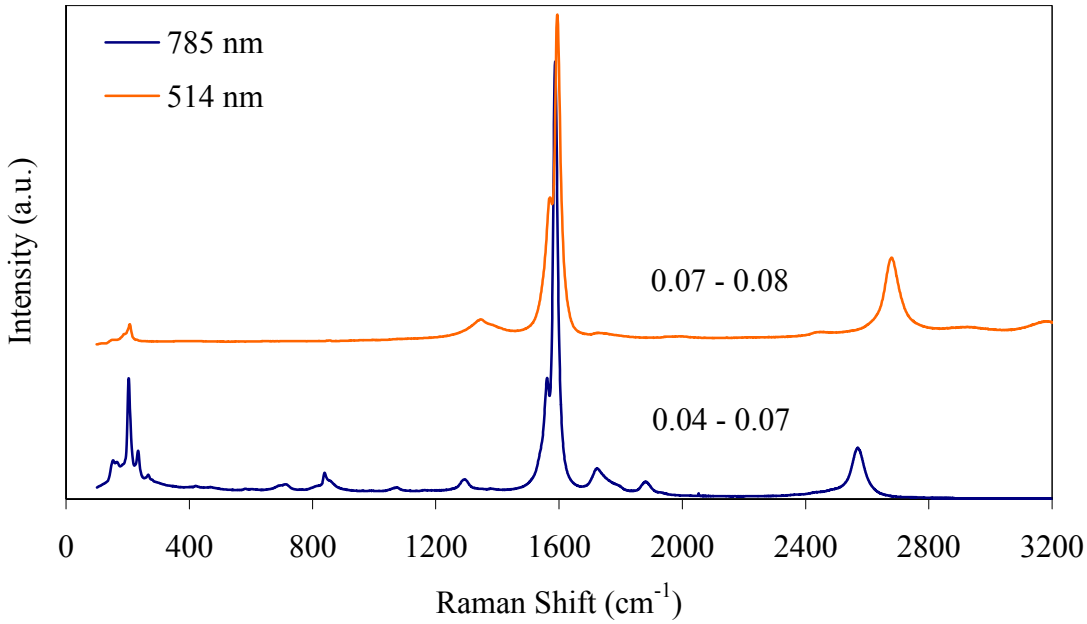

Figure 125: Raman Spectra of SWNTs after 2 h acid oxidation and lyophilization.

The final oxidized and lyophilized product was found to still be water soluble. Figure 126 shows a comparison of the SWNT 183.6 Pure sample in water after aggressive tip sonication against that of the 6 h oxidized sample dispersed by bath sonication.

Figure 126: Image of (left) SWNT 183.6 after aggressive tip sonication in water for 30 min. pulsed at 5 s on 1 s off and (right) dilute aqueous solution of lyophilized 6 h oxidized SWNT 183.6 re-dispersed in water by bath sonication.

The insolubility of pristine SWNT 183.6 is water is apparent. For the 6 h oxidized sample dissolution in the aqueous phase is believed to be controlled by more favorable solute-solvent interactions induced by the oxygen rich groups on the surface as well as the presence of carboxylate ions. Figure 127 shows the result of a pH dependant UV-visible spectra to determine the presence of SWNT charging. The as-produced sample had a *pH* of 6 and was raised to *pH* 10 by addition of NaOH. Examining Figure 127, the peak near 650 nm is attributed to the 1st Van Hove transition of metallic SWNTs [209]. The effect of slight dilution with the addition of base appears to be negated by an increase

in absorbance and feature definition. The increase in bandgap fluorescence is believed to be a result of tube charging from the formation of carboxylate ions and thus again proves carboxylic functionalization. This absorbance behavior is in agreement with photon quenching observed in poor SWNT dispersions by Graff et al. (2005) [210].

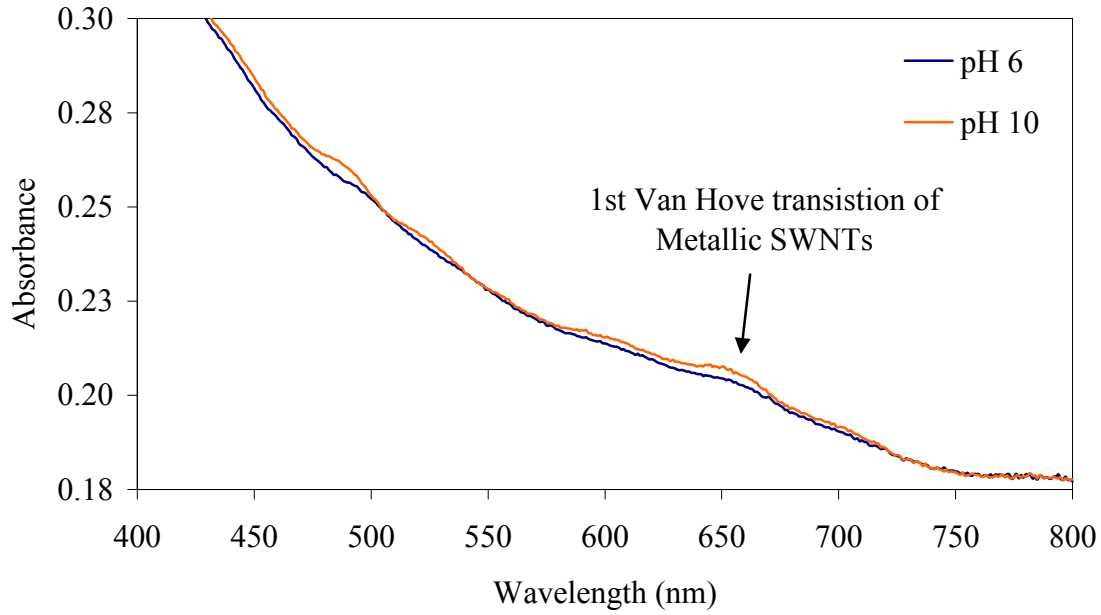

Figure 127: The UV-visible spectra for 6 h acid oxidized SWNTs after lypholization and re-dispersion in water and variation of solution *pH*.

The aqueous solution from the 6 h oxidized sample was also dropped directly onto an SEM stub for imaging both before and after centrifugation. The sample without centrifugation in Figure 128 appears to have a significant amount of amorphous carbon generated from the oxidation and sonication treatment. After centrifugation the sample appears markedly different as seen by Figure 129. Here, the amorphous carbon is not noticeable and "crack bridging" can be seen over distances approximately 600-800 nm, presumably longer than the SWNT contour length. Higher magnification images across

the cracks can be seen in Figure 130. The SWNT film appears to be mechanically robust as indicated by the intertube-interfacial adhesion allowing for crack bridging. Furthermore, this can be seen from examining Figure 131 showing the leading edge of a crack in the dried drop. Here, the crack propagation, created by capillary forces as the solvent evaporated, appears to have been halted from progression by crack bridging of the SWNTs.

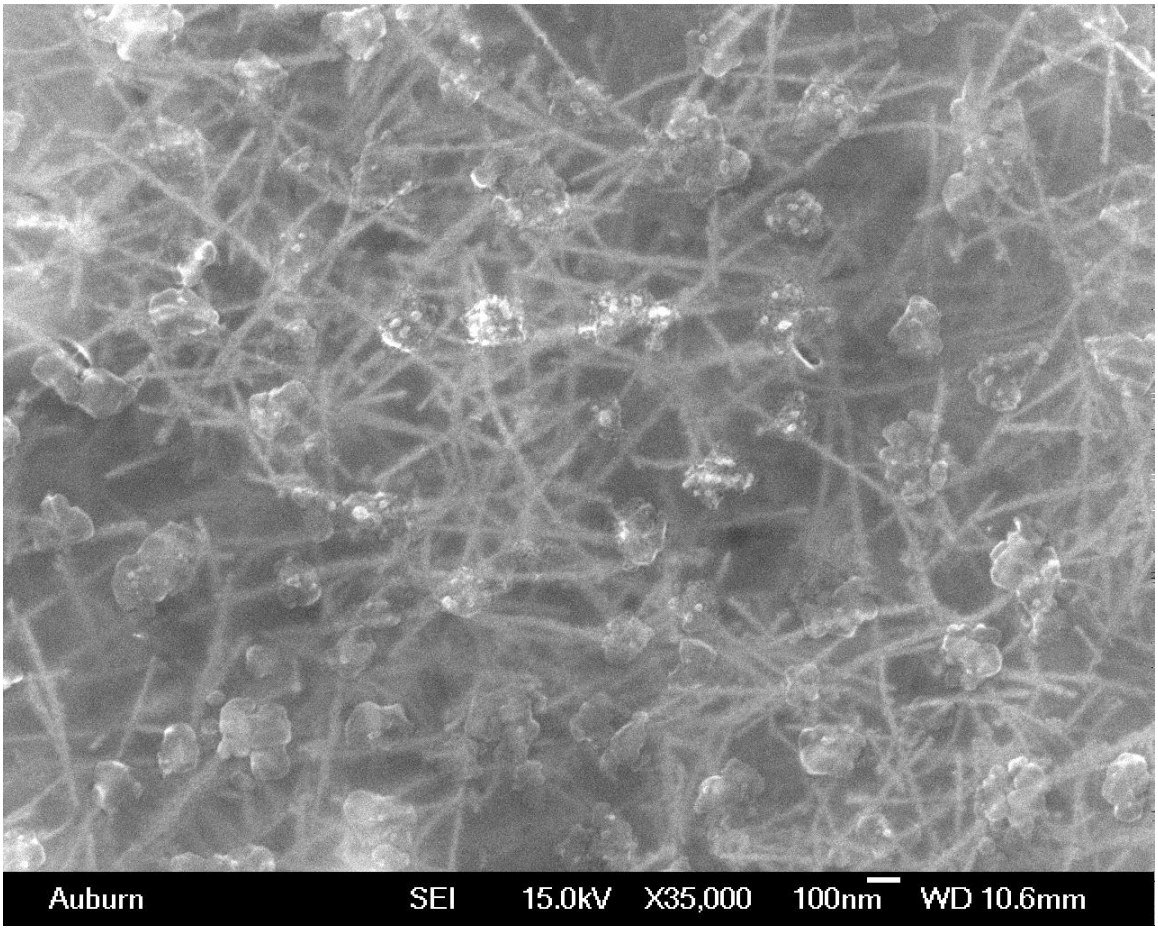

Figure 128: Drop dried image of lyophilized 6 h acid oxidized SWNTs that were re-dispersed in water. Both SWNTs and amorphous carbon generated from the oxidation can be seen.

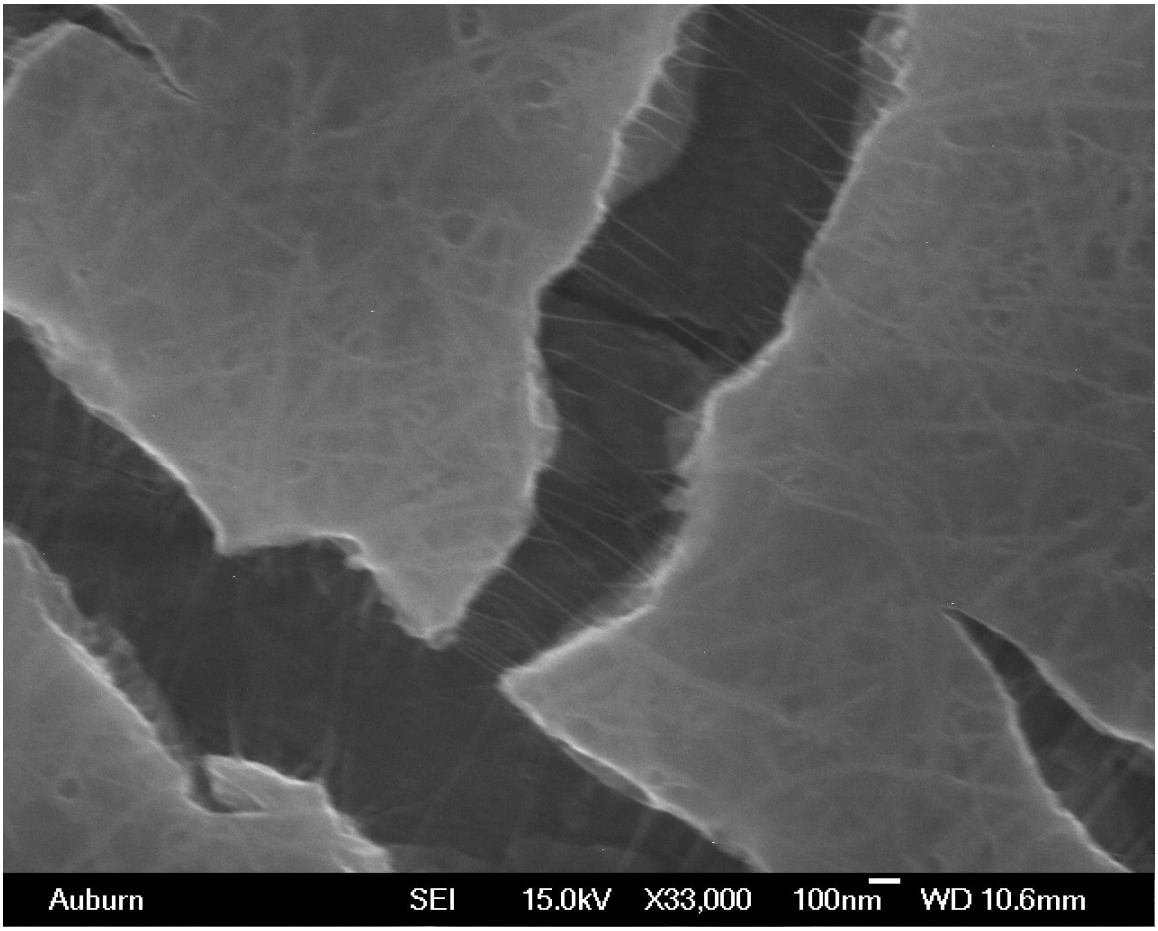

Figure 129: Drop dried image of lyophilized 6 h acid oxidized SWNTs that were re-dispersed in water and centrifuged at 17k x g for 90 min.

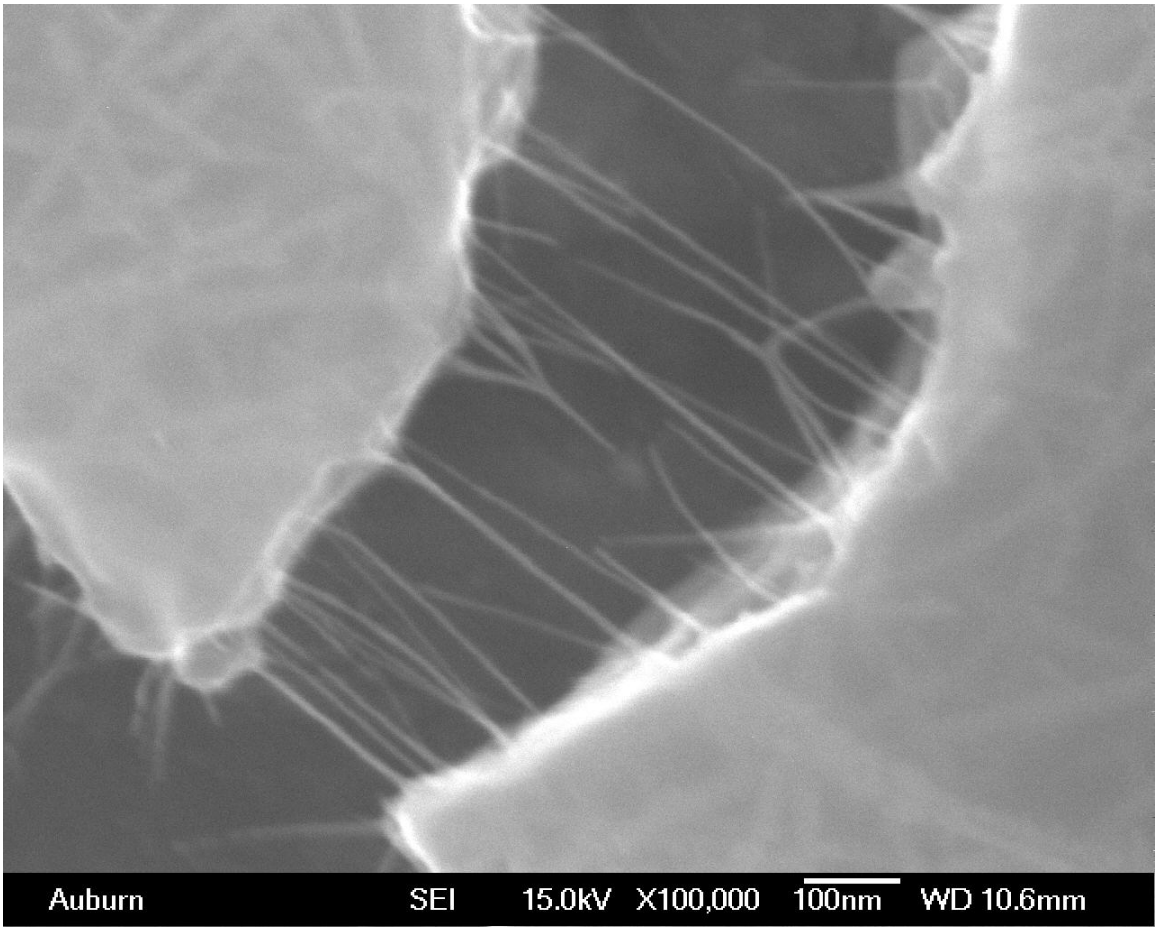

Figure 130: High resolution image of crack bridging from a drop dried and centrifuged aqueous dispersion of lyophilized 6 h acid oxidized SWNTs.

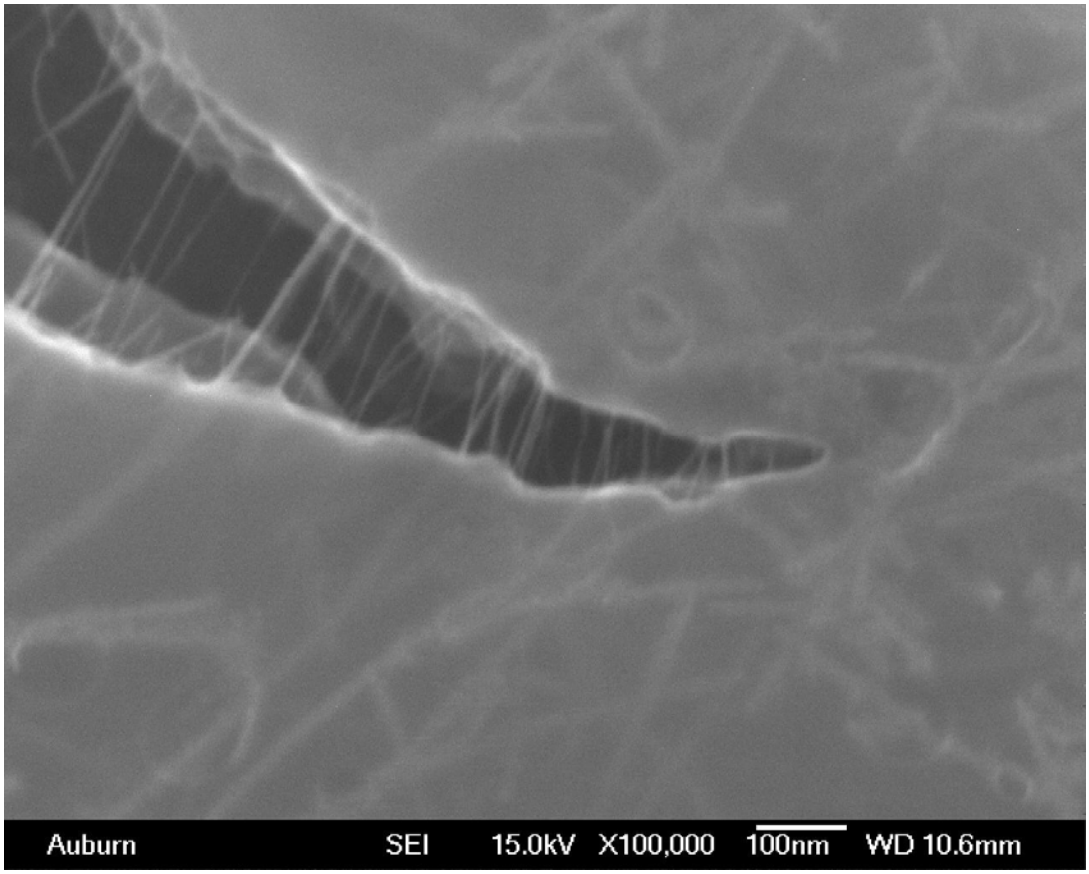

Figure 131: Drop dried image of the 6 h oxidized dispersion after centrifugation and drop drying showing crack propagation/bridging phenomena.

The apparent mechanical robustness of the sample after oxidation can be explained by examining the Raman spectra before and after oxidation. Specifically, by comparing the diameter dependant radial breathing modes as shown in Figure 132. The disappearance of the peaks at 247 nm and 261 nm indicates the consumption of small diameter metallic SWNTs during treatment. This resulted in a narrower tube diameter distribution, which increased the shear modulus of the tube bundles, resulting in higher film modulus. Furthermore, the amorphous carbon generated can fill voids in the films [126].

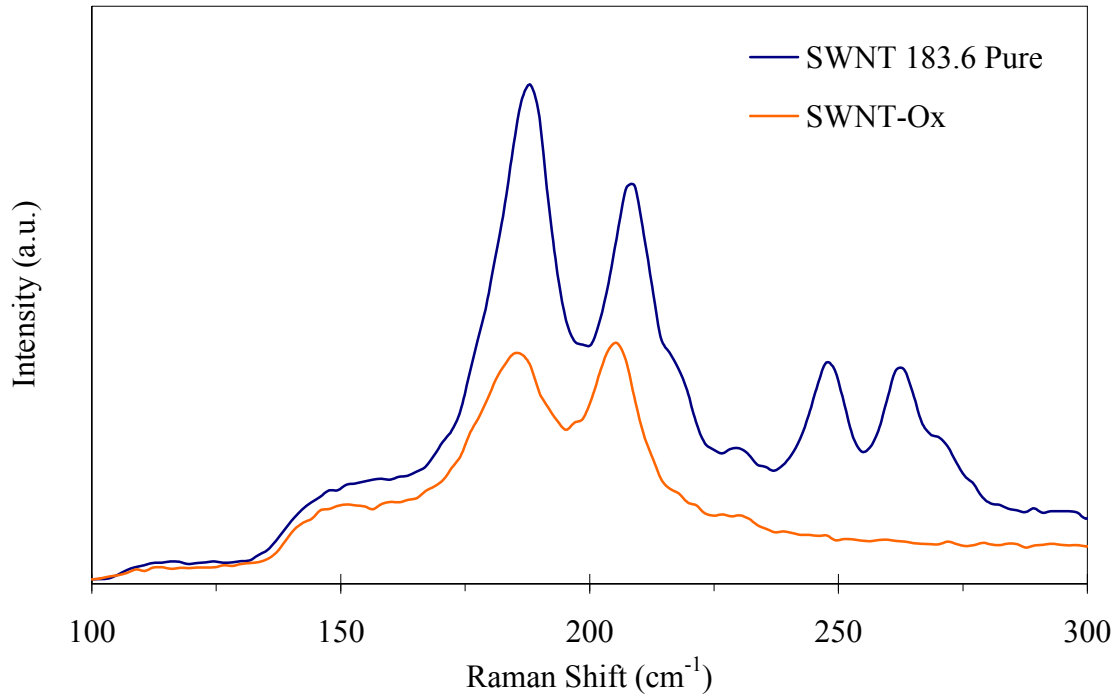

Figure 132: Comparison of the Raman Spectra at 514 nm excitation of SWNT 183.6 Pure before and after (183.6 Ox) acid oxidation showing small diameter digestion.

In summary, this method for creating aligned films is attractive for a number of reasons. First, the water is used instead of an exotic organic solvent. Second, the oxidation method described for this process can replace the purification step in raw tubes, which may reduce the amount of damage introduced onto the nanotube sidewalls. Early attempts to template macroscale films have also been successful by freezing aqueous dispersions of the 6 h oxidized tubes inside a Petri dish. Through these experiments the mode of self-assembly has been partially identified. It appears that the act of freezing itself initiates the process, not the subsequent treatment under high vacuum in the lyophilization chamber. This may be a result of a change in solvent strength upon phase change.

5. CONCLUSIONS AND RECOMMENDATIONS

The intention of this work was to provide a detailed analysis on the critical aspects related to the dispersion of carbon nanotubes in a viscous unsaturated polyester resin. The results of various nanotube dispersion techniques such as bath sonication, syringe extrusion, and high shear mixing were characterized. Only high shear mixing was successful in dispersing single-walled carbon nanotubes, but was unable to exfoliate individual tubes alone. Bulk rheological measurements were made pre-cure in order to probe fluid microstructure and draw conclusions on the effect of nanotube specific viscoelastic property enhancement. It was determined that pristine single-walled carbon nanotubes (SWNT 183.6 Pure) showed the greatest reinforcing potential over acid oxidized nanotubes (SWNT-Ox Film) and vapor grown carbon fibers. Using primarily controlled strain oscillatory shear measurements, two major types of concentration dependant behavior were identified for SWNT 183.6 Pure dispersions.

First, over the range of concentrations from 0.025% - 0.250% vol., viscoelastic behavior was found. Colloidal scaling was used to remove the dependence of concentration on the viscoelastic response while providing insight into network development. The resulting mastercurve showed two separate subtypes of rheological response. At concentrations near 0.025% vol., a developing nanotube network structure was observed. At concentrations near and above 0.100% vol. a saturated and elastic network structure began to form. These observations were correlated with percolation.

Common methods for examining percolation such as low frequency storage modulus response and power-law scaling were employed. Additionally, a recently developed method tracking the network yield stress was compared. It was determined that the onset of rheological percolation occurred at ~0.100% vol. loading in all methods. However, the network strength was weaker than predicted for bond force percolation theory. This was attributed for the bundled dispersion state of the nanotubes as indicated by the effective hydrodynamic aspect ratio and TEM analysis. In addition, parallels between the onset of percolation from storage modulus data and the trend in crossover parameters were found.

In the second type of rheological behavior, for the range of concentrations from 0.0030% - 0.010% vol., the dispersions were found to behave as a viscous liquid. Through the linear viscoelastic response, no indication of nanotube interaction or network development was observed over this concentration regime. Using a reduced complex viscosity, the concentration dependence on rheological response was removed. The slope of the shear thinning data revealed non-Brownian behavior. This was supported by theoretical calculations for the rotational Peclet number, based on a conservative estimation of the rotary diffusivity. As a result of the bundled nanotube dispersion state, experimentally imposed hydrodynamic forces were dominant. Thus, the SWNT 183.6 Pure samples were extremely sensitive to shear history.

Through the application of small shear rates over long time scales, shear dependant aggregation behavior was observed in dilute nanotube dispersions. Experiments using various single-walled carbon nanotubes indicated the driving force for shear aggregation was chemical in nature, as opposed to being a function of the

dispersion state. Surface analysis and comparative measurements indicated oxygen rich functionalities were capable of providing dispersion stability. Specifically, experiments suggest hydroxyl and phenolic groups helped prevent nanotubes from re-aggregation. Physically, the ability for these functional groups to hydrogen bond with the isophthalic polyester structure supports this finding.

All attempts at dispersing acid oxidized nanotubes failed without prior treatment in ethanol (SWNT-Ox Film). It was concluded that carboxylic functional groups were not compatible with unsaturated polyester resin. The presence of adsorbed ethanol was believed to aid in increasing the compatibility between oxidized nanotubes and the resin. The specific nature of the chemical interaction in the presence of ethanol is unknown. From this study, it is recommended that future experiments be carried out with a treatment method capable of oxidizing nanotubes to primarily alcohol based functionalities (hydroxyl, phenolic), rather than from carbonyl to carboxylic groups.

The current state of nanotube solution thermodynamics was critically analyzed and used to estimate the heat of mixing in SWNT-UPR dispersions. Calculations support experimental evidence showing the enthalpy of mixing to be large and positive. Estimates of the Gibbs free energy indicate the dispersions were only kinetically stable. The observation of low shear aggregation and dispersion phase separation over prolonged periods of storage support this conclusion.

Finally, the discovery of a lyophilization based method for creating aligned self-assembled films from aqueous, oxidized nanotube dispersions was reported. In future applications, it is recommended that this method be used to replace typical nanotube

purification steps, thus minimizing nanotube damage from overprocessing. The nanotube self-assembly was believed to occur during the freezing of the dispersion.

In summary, the state of the art in commercial thermoset polymer composites reflects an interest in utilizing high performance and lightweight materials to push the limits of design and application. With this in mind, the intent of this work was to characterize a potential next generation lightweight thermoset composite material with the hope of motivating new applications for older technologies, such as unsaturated polyester resins. This research provides a significant advancement the in the scientific understanding of dispersion and physical behavior of carbon nanotube-unsaturated polyester resin systems.

REFERENCES

1. Moniruzzaman, M. and K.I. Winey, *Polymer Nanocomposites Containing Carbon Nanotubes.* Macromolecules, 2006. **39**(16): p. 5194-5205.
2. Vaia, R.A. and H.D. Wagner, *Framework for nanocomposites.* Materials Today, 2004. **7**(11): p. 32-37.
3. Kumar, A. and R.K. Gupta, *Fundamentals of Polymer Engineering*. 2003: CRC Press.
4. Mallick, P.K., *Fiber-reinforced Composites: Materials, Manufacturing, and Design*. 1993: CRC Press.
5. Callister, W.D., *Materials Science and Engineering: An Introduction*. 1997: John Wiley & Sons.
6. Hussain, F., et al., *Review article: Polymer-matrix nanocomposites, processing, manufacturing, and application: An overview.* Journal of Composite Materials, 2006. **40**(17): p. 1511-1575.
7. Tasis, D., et al., *Chemistry of carbon nanotubes.* Chemical Reviews, 2006. **106**(3): p. 1105-1136.
8. Thostenson, E.T., C. Li, and T.-W. Chou, *Nanocomposites in context.* Composites Science and Technology, 2005. **65**(3-4): p. 491-516.
9. Gojny, F.H., et al., *Carbon nanotube-reinforced epoxy-composites: enhanced stiffness and fracture toughness at low nanotube content.* Composites Science and Technology, 2004. **64**(15): p. 2363-2371.
10. O. Breuer, U.S., *Big returns from small fibers: A review of polymer/carbon nanotube composites*. 2004. p. 630-645.
11. Xie, X.-L., Y.-W. Mai, and X.-P. Zhou, *Dispersion and alignment of carbon nanotubes in polymer matrix: A review.* Materials Science and Engineering: R: Reports, 2005. **49**(4): p. 89-112.
12. J. N. Coleman, U.K.Y.K.G.k., *Mechanical Reinforcement of Polymers Using Carbon Nanotubes*. 2006. p. 689-706.
13. Park, J.-M., et al., *Self-sensing and interfacial evaluation of Ni nanowire/polymer composites using electro-micromechanical technique.* Composites Science and Technology, 2007. **67**(10): p. 2121-2134.
14. Seyhan, A.T., et al., *Rheological and dynamic-mechanical behavior of carbon nanotube/vinyl ester-polyester suspensions and their nanocomposites.* European Polymer Journal, 2007. **43**(7): p. 2836-2847.
15. Thostenson, E.T., S. Ziaee, and T.-W. Chou, *Processing and electrical properties of carbon nanotube/vinyl ester nanocomposites.* Composites Science and Technology. **In Press, Corrected Proof**.

16. Fan, Z. and S.G. Advani, *Characterization of orientation state of carbon nanotubes in shear flow.* Polymer, 2005. **46**(14): p. 5232-5240.
17. Malik, M., V. Choudhary, and I.K. Varma, *Current status of unsaturated polyester resins.* Journal of Macromolecular Science-Reviews in Macromolecular Chemistry and Physics, 2000. **C40**(2-3): p. 139-165.
18. Mallick, P.K., *Composites Engineering Handbook*. 1997: CRC Press.
19. Seyhan, A.T., et al., *Critical aspects related to processing of carbon nanotube/unsaturated thermoset polyester nanocomposites.* European Polymer Journal, 2007. **43**(2): p. 374-379.
20. Battisti, A., A.A. Skordos, and I.K. Partridge, *Monitoring dispersion of carbon nanotubes in a thermosetting polyester resin.* Composites Science and Technology. **In Press, Corrected Proof**.
21. *CARBON NANOTUBE (CNT) TECHNOLOGY IN EASTON'S ENHANCED RESIN SYSTEM*. [cited 2008 9/21]; Available from: http://www.eastonbike.com/PRODUCTS/TECHNOLOGY/tech_cnt.html.
22. *Tennis Technology*. [cited 2008 9/20]; Available from: http://www.babolat.com/english/tennis/technology/index.php?src=tennis.
23. *Products: STULTZ Tri-Edge Golf Shaft*. [cited 2008 9/20]; Available from: http://www.stulzgolf.com/products.html.
24. *787 Dreamliner*. 2008 05/20/2008 [cited 2008 09/21]; Available from: http://www.boeing.com/commercial/787family/background.html.
25. Walz, M. *The Dream of Composites*. Rdmag **Volume**,
26. Chanda, M. and S.K. Roy, *Plastics Technology Handbook*. 1998: Marcel Dekker.
27. Fried, J.R., *Polymer Science and Technology*. 1995: Prentice Hall PTR.
28. Leffingwell, R. and D. Newhardt, *Corvette: Fifty Years*. 2002: MotorBooks/MBI Publishing Company.
29. Rodriguez, F., et al., *Principles of polymer systems*. 5 ed. 2003: Taylor & Francis.
30. Uchida, T., et al., *Morphology and modulus of vapor grown carbon nano fibers.* Journal of Materials Science, 2006. **41**: p. 5851-5856.
31. Ting, J.-M. and M.L. Lake, *Vapor-grown carbon-fiber reinforced carbon composites.* Carbon, 1995. **33**(5): p. 663-667.
32. Dresselhaus, M.S., G. Dresselhaus, and P.C. Eklund, *Science of Fullerenes and Carbon Nanotubes: Their Properties and Applications*. 1995: Academic Press.
33. Merkulov, V.I., et al., *Patterned growth of individual and multiple vertically aligned carbon nanofibers.* Applied Physics Letters, 2000. **76**(24): p. 3555-3557.
34. Endo, M., et al., *Selective and Efficient Impregnation of Metal Nanoparticles on Cup-Stacked-Type Carbon Nanofibers*. 2003. p. 723-726.
35. Tibbetts, G.G. and C.P. Beetz, *Mechanical properties of vapour-grown carbon fibres.* Journal of Physics D: Applied Physics, 1987. **20**(3): p. 292-297.
36. Chen, Y.-M. and J.-M. Ting, *Ultra high thermal conductivity polymer composites.* Carbon, 2002. **40**(3): p. 359-362.
37. Endo, M., et al., *Vapor-grown carbon fibers (VGCFs): Basic properties and their battery applications.* Carbon, 2001. **39**(9): p. 1287-1297.
38. Iijima, S., *Helical Microtubules of Graphitic Carbon.* Nature, 1991. **354**(6348): p. 56-58.

39. Ebbesen, T.W. and P.M. Ajayan, *Large-Scale Synthesis of Carbon Nanotubes.* Nature, 1992. **358**(6383): p. 220-222.
40. Iijima, S. and T. Ichihashi, *Single-Shell Carbon Nanotubes of 1-Nm Diameter.* Nature, 1993. **363**(6430): p. 603-605.
41. Bethune, D.S., et al., *Cobalt-Catalyzed Growth of Carbon Nanotubes with Single-Atomic-Layerwalls.* Nature, 1993. **363**(6430): p. 605-607.
42. Dyke, C.A. and J.M. Tour, *Covalent functionalization of single-walled carbon nanotubes for materials applications.* Journal of Physical Chemistry A, 2004. **108**(51): p. 11151-11159.
43. Zheng, L.X., et al., *Ultralong single-wall carbon nanotubes.* Nat Mater, 2004. **3**(10): p. 673-676.
44. Haddon, R.C., *Chemistry of the Fullerenes: The Manifestation of Strain in a Class of Continuous Aromatic Molecules.* Science, 1993. **261**(5128): p. 1545-1550.
45. Ebbesen, T.W. and T. Takada, *Topological and SP3 defect structures in nanotubes.* Carbon, 1995. **33**(7): p. 973-978.
46. Yao, N., et al., *Structure and oxidation patterns of carbon nanotubes.* Journal of Materials Research, 1998. **13**(9): p. 2432-2437.
47. Baughman, R.H., A.A. Zakhidov, and W.A. de Heer, *Carbon nanotubes - the route toward applications.* Science, 2002. **297**(5582): p. 787-792.
48. Gao, G.H., T. Cagin, and W.A. Goddard, *Energetics, structure, mechanical and vibrational properties of single-walled carbon nanotubes.* Nanotechnology, 1998. **9**(3): p. 184-191.
49. Krishnan, A., et al., *Young's modulus of single-walled nanotubes.* Physical Review B, 1998. **58**(20): p. 14013.
50. Yu, M.F., et al., *Tensile loading of ropes of single wall carbon nanotubes and their mechanical properties.* Physical Review Letters, 2000. **84**(24): p. 5552-5555.
51. Walters, D.A., et al., *Elastic strain of freely suspended single-wall carbon nanotube ropes.* Applied Physics Letters, 1999. **74**(25): p. 3803-3805.
52. Frank, S., et al., *Carbon nanotube quantum resistors.* Science, 1998. **280**(5370): p. 1744-1746.
53. Hone, J., et al., *Electrical and thermal transport properties of magnetically aligned single wall carbon nanotube films.* Applied Physics Letters, 2000. **77**(5): p. 666-668.
54. Thess, A., et al., *Crystalline ropes of metallic carbon nanotubes.* Science, 1996. **273**(5274): p. 483-487.
55. Kim, P., et al., *Thermal transport measurements of individual multiwalled nanotubes.* Physical Review Letters, 2001. **8721**(21).
56. Hone, J., et al., *Thermal conductivity of single-walled carbon nanotubes.* Physical Review B, 1999. **59**(4): p. R2514.
57. Kociak, M., et al., *Superconductivity in ropes of single-walled carbon nanotubes.* Physical Review Letters, 2001. **86**(11): p. 2416-2419.
58. Tang, Z.K., et al., *Superconductivity in 4 angstrom single-walled carbon nanotubes.* Science, 2001. **292**(5526): p. 2462-2465.

59. Collins, P.G. and P. Avouris, *Nanotubes FOR Electronics.* Scientific American, 2000. **283**(6): p. 62.
60. O'Connell, M.J., et al., *Reversible water-solubilization of single-walled carbon nanotubes by polymer wrapping.* Chemical Physics Letters, 2001. **342**(3-4): p. 265-271.
61. Autumn, K., et al., *Evidence for van der Waals adhesion in gecko setae.* Proceedings of the National Academy of Sciences of the United States of America, 2002. **99**(19): p. 12252-12256.
62. Prausnitz, J.M., R.N. Lichtenthaler, and E.G.d. Azevedo, *Molecular Thermodynamics of Fluid-phase Equilibria*. 3 ed. 1999: Prentice Hall PTR.
63. Parsegian, V.A., *Van Der Waals Forces: A Handbook for Biologists, Chemists, Engineers, and Physicists*. 2005: Cambridge University Press.
64. Hamaker, H.C., *The London-van der Waals attraction between spherical particles.* Physica, 1937. **4**(10): p. 1058-1072.
65. Israelachvili, J.N., *Intermolecular and Surface Forces*. 1991.
66. Derjaguin, B., *Research on Friction and Adhesion .4. Theory of Adhesion of Small Particles (Reprinted from Kolloid Z, Vol 69, Pg 155-164, 1934).* Progress in Surface Science, 1992. **40**(1-4): p. 6-15.
67. Macosko, C.W. and R.G. Larson, *Rheology: Principles, Measurements, and Applications*. 1994.
68. O'Connell, M.J., et al., *Band gap fluorescence from individual single-walled carbon nanotubes.* Science, 2002. **297**(5581): p. 593-596.
69. Girifalco, L.A., M. Hodak, and R.S. Lee, *Carbon nanotubes, buckyballs, ropes, and a universal graphitic potential.* Physical Review B, 2000. **62**(19): p. 13104-13110.
70. Sun, C.H., et al., *Van der Waals interactions between two parallel infinitely long single-walled nanotubes.* Chemical Physics Letters, 2005. **403**(4-6): p. 343-346.
71. O'Connell, M.J., et al., *Band Gap Fluorescence from Individual Single-Walled Carbon Nanotubes.* Science, 2002. **297**(5581): p. 593-596.
72. Coffin, D.W., L.A. Carlsson, and R.B. Pipes, *On the separation of carbon nanotubes.* Composites Science and Technology, 2006. **66**(9): p. 1132-1140.
73. Sun, C.-H., et al., *Van der Waals interactions between two parallel infinitely long single-walled nanotubes.* Chemical Physics Letters, 2005. **403**(4-6): p. 343-346.
74. Chen, B., et al., *Binding energy of parallel carbon nanotubes.* Applied Physics Letters, 2003. **83**(17): p. 3570-3571.
75. Huang, Y.Y. and E.M. Terentjev, *Dispersion and rheology of carbon nanotubes in polymers.* International Journal of Material Forming, 2008. **1**(2): p. 63-74.
76. Lau, K.-T. and D. Hui, *Effectiveness of using carbon nanotubes as nano-reinforcements for advanced composite structures.* Carbon, 2002. **40**(9): p. 1605-1606.
77. Schadler, L.S., S.C. Giannaris, and P.M. Ajayan, *Load transfer in carbon nanotube epoxy composites.* Applied Physics Letters, 1998. **73**(26): p. 3842-3844.
78. Miyagawa, H. and L.T. Drzal, *Thermo-physical and impact properties of epoxy nanocomposites reinforced by single-wall carbon nanotubes.* Polymer, 2004. **45**(15): p. 5163-5170.

79. Miyagawa, H., M. Misra, and A.K. Mohanty, *Mechanical properties of carbon nanotubes and their polymer nanocomposites.* Journal of Nanoscience and Nanotechnology, 2005. **5**(10): p. 1593-1615.
80. Krishnamoorti, R. and R.A. Vaia, *Polymer nanocomposites.* Journal of Polymer Science Part B-Polymer Physics, 2007. **45**(24): p. 3252-3256.
81. Fan, Z.H. and S.G. Advani, *Rheology of multiwall carbon nanotube suspensions.* Journal of Rheology, 2007. **51**(4): p. 585-604.
82. Sandler, J., et al., *Development of a dispersion process for carbon nanotubes in an epoxy matrix and the resulting electrical properties.* Polymer, 1999. **40**: p. 5967-5971.
83. Gong, X., et al., *Surfactant-Assisted Processing of Carbon Nanotube/Polymer Composites*. 2000. p. 1049-1052.
84. Lin-Gibson, S., et al., *Elastic Flow Instability in Nanotube Suspensions.* Physical Review Letters, 2004. **92**(4): p. 048302.
85. Haggenmueller, R., J.E. Fischer, and K.I. Winey, *Single Wall Carbon Nanotube/Polyethylene Nanocomposites: Nucleating and Templating Polyethylene Crystallites.* Macromolecules, 2006. **39**(8): p. 2964-2971.
86. Fangming Du, J.E.F.K.I.W., *Coagulation method for preparing single-walled carbon nanotube/poly(methyl methacrylate) composites and their modulus, electrical conductivity, and thermal stability.* Journal of Polymer Science Part B: Polymer Physics, 2003. **41**(24): p. 3333-3338.
87. Islam, M.F., et al., *High Weight Fraction Surfactant Solubilization of Single-Wall Carbon Nanotubes in Water*. 2003. p. 269-273.
88. Badaire, S., et al., *In Situ Measurements of Nanotube Dimensions in Suspensions by Depolarized Dynamic Light Scattering*. 2004. p. 10367-10370.
89. Zhu, J., et al., *Improving the Dispersion and Integration of Single-Walled Carbon Nanotubes in Epoxy Composites through Functionalization*. 2003. p. 1107-1113.
90. Banerjee, S., T. Hemraj-Benny, and S.S. Wong, *Covalent surface chemistry of single-walled carbon nanotubes.* Advanced Materials, 2005. **17**(1): p. 17-29.
91. Huang, Y.Y., S.V. Ahir, and E.M. Terentjev, *Dispersion rheology of carbon nanotubes in a polymer matrix.* Physical Review B, 2006. **73**(12).
92. Sandler, J.K.W., et al., *Ultra-low electrical percolation threshold in carbon-nanotube-epoxy composites.* Polymer, 2003. **44**(19): p. 5893-5899.
93. Martin, C.A., et al., *Formation of percolating networks in multi-wall carbon-nanotube-epoxy composites.* Composites Science and Technology, 2004. **64**(15): p. 2309-2316.
94. Rahatekar, S.S., et al., *Optical microstructure and viscosity enhancement for an epoxy resin matrix containing multiwall carbon nanotubes.* Journal of Rheology, 2006. **50**(5): p. 599-610.
95. Gojny, F.H., et al., *Influence of different carbon nanotubes on the mechanical properties of epoxy matrix composites - A comparative study.* Composites Science and Technology, 2005. **65**(15-16): p. 2300-2313.
96. Wichmann, M., et al., *Multiwall carbon nanotube/epoxy composites produced by a masterbatch process.* Mechanics of Composite Materials, 2006. **42**: p. 395-406.

97. Lin-Gibson, S., et al., *Elastic flow instability in nanotube suspensions.* Physical Review Letters, 2004. **92**(4).
98. Hobbie, E.K., et al., *Ubiquity of domain patterns in sheared viscoelastic fluids.* Physical Review E, 2004. **69**(6).
99. Shaffer, M.S.P., X. Fan, and A.H. Windle, *Dispersion and packing of carbon nanotubes.* Carbon, 1998. **36**(11): p. 1603-1612.
100. Schaefer, D., et al., *Structure and dispersion of carbon nanotubes.* Journal of Applied Crystallography, 2003. **36**: p. 553-557.
101. Schaefer, D.W., et al., *Morphology of dispersed carbon single-walled nanotubes.* Chemical Physics Letters, 2003. **375**(3-4): p. 369-375.
102. Bauer, B.J., E.K. Hobbie, and M.L. Becker, *Small-angle neutron scattering from labeled single-wall carbon nanotubes.* Macromolecules, 2006. **39**(7): p. 2637-2642.
103. Du, F., et al., *Nanotube Networks in Polymer Nanocomposites: Rheology and Electrical Conductivity*. 2004. p. 9048-9055.
104. Davis, V.A., et al., *Phase Behavior and rheology of SWNTs in superacids.* Macromolecules, 2004. **37**(1): p. 154-160.
105. Rai, P.K., et al., *Dispersions of functionalized single-walled carbon nanotubes in strong acids: Solubility and rheology.* Journal of Nanoscience and Nanotechnology, 2007. **7**(10): p. 3378-3385.
106. Hough, L.A., et al., *Viscoelasticity of single wall carbon nanotube suspensions.* Physical Review Letters, 2004. **93**(16).
107. Hobbie, E.K. and D.J. Fry, *Rheology of concentrated carbon nanotube suspensions.* Journal of Chemical Physics, 2007. **126**(12).
108. Kinloch, I.A., S.A. Roberts, and A.H. Windle, *A rheological study of concentrated aqueous nanotube dispersions.* Polymer, 2002. **43**(26): p. 7483-7491.
109. Schueler, R., et al., *Agglomeration and electrical percolation behavior of carbon black dispersed in epoxy resin.* Journal of Applied Polymer Science, 1997. **63**(13): p. 1741-1746.
110. Schmid, C.F., L.H. Switzer, and D.J. Klingenberg, *Simulations of fiber flocculation: Effects of fiber properties and interfiber friction.* Journal of Rheology, 2000. **44**(4): p. 781-809.
111. Rasheed, A., et al., *The efficiency of the oxidation of carbon nanofibers with various oxidizing agents.* Carbon, 2007. **45**(5): p. 1072-1080.
112. Li, C.C., et al., *A new and acid-exclusive method for dispersing carbon multi-walled nanotubes in aqueous suspensions.* Colloids and Surfaces a-Physicochemical and Engineering Aspects, 2007. **297**(1-3): p. 275-281.
113. Hirsch, A., *Functionalization of single-walled carbon nanotubes.* Angewandte Chemie-International Edition, 2002. **41**(11): p. 1853-1859.
114. Zhang, J., et al., *Effect of Chemical Oxidation on the Structure of Single-Walled Carbon Nanotubes*. 2003. p. 3712-3718.
115. Bruice, P.Y., *Organic Chemistry*. 3 ed. 2001: Prentice Hall.
116. McKay, S.F., *Expansion of Annealed Pyrolytic Graphite.* Journal of Applied Physics, 1964. **35**(6): p. 1992-&.

117. Esumi, K., et al., *Chemical treatment of carbon nanotubes.* Carbon, 1996. **34**(2): p. 279-281.
118. Tsang, S.C., et al., *A simple chemical method of opening and filling carbon nanotubes.* Nature, 1994. **372**(6502): p. 159-162.
119. Lago, R.M., et al., *Filling Carbon Nanotubes with Small Palladium Metal Crystallites - the Effect of Surface Acid Groups.* Journal of the Chemical Society-Chemical Communications, 1995(13): p. 1355-1356.
120. Liu, J., et al., *Fullerene pipes.* Science, 1998. **280**(5367): p. 1253-1256.
121. Jia, Z.J., et al., *Production of short multi-walled carbon nanotubes.* Carbon, 1999. **37**(6): p. 903-906.
122. Saito, T., K. Matsushige, and K. Tanaka, *Chemical treatment and modification of multi-walled carbon nanotubes.* Physica B-Condensed Matter, 2002. **323**(1-4): p. 280-283.
123. Wang, Y., J. Wu, and F. Wei, *A treatment method to give separated multi-walled carbon nanotubes with high purity, high crystallization and a large aspect ratio.* Carbon, 2003. **41**(15): p. 2939-2948.
124. Rosca, I.D., et al., *Oxidation of multiwalled carbon nanotubes by nitric acid.* Carbon, 2005. **43**(15): p. 3124-3131.
125. Zhang, X.F., et al., *Properties and structure of nitric acid oxidized single wall carbon nanotube films.* Journal of Physical Chemistry B, 2004. **108**(42): p. 16435-16440.
126. Liu, T. and S. Kumar, *Effect of Orientation on the Modulus of SWNT Films and Fibers*. 2003. p. 647-650.
127. Chen, S.M., et al., *A new approach to the functionalization of single-walled carbon nanotubes with both alkyl and carboxyl groups.* Chemical Physics Letters, 2005. **402**(4-6): p. 312-317.
128. Hwang, K.C., *Efficient Cleavage of Carbon Graphene Layers by Oxidants.* Journal of the Chemical Society-Chemical Communications, 1995(2): p. 173-174.
129. Hernadi, K., et al., *Reactivity of different kinds of carbon during oxidative purification of catalytically prepared carbon nanotubes.* Solid State Ionics, 2001. **141**: p. 203-209.
130. Ziegler, K.J., et al., *Cutting single-walled carbon nanotubes.* Nanotechnology, 2005. **16**(7): p. S539-S544.
131. Zhao, W., C. Song, and P.E. Pehrsson, *Water-Soluble and Optically pH-Sensitive Single-Walled Carbon Nanotubes from Surface Modification*. 2002. p. 12418-12419.
132. Marshall, M.W., S. Popa-Nita, and J.G. Shapter, *Measurement of functionalised carbon nanotube carboxylic acid groups using a simple chemical process.* Carbon, 2006. **44**(7): p. 1137-1141.
133. Forrest, G.A. and A.J. Alexander, *A model for the dependence of carbon nanotube length on acid oxidation time.* Journal of Physical Chemistry C, 2007. **111**(29): p. 10792-10798.
134. Tzavalas, S., et al., *Effect of carboxy-functionalized multiwall nanotubes (MWNT-COOH) on the crystallization and chain conformations of poly(ethylene*

terephthalate) PET in PET-MWNT nanocomposites. Macromolecules, 2006. **39**(26): p. 9150-9156.
135. Kim, U.J., et al., *Raman and IR spectroscopy of chemically processed single-walled carbon nanotubes.* Journal of the American Chemical Society, 2005. **127**(44): p. 15437-15445.
136. Socrates, G., *Infrared and Raman Characteristic Group Frequencies: Tables and Charts*. 3 ed. 2004: John Wiley and Sons.
137. Kuznetsova, A., et al., *Oxygen-containing functional groups on single-wall carbon nanotubes: NEXAFS and vibrational spectroscopic studies.* Journal of the American Chemical Society, 2001. **123**(43): p. 10699-10704.
138. Kyotani, T., et al., *Chemical modification of the inner walls of carbon nanotubes by HNO3 oxidation.* Carbon, 2001. **39**(5): p. 782-785.
139. Wang, Y.B., Z. Iqbal, and S. Mitra, *Rapidly functionalized, water-dispersed carbon nanotubes at high concentration.* Journal of the American Chemical Society, 2006. **128**(1): p. 95-99.
140. McCreery, R.L., *Raman Spectroscopy for Chemical Analysis*. 2000: John Wiley & Sons.
141. Ferraro, J.R., K. Nakamoto, and C.W. Brown, *Introductory raman spectroscopy*. 2003: Academic Press.
142. Dresselhaus, M.S., et al., *Raman spectroscopy of carbon nanotubes.* Physics Reports-Review Section of Physics Letters, 2005. **409**(2): p. 47-99.
143. Saito, R., et al., *Raman intensity of single-wall carbon nanotubes.* Physical Review B, 1998. **57**(7): p. 4145.
144. Davis, V.A., *Phase behavior and rheology of single-walled carbon nanotubes (SWNTs) in superacids with application to fiber spinning*, in *Engineering, Chemical*. 2006, Rice: Houston.
145. Jorio, A., et al., *Characterizing carbon nanotube samples with resonance Raman scattering.* New Journal of Physics, 2003. **5**: p. 139-139.
146. Dresselhaus, M.S., et al., *Raman spectroscopy on isolated single wall carbon nanotubes.* Carbon, 2002. **40**(12): p. 2043-2061.
147. Ferrari, A.C. and J. Robertson, *Interpretation of Raman spectra of disordered and amorphous carbon.* Physical Review B, 2000. **61**(20): p. 14095.
148. Bahr, J.L. and J.M. Tour, *Covalent chemistry of single-wall carbon nanotubes.* Journal of Materials Chemistry, 2002. **12**(7): p. 1952-1958.
149. Bahr, J.L., et al., *Functionalization of Carbon Nanotubes by Electrochemical Reduction of Aryl Diazonium Salts: A Bucky Paper Electrode.* J. Am. Chem. Soc., 2001. **123**(27): p. 6536-6542.
150. Banerjee, S. and S.S. Wong, *Rational Sidewall Functionalization and Purification of Single-Walled Carbon Nanotubes by Solution-Phase Ozonolysis.* J. Phys. Chem. B, 2002. **106**(47): p. 12144-12151.
151. Dresselhaus, M.S., G. Dresselhaus, and A. Jorio, *Raman Spectroscopy of Carbon Nanotubes in 1997 and 2007.* J. Phys. Chem. C, 2007. **111**(48): p. 17887-17893.
152. Chou, S.G., et al., *Length characterization of DNA-wrapped carbon nanotubes using Raman spectroscopy.* Applied Physics Letters, 2007. **90**(13): p. 131109-3.

153. Briggs, D., *Handbook of X-ray and Ultraviolet Photoelectron Spectroscopy*. 1977: Heyden.
154. Watts, J.F. and J. Wolstenholme, *An Introduction to Surface Analysis by XPS and AES*. 2003: John Wiley & Sons.
155. Jimenez, G.A. and S.C. Jana, *Oxidized carbon nanofiber/polymer composites prepared by chaotic mixing.* Carbon, 2007. **45**(10): p. 2079-2091.
156. Moreno-Castilla, C., M.V. Lopez-Ramon, and F. Carrasco-Marin, *Changes in surface chemistry of activated carbons by wet oxidation.* Carbon, 2000. **38**(14): p. 1995-2001.
157. Hou, P.X., et al., *Multi-step purification of carbon nanotubes.* Carbon, 2002. **40**(1): p. 81-85.
158. Zielke, U., K.J. Huttinger, and W.P. Hoffman, *Surface-oxidized carbon fibers .1. Surface structure and chemistry.* Carbon, 1996. **34**(8): p. 983-998.
159. Yue, Z.R., et al., *Surface characterization of electrochemically oxidized carbon fibers.* Carbon, 1999. **37**(11): p. 1785-1796.
160. Biniak, S., et al., *The characterization of activated carbons with oxygen and nitrogen surface groups.* Carbon, 1997. **35**(12): p. 1799-1810.
161. Yang, C.M., et al., *Surface chemistry and pore structure of purified HiPco single-walled carbon nanotube aggregates.* Physica B-Condensed Matter, 2002. **323**(1-4): p. 140-142.
162. Martinez, M.T., et al., *Sensitivity of single wall carbon nanotubes to oxidative processing: structural modification, intercalation and functionalisation.* Carbon, 2003. **41**(12): p. 2247-2256.
163. Okpalugo, T.I.T., et al., *High resolution XPS characterization of chemical functionalised MWCNTs and SWCNTs.* Carbon, 2005. **43**(1): p. 153-161.
164. Sabba, Y. and E.L. Thomas, *High-concentration dispersion of single-wall carbon nanotubes.* Macromolecules, 2004. **37**(13): p. 4815-4820.
165. Bergin, S.D., et al., *Towards solutions of single-walled carbon nanotubes in common solvents.* Advanced Materials, 2008. **20**(10): p. 1876-+.
166. Flory, P.J., *Statistical Thermodynamics of Semi-Flexible Chain Molecules.* Proceedings of the Royal Society of London Series a-Mathematical and Physical Sciences, 1956. **234**(1196): p. 60-73.
167. Onsager, L., *The Effects of Shape on the Interaction of Colloidal Particles.* Annals of the New York Academy of Sciences, 1949. **51**(4): p. 627-659.
168. Isihara, A., *Determination of Molecular Shape by Osmotic Measurement.* The Journal of Chemical Physics, 1950. **18**(11): p. 1446-1449.
169. Isihara, A., *Theory of Anisotropic Colloidal Solutions.* The Journal of Chemical Physics, 1951. **19**(9): p. 1142-1147.
170. Flory, P.J., *Phase Equilibria in Solutions of Rod-Like Particles.* Proceedings of the Royal Society of London Series a-Mathematical and Physical Sciences, 1956. **234**(1196): p. 73-89.
171. *Liquid Crystallinity in Polymers: Principles and Fundamental Properties*, ed. A. Ciferri. 1991: John Wiley & Sons, Incorporated.
172. Huggins, M.L., *Theory of Solutions of High Polymers.* J. Am. Chem. Soc., 1942. **64**(7): p. 1712-1719.

173. Huggins, M.L., *Some Properties of Solutions of Long-chain Compounds.* J. Phys. Chem., 1942. **46**(1): p. 151-158.
174. Beris, A.N. and B.J. Edwards, *Thermodynamics of Flowing Systems: With Internal Microstructure*. 1994: Oxford University Press US.
175. Wang, X.-J. and Q. Zhou, *Liquid Crystalline Polymers*. 2004: World Scientific.
176. Bergin, S.D., et al., *Towards solutions of single-walled carbon nanotubes in common solvents: Supporting Information.* Advanced Materials, 2008. **20**(10): p. 1876-+.
177. Flory, P.J., *Principles of Polymer Chemistry*. 1953: Cornell University Press.
178. Gupta, R.K., *Polymer and Composite Rheology*. 2 ed. 2000, New York: Marcel Dekker, Inc.
179. Larson, R.G., *The Structure and Rheology of Complex Fluids*. Topics in Chemical Engineering, ed. K.E. Gubbins. 1998: Oxford University Press.
180. Mezger, T.G., *The Rheology Handbook*, ed. U. Zorll. 2002: Vincentz Verlag.
181. Ferry, J.D., *Viscoelastic Properties of Polymers*. 3 ed. 1980: John Wiley and Sons.
182. Baghdadi, H.A., J. Parrella, and S.R. Bhatia, *Long-term aging effects on the rheology of neat laponite and laponite-PEO dispersions.* Rheologica Acta, 2008. **47**(3): p. 349-357.
183. Bird, B., E.N. Lightfoot, and W.E. Stewart, *Transport phenomena*. 2 ed. 2001: Wiley.
184. Lemons, D.S., P. Langevin, and A. Gythiel, *An Introduction to Stochastic Processes in Physics*. 2002: JHU Press.
185. Doi, M. and S.F. Edwards, *The Theory of Polymer Dynamics*. 1986: Oxford University Press.
186. Kirkwood, J.G. and P.L. Auer, *The Visco-Elastic Properties of Solutions of Rod-Like Macromolecules.* The Journal of Chemical Physics, 1951. **19**(3): p. 281-283.
187. Yamane, Y., Y. Kaneda, and M. Dio, *Numerical-Simulation of Semidilute Suspensions of Rodlike Particles in Shear-Flow.* Journal of Non-Newtonian Fluid Mechanics, 1994. **54**: p. 405-421.
188. Bibbo, M.A., *Rheology of semiconcentrated fiber suspensions*, in *Chemical Engineering*. 1987, Massachusetts Institute of Technology: Cambridge.
189. Hu, G., et al., *Low percolation thresholds of electrical conductivity and rheology in poly(ethylene terephthalate) through the networks of multi-walled carbon nanotubes.* Polymer, 2006. **47**(1): p. 480-488.
190. Garboczi, E.J., et al., *Geometrical percolation threshold of overlapping ellipsoids.* Physical Review E, 1995. **52**(1): p. 819.
191. Celzard, A., et al., *Critical concentration in percolating systems containing a high-aspect-ratio filler.* Physical Review B, 1996. **53**(10): p. 6209.
192. Xu, Y.Q., et al., *Controlled Multistep Purification of Single-Walled Carbon Nanotubes.* Nano Lett., 2005. **5**(1): p. 163-168.
193. Bozack, M.J., *Single Crystal 6H-SiC(0001) by XPS.* Surface Science Spectra, 1994. **3**(1): p. 82-85.

194. Bozack, M.J., Y. Zhou, and S.D. Worley, *Structural modifications in the amino acid lysine induced by soft x-ray irradiation.* The Journal of Chemical Physics, 1994. **100**(11): p. 8392-8398.
195. Abdalla, M., et al., *The effect of interfacial chemistry on molecular mobility and morphology of multiwalled carbon nanotubes epoxy nanocomposite.* Polymer, 2007. **48**(19): p. 5662-5670.
196. Sato, J. and V. Breedveld, *Evaporation blocker for cone-plate rheometry of volatile samples.* Applied Rheology, 2005. **15**(6): p. 390-397.
197. Chen, X.B., G. Shoenau, and W.J. Zhang, *Modeling of time-pressure fluid dispensing processes.* Electronics Packaging Manufacturing, IEEE Transactions on, 2000. **23**(4): p. 300-305.
198. Walters, D.A., et al., *In-plane-aligned membranes of carbon nanotubes.* Chemical Physics Letters, 2001. **338**(1): p. 14-20.
199. Trappe, V. and D.A. Weitz, *Scaling of the viscoelasticity of weakly attractive particles.* Physical Review Letters, 2000. **85**(2): p. 449-452.
200. Mitchell, C.A. and R. Krishnamoorti, *Dispersion of Single-Walled Carbon Nanotubes in Poly(e-caprolactone).* Macromolecules, 2007. **40**(5): p. 1538-1545.
201. Sahimi, M. and S. Arbabi, *Mechanics of disordered solids. II. Percolation on elastic networks with bond-bending forces.* Physical Review B, 1993. **47**(2): p. 703.
202. Mason, T.G., et al., *Rheology of F-actin solutions determined from thermally driven tracer motion.* Journal of Rheology, 2000. **44**(4): p. 917-928.
203. Morse, D.C., *Viscoelasticity of tightly entangled solutions of semiflexible polymers.* Physical Review E, 1998. **58**(2): p. R1237.
204. Chaouche, M. and D.L. Koch, *Rheology of non-Brownian rigid fiber suspensions with adhesive contacts.* Journal of Rheology, 2001. **45**(2): p. 369-382.
205. Morawetz, H., *Macromolecules in Solution*. 1983: Krieger Pub Co.
206. Marcus, Y., *The effectiveness of solvents as hydrogen bond donors.* Journal of Solution Chemistry, 1991. **20**(9): p. 929-944.
207. Ausman, K.D., et al., *Organic Solvent Dispersions of Single-Walled Carbon Nanotubes: Toward Solutions of Pristine Nanotubes.* J. Phys. Chem. B, 2000. **104**(38): p. 8911-8915.
208. Lyklema, J., *The surface tension of pure liquids: Thermodynamic components and corresponding states.* Colloids and Surfaces A: Physicochemical and Engineering Aspects, 1999. **156**(1-3): p. 413-421.
209. Chiang, I.W., et al., *Purification and Characterization of Single-Wall Carbon Nanotubes.* J. Phys. Chem. B, 2001. **105**(6): p. 1157-1161.
210. R. A. Graff, J.P.S.P.W.B.S.B.D.A.H.M.S.S., *Achieving Individual-Nanotube Dispersion at High Loading in Single-Walled Carbon Nanotube Composites.* Advanced Materials, 2005. **17**(8): p. 980-984.

APPENDIX A – DERIVATION FOR ENTHALPY OF MIXING

$$\Delta H_{mix} = E_1^{NT} + E_1^{Sol} - (E_2^{NT} + E_2^{Sol} + E_2^{NT-Sol}) \tag{A.1}$$

With:

$$E_1^{NT} = N_1\left[\left(\frac{\pi R_1^2 L_1}{\pi r^2 l}\right)2\pi r l - 2\pi R_1 L_1\right]E_{Sur}^{NT} \tag{A.2}$$

$$E_2^{NT} = N_2\left[\left(\frac{\pi R_2^2 L_2}{\pi r^2 l}\right)2\pi r l - 2\pi R_2 L_2\right]E_{Sur}^{NT} \tag{A.3}$$

$$N_2 = \frac{M_{NT}}{\rho_{NT}\pi R_2^2 L_2} \tag{A.4}$$

$$E_1^{Sol} = V_{Sol}E_{Coh}^{Sol} - A_1^{Sol}E_{Sur}^{Sol} \tag{A.5}$$

$$E_2^{Sol} = V_{Sol}E_{Coh}^{Sol} - A_2^{Sol}E_{Sur}^{Sol} - A_{Inter}^{NT-Sol}E_{Sur}^{Sol} \tag{A.6}$$

$$E_2^{NT-Sol} = 2A_{Inter}^{NT-Sol}E_{Inter}^{NT-Sol} = 2N_2 2\pi R_2 L_2 E_{Inter}^{NT-Sol} \tag{A.7}$$

$$\Delta H_{mix} = N_1\left[\left(\frac{\pi R_1^2 L_1}{\pi r^{\cdot 2} l}\right)2\pi r l - 2\pi R_1 L_1\right]E_{Sur}^{NT} + V_{Sol}E_{Coh}^{Sol} - A_1^{Sol}E_{Sur}^{Sol}$$
$$-\left(N_2\left[\left(\frac{\pi R_2^2 L_2}{\pi r^{\cdot 2} l}\right)2\pi r l - 2\pi R_2 L_2\right]E_{Sur}^{NT} + \left(V_{Sol}E_{Coh}^{Sol} - A_2^{Sol}E_{Sur}^{Sol} - A_{Inter}^{NT-Sol}E_{Sur}^{Sol}\right) + 2N_2 2\pi R_2 L_2 E_{Inter}^{NT-Sol}\right) \quad \text{(A.8)}$$

Assumption: $A_2^{Sol} \approx A_1^{Sol}$ at low loading, therefore:

$$\Delta H_{mix} = N_1\left[\left(\frac{\pi R_1^2 L_1}{\pi r^{\cdot 2} l}\right)2\pi r l - 2\pi R_1 L_1\right]E_{Sur}^{NT}$$
$$-\left(N_2\left[\left(\frac{\pi R_2^2 L_2}{\pi r^{\cdot 2} l}\right)2\pi r l - 2\pi R_2 L_2\right]E_{Sur}^{NT} + A_{Inter}^{NT-Sol}E_{Sur}^{Sol} + 2N_2 2\pi R_2 L_2 E_{Inter}^{NT-Sol}\right) \quad \text{(A.9)}$$

$$A_{Inter}^{NT-Sol} = N_2 2\pi R_2 L_2 \quad \text{(A.10)}$$

$$\Delta H_{mix} = N_1\left[\left(\frac{\pi R_1^2 L_1}{\pi r^{\cdot 2} l}\right)2\pi r l - 2\pi R_1 L_1\right]E_{Sur}^{NT} - \left(N_2\left[\left(\frac{\pi R_2^2 L_2}{\pi r^{\cdot 2} l}\right)2\pi r l - 2\pi R_2 L_2\right]E_{Sur}^{NT} + N_2 2\pi R_2 L_2\left(2E_{Inter}^{NT-Sol} - E_{Sur}^{Sol}\right)\right) \quad \text{(A.11)}$$

$$\Delta H_{mix} = \frac{M_{NT}}{\rho_{NT}\pi R_1^2 L_1}\left[\left(\frac{\pi R_1^2 L_1}{\pi r^2 l}\right)2\pi r l - 2\pi R_1 L_1\right]E_{Sur}^{NT} - \frac{M_{NT}}{\rho_{NT}\pi R_2^2 L_2}\left[\left(\frac{\pi R_2^2 L_2}{\pi r^2 l}\right)2\pi r l - 2\pi R_2 L_2\right]E_{Sur}^{NT} - N_2 2\pi R_2 L_2\left(2E_{Inter}^{NT-Sol} - E_{Sur}^{Sol}\right) \quad (A.12)$$

$$\Delta H_{mix} = \frac{2M_{NT}}{\rho_{NT}}\left[\frac{\pi}{r} - \frac{1}{R_2}\right]E_{Sur}^{NT} - \frac{2M_{NT}}{\rho_{NT}}\left[\frac{\pi}{r} - \frac{1}{R_1}\right]E_{Sur}^{NT} + \frac{2M_{NT}}{\rho_{NT}R_2}\left(E_{Sur}^{Sol} - 2E_{Inter}^{NT-Sol}\right) \quad (A.13)$$

$$\Delta H_{mix} = \frac{2M_{NT}}{\rho_{NT}}\left[\frac{1}{R_2} - \frac{1}{R_1}\right]E_{Sur}^{NT} + \frac{2M_{NT}}{\rho_{NT}R_2}\left(E_{Sur}^{Sol} - 2E_{Inter}^{NT-Sol}\right) \quad (A.14)$$

Assumption: If $R_1 >> R_2$, then R_1^{-1} negligible.

$$\Delta H_{mix} = \frac{2M_{NT}}{\rho_{NT}R_2}\left(E_{Sur}^{NT} + E_{Sur}^{Sol} - 2E_{Inter}^{NT-Sol}\right) \quad (A.15)$$

$$\phi = \frac{M_{NT}}{\rho_{NT}V_{Mix}} \quad (A.16)$$

$$\frac{\Delta H_{mix}}{V_{Mix}} \approx \frac{2\phi}{R_2}\left(E_{Sur}^{NT} + E_{Sur}^{Sol} - 2E_{Inter}^{NT-Sol}\right) \quad (A.17)$$

If this is true: $E_{Inter}^{NT-Sol} \approx \left(E_{Inter}^{NT} E_{Inter}^{Sol}\right)^{1/2}$ then;

$$\frac{\Delta H_{mix}}{V_{Mix}} \approx \frac{2\phi}{R_2}\left[E_{Sur}^{NT} - 2\left(E_{Inter}^{NT} E_{Inter}^{Sol}\right)^{1/2} + E_{Sur}^{Sol}\right] \tag{A.18}$$

with,

$$\delta_i \approx \left(E_{Sur}^{i}\right)^{1/2} \tag{A.19}$$

$$\frac{\Delta H_{mix}}{V_{Mix}} \approx \frac{2\phi}{R_2}\left[\delta_{NT}^2 - 2\delta_{NT}\delta_{Sol} + \delta_{Sol}^2\right] = \frac{2\phi}{R_2}\left(\delta_{NT} - \delta_{Sol}\right)^{1/2} \tag{A.20}$$

To determine E_{Sur}^{Sol} from the measured surface tension γ, given that in general: $S_{Sur}^{Sol} = 0.1\, mJm^{-2}K^{-1}$

$$\gamma = E_{Sur}^{Sol} - TS_{Sur}^{Sol} \tag{A.21}$$

APPENDIX B – ALTERNATE PERCOLATION GRAPHS

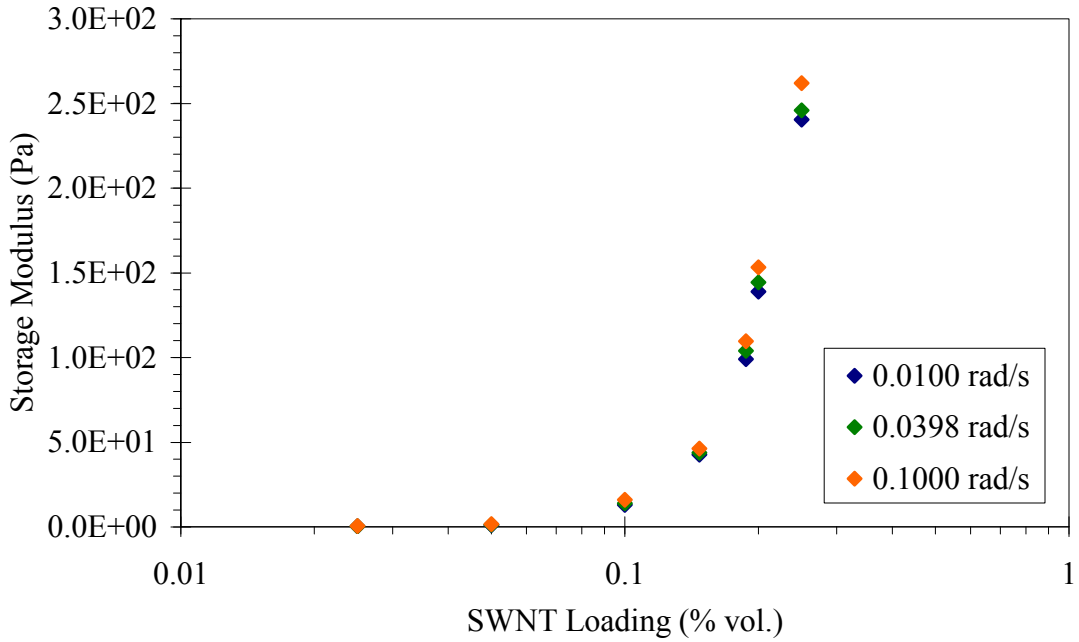

Figure B1: The storage modulus as a function of SWNT loading for fixed angular frequencies on a lin-log axis.

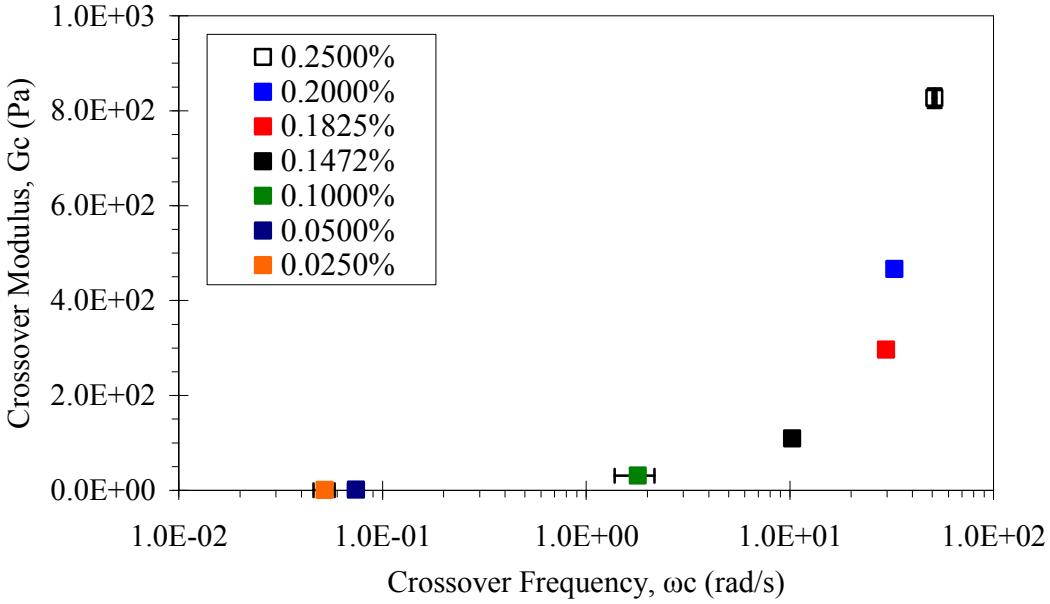

Figure B2: Plot of the crossover modulus and frequency on a lin-log axis.

APPENDIX C – FTIR OF SWNT 187.3

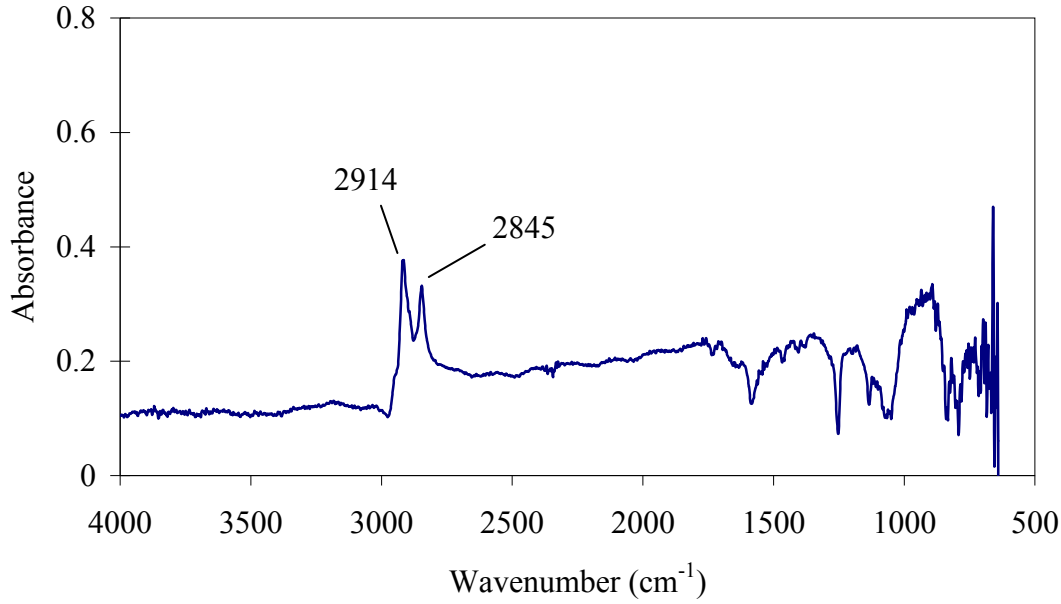

Figure C1: FTIR spectra for SWNT 187.3. The sample was dispersed in 1,2-dichlorobenzene and dropped on a ZnSe ATR crystal. The peaks are representative of sp^2 hybridized carbons.